Design and application of sensitive detection methods for the study of biological systems

A thesis submitted in partial fulfilment
of the requirements for
the degree of Doctor of Philosophy

Trinity 2015

Catlin Gunn Merton College

Ah, there's nothing more exciting than science.
You get all the fun of... sitting still, being quiet,
writing down numbers, paying attention...
Science has it all.

SKINNER — BART'S COMET (2F11)

Design and application of sensitive detection methods for the study of biological systems

Catlin Gunn Merton College Trinity 2015

A thesis submitted in partial fulfilment of the requirements for the degree of Doctor of Philosophy

Molten globules are compact intermediates in the protein folding process which retain native-like secondary structure, but have a fluctuating ensemble of tertiary folds. Human α-lactalbumin is a Ca^{2+} binding protein which forms a molten globule at pH 2. Although much is known about the secondary structure of the α-lactalbumin molten globule, the tertiary structure has so far not been elucidated. Presented in Chapter 2 is a double electron-electron resonance study of α-lactalbumin. The C-helix was found to be fully folded in the molten globule, in agreement with previous studies. Furthermore, it is also shown that both the N- and C-termini are in close proximity to the C-helix, forming part of the hydrophobic core of the protein. Data collected in the presence of 8 M urea show that the protein is unfolded under these conditions, and distinguishes the molten globule state from this. These data provide quantitative information about the tertiary structure of the α-lactalbumin molten globule, and may provide important insight into the protein folding process.

Although a wide variety of chemical and biological systems are known to be sensitive to the strength of an applied magnetic field, no biological systems, such as the cryptochrome proteins believed to be the magnetoreceptors in migratory birds, have yet been shown to be sensitive to the field direction. Traditionally, the anisotropic response of such systems to the magnetic field has been probed using photoselection or alignment with liquid crystals. The experimental sensitivity to anisotropy could, however, be improved by increasing the degree of molecular alignment, such as by crystallisation. Presented in Chapter 3 is a study of hen egg white lysozyme crystals doped with FMN, which together form a magnetically sensitive system. The crystals were studied using confocal microscopy, with the magnetic field effect being spatially resolved. The diffusion of FMN through the crystals was also studied, with the spatial variation of the magnetic field effect being explained with reference to the diffusion of FMN. Although no anisotropy of the magnetic field effect was observed in this system, the use of crystallisation as a method of controlling molecular orientation is potentially useful in systems which are expected to show anisotropy (such as cryptochrome).

The behaviour of many chemical systems differs between the bulk solution and at the interface. These interfacial processes can be difficult to probe using conventional absorption spectroscopy due to the relatively low absorbance of species at the interface as compared to the bulk. Cavity ring down and cavity enhanced absorption spectroscopy are two techniques which increase the sensitivity of absorption measurements, and evanescent wave variants of both have been applied to interfacial studies. Presented in Chapter 4 is a polarisation sensitive, broad band, evanescent wave cavity enhanced absorption experiment, which allows the study of the spectra of species at the silica/solvent interface across the visible region. A variety of systems which show interesting interfacial behaviour have been studied, including crystal violet at the silica/water interface, and with polyelectrolyte films. The data could be fitted to extract spectra, kinetics, and average orientations of three individual species. These studies demonstrate the power of the polarisation sensitive, broad band nature of this experiment in determining complex interfacial behaviour involving more than one species.

Acknowledgements

I'd like to thank Prof. Christiane Timmel first and foremost. Your guidance over the past five years has been invaluable, and your support has been second to none. To Prof. Stuart Mackenzie, thank you for all of your advice, your help, and your good humour. I wouldn't have been able to do it without you.

Thank you Prof. Mark Wallace for letting me have a go at some biochemistry, and to Dr Charlotte Dodson for teaching me almost everything I know about it. Cheers to everyone else in the Wallace group too for all the fun.

Thank you to Dr Kevin Henbest and Dr Kiminori Maeda for getting me started in the lab all those years ago, and for all your help since. Thanks to Dr Jeff Harmer, Dr Alice Bowen, and Dr Will Myers for teaching me how to play the Elexysphone, a truly bizarre instrument. Apologies to Dr Christian Kerpal for passing on the EW to you—you'll get it one day, I promise—and thank you for all the discussions we've had. Thanks too to Prof. Peter Hore, Dr Daniel Kattnig, and Dr Lauren Jarocha for your helpful suggestions.

Thank you Prof. Christina Redfield and Dr Matt Young for your collaboration on the α-lactalbumin project, Nils Pompe on the microscopy, and Dr Steven Johnson and Prof. Susan Lea for the X-ray crystallography. I enjoyed working with you very much.

Thank you Jon for putting up with me whispering over your shoulder all the time; you are the best rubber duckie anyone could want. Thanks Kelly-Anne, Claudia, Sabine, and Emrys for the laughs, the tears, the camaraderie. And to all of the Part IIs, visiting students, and friends around the department: thanks for the good times, and to those who have since left Oxford, well done for escaping.

A huge thanks to all of my friends outside the lab; housemates, folks from college, or on the scene. You're all fab.

And finally, thank you to my family for everything you've done for me. They say you can't chose your family, but if I could, I'd chose you.

Inevitably, every acknowledgement leaves out one or two people. If you feel like you should have been acknowledged here, but haven't, please fill in the gaps below as you feel fit.

I'd like to thank _____ (name) for all of their _____ (noun), their _____ (adjective) _____ (noun), and their _____ (adjective) sense of _____ (noun). They have been a _____ (adjective) _____ (noun) in getting my thesis finished, and I would have certainly _____ (past participle) _____ (adjective/adverb) without them. I can honestly say that _____ (name) is the _____ (adjective) _____ (noun) I have ever had the _____ (noun) of knowning, and I only wish I could make them truly understand how much I _____ (verb) their _____ (noun).

Contents

1 Introduction **1**

1.1 Spin . . . 1

1.1.1 Original spin . . . 1

1.1.2 Spin quantum numbers and the vector model . . . 1

1.1.3 The Zeeman effect . . . 3

1.1.4 Coupled spins . . . 4

1.1.5 The exchange interaction . . . 5

1.1.6 The dipolar interaction . . . 5

1.1.7 The hyperfine interaction . . . 6

1.1.8 The total spin Hamiltonian . . . 7

1.2 Light . . . 8

1.2.1 The transition dipole moment . . . 8

1.2.2 The Beer-Lambert law . . . 10

1.2.3 Fates of excited molecules . . . 10

1.2.3.1 Internal conversion . . . 11

1.2.3.2 Intersystem crossing . . . 11

1.2.3.3 Fluorescence . . . 11

1.2.3.4 Electron transfer . . . 12

2 Distance measurement in a partially folded protein **13**

2.1 Protein folding . . . 13

2.1.1 Levinthal's paradox . . . 13

2.1.2 Interactions driving protein folding . . . 15

2.1.3 Folding pathways . . . 15

2.1.4 The molten globule state . . . 16

2.2 α-lactalbumin . . . 16

2.2.1 Disulphide bonds in the α-lactalbumin molten globule 17
2.2.2 Non-cooperative folding in α-lactalbumin 18
2.2.3 All-Ala α-lactalbumin 18
2.2.4 Distance constraints on the tertiary fold 19
2.3 Introduction to EPR 20
2.3.1 Continuous wave EPR 20
2.3.2 Pulsed EPR 20
2.3.2.1 The rotating frame 21
2.3.3 Relaxation processes 22
2.3.3.1 Spin-lattice (longitudinal) relaxation 22
2.3.3.2 Spin-spin (transverse) relaxation 23
2.3.3.3 Spectral diffusion 23
2.3.3.4 Instantaneous diffusion 24
2.3.3.5 Nuclear spin diffusion 24
2.3.3.6 The phase memory time 24
2.3.4 A Pulsed EPR experiment 24
2.4 Double electron-electron resonance 26
2.4.1 The DEER experiment 26
2.4.2 Extraction of distance information from DEER traces 29
2.4.3 Experimental considerations 31
2.4.4 The nitroxide spin label 32
2.4.5 Choosing labelling sites and native state distance prediction 33
2.4.6 Experimental protocol 36
2.5 Short range distance measurement by Gaussian convolution of cw spectra . 37
2.6 Results and discussion 38
2.6.1 Singly-labelled samples for background correction 38
2.6.2 D87C-D97C and the C-helix 40
2.6.3 Q10C-D87C, Q10C-D97C, and the N-terminus 42
2.6.4 E121C and the C-terminus 45
2.6.5 α-lactalbumin in the prescence of 8 M urea 52
2.6.5.1 D87C-D97C 53
2.6.5.2 Q10C-D87C and Q10C-D97C 53
2.7 Conclusions and future directions 58

3 Magnetic field effects in protein crystals 60

3.1 Motivation for the work . . . 60

3.2 Spin correlated radical pairs . . . 62

3.2.1 A one-nucleus radical pair . . . 62

3.2.2 Zero field . . . 63

3.2.3 The low field effect . . . 63

3.2.4 At high magnetic fields . . . 64

3.2.4.1 Δg mixing . . . 64

3.2.4.2 Hyperfine mixing . . . 65

3.2.4.3 Relaxation . . . 65

3.2.4.4 Spin mixing in the context of the Hamiltonian . . . 66

3.2.4.5 Anisotropic spin mixing . . . 66

3.2.5 Magnetic field effects . . . 67

3.2.6 The FMN-HEWL system . . . 69

3.3 Fluorescence detected MFEs . . . 71

3.4 MFEs in protein crystals . . . 73

3.5 Protein crystallisation . . . 74

3.5.1 Crystallisation methods . . . 76

3.5.2 Crystallisation protocol . . . 77

3.6 Confocal microscopy . . . 78

3.6.1 MFE detection by confocal microscopy . . . 79

3.6.2 Fluorescence recovery after photobleaching . . . 81

3.7 Results . . . 84

3.7.1 Laser power dependence for HEWL crystals . . . 84

3.7.2 Solution phase concentration dependence . . . 87

3.7.3 MFEs in crystals . . . 89

3.7.4 Spatially resolved MFEs . . . 90

3.7.5 Diffusion in lysozyme crystals . . . 94

3.8 Conclusions and future directions . . . 97

4 Evanescent-wave broadband cavity enhanced absorption spectroscopy 99

4.1 Optical spectroscopy methods . . . 99

4.1.1 UV/vis spectroscopy . . . 99

4.1.2 Multipass spectroscopy . . . 100

4.2 Cavity methods . . . 101
4.2.0.1 The étalon . . . 101
4.2.0.2 Spherical mirror cavities . . . 103
4.2.0.3 Stability of the cavity . . . 104
4.2.1 Cavity ring-down . . . 105
4.2.2 Cavity enhanced absorption spectroscopy . . . 107
4.2.3 Broad-band CEAS . . . 109
4.2.4 Evanescent-wave CEAS . . . 112
4.2.4.1 The evanescent wave . . . 113
4.2.4.2 Evanescent wave spectroscopy . . . 115
4.2.5 Polarisation-sensitive evanescent-wave broad-band CEAS . . . 117
4.3 The silica-water interface . . . 120
4.3.1 The silica surface . . . 120
4.3.2 Aggregation at the surface . . . 121
4.4 Experimental considerations . . . 123
4.4.1 Cavity mirrors . . . 123
4.4.2 Prisms . . . 123
4.4.3 Supercontinuum source . . . 124
4.4.4 Spectrograph and CCD . . . 125
4.4.4.1 Optimum integration time . . . 126
4.4.5 Cavity calibration . . . 128
4.4.6 Limit of detection . . . 128
4.4.7 Angular resolution . . . 130
4.5 Cresol red . . . 133
4.6 Gold nanoparticles . . . 135
4.7 Methylene blue . . . 138
4.7.1 Bulk absorption spectra . . . 138
4.7.2 Methylene blue at the silica/ethanol interface . . . 140
4.7.3 Methylene blue at the silica/water interface . . . 142
4.7.4 Fitting the methylene blue spectra . . . 144
4.8 Crystal violet . . . 148
4.8.1 Crystal violet adsorption on the poly-L-lysine/water interface . . . 150
4.8.2 Crystal violet adsorption on the bare silica/water interface . . . 153

4.8.2.1 At 250 nM . . . 153
4.8.2.2 At 1.25 μM . . . 155
4.8.2.3 At 25 μM . . . 157
4.8.3 Fitting the crystal violet spectra . . . 160
4.8.4 Crystal violet adsorption on the poly-L-glutamic acid/water interface 164
4.8.4.1 At 250 nM . . . 164
4.8.4.2 At 25 μM . . . 168
4.9 Radical pairs at the interface . . . 171
4.9.1 Experimental considerations . . . 171
4.9.2 FMN . . . 172
4.9.3 FMN-HEWL . . . 172
4.10 Conclusions and future directions . . . 177

Nomenclature

AOTF	Acousto-optical tunable filter
ATR	Attenuated total reflection
AuNPs	Gold nanoparticles
BBCEAS	Broad-band cavity enhanced absorption spectroscopy
CEAS	Cavity enhanced absorption spectroscopy
CEF	Cavity enhancement factor
CRDS	Cavity ring down spectroscopy
CV	Crystal violet
DEER	Double electron-electron resonance
EPR	Electron paramagnetic resonance
EW-CEAS	Evanescent-wave cavity enhanced absorption spectroscopy
FID	Free induction decay
FMN	Flavin mononucleotide
FRAP	Fluorescence recovery after photobleaching
HEWL	Hen egg white lysozyme
IBBCEAS	Incoherent broad-band cavity enhanced absorption spectroscopy
ICOS	Integrated cavity output spectroscopy
ISC	Intersystem crossing

LSCM	Laser scanning confocal microscopy
LSPR	Localized surface plasmon resonance
MARY	Magnetically altered reaction yield
MB	Methylene blue
MD	Molecular dynamics
MTSL	Methanethiosulfonate spin label
PLGA	Poly-L-glutamic acid
PLL	Poly-L-lysine
RPM	Radical pair mechanism
SCRP	Spin correlated radical pair
SCS	Supercontinuum source
TDM	Transition dipole moment
TIR	Total internal reflection
Trp	Tryptophan

Chapter 1

Introduction

Presented in this chapter are introductions to the basics of spin and light. These two fundamentals of nature are a common thread throughout the projects presented here; the specifics relevant to each chapter are introduced later as needed.

1.1 Spin

1.1.1 Original spin

Electrons possess an intrinsic form of angular momentum known as spin. The first experimental evidence of spin was the Stern-Gerlach experiment,[1] the theory being developed by Pauli, Uhlenbeck and Goudsmit, and Dirac.[2–4] In this experiment, a beam of silver atoms is passed through an inhomogeneous magnetic field, and is split into two spatial components. The ground state of silver atoms possesses no orbital angular momentum, $L = 0$, so the splitting of the beam must arise from some other magnetic moment, and hence some other angular momentum. Furthermore, the spatial quantisation of the beam into two components means that this angular momentum is also quantised. This angular momentum is spin.

1.1.2 Spin quantum numbers and the vector model

Spin is an angular momentum that can be described by the normal operators for angular momenta, $\hat{s}$, the total spin operator, and $\hat{s}_z$, the spin projection operator onto an arbitrary

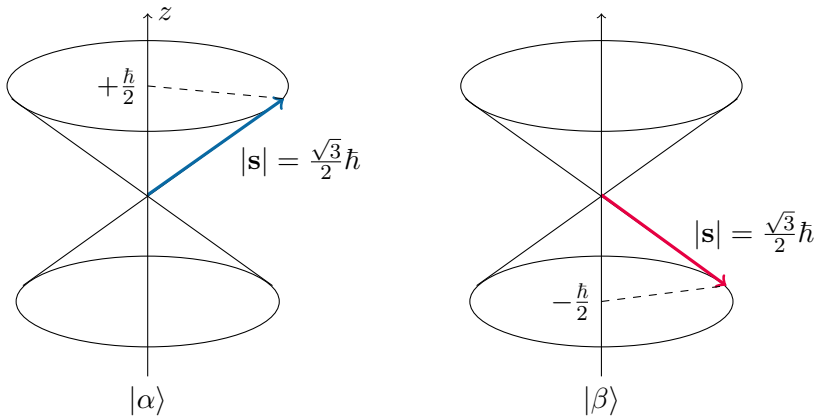

Figure 1.1: *Vector model spin cones for $s = \frac{1}{2}$. The magnitude of the spin, $|\mathbf{s}|$, and projection onto an arbitrary axis, s_z, can be specified.*

axis (conventionally z).

$$\begin{aligned} \hat{s}^2|\Psi\rangle &= \hbar^2 s(s+1)|\Psi\rangle \\ \hat{s}_z|\Psi\rangle &= m_s\hbar|\Psi\rangle. \end{aligned} \tag{1.1}$$

The magnitude of the spin and projection onto the arbitrary z-axis are therefore

$$\begin{aligned} |\mathbf{s}| &= \hbar\sqrt{s(s+1)} \\ s_z &= m_s\hbar. \end{aligned} \tag{1.2}$$

The two quantum numbers here are s, the spin angular momentum quantum number, and m_s, the spin projection quantum number, m_s taking the values $m_s = s, s-1, ..., -s$. For an electron, $s = \frac{1}{2}$, and $m_s = \pm\frac{1}{2}$. The two states can be labelled according to their quantum numbers $|s, m_s\rangle$, or as $|\alpha\rangle$ and $|\beta\rangle$ for the $|\frac{1}{2}, \frac{1}{2}\rangle$ and $|\frac{1}{2}, -\frac{1}{2}\rangle$ states respectively. The projection of $\mathbf{s}$ onto the two orthogonal axes (x and y) is unspecified as

$$\begin{aligned} [\hat{s}_z, \hat{s}_x] &= i\hbar\hat{s}_y \\ [\hat{s}_y, \hat{s}_z] &= i\hbar\hat{s}_x. \end{aligned} \tag{1.3}$$

The spin angular momentum has many vector properties, and can be visualised as a vector with magnitude $|\mathbf{s}|$ and projection s_z. Since we cannot specify s_x and s_y at the same time as s_z, we must represent the spin vector as lying at an indeterminate position on a cone (Figure 1.1). It is important not to overinterpret the vector model as the spins

actually pointing in a specific direction around the cone, as this is unspecified.

1.1.3 The Zeeman effect

The spin of the electron gives rise to a magnetic moment, $\mathbf{m}$, where

$$\mathbf{m} = -\frac{g_\mathbf{e}\mu_\mathrm{B}\mathbf{s}}{\hbar} \tag{1.4}$$

with μ_B being the Bohr magneton, and $g_e = 2.00232$, the g-factor of the free electron.

In a magnetic field, $\mathbf{B}$, the magnetic moment of the electron is quantised along the field direction, and the energy depends on the orientation of the magnetic moment (and hence the spin vector) relative to the magnetic field direction. This is the Zeeman effect. The Hamiltonian for the interaction, where $\mathbf{B}$ is defined as lying along the $+z$ direction, is

$$\begin{aligned} \hat{H}_\mathrm{zee} &= -\mathbf{B}\cdot\mathbf{m} \\ &= +g_e\mu_B B_0 \hat{s}_z \end{aligned} \tag{1.5}$$

where B_0 is the strength of the magnetic field, and the energies of the two m_s states are

$$E_{\mathrm{zee},m_s} = +g_e\mu_B B_0 m_s. \tag{1.6}$$

In the case of a single electron, the two states $|\alpha\rangle$ and $|\beta\rangle$ are split, with the $|\beta\rangle$ state being lowered in energy and the $|\alpha\rangle$ state being raised.

For an electron confined to a molecule, spin-orbit coupling mixes orbital angular momentum into the ground state. This has two results. Firstly, the g-factor of the electron is no longer isotropic, instead depending on the angle of the magnetic field relative to the molecular frame. Secondly, the value of g is no longer necessarily equal to the free-electron g-factor. Both of these factors are taken into account by replacing the g-factor with a g-tensor, $\mathbf{g}$, with the Zeeman Hamiltonian becoming:

$$\hat{H}_\mathrm{zee} = \mu_B \hat{\mathbf{s}}^\mathsf{T}\cdot\mathbf{g}\cdot\mathbf{B}. \tag{1.7}$$

The size of the spin-orbit coupling (and hence the deviation of $\mathbf{g}$ from g_e) depends on the orbital contributions (s-, p-, d-) to the ground state. For most carbon-centred

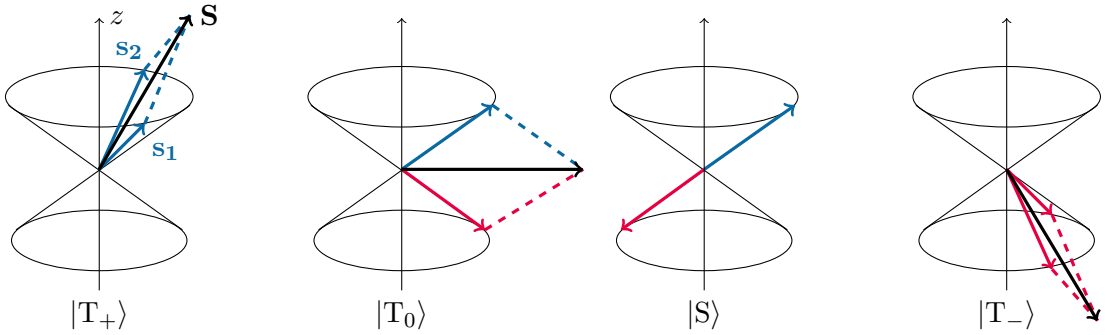

Figure 1.2: *Vector model spin cones for $S = 1, 0$. The three triplet states and one singlet state are distinguished by the total spin quantum numbers S and M_S.*

radicals both the anisotropy and deviation from g_e is small, so the g-tensor anisotropy is not resolved at low fields. Additionally, the g-tensor is averaged by molecular tumbling in solution. In this case, g_e in Equation 1.6 can be replaced with a molecular g-factor:

$$E_{\text{zee},m_s} = +g\mu_B B_0 m_s. \tag{1.8}$$

1.1.4 Coupled spins

For two spins coupling together, the total spin quantum number, S, is

$$S = s_1 + s_2, s_1 + s_2 - 1, ..., |s_1 - s_2| \tag{1.9}$$

with the total spin projection quantum number, M_S, being

$$M_S = S, S - 1, ..., -S. \tag{1.10}$$

This coupled representation, depicted in Figure 1.2, gives four states:

S	M_S	$\|\Psi\rangle$	label
0	0	$\frac{1}{\sqrt{2}}(\|\alpha\beta\rangle - \|\beta\alpha\rangle)$	$\|\text{S}\rangle$
1	+1	$\|\alpha\alpha\rangle$	$\|\text{T}_+\rangle$
1	0	$\frac{1}{\sqrt{2}}(\|\alpha\beta\rangle + \|\beta\alpha\rangle)$	$\|\text{T}_0\rangle$
1	−1	$\|\beta\beta\rangle$	$\|\text{T}_-\rangle$

The coupling results in three triplet states, $|\text{T}_+\rangle$, $|\text{T}_0\rangle$, $|\text{T}_-\rangle$, and one singlet state, $|\text{S}\rangle$. Note that the four states given here are not necessarily eigenstates of the spin Hamiltonian, but are often the most convenient basis in which to work.

In the absence of any external fields, and in the limit of no coupling between the two

electrons, the four states are degenerate. Equation 1.8 shows that the Zeeman effect raises the energy of $|\mathrm{T}_+\rangle$, and lowers $|\mathrm{T}_-\rangle$, with S and T_0 being unaffected.

Coupling of the two electrons together also affects the energies of the states in the following ways.

1.1.5 The exchange interaction

For a pair of electrons, overlap of the individual wavefunctions gives rise to an interaction term, the exchange interaction.

This is given by

$$\hat{H}_{\mathrm{ex}} = \hat{S}_1^{\intercal} \cdot \mathbf{J} \cdot \hat{S}_2 \tag{1.11}$$

where $\hat{S}_i$ is the total spin operator for the spin i. The anisotropic component of this interaction is normally negligible, and can anyway be taken into the dipolar interaction tensor below, so this simplifies to

$$\hat{H}_{\mathrm{ex}} = J \cdot \hat{S}_1^{\intercal} \cdot \hat{S}_2. \tag{1.12}$$

The result of this interaction is to split the energies of the singlet and triplet states. J decays exponentially with inter-radical separation, and is considered negligible for inter-spin distances exceeding $\sim$1.5 nm.[5]

1.1.6 The dipolar interaction

The dipolar interaction between two spins is described by the Hamiltonian

$$\hat{H}_{\mathrm{dd}} = \hat{S}_1^{\intercal} \cdot \mathbf{D} \cdot \hat{\mathrm{S}}_2 \tag{1.13}$$

where $\mathbf{D}$ is the dipolar interaction tensor. This interaction is purely anisotropic, and lifts the degeneracy of the triplet states. In the limit of zero field, the three states are characterised by the principal components of the dipolar tensor, D_x, D_y, and D_z, and are labelled $|\mathrm{T}_x\rangle$, $|\mathrm{T}_y\rangle$, and $|\mathrm{T}_z\rangle$. Within the high-field approximation, and neglecting the anisotropy of the g-tensors, this can be written

$$\mathbf{D} = \frac{\mu_0}{4\pi\hbar} \frac{\mathrm{g}_1 \mathrm{g}_2 \mu_{\mathrm{B}}^2}{\mathrm{r}_{12}^3} \begin{pmatrix} -1 & & \\ & -1 & \\ & & 2 \end{pmatrix} = \begin{pmatrix} -\omega_{\mathrm{dd}} & & \\ & -\omega_{\mathrm{dd}} & \\ & & 2\omega_{\mathrm{dd}} \end{pmatrix} \tag{1.14}$$

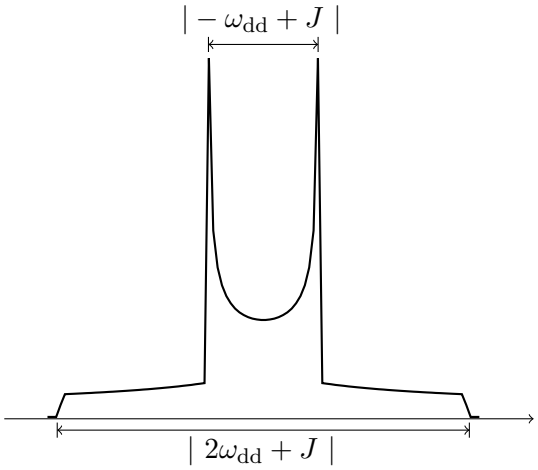

Figure 1.3: *Powder spectrum, with splitting caused by dipolar and exchange interactions. For the case of $J \ll \omega_{dd}$ and weak coupling, this is a Pake doublet.*

and the dipolar Hamiltonian can be rewritten as

$$\hat{H}_{\mathrm{dd}} = \omega_{\mathrm{dd}} \hat{S}_{1z}^{\intercal} \hat{S}_{2z} \tag{1.15}$$

with

$$\omega_{\mathrm{dd}} = \frac{\mu_0}{4\pi\hbar} \frac{g_1 g_2 \mu_B^2}{r_{12}^3} \left(3\cos^2\theta_{12} - 1\right) \tag{1.16}$$

where θ_{12} is the angle between $\mathbf{B_0}$ and the inter-radical axis. With an isotropic distribution of inter-radical angles (as in a powder or glass) the spectrum is as shown in Figure 1.3. In the case of $J \ll \omega_{\mathrm{dd}}$ and weak coupling, this is the familiar Pake doublet, and the value of the dipolar coupling, and hence inter-radical distance, can be read off directly from the singularities.

For molecules moving in solution, when the rotation is fast compared to the splitting, the angle θ_{12} is time-averaged over all possible orientations, and the $\int (3\cos^2\theta_{12} - 1)\sin\theta_{12}\mathrm{d}\theta_{12}$ term vanishes, the whole dipolar term becoming zero.

1.1.7 The hyperfine interaction

The electron spins can also couple to magnetic nuclei. This coupling is described by the hyperfine interaction, given by

$$\hat{H}_{\mathrm{hf}} = \sum_j \sum_i \hat{S}_i^{\intercal} \cdot \mathbf{A}_{ij} \cdot \hat{I}_j \tag{1.17}$$

where i and j are indices covering each electron and nucleus respectively, and $\mathbf{A}_{ij}$ is a tensor for the interaction between each pair.

The hyperfine coupling has two contributions. Firstly, there is an isotropic contribution due to the Fermi contact interaction between electron and nucleus. This contribution has the form

$$\hat{H}_{\text{hf,iso}} = \frac{2}{3}\gamma_e\gamma_n\mu_0|\psi(0)|^2\hat{S}^\intercal \cdot \hat{I}. \tag{1.18}$$

This term depends on the $|\psi(0)|^2$, the electron density at the nucleus, and hence depends on the s-character of the ground state.

Secondly, the dipole-dipole interaction between electron and nuclear magnetic moments adds an anisotropic contribution, given by

$$\hat{H}_{\text{hf,aniso}} = \frac{\mu_0\gamma_e\gamma_n}{4\pi r^3}\left(\frac{3\left(\hat{S}\cdot\hat{r}\right)\left(\hat{r}\cdot\hat{I}\right)}{r^2} - \hat{S}\cdot\hat{I}\right). \tag{1.19}$$

This contribution can be written in terms of a tensor $\mathbf{T}$

$$\hat{H}_{\text{hf,aniso}} = \hat{S}^\intercal \cdot \mathbf{T} \cdot \hat{\text{I}}. \tag{1.20}$$

In total, these contributions can be taken together into the hyperfine tensor, $\mathbf{A}_{ij}$.

In the limit of fast tumbling, the anisotropic component of the hyperfine coupling time-averages to zero, leaving only the isotropic contribution, a_{iso}. The hyperfine Hamiltonian can then be written as

$$\hat{H}_{\text{hf}} = a_{\text{iso}} \cdot \hat{S}^\intercal \cdot \hat{I}. \tag{1.21}$$

1.1.8 The total spin Hamiltonian

In order to calculate the energy of the electron, one must solve the Schrödinger equation for the system. It is possible, however, to write a reduced 'Spin Hamiltonian' containing only operators which act on spin, other operators (for instance for kinetic and potential energies) which do not act on spin being neglected.[6]

We can therefore solve a reduced Schrödinger equation

$$\hat{H}_{\text{spin}}|\Psi\rangle = E|\Psi\rangle \tag{1.22}$$

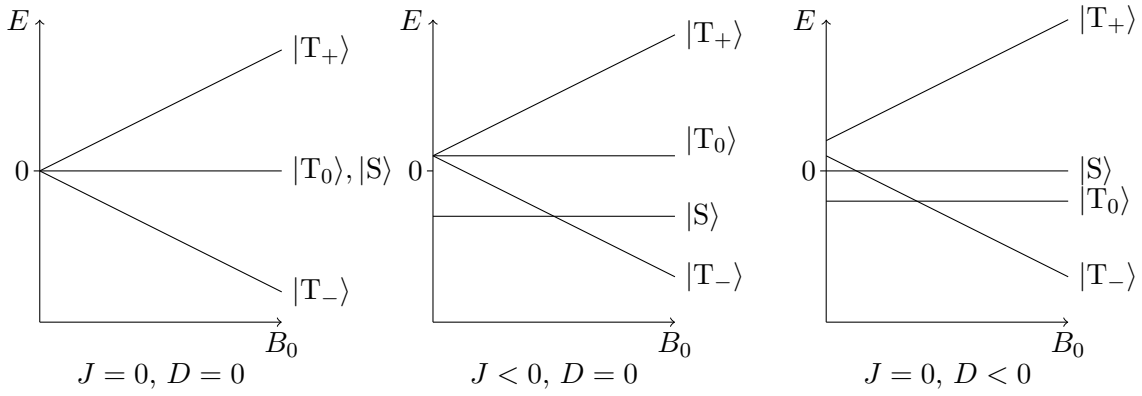

Figure 1.4: *The effect of the Zeeman, dipolar, and exchange interactions can be seen in the above diagrams. Note that the triplet levels have zero slope at $B_0 = 0$ (not shown at this scale). Hyperfine interactions will serve to split the states further, typically on the order of* MHz *to tens of* MHz*, compared to the Zeeman splitting of hundreds of* MHz *(MFE experiments) to* GHz *(EPR).*

with the total spin Hamiltonian for a pair of electrons with the above interactions being

$$\begin{aligned}\hat{H}_{\text{spin}} =& g_1\mu_B B_0\hat{S}_{1z} + g_2\mu_B B_0\hat{S}_{2z} \ ... \\ &+ J\hat{S}_1^{\intercal}\cdot\hat{S}_2 + \hat{S}_1^{\intercal}\cdot\mathbf{D}\cdot\hat{S}_2 \ ... \\ &+ \sum_i(\hat{S}_1^{\intercal}\cdot\mathbf{A}_{1i}\cdot\hat{I}_i + \hat{S}_2^{\intercal}\cdot\mathbf{A}_{2i}\cdot\hat{I}_i).\end{aligned} \tag{1.23}$$

The effect of B_0, J, and $\mathbf{D}$ on the energies of the states is summarised in Figure 1.4.

1.2 Light

1.2.1 The transition dipole moment

For a transition between two states by radiation of electric field amplitude E_0 and frequency ω, the total wavefunction must satisfy the time-dependent Schrödinger equation, such that

$$\hat{H}\Phi = i\hbar\frac{\partial\Phi}{\partial t} \tag{1.24}$$

where

$$\hat{H} = \hat{H}_0 - \mu E_0\cos(\omega t) \tag{1.25}$$

and μ is the electric dipole moment operator. For eigenstates, Ψ_n, the total wavefunction is

$$\Phi = \sum_n c_n(t)\Psi_n \exp\{-iE_n^0 t/\hbar\} \tag{1.26}$$

with time dependent coefficients, $c_n(t)$. The rate of transition from state i to state f is given by

$$\frac{\mathrm{d}c_f(t)}{\mathrm{d}t} = \frac{E_0}{2i\hbar}\left(\exp\frac{i(E_f^0 - E_i^0 + \hbar\omega)t}{\hbar} + \exp\frac{i(E_f^0 - E_i^0 - \hbar\omega)t}{\hbar}\right)\langle\Psi_f|\hat{\mu}|\Psi_i\rangle. \tag{1.27}$$

The last term in this equation is the transition dipole moment (TDM), μ_{fi},

$$\mu_{fi} = \langle\Psi_f|\hat{\mu}|\Psi_i\rangle \tag{1.28}$$

where $\hat{\mu} = \sum_k q_k\hat{r}_k$ is the dipole moment operator, q_k and $\hat{r}_k$ being the charge and position of the kth particle, respectively.

Considering this term within the Born-Oppenheimer approximation, such that the nuclei are stationary on the timescale of electronic transitions, we can separate Ψ into electronic and vibrational wavefunctions.

$$\Psi = \psi_{el}(r, R)\psi_{vib}(R). \tag{1.29}$$

The dipole moment operator acts on the electronic coordinates only, so the TDM becomes

$$\mu_{fi} = \langle\psi_{el,f}|\hat{\mu}|\psi_{el,i}\rangle\langle\psi_{vib,f}|\psi_{vib,i}\rangle \tag{1.30}$$

and the probability of transition between the initial and final states is proportional to the square of the TDM:

$$P_{fi} \propto |\langle\psi_{el,f}|\hat{\mu}|\psi_{el,i}\rangle|^2|\langle\psi_{vib,f}|\psi_{vib,i}\rangle|^2. \tag{1.31}$$

The first part of this is the electronic transition moment, and is the origin of the electronic selection rules. The second part is the Franck-Condon factor, and means that the transition probability depends on the square of the vibrational overlap.

For excitation with polarised light, the transition probability is proportional to $\cos^2(\theta)$, where θ is the angle between the electric field vector and a vector defined by the transition moment. The probability distribution for excitation takes the familiar 'dumbbell' shape. Using this property, it is possible to probe molecular orientation using polarised light: if an

ensemble of molecules have a specific orientation, the absorbance will be highest for light polarised along the TDM axis, and zero perpendicular to it. For an isotropic distribution, the absorbance will be equal for orthoganal polarisations.

1.2.2 The Beer-Lambert law

On a macroscopic level, the attenuation of a beam of light by a sample decays, to a first approximation, exponentially with both path length[7] and sample concentration.[8] This behaviour is captured in the Beer-Lambert law that states

$$I(\lambda) = I_0(\lambda)10^{-\epsilon(\lambda)cl} \tag{1.32}$$

where $I(\lambda)$ and $I_0(\lambda)$ are the intensities of the beam before and after the sample, respectively, l is the path length, c is the concentration of the sample, and $\epsilon(\lambda)$ is the decadic absorption coefficient, a wavelength-dependent parameter characteristic to each molecule.

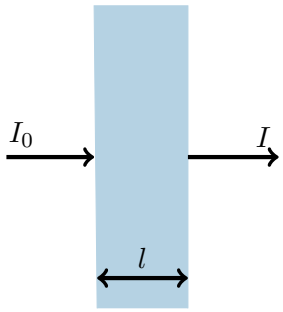

Figure 1.5: *The Beer-Lambert law describes the attenuation of a beam of light from intensity I_0 to I by a material of length, l, absorption coefficient, ϵ, and concentration, c.*

For samples at low concentration, with a small absorption coefficient, or small volume such that the path length must be short, I may be very similar to I_0. This can be experimentally challenging, as the small difference between two large signals can be obscured by noise. Traditional solutions to this problem include multipass cells, where the path length is increased by reflecting the beam through the sample multiple times. Taking this idea further, using an optical cavity would maximise the number of passes.

1.2.3 Fates of excited molecules

The electronic ground state of most molecules is a singlet, with all spins paired. The electronic transition moment (Equation 1.31) is zero unless $\Delta S = 0$ (the spin selection

rule). This means that the allowed transitions from the ground state, S_0, are to higher energy singlet states, S_1, S_2, etc. The initial vibrational levels of the excited states are determined by the Franck-Condon factor (Equation 1.31), but the vibrational structure of the bands is generally not resolved in solution due to broadening caused by supramolecular configurations of solvent molecules around the molecule, and by coupling of the vibrations within the molecule and to the solvent.

Once excited to, say, the S_1 state, collisions with solvent molecules rapidly vibrationally relax the molecule to the lowest vibrational level. Different fates then can befall the molecule (summarised in Figure 1.6.)

1.2.3.1 Internal conversion

Internal conversion is the radiationless transition between states of the same multiplicity. In the case of S_1, in solution, this transition will occur from the lowest vibrational level to an excited level of S_0. This process is spin-allowed, and deactivates the excited state.

The rate of internal conversion is given by Fermi's "Golden rule", which states that for a perturbation between eigenstates, to first order in the perturbation, the rate is given by

$$\Gamma_{i\to f} = \frac{2\pi}{\hbar}|\langle\Psi_f|\hat{H}'|\Psi_i\rangle|^2\rho \tag{1.33}$$

where ρ is the density of final states and $\hat{H}'$ is the Hamiltonian for the perturbation. For internal conversion, $\hat{H}'$ is the nuclear kinetic energy operator.

1.2.3.2 Intersystem crossing

Intersystem crossing (ISC) is the radiationless transition between states of different multiplicity. In many cases, this will predominantly be from S_1 to a low lying triplet state. This process is spin-forbidden, but partially allowed by spin-orbit coupling (the perturbation Hamiltonian relevant to Fermi's Golden rule now being $\hat{H}_{so} = \zeta\hat{L}\cdot\hat{S}$, where ζ is the spin-orbit coupling constant), and hence is enhanced by the presence of heavy atoms.

1.2.3.3 Fluorescence

Fluorescence is the radiative transition between states of the same multiplicity, for example $S_1 \to S_0 + h\nu$. The polarisation of the emitted light also depends on the transition dipole moment (Section 1.2.1); in solution the fluorescence anisotropy will be reduced depending on the rotational diffusion of the fluorophore.

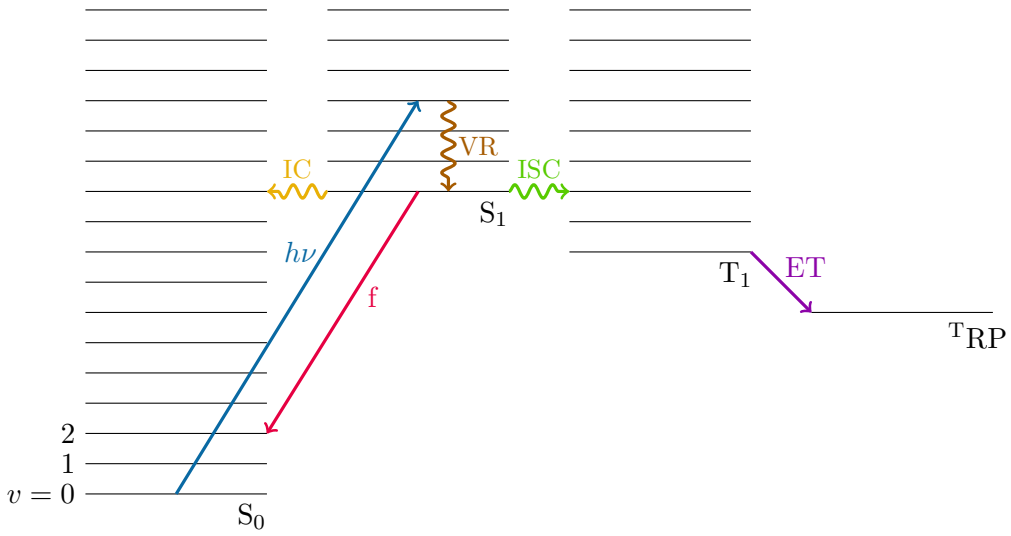

Figure 1.6: *Jablonski diagram for the common fates befalling an excited singlet state, including fluorescence (f), internal conversion (IC), intersystem crossing (ISC), electron transfer (ET) to form a radical pair (RP), and vibrational relaxation (VR).*

1.2.3.4 Electron transfer

If there is a suitable donor or acceptor molecule, electron transfer to or from the excited state can occur, forming a radical pair. This process can occur from either the singlet or triplet state, and this process occurs with conservation of total spin. i.e. $S_1 \rightarrow |S\rangle$ and $T_1 \rightarrow |T_i\rangle$.

Chapter 2

Distance measurement in a partially folded protein

2.1 Protein folding

Protein folding is the process by which a protein moves from a random coil (say, after transcription) to its native conformation. After synthesis in the ribosome, many proteins will fold rapidly and spontaneously to the native state – the question of how this occurs was considered by Levinthal in 1969.[9]

2.1.1 Levinthal's paradox

Consider a protein that is made up of 100 amino acids. Each amino acid unit has two conformational degrees of freedom (rotation about the angles ψ and ϕ, Figure 2.1), giving the backbone 198 degrees of freedom in total. Assuming three low energy states for each bond rotation, and neglecting steric effects, there are therefore 3^{198} or 10^{94} possible conformations. If, on moving from the completely unfolded state, the protein were to

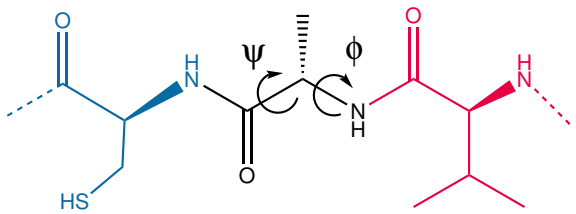

Figure 2.1: *Amino acid chain, showing backbond angles ψ and ϕ. Rotation around the backbone gives a huge number of potential conformers, approximately 10^{94} for a 100 amino acid long chain.*

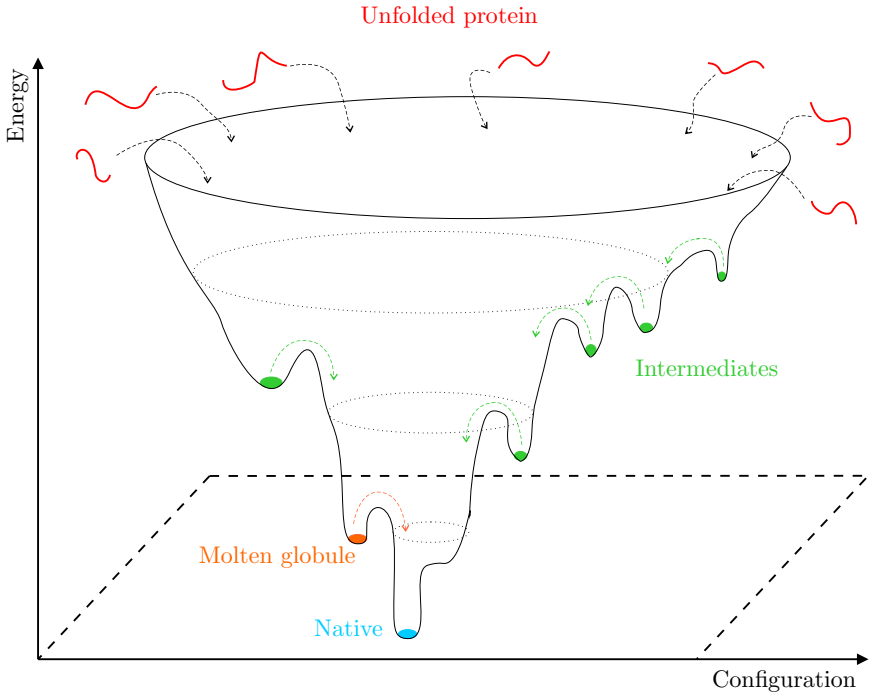

Figure 2.2: *Protein folding funnel, including a molten globule state. The number of possible configurations is reduced as the protein travels down the free energy landscape, being guided towards the native state.*[11] *Figure adapted from Schultz.*[12]

execute a random search of all possible conformations, even sampling each conformation for only picoseconds, the chance of the protein 'finding' the correct conformation within the lifetime of the universe would be exceedingly small. Proteins commonly fold within milliseconds to seconds; this conflict between the apparently long time needed to search for the correct conformation and observed folding times is 'Levinthal's paradox'.

Clearly there are some factors which must guide the protein from the completely unfolded state to the folded one. The most plausible resolution to the paradox is that the protein is guided by local interactions such that, as the protein moves down the free energy landscape towards the native state, the number of possible configurations shrinks.[10] This is represented schematically in Figure 2.2. The protein folding process need not take place along a single pathway, indeed, the great number of possible configurations suggest this would be unlikely. Instead, the protein can potentially move through many different routes, passing through local energy minima, towards the native state, the global energy minimum.

2.1.2 Interactions driving protein folding

Protein folding is driven by a combination of the following factors:[13]

1. **Hydrogen bonds** are important in the formation of secondary structure (in particular between residues $i \rightarrow i + 4$ in α-helices and between adjacent strands in β-sheets).

2. **van der Waals interactions** between atoms in the tightly packed native state.

3. **Backbone angle preference** of individual residues. Certain combinations of backbone angles are energetically favourable, as expressed in Ramachandran plots.[14]

4. **Electrostatic interactions** between positively and negatively charged side chains.

5. **Hydrophobic interactions** between hydrophobic side chains clustering within the core of the protein to minimise solvent exposure.

6. **Chain entropy** which opposes folding as the number of possible configurations is reduced by moving towards the native state.

The sequence of the protein will determine the balance of interactions which drive the path or paths of the protein across the free energy landscape towards the native state.

2.1.3 Folding pathways

A number of different models of protein folding have been proposed, including:

1. **The hydrophobic collapse model** within which hydrophobic residues cluster together to minimise solvent exposure, forming a compact intermediate. The secondary structure is then formed, with electrostatic interactions driving subsequent formation of the tertiary fold.

2. **The framework model** states that elements of secondary structure are formed initially through local interactions between residues. This reduces the number of possible conformations, and these elements then take on the native tertiary fold.

3. **The nucleation model** has secondary and tertiary structure forming simultaneously, with the native fold radiating out from a point of secondary structure formation.

Different proteins may fold under different models; there is no universal pathway for protein folding. One model of protein folding relevant here was proposed by Ptitsyn, who suggested that stepwise involvement of the various interactions could lead to intermediate folding states.[15]

2.1.4 The molten globule state

Kuwajima and coworkers showed in 1976 that, unlike some proteins which obey a simple two-state model of folding, bovine α-lactalbumin undergoes a three state denaturation process in the presence of guanidine hydrochloride, with the intermediate being the same as that formed at acidic pH.[16,17] This is the 'molten globule' state, a compact intermediate in the hydrophobic collapse model that retains native-like secondary structure, but has a fluctuating ensemble of tertiary structures. Molten globules are not only folding intermediates, as suggested by Ptitsyn, but can be formed under mildly denaturing conditions, including low pH, low concentrations of denaturants, and removal of cofactors such as metal ions or haem groups.

The ability to study the kinetically stable molten globule state which resembles folding intermediates may therefore provide insight into both the protein folding pathway, and the balance of forces which dictate both stages of the hydrophobic collapse process.

2.2 α-lactalbumin

Human α-lactalbumin is a small (typically 123 residue,[18] 14.2 kDa) Ca^{2+} binding protein which is present in mammalian milk, being a component of lactose synthase, an enzyme which catalyses the final step of lactose biosynthesis. It is homologous with lysozyme, but has almost zero cell lytic activity.[19]

The structure of α-lactalbumin, shown in Figure 2.3, consists of two domains: the large α domain, and the smaller β domain. The α domain consists of four α-helices (A: K5–L11, B: L23–S34, C: T86–I98, D: L105–A109) and two 3_{10} helices (L11–G20, L115–W118). The β domain contains a small, three stranded antiparallel β-pleated sheet (I41–E44, S47–Y50, I55–S56) and a short 3_{10} helix (A77–F80). The two domains are joined by a disulphide bridge (C73–C91), with a helix–turn–helix motif (D74–D88) making up the Ca^{2+} binding loop. α-lactalbumin also contains three other disulphide bridges (C6–C120, C61–C77, C28–C111).

At low pH, α-lactalbumin forms the 'classic' molten globule, retaining a high degree of

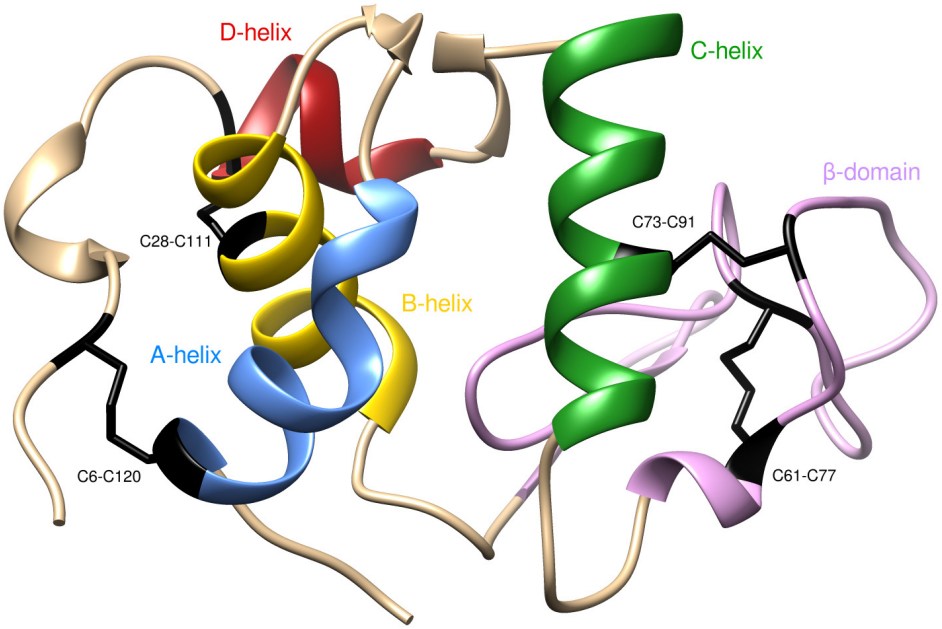

Figure 2.3: *The native state structure of α-lactalbumin. A-, B-, C-, and D-helices, the β-domain, and the four disulphide bonds are highlighted. Generated from PDB:1A4V*[20] *using UCSF Chimera.*[21]

secondary structure, and a native-like fold, with a compactness similar to the native state (radius of gyration of 17.2 Å for the molten globule versus 15.7 Å for the native state).[22]

2.2.1 Disulphide bonds in the α-lactalbumin molten globule

The disulphide bonds are crucial in maintaining the native fold of α-lactalbumin, and to its ability to bind calcium. Wu and coworkers[23] made mutants with the disulphide-forming cysteines mutated to alanine: α-LA(α) has the α domain bridges (C6–C120 and C28–C111) removed; α-LA(β) has the β domain bridges (C61–C77 and C73–C91) removed. Both α-LA(α) and α-LA(β) form molten globules, even at neutral pH. However, they differ in their calcium binding response. α-LA(α) retains its ability to bind Ca^{2+}, with the β domain regaining native-like structure upon binding. α-LA(β) on the other hand cannot bind Ca^{2+}, and remains a molten globule in the presence of calcium.

Studies on α-LA(α) and α-LA(β) also revealed that the α domain of the molten globule resembles an expanded native-like domain, while the β domain is largely unfolded, demonstrating that α-lactalbumin molten globule is bipartite, with the individual domains unfolding in a non-cooperative manner.[23]

2.2.2 Non-cooperative folding in α-lactalbumin

Studies by Schulman and coworkers of a single-disulphide variant containing only the C28–C111 bridge have shown that introduction of helix-breaking proline mutations into each of the α-helices caused destabilisation of only the individual helix, not the other helices nor the protein as a whole,[24] further demonstrating the non-cooperativity of unfolding. This work also suggested that the C-helix is unfolded in the molten globule, as the introduction of two proline mutations did not effect any change in the helical content of the protein.

Unfolding of α-lactalbumin by urea, monitored by Schulman *et al.* by broadening of NMR resonances, has also shown that the molten globule is not formed cooperatively.[25] In this work, the resonances in the ^{15}N–^{1}H HSQC NMR spectrum were found to be broad and poorly resolved for residues inside the compact core of the protein due to conformational fluctuations, as is characteristic of compact regions of non-native states.[26] The resonances become sharper as the protein unfolds, however. The unfolding behaviour of different parts of the secondary structure can therefore be monitored separately as increasing concentrations of denaturant (urea) are added. Very few resonances are resolved in the absence of urea, indicating that both domains are at least partially collapsed. At low concentrations of urea (3 M, 20°C), the β domain resonances appear. The peaks from the C helix appear at 10 M urea, 20°C, and only half of the resonances in the A and B helices can be observed at 10 M urea, 50°C. No peaks from the D or C-terminal 3_{10} helices can be observed under these conditions, only appearing under the rather extreme conditions of 8 M guanidine hydrochloride at 50°C. These results further support the non-cooperativity of unfolding, and of the collapsed nature of the molten globule.

2.2.3 All-Ala α-lactalbumin

The all-Ala variant of α-lactalbumin, for which all eight disulphide-forming cysteine residues have been mutated to alanine, also forms a compact molten globule with native-like helical content.[27] This result, from Redfield and coworkers, indicates that it is the amino acid sequence itself, and not the disulphide bonds, that determines the overall fold of the protein. Furthermore, urea unfolding experiments indicate that although the all-Ala variant is much less resistant to unfolding than the wild type, the unfolding events are similar between the two proteins. In both cases there is a concentration of urea at which the β domain has unfolded, but the α domain remains compact. In contrast to the wild type, the four α helices in all-Ala α-lactalbumin unfold over a relatively narrow range of urea

concentrations, indicating at least local cooperativity in the folding of these regions. Close interactions between the C-terminal residues and the A, B, and D helices also indicate that the C-terminus forms part of the compact core. Furthermore, in both variants, the final unfolding step occurs in a relatively concerted manner and involves a large number of residues at both N- and C-termini, indicating that the interaction between hydrophobic residues is a strong driving force in the formation of the core.

The secondary structure of the all-Ala variant has also been studied by NMR at high temperature (40°C) using the $^1H^\alpha$ chemical shifts.[28] In these experiments, the deviation of the $^1H^\alpha$ chemical shifts from their random coil values are used to detect secondary structure.[29] Shift deviations in residues 5–16 suggest that the A helix is lengthened in the all-Ala α-lactalbumin, compared to the wild type, and deviations are low for residues F31–S34, indicating that the B helix is shortened. Large deviations were seen for residues corresponding to the C, D, and C-terminal 3_{10} helix for both wild type and all-Ala α-lactalbumin, indicating a significant amount of native-like helical content in both molten globules. The β domain shows no sign of β-sheet content in these experiments, but does show shifts corresponding to helical or turn structure in the first half of the domain (A40–W60), suggesting that, although not native-like, this domain does contain some structure. The latter half (W60–A77) shows only small shift deviations, indicating random-coil structure.

2.2.4 Distance constraints on the tertiary fold

Although the work above has elucidated much about the secondary structure of α-lactalbumin, questions still remain about the tertiary structure. It is known that the molten globule comprises a hydrophobic core consisting mainly of the α domain and C-terminus, retaining much of the structure of the native state, while the β domain is partially disordered (although the first half does show some helical or turn structure). However, the tertiary fold of the molten globule is not a single, well defined structure, instead being made up of an ensemble of rapidly interconverting forms. Experiments which are able to study this ensemble would be a valuable next step in elucidating the structure and dynamics of the molten globule, as well as providing valuable insights into the folding process. To this end, presented here is a study of all-Ala α-lactalbumin using double electron-electron resonance (DEER), an EPR technique for interspin distance measurement, enabling long-range (1.5–4 nm) distance constraints to be placed on the molten globule.

2.3 Introduction to EPR

2.3.1 Continuous wave EPR

Electron paramagnetic resonance (EPR) is a spectroscopic technique probing transitions between spin states of unpaired electrons (or systems of electrons.)

For an ensemble of uncoupled electrons, the equilibrium populations of the α and β states are governed by a Boltzmann distribution

$$\begin{aligned} \frac{n_\alpha}{n_\beta} &= e^{-\Delta E/kT} \\ &= e^{-g\mu_B B_0/kT}. \end{aligned} \tag{2.1}$$

The spins are uniformly distributed in the x–y plane, and the net magnetisation lies along $+z$, the direction of the magnetic field.

The resonance condition is given by

$$\omega = \frac{g\mu_B B_0}{\hbar} \tag{2.2}$$

with ω being the angular frequency of the radiation. For a spectrometer with a frequency of 9.6 GHz (X-band), this corresponds to a magnetic field of ∼340 mT. By application of radiation and a magnetic field at the appropriate frequency and strength, respectively, the transition between α and β states can be brought into resonance. In principle, this resonance could be detected via direct absorption of microwaves. However, relatively weak absorption makes this difficult. Instead, most EPR spectrometers work via reflectance, detecting the radiation reflected from a cavity within which the sample is placed.

2.3.2 Pulsed EPR

Pulsed EPR is a powerful technique that can be used to record a spectrum of interest, or perform other experiments such as relaxation time, hyperfine coupling, or electron-electron distance measurements. Pulsed EPR differs from continuous wave (cw) EPR in that short, powerful pulses of microwaves are employed in order to excite a range of resonances at once, and microwave pulse sequences can be used to manipulate the spins, and perform the aforementioned experiments.

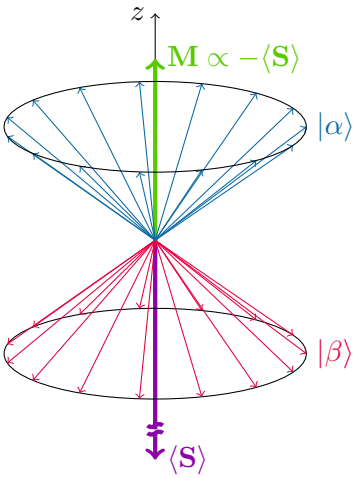

Figure 2.4: *An ensemble of uncoupled electrons have a net spin vector in the $-z$ direction, and a net magnetisation,* $\mathbf{M}$*, lying in the $+z$ direction.*

2.3.2.1 The rotating frame

In order to understand the effect of microwaves pulses on an ensemble of spins, the concept of the 'rotating frame' is often useful.

For an ensemble of uncoupled spins in a static magnetic field lying along the $+z$ axis, $\mathbf{B_0}$, a slight excess are in the β state, as described by the Boltzmann distribution in Equation 2.1. These spins are uniformly distributed in the x–y plane, and the ensemble has a net magnetisation in the $+z$ direction (Figure 2.4). A linearly polarised microwave field, $\mathbf{B_1}$, along the x direction with strength B_1 and frequency ω_{mw} will cause the net magnetisation to precess around the resultant of the two fields, $\mathbf{B_{eff}}$, where

$$|\mathbf{B_{eff}}| = \sqrt{\mathbf{B_0}^2 + \mathbf{B_1}^2}. \tag{2.3}$$

In order to simplify this description, it is useful to describe $\mathbf{B_1}$ as the sum of two counter-rotating components, each with the same frequency, ω_{mw}. The rotating frame is then defined such that the z-axes of the static and rotating frames are collinear, while the x- and y- axes of the rotating frame precess at ω_{mw} relative to the static frame. One of the counter-rotating components of $\mathbf{B_1}$ is therefore static within the rotating frame; the other precesses at $2\omega_{\mathrm{mw}}$. The component at $2\omega_{\mathrm{mw}}$ can be neglected as it is far off resonance, but the apparently static component will cause the magnetisation to precess around $\mathbf{B_{eff}}$ such

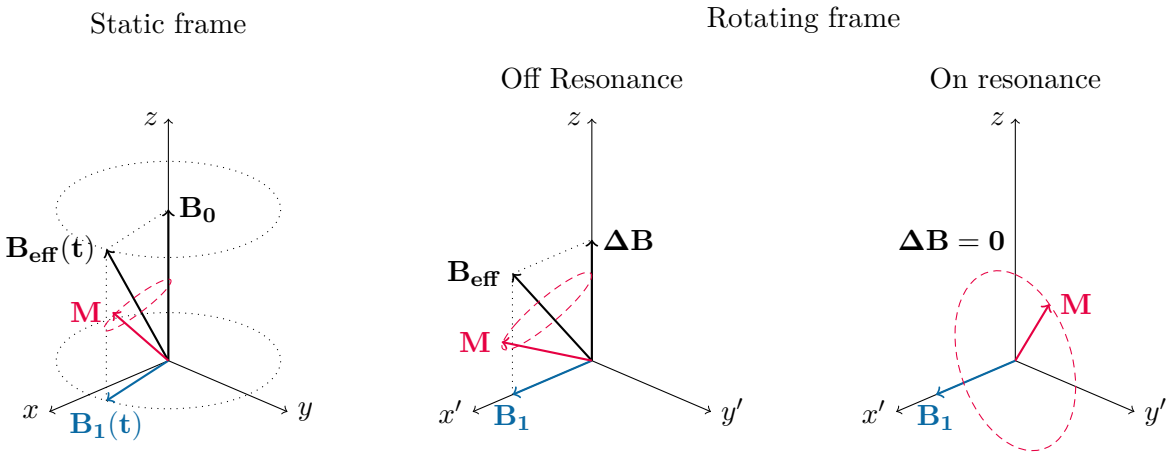

Figure 2.5: *Transformation from the static (lab) frame to the rotating frame. In the rotating frame the microwave field,* $\mathbf{B_1}$*, appears static along the* x' *axis, and the magnetisation precesses around* $\mathbf{B_{eff}}$*; for on-resonance spins,* $\mathbf{B_{eff}} = \mathbf{B_1}$*, and the magnetisation precesses in the* y'*–*z *plane.*

that

$$|\mathbf{B_{eff}}| = \sqrt{\mathbf{\Delta B^2} + \mathbf{B_1}^2}$$
$$|\mathbf{\Delta B}| = \frac{\omega - \omega_{\mathrm{mw}}}{\gamma} \tag{2.4}$$

where $\gamma = -\frac{g\mu_B}{\hbar}$. For on-resonance spins (with $\omega = \omega_{\mathrm{mw}}$), $\mathbf{\Delta B} = \mathbf{0}$, and $\mathbf{M}$ precesses around the seemingly static $\mathbf{B_1}$. Spins that are far off-resonance (with ω very different from ω_{mw}) are unaffected by $\mathbf{B_1}$ as $\mathbf{B_{eff}} \approx \mathbf{B_0}$. This is shown in Figure 2.5. If the power and length of the microwave pulse are chosen such that the magnetisation is rotated onto the $-y$ direction (a $\frac{\pi}{2}$-pulse), then the ensemble of spins is no longer at equilibrium and coherence has been induced, such that the spins are now precessing in phase in the x–y plane. The ensemble will tend over time to return to the equilibrium state due to relaxation processes.

2.3.3 Relaxation processes

2.3.3.1 Spin-lattice (longitudinal) relaxation

After the aforementioned $\frac{\pi}{2}$-pulse, the magnetisation lies in the x'–y' plane. Fluctuations in the local magnetic field at the resonance frequency (Equation 2.2) can cause transitions between the α and β states, returning the magnetisation vector to its equilibrium position along the z-axis. These local fluctuations can arise from different sources. In liquids,

the main contribution is molecular motion; in particular, molecular tumbling serves to modulate the local magnetic field at a range of frequencies determined by the rotational correlation time, as described by the spectral density function. Typically, spin-lattice relaxation is slowest for either slow or fast rotation (as the spectral component of the motion at the required frequency will be small), with the fastest relaxation for intermediate tumbling rates. In solids, lattice vibrations can induce fluctuating fields at the correct frequency.

Return of the z-magnetisation towards the equilibrium value, M_0, by spin-lattice relaxation is characterised by the spin-lattice relaxation time, T_1, as in the Bloch equation:[30]

$$\frac{\mathrm{d}M_z}{\mathrm{d}t} = -\frac{(M_z - M_0)}{T_1}. \tag{2.5}$$

2.3.3.2 Spin-spin (transverse) relaxation

The coherence between spins induced by the $\frac{\pi}{2}$-pulse does not remain indefinitely. Instead, random local contributions to the total magnetic field serve to modify the Larmor frequency of each spin, with the net magnetisation in the x-y plane decaying with time. This process is characterised by the spin-spin relaxation time, T_2:

$$\frac{\mathrm{d}M_{x,y}}{\mathrm{d}t} = -\frac{M_{x,y}}{T_2}. \tag{2.6}$$

In liquids, a large contribution to T_2 arises from molecular rotation. In this case, T_2 is longest for fast tumbling as the differences in local field due to molecular orientation are time averaged, and shortest for slow tumbling (as the molecules approach the static limit).

2.3.3.3 Spectral diffusion

In many pulsed EPR experiments, the total width of the spectrum is greater than the bandwidth of the microwave pulse, meaning that only a fraction of the spins can be excited by it. Relaxation processes on nearby spins which were not excited will change the local magnetic field at the observed spin, leading to magnetisation transfer to parts of the spectrum that are not probed. Simultaneously, equilibrium magnetisation is transferred to the probed part of the spectrum. This process, known as spectral diffusion, appears to the observer as a relaxation process (although the magnetisation is still present in other parts of the spectrum).

2.3.3.4 Instantaneous diffusion

In many EPR experiments the distance between neighbouring electrons is not large enough to make their interaction insignificant. If each spin A is surrounded by a number of coupled spins, B, at random distances and angles, then a microwave pulse which excites the B spins will change the local field at each A spin differently. This effect also contributes to the loss of transverse magnetisation.

2.3.3.5 Nuclear spin diffusion

If the dipolar coupling between nuclear spins is on the order of their difference in resonance frequencies, then the flip-flop term in the dipolar Hamiltonian, $\omega_{\text{ff}}(S_x^A S_x^B + S_y^A S_y^B)$, can cause mixing between the A and B nuclei, modulating the hyperfine field at the coupled electron and contributing to the loss of transverse magnetisation. This effect can be significantly reduced by replacing protons with deuterons, either within the molecule itself or, more commonly, by using a deuterated solvent.

2.3.3.6 The phase memory time

Empirically, the rate of loss of $M_{x,y}$ is measured by a parameter T_m, the phase memory time. This includes the effect of all processes which cause a loss of phase coherence, such as spin-spin relaxation, lifetime broadening due to T_1, spin flip-flops, instantaneous diffusion, and nuclear spin diffusion.

2.3.4 A Pulsed EPR experiment

A simple EPR experiment might consist of the a $\frac{\pi}{2}$-pulse followed by detection of $M_{x,y}$, as shown in Figure 2.6. The microwaves excite spins within the bandwidth of the pulse, and flip the magnetisation onto the $-y$ direction. From there it precesses around the z-axis, relaxing back to equilibrium in the z direction with time constant T_1 and in the x, y direction with T_m. $M_{x,y}(t)$ is the free induction decay (FID), the time domain signal which, for spectral widths narrower than the excitation bandwidth, can be Fourier transformed into the frequency domain to give the spectrum. The FID can be detected via quadrature detection, equivalent to measuring both x and y components of the magnetisation in the rotating frame. This is useful as the absolute phase of the FID is arbitrary, and quadrature detection allows the signal to be rephased into two components, the pure absorption and

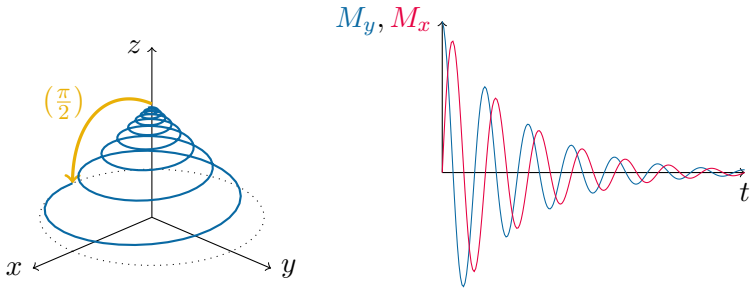

Figure 2.6: *A simple FID-dectected pulsed EPR experiment. Left: The $\frac{\pi}{2}$-pulse flips the magnetisation into the x–y plane. The magnetisation subsequently precesses around the z-axis at the Larmor frequency, and relaxes back to the equilibrium position with time constants T_1 and T_m. Right: The FID, $M_{x,y}(t)$.*

dispersion signals. Typically the FID is not directly detected as the dead-time* covers much of the decay. Instead, a sequence of pulses can be used to create an 'echo' and detect the magnetisation.

One such pulse sequence is $\frac{\pi}{2} - \tau_1 - \pi - \tau_1 -$echo, as shown in Figure 2.7a), also known as a 'Hahn-echo'. Here the initial $\frac{\pi}{2}$ pulse flips the magnetisation onto the $-y$ axis; from this moment both transverse and longitudinal relaxation will cause the magnetisation to move towards its equilibrium position. Recall that one of the contributions to spin dephasing is from differing local magnetic fields (due to, for instance, g-factor dispersion and hyperfine couplings) which gives each spin a different Larmor frequency, faster or slower than average, causing the spin vectors to dephase or 'spread out' in the x–y plane.

After the delay τ_1 the π pulse flips the magnetisation from the $-y$ direction onto the $+y$. The spins which previously had gained phase relative to the average now begin to lose phase, and vice-versa. Over the second τ_1 delay period the spin vectors will therefore come back into phase, and the magnetisation will grow along the $+y$ axis to give an 'echo'.

Note that the echo sequence can only refocus magnetisation that has been lost due to *inhomogeneous* dephasing, as caused by field inhomogeneity or local fields that are constant over the experimental timescale. Relaxation processes such as instantaneous or nuclear spin diffusion cannot be refocussed, and will cause the echo intensity to fall as τ_1 is increased, as will spin-lattice relaxation. Additional π pulses can be used to create further echoes, as shown in Figure 2.7, b), as long as the magnetisation has not been completely relaxed by these processes.

If the spectral width is less than the excitation bandwidth then the echo intensity is

*the time when the detector must be protected from the high microwave power in the resonator, and therefore cannot detect the signal

independent of the lineshape, and is simply two FIDs back-to-back. For spectral widths greater than the excitation bandwidth, the spectrum can be measured by taking the integral over the echo with respect to B_0.

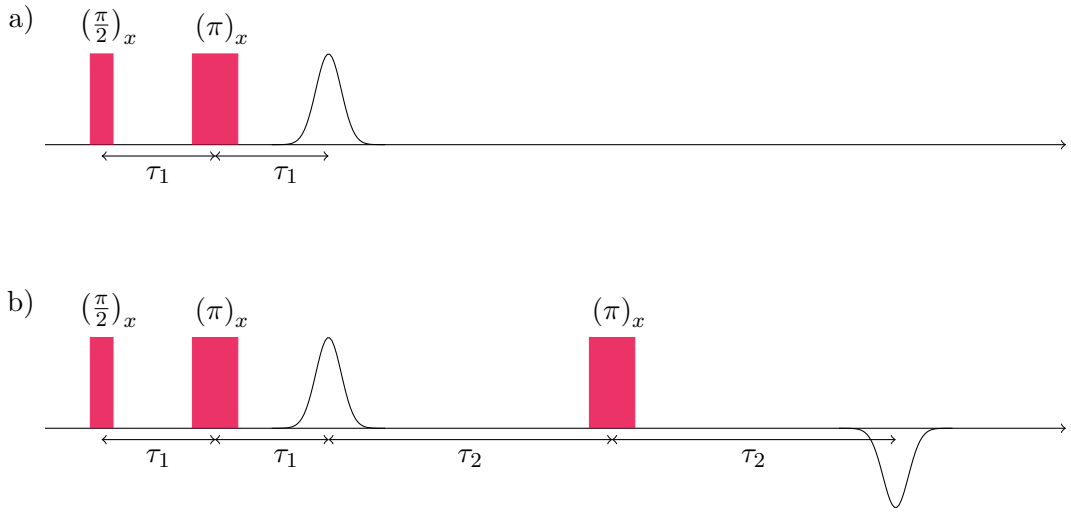

Figure 2.7: *Two and three pulse Hahn-echo experiments. After the magnetisation is flipped into the x–y plane by the $\pi/2$ pulse, the subsequent π pulses refocus the magnetisation and allow the signal to be detected. This can be performed as long as inhomogeneous dephasing has not completely relaxed the magnetisation.*

2.4 Double electron-electron resonance

2.4.1 The DEER experiment

Double electron-electron resonance (DEER, also known as pulsed electron double resonance, or PELDOR) is a pulsed EPR technique which allows the determination of the distance between two paramagnetic centres coupled via their dipolar interaction.[31,32]

DEER can be performed using radicals intrinsically contained within a molecule (for example, Cu^{II} centres[33]). However, for the investigation of proteins which do not contain such centres, the radicals can instead be provided by labels containing unpaired spins, attached in a site-directed manner. This allows for flexibility in radical positioning, as spin labels can be attached to potentially any part of the protein as long as the mutagenesis process does not disrupt the structure too much. The α-lactalbumin molten globule does not contain any intrinsic radical centres, so nitroxide spin labels were used here for distance measurements. The nitroxide labels are introduced further in Section 2.4.4.

The pulse sequence for the four-pulse DEER experiment used in this thesis is shown in Figure 2.8. The experiment is conducted as follows.

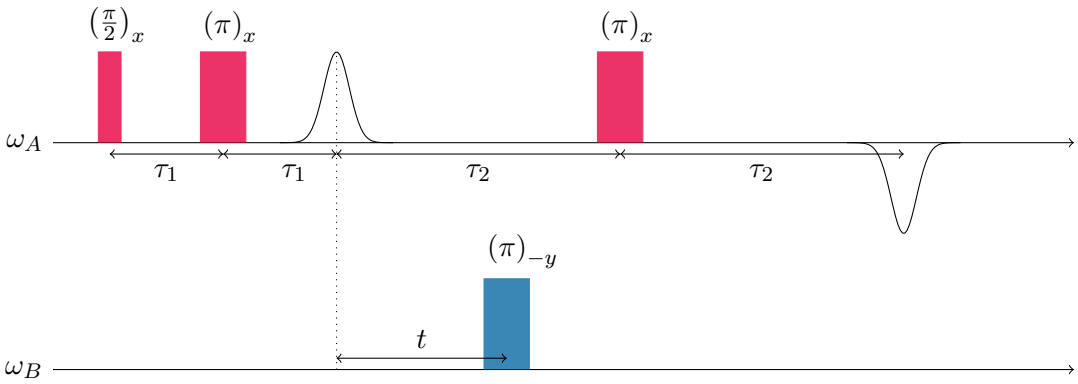

Figure 2.8: *Four-pulse DEER experiment, showing pump and observation pulses. The* $(\pi)_{-y}$ *pulse is incremented in* t*, modulating the intensity of the final echo with the dipolar frequency,* ω_{AB}*.*

An 'observation' sequence is performed at a particular frequency, ω_A, consisting of a three pulse echo sequence. The initial $\frac{\pi}{2}$-pulse flips these A-spins (with resonant frequency ω_A) into the x–y plane. The spins evolve under their Hamiltonian, including the dipole-dipole interaction with coupled electrons, hyperfine interactions, g-factor dispersion, etc. After a delay, τ_1, a π-pulse refocuses the magnetisation to give a primary echo at $2\tau_1$. Another π-pulse is then applied after additional delay τ_2 leading to a refocussed echo at time $2\tau_1 + 2\tau_2$. The delay parameters τ_1 and τ_2 are chosen such that the secondary echo has sufficient intensity to be detected, but that τ_2 is long enough to allow a sufficiently long DEER trace to be collected (as discussed later in Section 2.4.3).

A π-pulse is applied at a different (pump) frequency, ω_B, at time $2\tau_1 + t$, where t is the experimental variable. Some spins coupled to the A-spins, which we will label the B-spins, will be excited by this pulse, and their spin state will therefore be flipped by it.

We can see the effect of the pump pulse by considering the rotating frame Hamiltonian for the A-spins[34]

$$\hat{H}_A = \Delta\omega_A \hat{S}_z^A + \omega_{AB} \hat{S}_z^A \hat{S}_z^B \tag{2.7}$$

where $\Delta\omega_A = \omega_A - \omega_{\text{mw}}$. The dipolar interaction leads to a splitting of the resonant frequencies of the A-spins, $\omega_A^{\pm} = \Delta\omega_A \pm \frac{1}{2}\omega_{AB}$, depending on whether the coupled B-spin is in the α or β state. The pump pulse causes the spin state of the B-spins to flip, and the A-spins formerly evolving at frequency ω_A^+ will now evolve at ω_A^- and vice-versa. At time

$2\tau_1 + 2\tau_2$, the final echo has been refocussed, and the A-spins will have acquired phase

$$\begin{aligned}\psi &= \omega_A^{\pm}\tau_1 - \omega_A^{\pm}(\tau_1 + t) - \omega_A^{\mp}(\tau_2 - t) + \omega_A^{\mp}\tau_2 \\ &= \pm\omega_{\mathrm{AB}}t. \end{aligned} \tag{2.8}$$

As t is incremented during the experiment the echo intensity (normalised at $t = 0$) will vary as

$$v(t) = \cos(\omega_{\mathrm{AB}}t). \tag{2.9}$$

Returning to Equation 1.16, the modulation frequency is given by

$$\omega_{\mathrm{AB}} = \frac{\mu_0}{4\pi\hbar}\frac{g_A g_B \mu_B^2}{r_{AB}^3}\left(3\cos^2\theta_{AB} - 1\right) \tag{2.10}$$

assuming that the exchange coupling can be neglected[†]. The modulation frequency of the echo can therefore be related to the inter-radical distance, r_{AB}.

For all spins B_i coupled to A, the total echo amplitude will be[35]

$$V(t) = \prod_i \{1 - \lambda_i[1 - \cos(\omega_{AB,i}t)]\} \tag{2.11}$$

where λ_i is the fraction of spins B_i excited by the pump pulse.

The total signal intensity, $V(t)$, is the product of two contributions, the background factor, $B(t)$, which is caused by intermolecular pairs of coupled spins, and the form factor, $F(t)$, the result of intramolecular pairs of coupled spins.

$$V(t) = F(t)B(t). \tag{2.12}$$

For a sample with molecules homogeneously distributed in D spatial dimensions the background factor is $B(t) = \exp(-\alpha t^{D/3})$. Typically α and D are treated as experimental parameters. Alternatively, an experimental background using singly-labelled molecules can be recorded and used in the extraction of the form factor $F(t)$. The form factor can then be used to extract information about the distance distribution of intramolecular spins.

The modulation depth, Δ, is the difference in intensity of the form factor between

[†] ω_{exch} would add an additional component to the phase gained/lost by the A-spins

$t = 0$ and long times, and can be used to define the reduced form factor, $f(t)$, as

$$f(t) = \frac{F(t) - (1 - \Delta)}{\Delta}. \tag{2.13}$$

The modulation depth is related to the number of spins in the system, N, the B-spin inversion efficiency, λ, and labelling efficiency, f, by[35]

$$N = 1 - \frac{\ln(1 - \Delta)}{\ln(1 - \lambda f)}. \tag{2.14}$$

2.4.2 Extraction of distance information from DEER traces

Determination of distance information from the DEER trace at first appears to be a trivial problem. However, accurate extraction of the form factor $F(t)$ from $V(t)$ requires precise knowledge of the background function $B(t)$. This can be difficult if aggregation or other effects make the molecular distribution non-homogeneous. Experimental measurement of the background function using singly-labelled molecules can be used instead, so long as the presence of the second label does not have an effect on the distribution, for instance by changing the conformation such that aggregation is promoted or impeded.

Given faithful extraction of $F(t)$, transformation to give the distance distribution, $P(r)$ is a moderately ill-posed inverse problem, meaning that a number of possible (including unphysical) distributions $P(r)$ could give the same $F(t)$, and that the solution is highly sensitive to small changes in $F(t)$ (arising from inaccurate background correction or noise in the experimental data, or both).

For molecules with well-defined molecular geometries, Fourier transformation of the form factor can give a fairly well defined Pake doublet, allowing direct extraction of the distance information from the singularities.[34,36] However, for molecules with a broader distribution of conformations, the superposition of Pake patterns corresponding to all distances represented makes direct distance extraction from the Fourier transform difficult, if not impossible. In this case, Tikhonov regularisation[37,38] may be employed to determine the solution to the ill-posed problem.

In this approach, a functional is constructed such that

$$\Psi[P] = \|KP(r) - f(t)\|^2 + \alpha\|P(r)''\|^2 \tag{2.15}$$

where $KP(r)$ is a calculated form factor, with $P(r)$ being the distance distribution, K

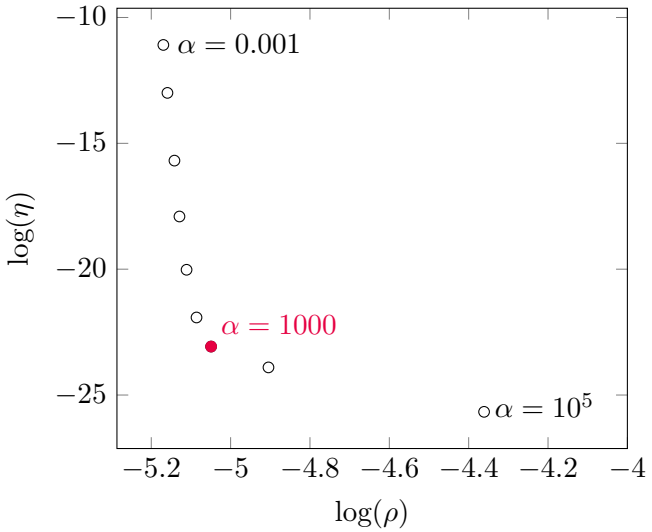

Figure 2.9: *L-curve plot for optimising the choice of regularisation parameter, α. The optimal value (highlighted), in this case 1000, was chosen as the value at the 'kink' of the L shape at bottom left.*

being the kernel function

$$K = \int_0^1 \cos\left[(1 - 3\cos^2\theta)\omega_{\mathrm{AB}}t\right] d\cos\theta \tag{2.16}$$

and α the regularisation parameter.

The functional is then minimised to obtain the regularised solution. The first term on the right hand side ensures the calculated form factor fits the experimental data. The second term is a measure of the roughness of $P(r)$, weighted by the regularisation parameter, and imposes a smoothness constraint on the solution. Optimal regularisation depends on choosing the appropriate value of α: too small and noise will be represented as spurious peaks in the final distribution; too large and the distribution will be over-smoothed and real distance information will be lost. Choice of optimal α is generally accomplished by means of the L-curve criterion.

The L-curve is a parametric plot of $\log(\rho(\alpha))$ vs $\log(\eta(\alpha))$, with

$$\begin{aligned} \rho &= \|P''(r)\| \\ \eta &= \|KP(r) - f(t)\| \end{aligned} \tag{2.17}$$

found by minimisation of Equation 2.15 with a range of α. This generally forms an 'L' shaped curve, and by minimising both ρ and η (i.e. the point of the 'L' at bottom left, Figure 2.9) the optimal value can be chosen that neither under-smooths (small α, back-

bone of the 'L') nor over-smooths (large α, foot of the 'L'). In effect, the optimal α is a compromise between faithful representation of $f(t)$ and suppression of spurious peaks resulting from fitting experimental noise.

All DEER data analysis in this thesis was carried out using the DeerAnalysis2013 package,[39] which implements background correction and Tikhonov regularisation within the MATLAB[40] software environment.

2.4.3 Experimental considerations

The pulse delays, τ_1 and τ_2, must be chosen with care in four-pulse DEER. The length of the time domain DEER signal has a maximum of $\tau_2 - \tau_d$ where τ_d is the delay between the pump π-pulse and the last observer π-pulse needed to avoid artefacts. The ability to faithfully extract distances depends on accurate simulation of the form factor, and successful simulation of low frequency (long distance) modulations depends on $t_{\max}$ being large enough: at least half a modulation is needed to determine the mean distance, one and a half modulations for the width, and more than three to determine the shape of the distribution accurately.[41] The value of τ_2 therefore places an upper limit on distance detection by DEER. For a 2 µs long trace, a rule of thumb states that the shape of the distribution is reliable up to 3 nm, the mean distance and width up to 4 nm, the mean distance but not width up to 5 nm, and the presence of a distance alone up to 6 nm.[42] These guidelines are displayed in the distribution plots as shaded green, yellow, orange, and red regions respectively. For other values of $t_{\max}$, these regions are scaled as $(\frac{t_{\max}}{2\mu s})^{1/3}$.

However, the signal intensity decays with $1/T_{m,A}$, and since the final distribution is highly sensitive to noise in the form factor, a balance must be struck between the $t_{\max}$ necessary to detect long distances and the increasing noise caused by transverse relaxation. The DEER experiment is therefore best performed in the low temperature limit of transverse relaxation, typically between 40 and 60 K for nitroxide-labelled proteins.[43] The transverse relaxation time can also be prolonged by deuteration of the solvent, and in extreme cases by deuteration of the protein matrix. Measurements on deuterated proteins of distances up to 10 nm have been reported.[44]

In addition to the upper limit on measurable distances, DEER becomes unreliable below 1.5 nm. This is due to a combination of factors, including the increasing exchange coupling at short distances and the limited bandwidth of the pulse being unable to excite the extent of the dipolar spectrum.[43] For short distances, other techniques such as observer-

selective DEER[45] or deconvolution of cw spectra[46] are more appropriate.

2.4.4 The nitroxide spin label

An important class of spin labels used for distance measurement in proteins are nitroxides, which are relatively stable, available commercially, cheap, and can be covalently attached to proteins in a straightforward manner. Of the nitroxide spin labels, the most commonly used is the methanethiosulfonate spin label (MTSL, also known as R1). MTSL can be attached to cysteine residues in proteins, which can be inserted by site-directed mutagenesis of the protein of interest with minimal disruption of the structure.

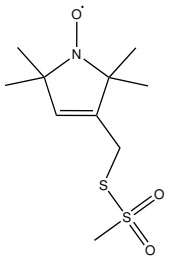

Figure 2.10: *MTSL spin label. MTSL can be attached to free cysteine in proteins, allowing labelling at chosen sites.*

A question that might arise is, how is it possible to use a single type of spin label at both positions, when in order to carry out the DEER experiment different spins must be excited using pump and observer pulses? The answer lies in the fact that the EPR spectrum of the nitroxide radical is split into three lines due to the nuclear spin levels of the coupled ^{14}N. The ^{14}N nucleus has $I = 1$, the EPR line therefore being split into three, corresponding to the three nuclear spin states $m_I = -1, 0, +1$ (Figure 2.11). In frozen solution, these lines are broadened by the anisotropic g-tensor, and the $m_I = \pm 1$ lines are broadened by the anisotropy of the hyperfine coupling, so that the three lines overlap to form the spectrum shown in Figure 2.11. Despite the overlap of the three lines (and the bandwidth of the microwave pulses), it is possible to chose the DEER pump and observer frequencies such that the majority of spins excited belong to one of the nuclear spin manifolds. For instance, pumping on the central peak will excite primarily those spins with the coupled nitrogen in the $m_I = 0$ level (with minor contributions by the $m_I = \pm 1$ levels). Similarly, pumping on the low-field peak corresponds to those electron spins with the coupled nitrogen in the $m_I = +1$ level. Given that nuclear relaxation is slow on the EPR timescale, it is therefore possible to selectively excite a given set of spins, and thus use the same spin label for both positions.

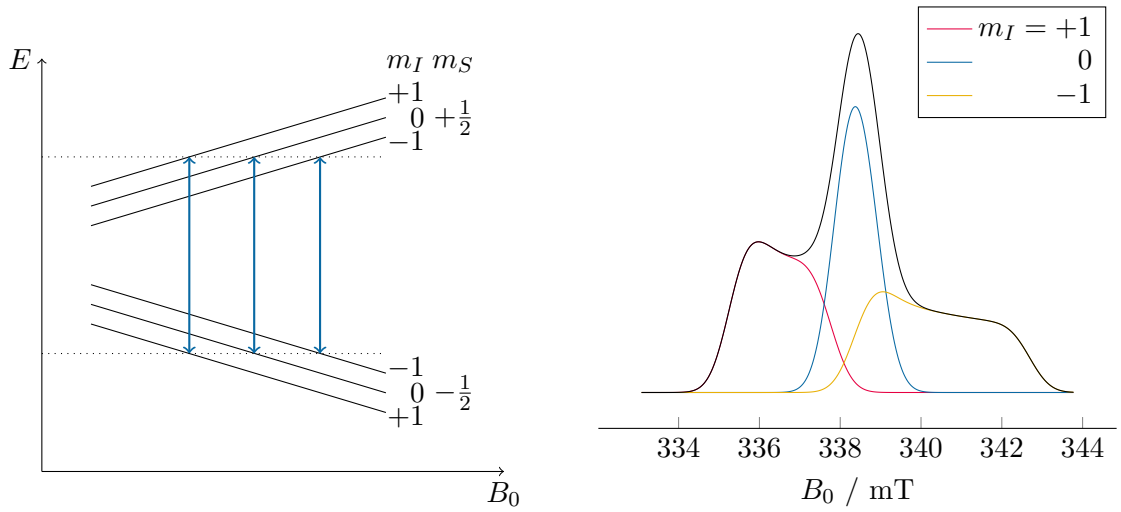

Figure 2.11: *Left: Energy level diagram for the nitroxide radical, showing the splitting of the EPR spectrum into three lines by the nuclear spin levels of the nitrogen. Right: Simulated frozen solution spectrum of a nitroxide, showing broadening of the peaks due to the anisotropy of the hyperfine and g-tensors. Spectra were simulated using EasySpin,*[47] *with parameters* $g = [2.0091, 2.0061, 2.0022]$, $A_N = [0.45, 0.45, 3.7]$ mT, $\nu = 9.5$ GHz.

Since MTSL is covalently attached to the protein by coupling to a cysteine residue, if selective labelling is to be carried out, the protein must not contain any solvent accessible cysteine residues which could be labelled in addition to the desired targets. This means that MTSL is unsuitable in the case of proteins that rely on disulfide bridges to maintain tertiary structure, or that have functional cysteine residues. In these cases, other labelling strategies can be used.[48] In order to selectively target just two positions of choice, the protein must be modified to remove any solvent accessible cysteine, with two cysteines being inserted at the positions of choice. This is typically done by site directed mutagenesis.

2.4.5 Choosing labelling sites and native state distance prediction

The choice of spin labelling sites is an important one, as they must be chosen according to several criteria:

1. The labels must not disrupt the structure of the protein too much. If the DEER experiment is to report accurately on the chosen distance, then that distance must not be drastically changed by the act of spin labelling.

2. The sites must be of scientific interest, i.e. the chosen measurement must be a distance that will provide insight into the structure or dynamics of the protein.

3. Most importantly, the expected distance should be within the measurable range for DEER, commonly 1.5–6 nm.

It must be remembered that the measured distance is between spin labels, and as such depends on the conformation(s) of the label in addition to that of the protein itself. Prediction of the spin label dynamics can be carried out using atomistic molecular dynamics (MD) simulations.[49–51] However, the computational expense of such method spurred the development of less expensive approximate approaches. One such method is to use a rotamer library, a discrete set of side chain conformations, combined with a known structure.[52]

The rotamer library for a particular spin label is obtained from MD trajectories for the five side chain angles, $\chi_1 - \chi_5$ (Figure 2.12), at the appropriate temperature (175 K in the case of frozen solutions, approximating the glass transition temperature of a glycerol/water mixture). These rotamers can then be used with a known model of the protein, with an external energy being computed by pairwise interactions with protein atoms within a specified radius, in order to give a distribution of spin label side chains for a particular labelling site. In the work in this thesis, this was carried out using the MMM software package.[52]

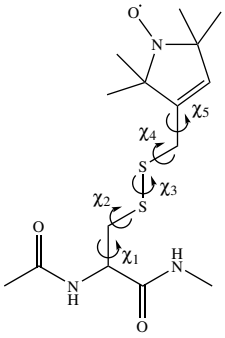

Figure 2.12: *MTSL attached to the protein backbone, showing the five bond angles, $\chi_1 - \chi_5$, that determine the spin label conformers. The distance distribution measured by DEER includes the effect of both the flexibility of the label and the protein backbone.*

The native state X-ray crystal structure of α-lactalbumin (PDB:1A4V[20]) was used to scan for suitable spin labelling sites, and to predict the native-state distance distributions. Of course, the molten globule has a fluctuating ensemble of tertiary structures that differs from the native fold, and so the distances measured in the molten globule are not necessarily expected to match those in the native state. However, the retention of native-like secondary structure suggests that the native state structure may act as a guide to suitable label positions, and as a point of comparison when discussing the measured distances.

Four labelling sites were chosen by Dr Matthew Young that were predicted to not disrupt the structure of the protein, had suitable distances for DEER measurement, and

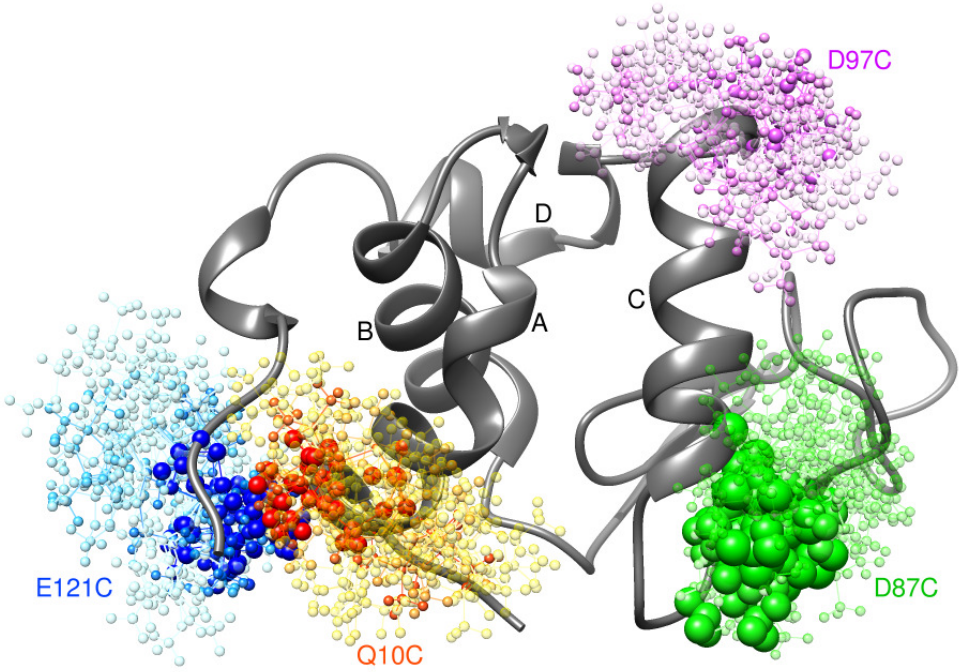

Figure 2.13: *Native state structure of α-lactalbumin, showing the four labelling sites and rotamer positions. The size and colour of each atom is rendered with respect to the relative population. Larger spheres and darker, more opaque colours correspond to a larger population of that particular rotamer. The rotamer positions were calculated using PDB:1A4V,[20] MMM,[53] and visualised using UCSF Chimera.[21] Helices are labelled in black text.*

were of scientific interest. These were: Q10C, on the A helix; D87C and D97C, on the C helix; and E121C, at the C-terminus. The six pairs of labels and predicted mean distances, $\langle r \rangle$, and distribution widths, σ_r, for the native state are shown in the Table 2.1, with the calculated rotamers being shown in Figure 2.13. The predicted native-state distribution, as well as a simulated form factor for the native state, for each pair is shown alongside the DEER data in later sections.

All spin-label pairs lie within the range suitable for DEER measurement, excepting Q10C-E121C, which is predicted to have a mean distance of 1.34 nm for the native state. The close contact between these residues in the native state is maintained by the 6-120 disulphide bond, which is absent in the all-Ala variant; the 10-121 distance in the all-Ala molten globule may therefore be significantly longer than predicted for the native state. The Q10C-E121C mutant was therefore analysed by both dipolar broadening of the cw EPR spectrum (Section 2.5), which is suitable for distances between 0.5 and 4 nm, and DEER.

Pair	$\langle r \rangle$ / nm	σ_r / nm
Q10C–D87C	2.20	0.40
Q10C–D97C	2.85	0.33
Q10C-E121C	1.34	0.47
D87C–D97C	2.09	0.38
D87C–E121C	3.12	0.39
D97C–E121C	3.50	0.35

Table 2.1: *Spin-label pairs chosen for DEER measurements. The mean distances and distribution widths were predicted for the native state using MMM[53] and PDB:1A4V.[20]*

Residues E25 and T33 were also labelled and measured with DEER by Dr Alice Bowen in an attempt to measure the unfolding of the B helix in the molten globule. These residues were not predicted to disrupt the structure and their distance was suitable ($\langle r \rangle$ = 2.09 nm, σ_r = 0.12 nm). However, it was found that labelling at these sites caused aggregation of the protein that prevented DEER measurements, suggesting that one or both of these residues plays a role in stabilising the core.

2.4.6 Experimental protocol

For each experiment the required mutant was cloned, expressed, purified, and labelled by Dr Matthew Young. Lyophilised protein was dissolved in 200 µL of 80:20 H_2O:glycerol (or D_2O:glycerol-d_8 for some samples) to a final concentration of 0.2 mM at pH 2. Approximately 100 µL of this was placed in a 3 mm OD quartz EPR tube and flash frozen using

liquid nitrogen. Samples were either used immediately or stored at −80°C.

Measurements were taken using a Bruker ELEXSYS E680 EPR spectrometer operating at X-band, fitted with a Bruker ER 4118X-MS3 split ring resonator. The temperature was maintained at 50 K for all experiments using an Oxford Instruments cryostat system flowing liquid helium.

16 and 32 ns pulses were used for observer $\frac{\pi}{2}$ and π pulses respectively. A 24 ns pulse was used for the pump π pulse. τ_1 was set to 176 ns, with τ_2 being varied between 1.5 and 2.5 µs depending on the echo intensity observed for each sample. τ_1 was incremented in eight steps of 8 ns (56 ns for deuterated samples) in order to suppress nuclear modulation of the echo. Experiments were typically run for around 18 hours in order to maximise the signal to noise ratio.

2.5 Short range distance measurement by Gaussian convolution of cw spectra

The distance distributions of mutants with distances below the lower limit for DEER (1.5 nm) can be determined by analysing the dipolar broadening of the cw spectrum of the doubly-labelled mutant relative to the corresponding singly-labelled variants. This can be accomplished by convolution of the spectrum of the singly-labelled mutant with a sum of Pake patterns corresponding to a Gaussian distribution of distances, which has been found to be a good approximation of the distance distribution of flexible spin labels.[54,55]

The convolution of the spectra presented in this thesis was carried out using an adapted version of the program DipCon by Banham *et al.*,[46] itself based on Dipfit by Steinhoff and coworkers.[55] This program determines the distribution function by minimising the difference between the doubly-labelled spectrum and the convolution of the singly-labelled spectrum and the sum of weak-coupling Pake patterns for a Gaussian distribution of distances.

The exchange coupling, J , was assumed to be zero when calculating the Pake patterns; an arbitrary lower limit of 0.51 nm was therefore placed on the distance (below which this assumption is assuredly no longer valid). An upper limit of 4 nm on the distance is used by DipCon, and it has been found that this method becomes increasingly unreliable for distances above 2 nm.[56]

2.6 Results and discussion

2.6.1 Singly-labelled samples for background correction

The singly-labelled mutants Q10C, D87C, D97C, and E121C were measured in order to provide an experimental background for the other measurements, as shown in Figures 2.14 to 2.17.

Both Q10C and D97C show deviation from the expected exponential decay in the form of a small initial drop in $V(t)/V_0$. This indicates that there is an extra contribution to the DEER traces (in addition to the expected homogeneous background functions) from aggregated protein.

A 1:1 weighted sum of the relevant fitted single-labelled background functions were used in the background correction of the doubly-labelled mutants.

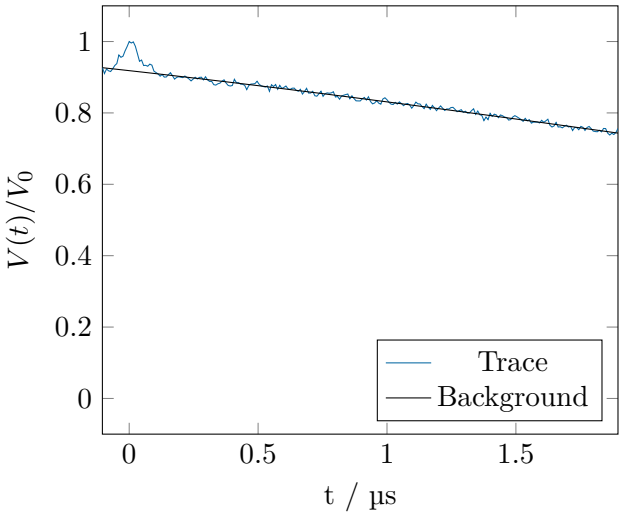

Figure 2.14: *DEER trace for singly-labelled mutant Q10C. Note the small initial drop in $V(t)/V_0$, indicating a non-homogeneous distribution of distances due to aggregation of the sample.*

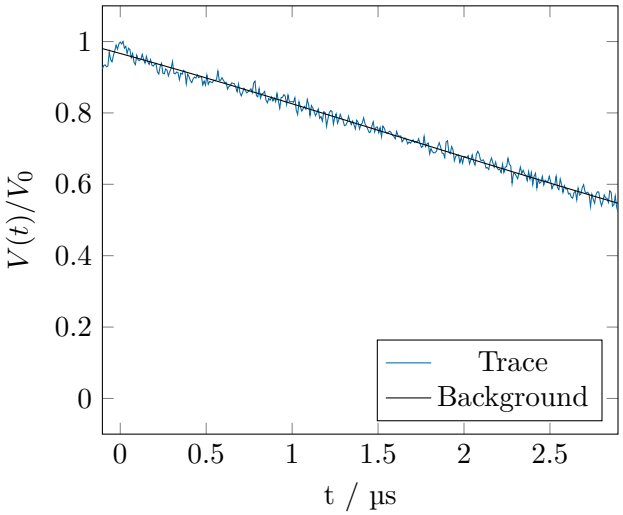

Figure 2.15: *DEER trace for singly-labelled mutant D87C.*

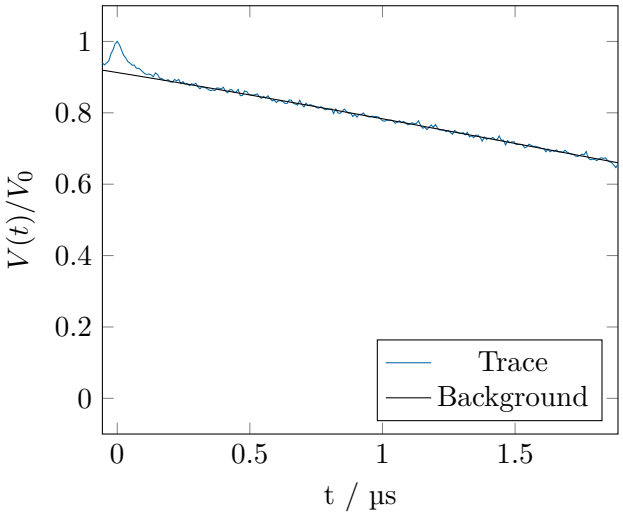

Figure 2.16: *DEER trace for singly-labelled mutant D97C. The small initial drop in $V(t)/V_0$ again indicates a non-homogeneous distribution of distances due to aggregation of the sample.*

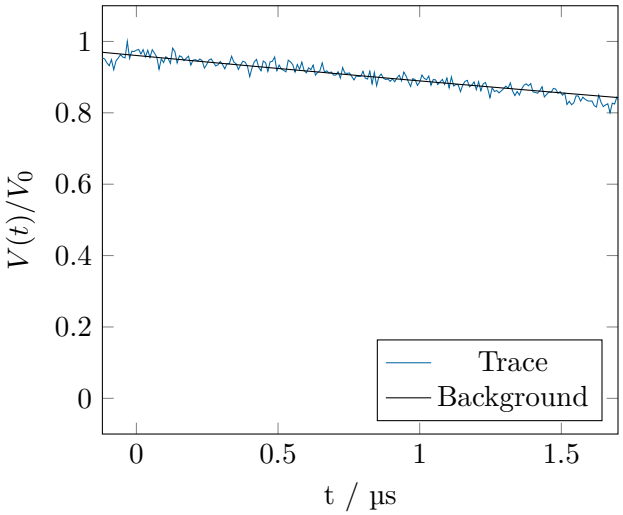

Figure 2.17: *DEER trace for singly-labelled mutant E121C.*

2.6.2 D87C-D97C and the C-helix

In Section 2.1, two studies with relevance to the C-helix were discussed. Firstly, Schulman *et al.* showed that the introduction of two helix-breaking proline mutations into the C-helix of a single-disulphide variant of α-lactalbumin did not affect the helical content of the protein, suggesting that this helix is unfolded in the molten globule.[24] These experiments were carried out at pH 7. Conversely, a study by Ramboarina and coworkers found that residues in the C-helix of both the single-disulphide and all-Ala variants have significant chemical shift deviations from random-coil at pH 2, suggesting the C-helix is folded in the molten globule.[28] This was studied further by Rösner and Redfield, who compared the structure at pH 2 and 7.[57] They found that the molten globule is generally less stable at pH 7, and suggested that this effect could account for the differences observed in the state of the C-helix. In order to probe the α-helical state of the C-helix in the molten globule at pH 2, presented here are measurements of the distance between residues D87 and D97, at opposite ends of the C-helix, quantitatively establishing the extent of C-helix unfolding.

The normalised DEER trace for D87C-D97C is shown in Figure 2.18, and the form factor obtained after background correction in Figure 2.19. There is a sharp initial drop in the form factor, indicating that there are short distances present. The decay of the echo is well described by the background function, with the form factor being flat after ~ 0.1 µs. A very small first modulation is observed, with no subsequent modulations being visible, indicating an absence of longer distances in the distribution.

The distance distribution extracted by Tikhonov regularisation is shown in Figure 2.20. The mean distance and distribution width predicted for the native state was $\langle r \rangle = 2.09$ nm, $\sigma_r = 0.38$ nm, compared to $\langle r \rangle = 1.95$ nm, $\sigma_r = 0.27$ nm for the molten globule. These figures are in good agreement and, remembering that the C-helix in the native state extends from T86 to I98, suggest that the entire C-helix is coiled in the molten globule.

The form factor for the native state, simulated using MMM, is compared to the measured form factor in Figure 2.21. The faster initial drop for the molten globule is caused by short distances in the distribution, and there is a clear lack of lower-frequency modulations which would be expected for the unfolded helix.

Interpreted in the context of previous work, these data add further evidence to the work of Ramboarina *et al.* that the C-helix is almost completely folded in the molten globule.

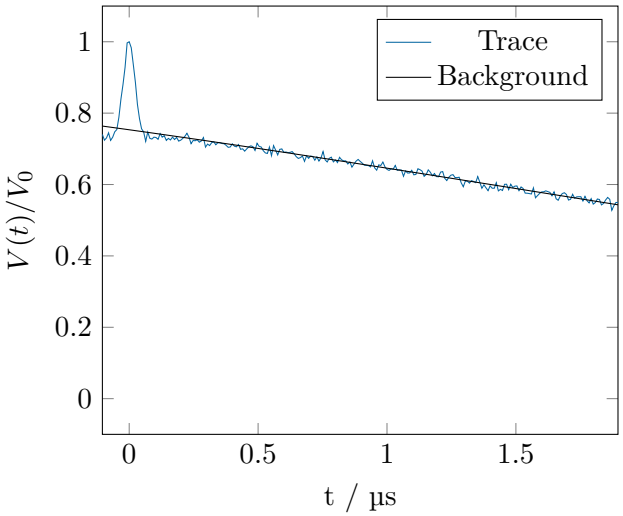

Figure 2.18: *DEER trace of D87C-D97C (blue) and background function (black).*

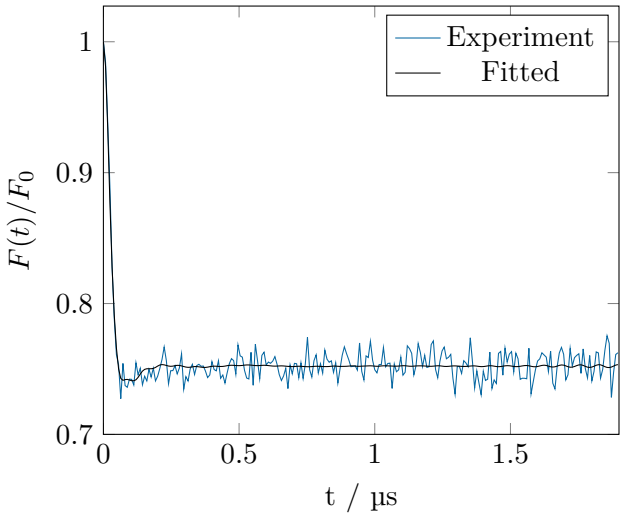

Figure 2.19: *Background corrected form factor for D87C-D97C, showing fitted form factor in black.*

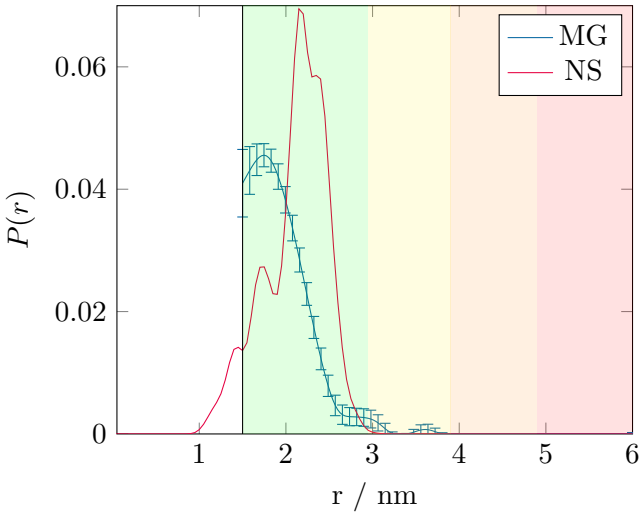

Figure 2.20: *Distance distributions for D87C-C97C for the molten globule (blue) and the native state (red).*

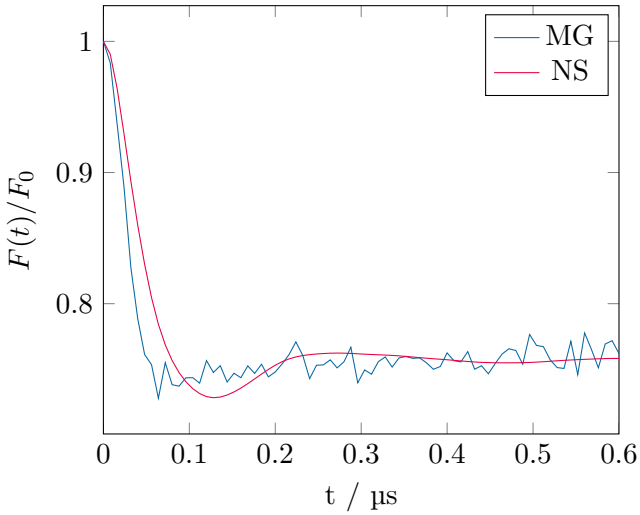

Figure 2.21: *Form factors as measured for D87C-D97C as measured for the molten globule (blue) and simulated for the native state (red).*

2.6.3 Q10C-D87C, Q10C-D97C, and the N-terminus

The DEER traces for Q10C-D87C and Q10C-D97C mutants are shown in Figures 2.22 and 2.26, and the calculated distance distributions in Figures 2.24 and 2.28 respectively. The traces for each mutant are similar, with clearly slower decays, and therefore longer distances, than for D87C-D97C.

Q10C-D87C has a mean distance and width of $\langle r \rangle = 2.44$ nm, $\sigma_r = 0.47$ nm from the DEER measurement, only slightly longer than the distance predicted by MMM for the native state ($\langle r \rangle =$ nm 2.20, $\sigma_r = 0.40$ nm). This moderate increase in distance would be expected from the expanded molten globule, and suggests that the A-helix is part of the hydrophobic core.

More speculatively, the modest increase in distance and width of the distribution might suggest that the A-helix remains in a similar position as in the native fold. The main difference between native-state predicted and molten globule observed distributions is an increased population at longer distances, which could be attributed to the intrinsically increased flexibility of the molten globule only. However, caution should be taken against overinterpretation of the distance distribution in this manner. The lack of visible modulations in the DEER trace make extraction of the distance distribution particularly fraught, and although the mean distance and width can be considered fairly reliable, the shape of the distribution is less certain.

For Q10C-D97C, the DEER measurement gave $\langle r \rangle = 2.60$ nm, $\sigma_r = 0.84$ nm, showing a significantly broader distribution than the native state ($\langle r \rangle = 2.85$ nm, $\sigma_r = 0.33$ nm). The distribution here is 80% wider than for Q10C-D87C, suggesting that there is an extra contribution to the flexibility of this mutant. This cannot be assigned purely to the A-helix, since the widths of the distributions for the native state and molten globule in Q10C-D87C are similar (0.40 nm vs 0.47 nm). If the A-helix did show a vastly increased range of positions then Q10C-D87C would also be expected to exhibit a broadened distribution.

Instead, the relatively unchanged width for Q10C-D87C suggests that both of these residues are comparatively well located in the hydrophobic core. Taking this together with the conclusion that the C-helix is almost completely folded in the molten globule, the only remaining explanation for the broad Q10C-D97C distribution is that there are vastly different positional constraints on the two ends of the C-helix. While the A-helix (Q10C) and N-terminal (D87C) end of the C-helix are relatively static, the C-terminal end must be less constrained, and contributes the majority of the width of the Q10C-D97C distribution.

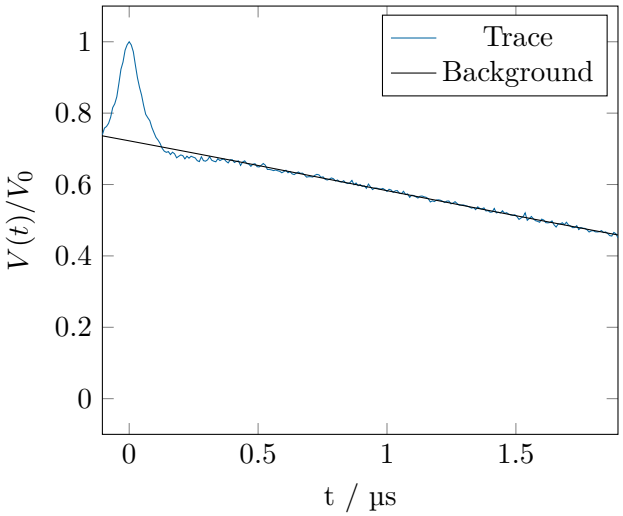

Figure 2.22: *DEER trace of Q10C-D87C (blue) and background function (black).*

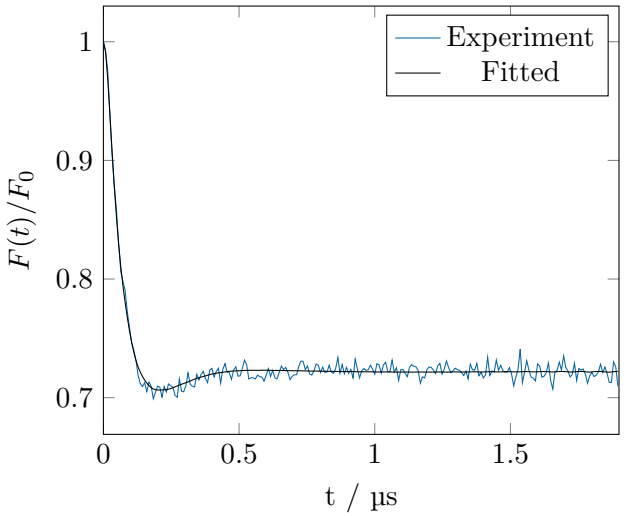

Figure 2.23: *Background corrected form factor for Q10C-D87C, showing fitted form factor in black.*

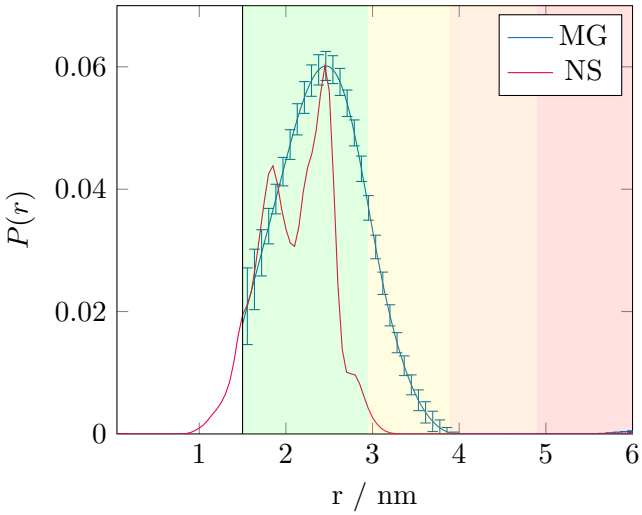

Figure 2.24: *Distance distributions for Q10C-D87C for the molten globule (blue) and the native state (red).*

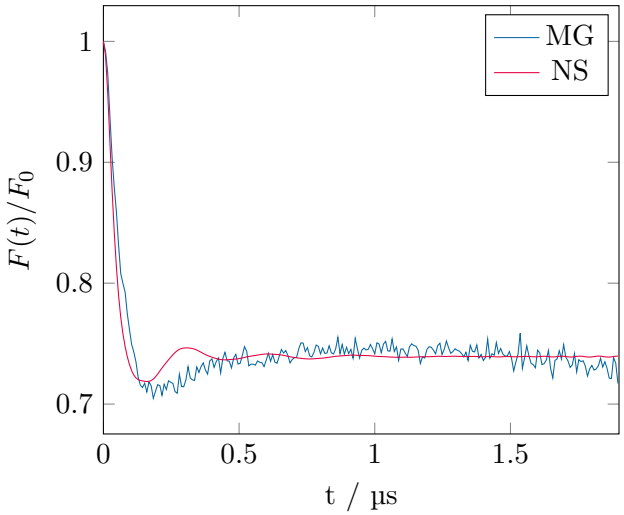

Figure 2.25: *Form factors as measured for Q10C-D87C as measured for the molten globule (blue) and simulated for the native state (red).*

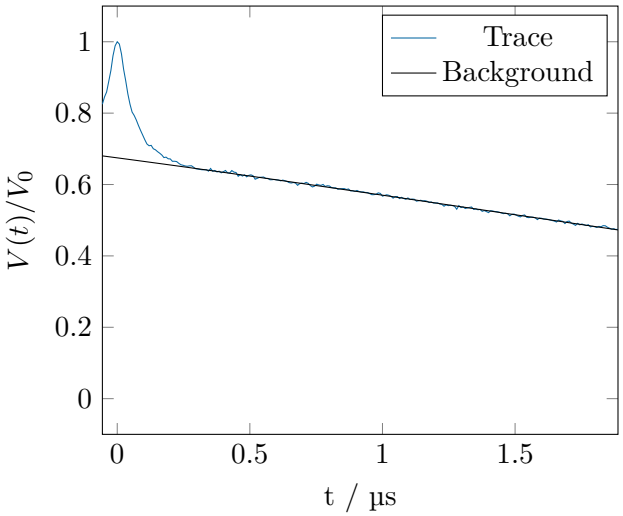

Figure 2.26: *DEER trace of Q10C-D97C (blue) and background function (black).*

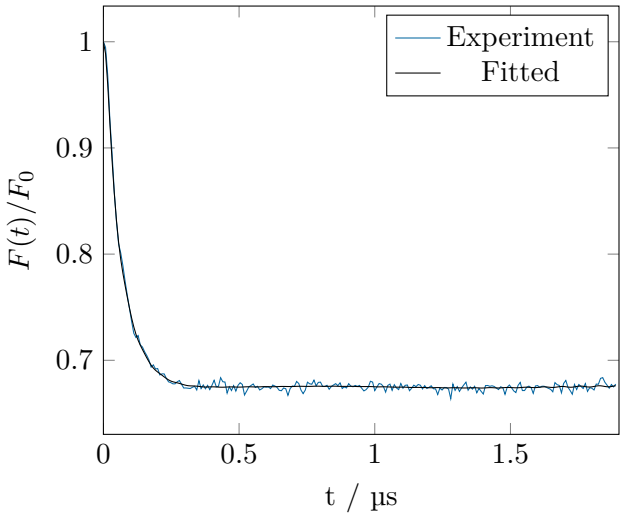

Figure 2.27: *Background corrected form factor for Q10C-D97C, showing fitted form factor in black.*

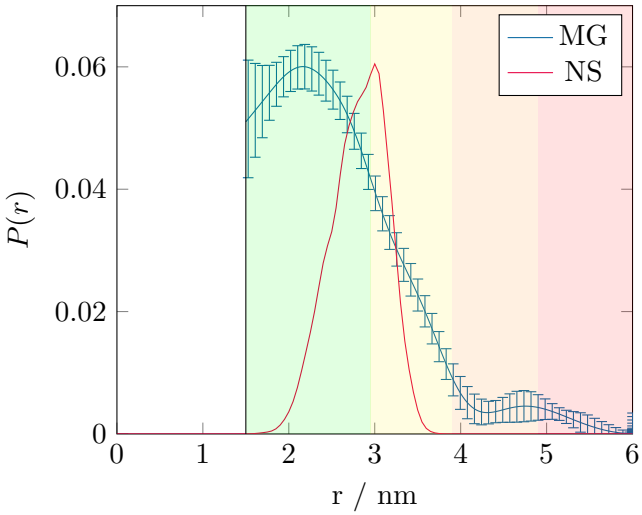

Figure 2.28: *Distance distributions for Q10C-D97C for the molten globule (blue) and the native state (red).*

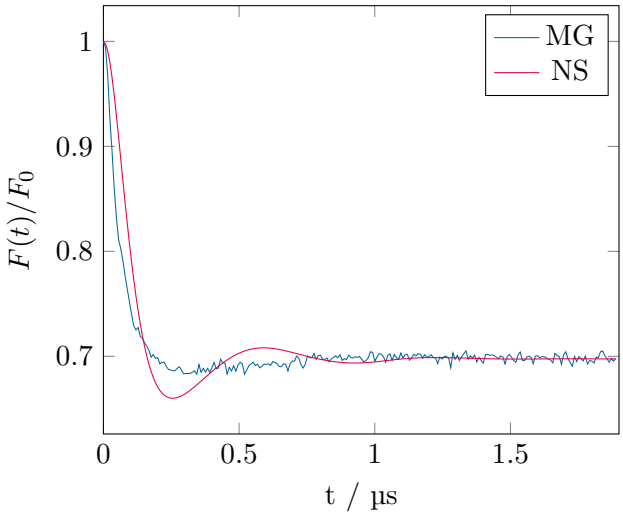

Figure 2.29: *Form factors as measured for Q10C-D97C as measured for the molten globule (blue) and simulated for the native state (red).*

2.6.4 E121C and the C-terminus

Studies of the all-Ala molten globule have previously reported that there are close interactions between residues at the C-terminus and the A, B, and D-helices, indicating that the C-terminus is contained within the hydrophobic core of the protein.[27] Quantitative information about the position of the C-terminus could aid in determining the role of the C-terminus in stabilising the molten globule core. Presented here are the results for distance between E121C and the three other chosen residues.

Firstly, Q10C-E121C allows a measurement of the distance between N- and C-terminal ends of the protein. This distance is predicted to be $\langle r \rangle = 1.34$ nm, $\sigma_r = 0.47$ nm for the native state, with the close association of the termini maintained by the C6-C120 disulphide bond. It might be somewhat surprising then that both termini form part of the molten globule core, even in the absence of the disulphide bridge (in the all-Ala) variant. However, the NMR unfolding experiments of Redfield *et al.* show that the HSQC peaks for residues Q10 and E121 do not appear for the wt until 8 M guanidinium chloride at 20°C (4 M urea for all-Ala), after almost the entirety of the protein has unfolded, suggesting that the termini are important in stabilising the core.[27] Due to the short predicted distance, Q10C-E121C was measured using both cw EPR and DEER.

Continuous-wave EPR spectra were recorded for Q10C, E121C, and Q10C-E121C. Convolution analysis of the spectra was then carried out as described in Section 2.5, using a modified version of the program DipCon[46] for the doubly-labelled sample with each singly-labelled mutant. The results are shown in Figures 2.30 to 2.37.

The convolution produces a good fit to the doubly-labelled spectrum for both singly-labelled mutants, and gives distributions with $\langle r \rangle = 2.15$ nm, $\sigma_r = 0.76$ nm and $\langle r \rangle = 2.39$ nm, $\sigma_r = 0.95$ nm for analysis with Q10C and E121C respectively. These distances are slightly above the limit of reliability for convolution analysis (~ 2 nm). Furthermore, for the analysis with E121C, a large part of the distribution lies outside of the range considered by DipCon. Care should therefore be taken in interpreting these data in the absence of other information. The analysis does, however, rule out native-like close contact between these two residues, and suggests that Q10C-E121C may be reliably measured using DEER.

The mean distance and width as measured by DEER are $\langle r \rangle = 2.66$ nm, $\sigma_r = 0.83$ nm (shown in Figures 2.38 to 2.41); both the mean distance and width of the distribution are similar to the values obtained from the cw data, suggesting that the data are indeed representative of the actual distribution.

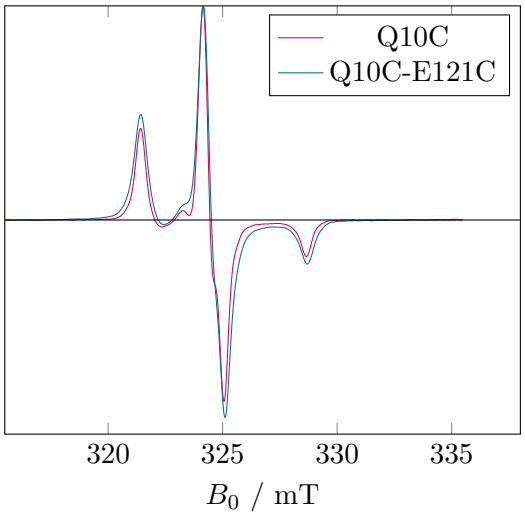

Figure 2.30: *cw spectra of Q10C (singly labelled) and Q10C-E121C (doubly labelled).*

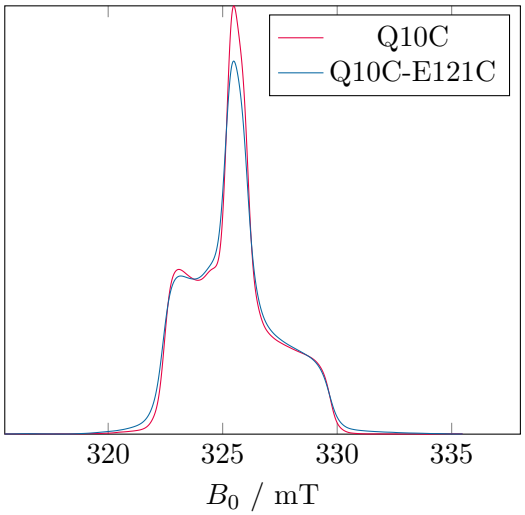

Figure 2.31: *Integrated cw spectra of Q10C and Q10C-E121C. Note the broadening caused by the presence of the second label.*

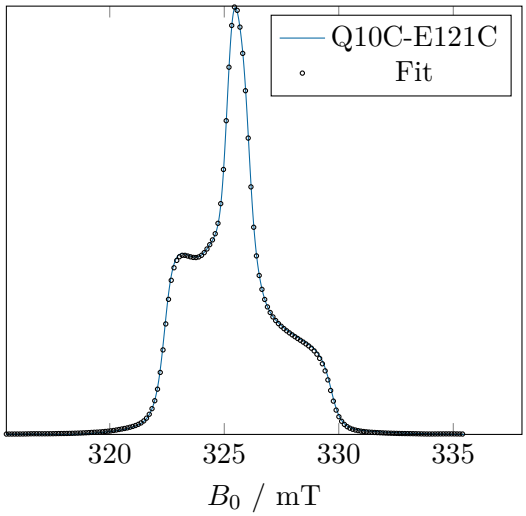

Figure 2.32: *Fitted cw spectra of Q10C-E121C by convolution of the Q10C spectrum with the sum of Pake patterns for a Gaussian distribution function.*

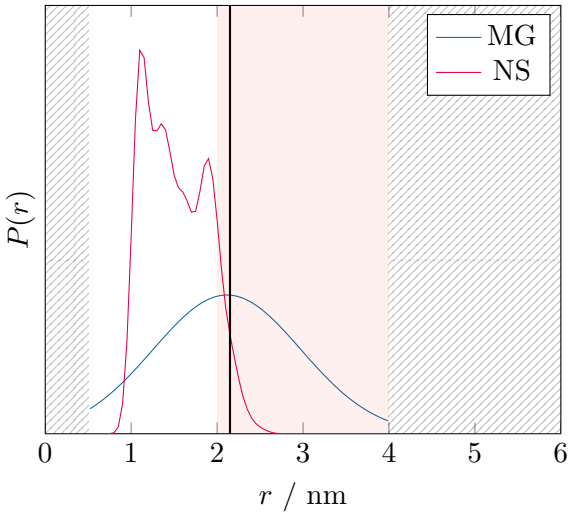

Figure 2.33: *Distance distribution for molten globule (MG) by convolution analysis and predicted by MMM for the native state (NS). Regions outside the scope of DipCon are hatched, unreliable region shaded in red, and the mean distance is highlighted by the black vertical line.*

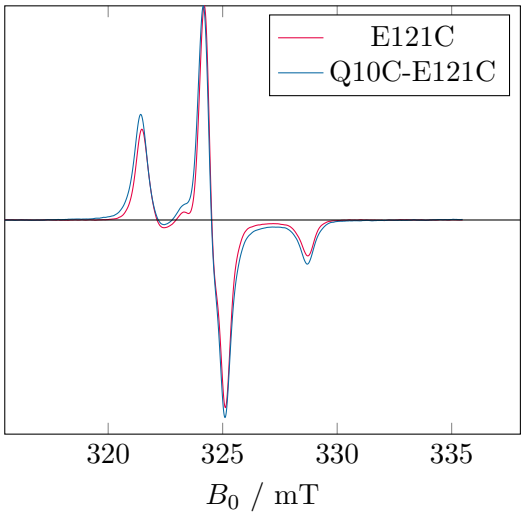

Figure 2.34: *cw spectra of E121C (singly labelled) and Q10C-E121C (doubly labelled).*

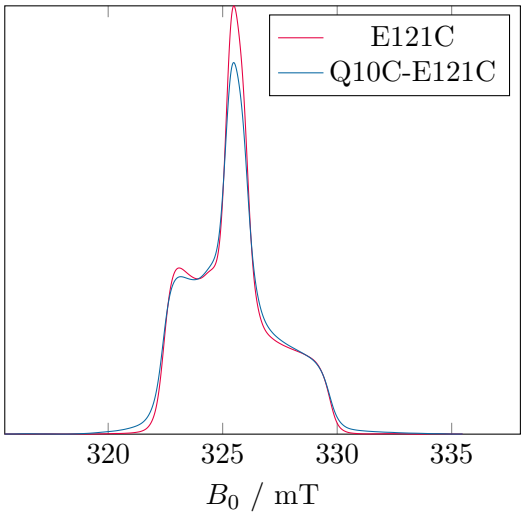

Figure 2.35: *Integrated cw spectra of E121C and Q10C-E121C. Note the broadening caused by the presence of the second label.*

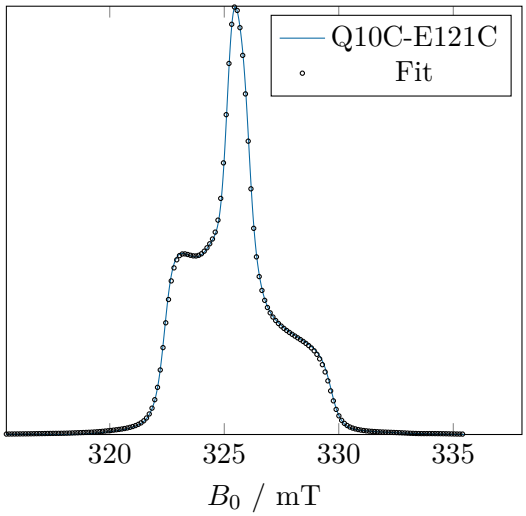

Figure 2.36: *Fitted cw spectrum of Q10C-E121C by convolution of the E121C spectrum with the sum of Pake patterns of a Gaussian distribution function.*

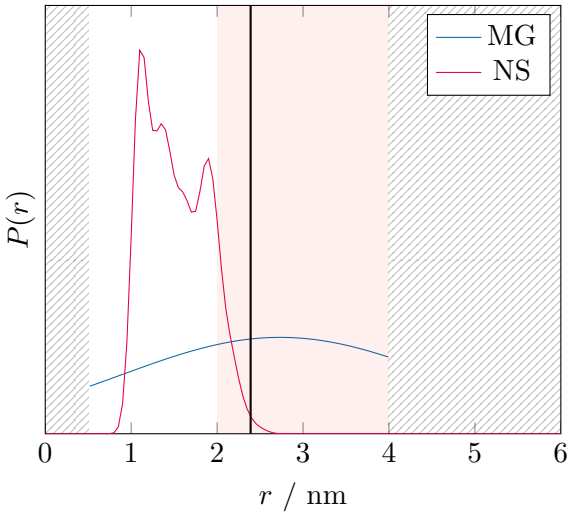

Figure 2.37: *Distance distribution for molten globule (MG) by convolution analysis and predicted by MMM for the native state (NS). Regions outside the scope of DipCon are hatched, unreliable region shaded in red, and the mean distance is highlighted by the black vertical line.*

Both the longer mean distance and broader distribution testify that the C-terminus is no longer in a native-like position. However, before concluding that E121C must be relatively free of the hydrophobic core, it is important to consider the remaining two measurements.

For D87C-E121C, the distance in the molten globule is $\langle r \rangle = 2.30$ nm, $\sigma_r = 0.58$ nm (Figure 2.44) compared to $\langle r \rangle = 3.12$ nm, $\sigma_r = 0.39$ nm for the native fold. For D97C-E121C it is $\langle r \rangle = 2.45$ nm, $\sigma_r = 0.62$ nm (Figure 2.48), compared to $\langle r \rangle = 3.50$ nm, $\sigma_r = 0.35$ nm for the native state. Both of these distances, although broader, are significantly shorter than predicted for the native state. This, along with the longer distance for Q10C-E121C, suggests that, although not in a native-like position, the C-terminus does indeed form part of the core, shifting to a new ensemble of positions, closer to the C-helix. Furthermore, the broadness of all three measurements involving E121C suggests that the terminus has increased flexibility, perhaps not becoming deeply buried in the core, but remaining close to the surface.

Note that the Q10C-E121C mean distance (2.66 nm), although not as short as in the native state, is still well within the range of the other measurements, and does not preclude the conclusion that E121C remains within the core. The mean distance would likely be much longer if it were unconstrained.

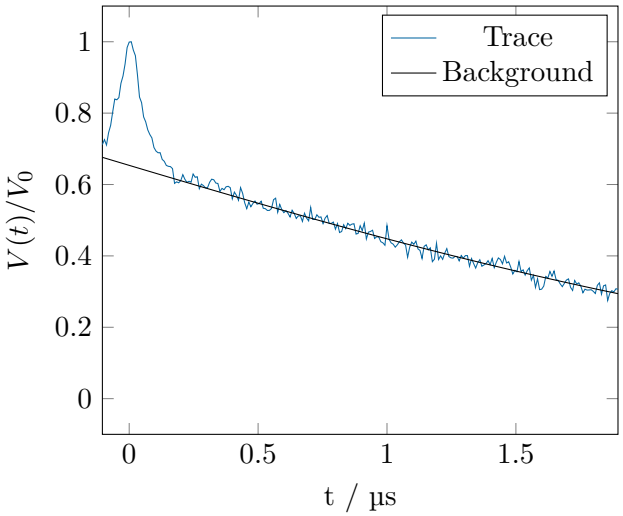

Figure 2.38: *DEER trace of Q10C-E121C (blue) and background function (black).*

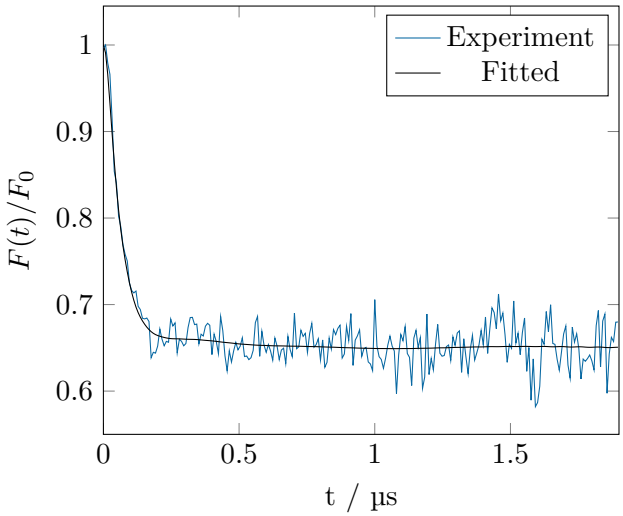

Figure 2.39: *Background corrected form factor for Q10C-E121C, showing fitted form factor in black.*

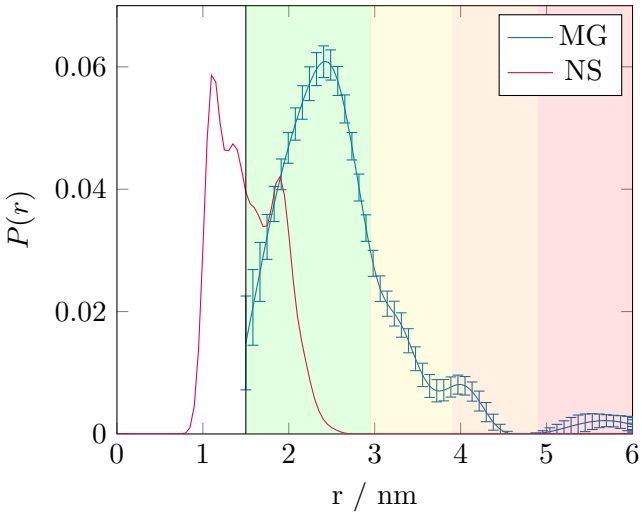

Figure 2.40: *Distance distributions for Q10C-E121C for the molten globule (blue) and the native state (red).*

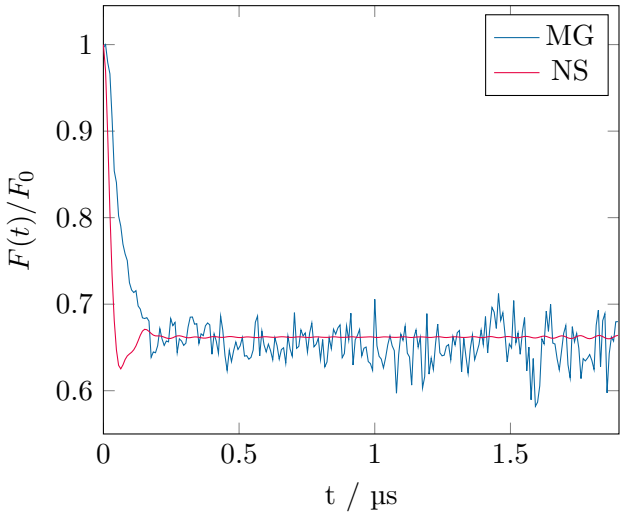

Figure 2.41: *Form factors as measured for Q10C-E121C as measured for the molten globule (blue) and simulated for the native state (red).*

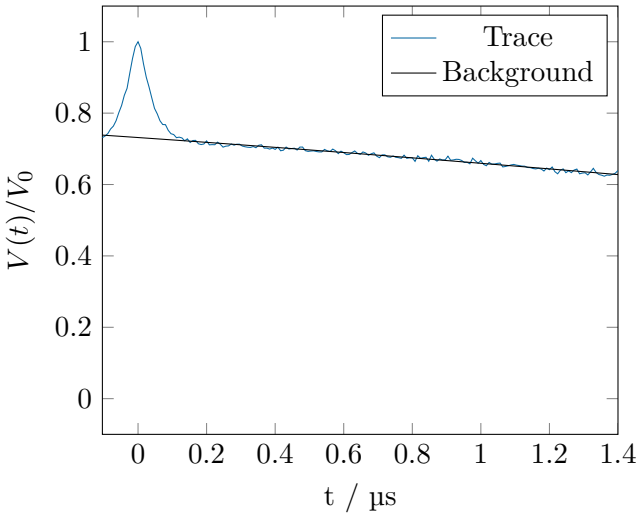

Figure 2.42: *DEER trace of D87C-E121C (blue) and background function (black).*

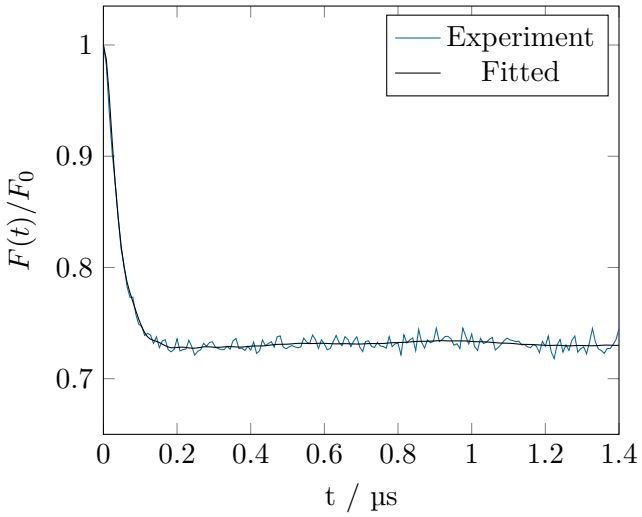

Figure 2.43: *Background corrected form factor for D87C-E121C, showing fitted form factor in black.*

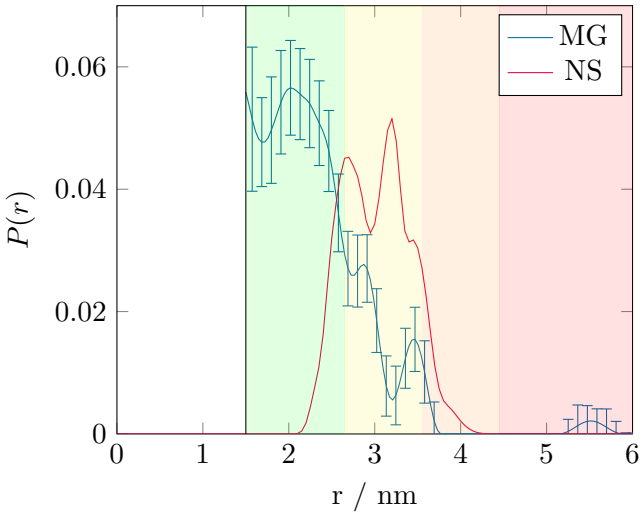

Figure 2.44: *Distance distributions for D87C-E121C for the molten globule (blue) and the native state (red).*

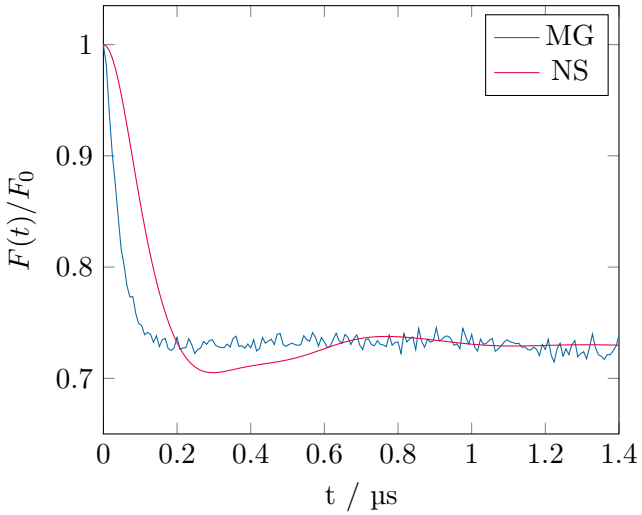

Figure 2.45: *Form factors as measured for D87C-E121C as measured for the molten globule (blue) and simulated for the native state (red).*

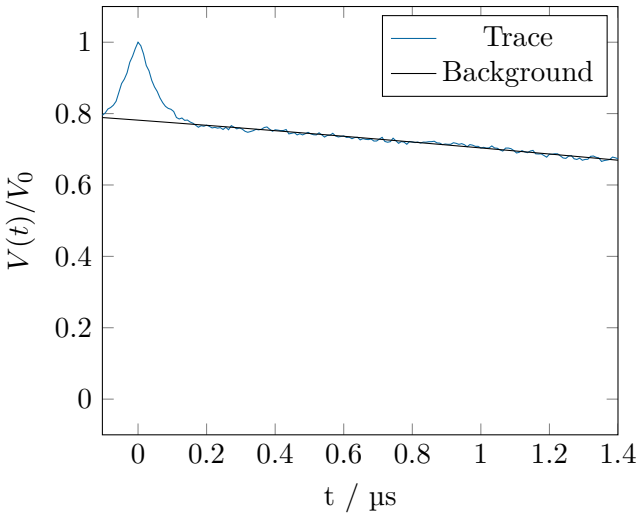

Figure 2.46: *DEER trace of D97C-E121C (blue) and background function (black).*

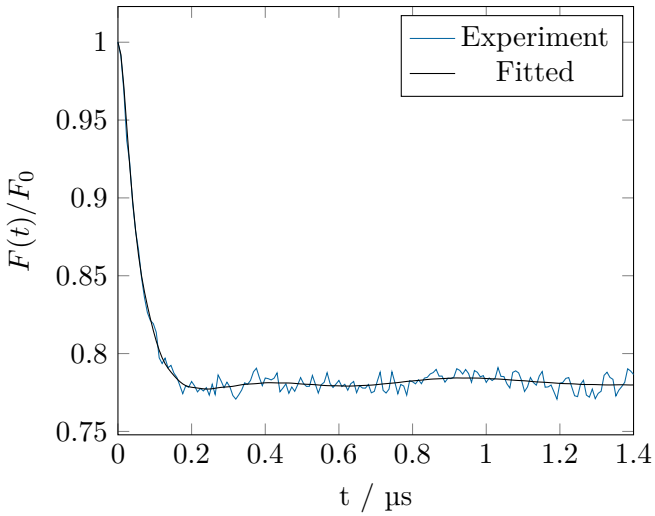

Figure 2.47: *Background corrected form factor for D97C-E121C, showing fitted form factor in black.*

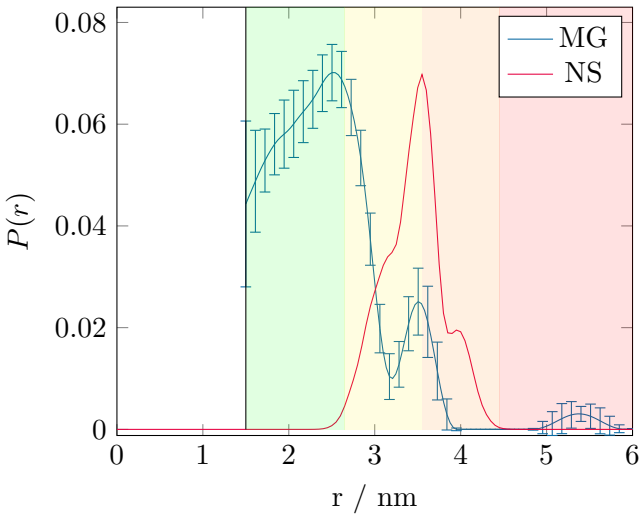

Figure 2.48: *Distance distributions for D97C-E121C for the molten globule (blue) and the native state (red).*

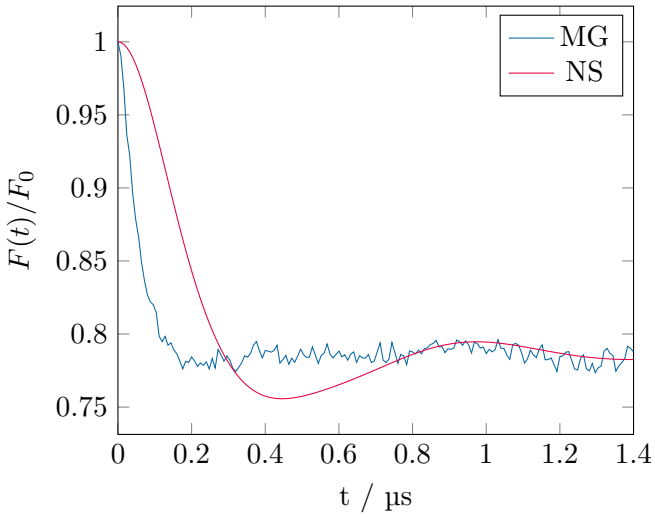

Figure 2.49: *Form factors as measured for D97C-E121C as measured for the molten globule (blue) and simulated for the native state (red).*

2.6.5 α-lactalbumin in the prescence of 8 M urea

The balance of forces which lead to the particular structure of molten globule state α-lactalbumin may be further understood by studying its progressive unfolding under the effect of a denaturant.

As discussed in Section 2.2.3, NMR studies of all-Ala α-lactalbumin by Redfield and coworkers were able to show the progressive unfolding of each part of the secondary structure with increasing urea concentration.[27] The addition of 8 M urea to the sample promotes the denaturation of the protein to form a random coil: the hydrodynamic radius of all-Ala α-lactalbumin is 33.3 Å in 8 M urea, consistent with the prediction of 35.1 Å for a fully-unfolded 124 amino acid protein.

Presented here are DEER data of all-Ala α-lactalbumin taken in the presence of 8 M urea. Three mutants were chosen to measure the effect of urea on the molten globule. Firstly, D87C-D97C was measured in further investigation of the unfolding of the C-helix. In addition, both Q10C-D87C and Q10C-D97C were used as a measure of the stability of the hydrophobic core to urea. All experimental details are as in Section 2.4.6, with the addition of 8 M urea (deuterated urea in the case of D87C-D97C).

The NMR results discussed above suggest that all-Ala α-lactalbumin is completely unfolded by 6 M urea; it is therefore expected that the distance distributions in 8 M urea will differ significantly from those in the absence of urea.

Measurements of the intrinsic viscosities of a range of proteins by Tanford *et al.* show that the unperturbed mean squared end-to-end distance of a random coil protein (in the presence of 6 M guanidine hydrochloride) follows the relation[58]

$$\langle L^2 \rangle_0 = (70 \text{ to } 140 \text{ Å}^2)N \tag{2.18}$$

where N is the number of amino acid residues. The ranges expected for the RMS end-to-end random coil distances for the three mutants are listed in Table 2.2.

Mutant	N	$\sqrt{\langle L^2 \rangle_0}$ / nm
Q10C-D87C	78	7.39 – 10.5
Q10C-D97C	88	7.85 – 11.1
D87C-D97C	11	2.77 – 3.92

Table 2.2: *List of predicted RMS distances for random coil proteins, from equation 2.18.*

Note that the mean distances for Q10C-D87C and Q10C-D97C are expected to be

beyond the typical range measured in these DEER experiments.

2.6.5.1 D87C-D97C

As discussed in Section 2.6.2, measurements on D87C-D97C confirm that the C-helix is fully folded in the molten globule. The chain between D87C and D97C is eleven amino acid units long, with the predicted RMS random coil distance being between 2.77 and 3.92 nm. It is therefore expected that the DEER effect should be observed for this mutant, even in the presence of a strong denaturant.

Figures 2.50 to 2.52 show the DEER data for D87C-D97C with 8 M urea. From the DEER trace (Figure 2.50) it is clear that there is indeed a modulation.

Studying the calculated distribution, Figure 2.52, it can be seen that, although there is significant error in the distribution, the C-helix does not retain the fully folded distribution seen in Figure 2.20; instead a broader range of distances are represented, indicating that C-helix is at least partially unfolded in 8 M urea. The measured distribution gives $\langle r \rangle = 4.28$ nm, $\sigma_r = 1.32$ nm, only slightly larger than the upper bound established using Equation 2.18. This can be accounted for by the additional contribution to the distance due to the spin-labels themselves; as such, the measured mean distance is broadly consistent with the prediction.

2.6.5.2 Q10C-D87C and Q10C-D97C

For both Q10C-D87C and Q10C-D97C in 8 M urea (Figures 2.53 and 2.57), the DEER traces show only very minor signs of measurable distances. The deviation from the experimental background is minor, and almost non-existent for a homogeneous 3D background (see Section 2.4.1 for a discussion of the background function). The distributions will therefore be highly sensitive to the accuracy of the background correction. As a point of comparison, the 3D homogeneous background functions are shown in Figures 2.56 and 2.60: the deviation of the DEER trace from the background is very small, indicating that only a minor difference from a homogeneous distribution.

The modulation depths here are small, even in comparison to the singly-labelled samples, demonstrating that only a minority of molecules are within the measurable distance. The majority of the distances in the calculated distributions are between 4.5 and 6 nm, at the upper end of the measurable range, but still shorter than the predicted RMS random coil distance for both mutants (7.5 to 11 nm). The data suggest that both mutants are in

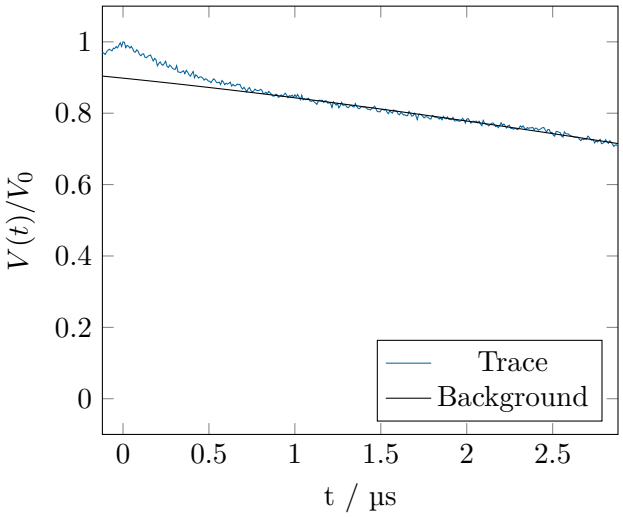

Figure 2.50: *DEER trace of D87C-D97C in 8* M *urea (blue) and experimental background function (black).*

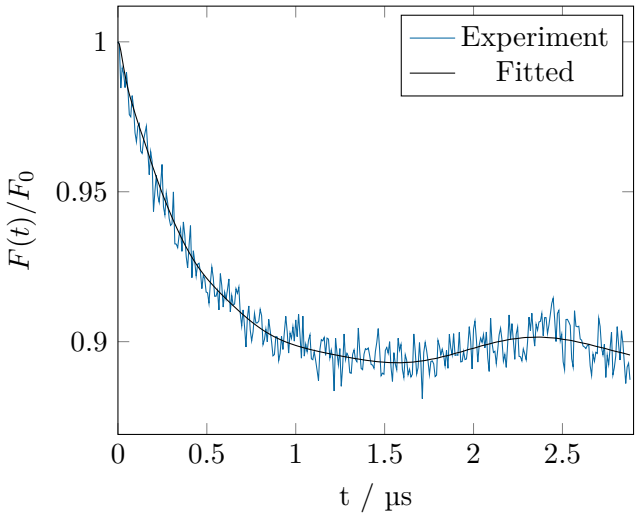

Figure 2.51: *Background corrected form factor for D87C-D97C in 8* M *urea, showing simulated trace in black.*

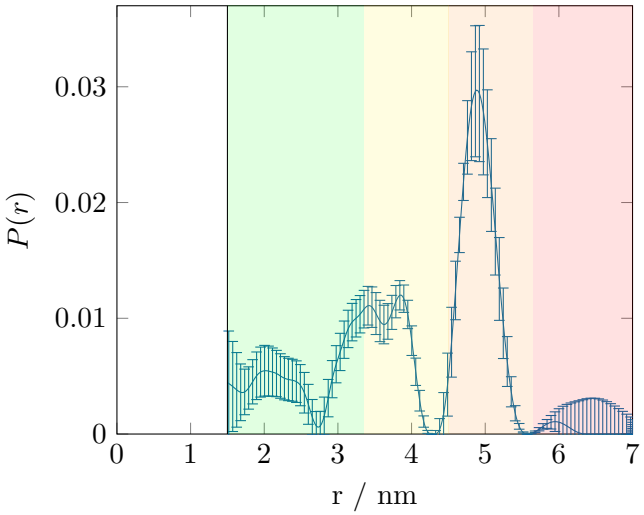

Figure 2.52: *Distance distributions for D87C-D97C in 8* M *urea.*

random coil states, with the majority of the label pairs having a longer distance than is measurable by DEER.

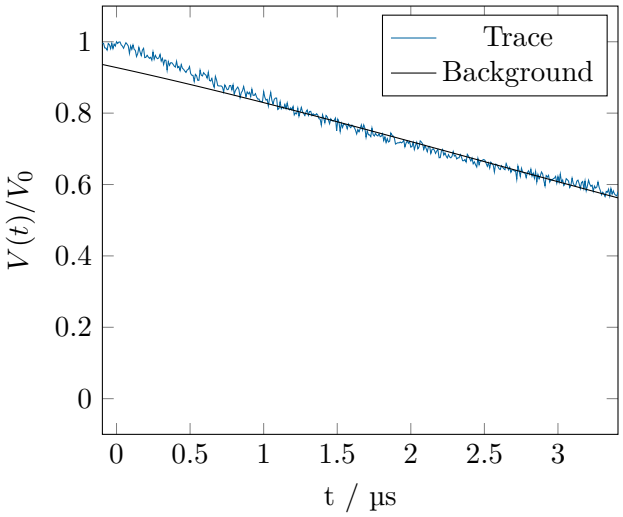

Figure 2.53: *DEER trace of Q10C-D87C in 8* M *urea (blue) and experimental background function (black).*

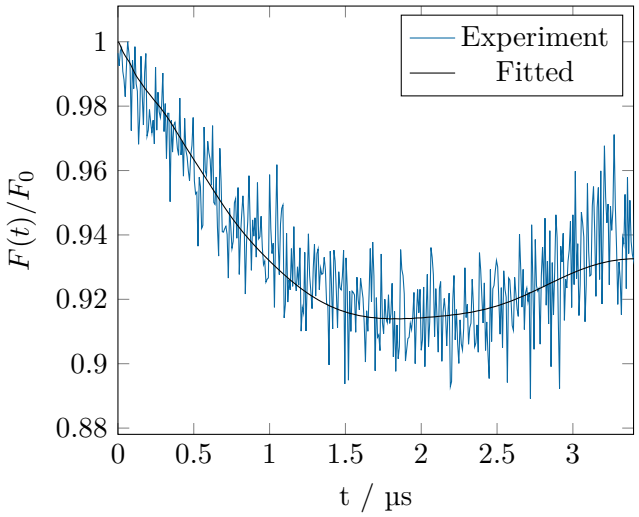

Figure 2.54: *Background corrected form factor for Q10C-D87C in 8* M *urea, showing simulated trace in black.*

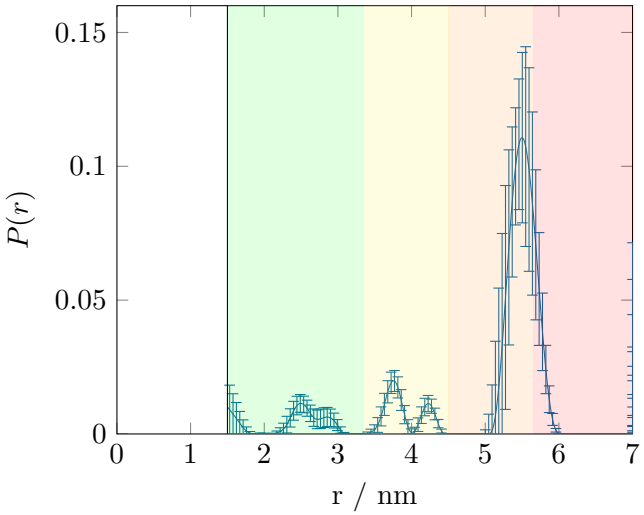

Figure 2.55: *Distance distributions for Q10C-D87C in 8* M *urea.*

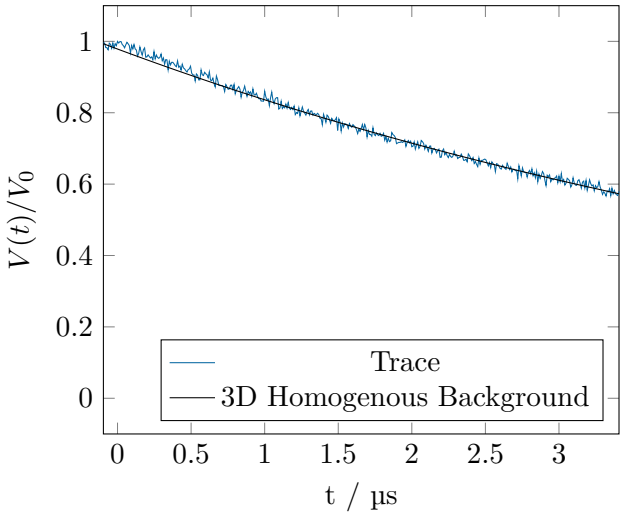

Figure 2.56: *DEER trace of Q10C-D87C in 8* M *urea (blue) and 3D homogenous background function (black).*

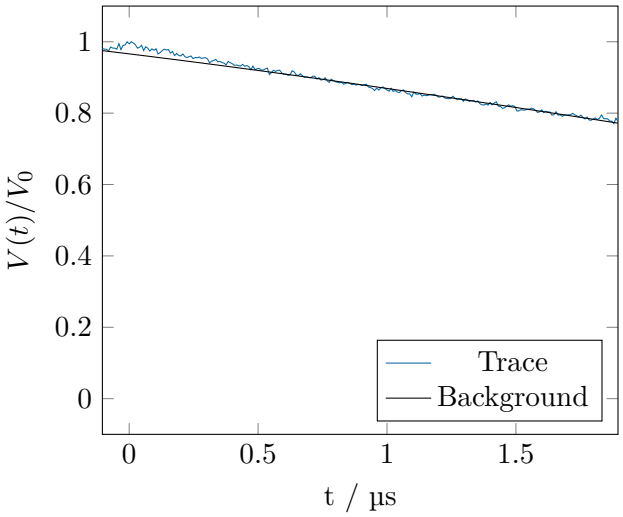

Figure 2.57: *DEER trace of Q10C-D97C in 8* M *urea (blue) and experimental background function (black).*

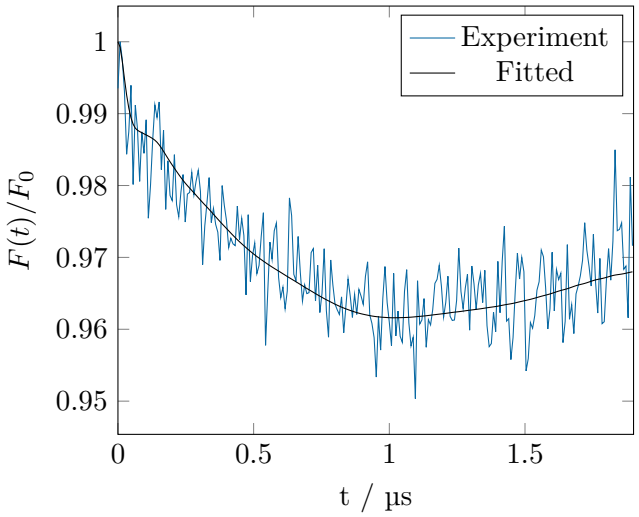

Figure 2.58: *Background corrected form factor for Q10C-D97C in 8* M *urea, showing simulated trace in black.*

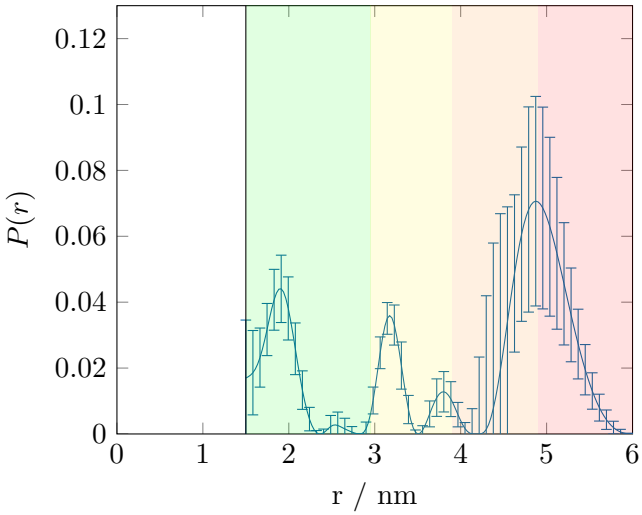

Figure 2.59: *Distance distributions for Q10C-D97C in 8* M *urea.*

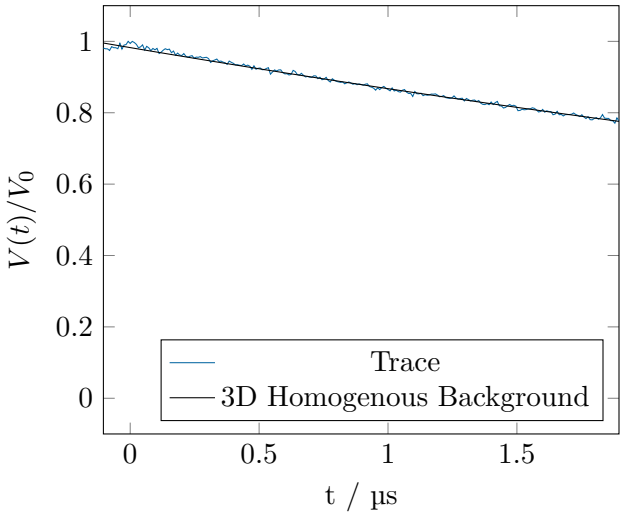

Figure 2.60: *DEER trace of Q10C-D97C in 8* M *urea (blue) and 3D homogenous background function (black).*

2.7 Conclusions and future directions

The DEER data presented here are the first steps in building a quantitative model of the α-lactalbumin molten globule. Adding to qualitative circular dichroism and NMR data about the unfolding process, these results provide vital insight into the structure of the molten globule. A summary of the collected data is provided in Table 2.3.

Pair	$\langle r \rangle$, σ_r (Predicted, NS) / nm	$\langle r \rangle$, σ_r (DEER) / nm
Q10C–D87C	2.20, 0.40	2.44, 0.47
Q10C–D97C	2.85, 0.33	2.60, 0.84
D87C–D97C	2.09, 0.38	1.95, 0.27
D87C–E121C	3.12, 0.39	2.30, 0.58
D97C–E121C	3.50, 0.35	2.45, 0.62
Q10C–E121C	1.34, 0.47	2.66, 0.83
		$\langle r \rangle$, σ_r (cw) / nm
Q10C-E121C (with Q10C)	1.34, 0.47	2.15, 0.76
Q10C-E121C (with E121C)	1.34, 0.47	2.39, 0.95
	$\langle r \rangle$ (Predicted, RC) / nm	$\langle r \rangle$, σ_r (DEER) / nm
Q10C–D87C (8 M urea)	7.39 to 10.5	5.19, 1.27
Q10C–D97C (8 M urea)	7.85 to 11.1	3.84, 1.49
D87C–D97C (8 M urea)	2.77 to 3.92	4.28, 1.32

Table 2.3: *Spin-label pairs chosen for measurement, predicted distances for native state (NS) or random coil (RC), and measured distances for the molten globule using DEER or cw EPR. The distances and standard deviations were predicted for the native state using MMM and PDB:1A4V.*

A number of conclusions can be drawn from the data presented here. Firstly, the measurements of D87C-D97C show that the C-helix is fully folded in the molten globule, concurring with the chemical shift data of Ramboarina *et al.*[28] The DEER measurements of D87C-D97C with 8 M urea confirm that the C-helix unfolds under these conditions.

Data from the Q10C mutants give insight into the behaviour of the N-terminus and C-helix. The distribution for Q10C-D87C shows a small increase in the mean distance; Q10C-D97C on the other hand shows a significant increase in width of the distribution, suggesting flexibility in the C-terminal end of the C-helix.

Finally, the three E121C mutants reveal interesting behaviour of the C-terminus of the protein. The Q10C-E121C distance is significantly lengthened, indicating that the C-terminus is not in a native-like position close to the N-terminus. This result is unsurprising, given the lack of the C6-C120 disulphide bridge. The data for D87C-E121C and D97C-E121C, however, show that both mean distances have decreased significantly in the molten globule compared to the native state. This indicates that the C-terminus, although not in

the native like position, is still part of the hydrophobic core of the molten globule. This agrees with data from Redfield *et al.*, who found that HSQC peaks for these residues do not appear until late in the unfolding process.[27]

This work could potentially be extended in order to measure more distance distributions for the molten globule. Areas of interest might include B- and D-helices, which are known to form part of the hydrophobic core.[27] Additionally, it has been suggested that the β-domain retains some structure in the molten globule,[28] and quantitative distance information from DEER studies of this domain may prove valuable in understanding the behaviour of this part of the protein.

Furthermore, although the experiments with urea presented here confirm a qualitative change in the distance distributions, DEER traces measured as a function of denaturant concentration could be used to give quantitative information about the unfolding process.

Finally, the data here could be used, combined with information from NMR studies, as long-range distance constraints in building a model of the molten globule state.

Chapter 3

Magnetic field effects in protein crystals

3.1 Motivation for the work

The interest of most scientists in the effect of magnetic fields on chemical systems is restricted to spectroscopic techniques, such as magnetic resonance. The incredible power of NMR to characterise organic molecules has made the use of the spin properties of molecules routine in many laboratories. A rather more esoteric field of study is the effect of magnetic fields on the fate of chemical reactions. Upon simple analysis, it might seem rather unlikely that a magnetic field could affect a chemical reaction, the typical interaction energy of a molecule with a magnetic field being more than six orders of magnitude smaller than the thermal energy, kT.[59] However, in the case of certain spin systems, most prominently spin correlated radical pairs (SCRPs), the recombination kinetics can be affected by magnetic fields as weak as 39 μT.[60]

General interest in this field with relevance to biological systems has been along two main threads. Firstly, widespread electrification during the twentieth century has spurred interest in the effect of relatively weak, low frequency (μT, 50 Hz) magnetic fields on human health,[61] in particular, on breast cancer[62,63] and childhood leukaemia.[64] Evidence is weak in both cases, with no evidence of fields < 0.4 μT being associated with an increase in the latter.[65]

The other main field of study has been the investigation of the mechanism by which some animals, most commonly birds, can use the earth's magnetic field to navigate. In order to function as a source of directional information to animals, a system must fulfil

several criteria. Firstly, the system must be anisotropic, i.e. the response of the system to the magnetic field must depend not only on the presence or absence of the field, but must also differ depending on the direction between the field and some axis of the animal. This axis could either be intrinsic to the molecular system, this system being in a fixed orientation within the animal,[66] or the axis could be defined by the biological system within which the molecules are contained.[67] Other requirements include a way for the magnetically sensitive molecules to interact with the nervous system of the animal, and an effect large enough to be detected.

Although magnetic sensitivity has been claimed in a range of plants[68,69] and animals,[70–72] much work has focussed on avian magnetoreception, and two competing hypotheses for the mechanism have been proposed. The first is that single-domain magnetite crystals provide the required alignment,[73,74] in much the same way as a compass needle works. Although some animals, for instance fish,[75] are known to use magnetite crystals to orient themselves, several peculiarities of the avian compass have been noted which suggest a different mechanism. Firstly, studies of European Robins have indicated that they do not respond to the polarity of the magnetic field, instead using the inclination of the field* to sense direction.[70] Secondly, the magnetic orientation behaviour shows a complex wavelength dependence, but preferred orientation is under blue and green light.[76–78] Furthermore, the European Robin has been shown to be disoriented under magnetic fields oscillating at between 50 kHz and 5 MHz.[79,80] These facts suggest that a SCRP could instead be responsible for the orientation behaviour.[81]

The study of the macroscopic magnetic response of animals has been complemented by work concentrating on the theoretical and microscopic behaviour and requirements of magnetically sensitive systems. Magnetically sensitive reactions involving SCRPs have been studied since the 1970s, but it was in 2000 that a potential candidate avian magnetoreceptor was proposed.[66,82] This protein, cryptochrome, is a blue light photoreceptor protein found in a wide variety of plants and animals, and is known to mediate a variety of biological responses, including the entrainment of circadian rhythms in mammals.[83] Cryptochromes are closely related to photolyases, proteins which transfer electrons to repair the cyclobutane-pyrimidine dimer or pyrimidine-pyrimidone (6–4) adducts resulting from UV-photodamage to DNA.[83]

Both photolyases and cryptochromes contain a highly conserved region, the photolyase homology region, which contains a flavin adenine dinucleotide (FAD) cofactor. Throughout

*Inclination is the angle between the field direction and the ground.

the photolyase/cryptochrome family there is a highly conserved tryptophan triad, a series of three tryptophan (Trp) residues which can serve as an electron transfer chain.[84] In the case of photolyases, W306 transfers an electron to the excited state of FAD, generating $FADH^-$, the catalytically active state.[85] In cryptochromes, the triad also mediates the transfer of an electron, forming a SCRP between the FAD and the terminal tryptophan.[86] In their speculated role as avian magnetoreceptors, it is this SCRP which acts as the magnetically sensitive apparatus.[66]

The difficulty of obtaining cryptochromes, which must be made recombinantly, typically in small quantities and at low concentrations, has meant that work has also focussed on model biological systems, often consisting of a flavin or other chromophore with a tryptophan residue.[87–90] In this work, carried out in collaboration with Mr Nils Pompe, the model system of flavin mononucleotide (FMN) with hen egg white lysozyme (HEWL) protein, was studied using bulk fluorescence and confocal microscopy.

3.2 Spin correlated radical pairs

A spin correlated radical pair consists of two electrons which are formed in a spin-selective manner, i.e. in either a singlet or triplet state. Interconversion between these states can take place, with the rate of this process being affected by an applied magnetic field. Spin-selective recombination of the SCRP can take place, either exclusively from the singlet or triplet state, or at different rates from the two states. This process of spin-selective formation, spin mixing, and spin-selective recombination is referred to as the radical pair mechanism (RPM). The spin dynamics can be broadly divided into three regimes: zero, low, and high field, which will each be discussed in turn.

3.2.1 A one-nucleus radical pair

In order to examine the process by which singlet and triplet radical pairs can be interconverted, we first consider the radical pair Hamiltonian for two electrons, in the absence of any electronic spin-spin coupling, with a single spin-$\frac{1}{2}$ nucleus isotropically coupled to one of the electrons:

$$\hat{H} = g_A \mu_B B_0 \hat{S}_{Az} + g_B \mu_B B_0 \hat{S}_{Bz} + a \hat{S}_A^{\intercal} \cdot \hat{I} \tag{3.1}$$

with all quantities as defined in Section 1.1.

F	F_z	State
$\frac{1}{2}$	$+\frac{1}{2}$	$\|\mathrm{S},\alpha\rangle$
$\frac{1}{2}$	$-\frac{1}{2}$	$\|\mathrm{S},\beta\rangle$
$\frac{1}{2}$	$+\frac{1}{2}$	$\sqrt{\frac{1}{3}}\|\mathrm{T}_0,\alpha\rangle-\sqrt{\frac{2}{3}}\|\mathrm{T}_+,\beta\rangle$
$\frac{1}{2}$	$-\frac{1}{2}$	$\sqrt{\frac{1}{3}}\|\mathrm{T}_0,\beta\rangle-\sqrt{\frac{2}{3}}\|\mathrm{T}_-,\alpha\rangle$
$\frac{3}{2}$	$+\frac{3}{2}$	$\|\mathrm{T}_+,\alpha\rangle$
$\frac{3}{2}$	$+\frac{1}{2}$	$\sqrt{\frac{2}{3}}\|\mathrm{T}_0,\alpha\rangle+\sqrt{\frac{1}{3}}\|\mathrm{T}_+,\beta\rangle$
$\frac{3}{2}$	$-\frac{1}{2}$	$\sqrt{\frac{2}{3}}\|\mathrm{T}_0,\beta\rangle+\sqrt{\frac{1}{3}}\|\mathrm{T}_+,\alpha\rangle$
$\frac{3}{2}$	$-\frac{3}{2}$	$\|\mathrm{T}_-,\beta\rangle$

Table 3.1: *Zero field eigenbasis of the Hamiltonian in Equation 3.1.*

3.2.2 Zero field

At zero field it is best to consider the states of the Hamiltonian in the total angular momentum basis. Defining an operator, $\hat{F}$, representing the total angular momentum of the system

$$\hat{F} = \hat{S} + \sum_j \hat{I}_j \tag{3.2}$$

where $\hat{S}$ is the total spin operator for the electrons and $\hat{I}$ is the spin operator for the nucleus, taking the sum over all nuclei j. Furthermore, $\hat{F}_z$ is the spin projection operator for F onto an arbitrary axis. The eigenbasis in F and F_z is given in Table 3.1.

The selection rules at zero field are

$$\Delta F = 0 \tag{3.3}$$

$$\Delta F_z = 0. \tag{3.4}$$

The only mixing of states that is allowed is therefore between the two pairs given in first half of Table 3.1.

3.2.3 The low field effect

In the presence of a magnetic field the selection rules are relaxed such that only F_z is conserved. Application of a magnetic field therefore additionally allows mixing with $|\frac{3}{2},+\frac{1}{2}\rangle$ and $|\frac{3}{2},-\frac{1}{2}\rangle$. This means that there is increased mixing between singlet and triplet states at small magnetic fields relative to zero field. This 'low field effect' is prominent in calculations of one-nucleus radical pairs,[91] and can be observed experimentally for some systems.[60] The

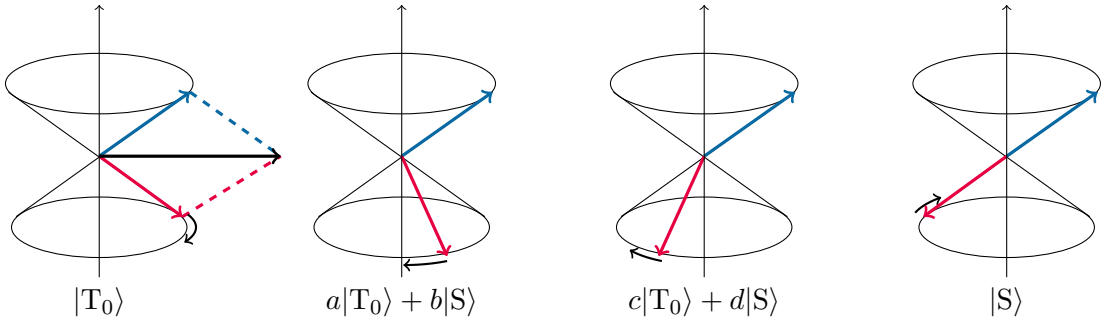

Figure 3.1: *Vector model of the mixing between S and T_0. A difference in the Larmor frequencies of the two radicals causes interconversion of S and T_0.*

low field effect is not observed in the work presented here, however, mostly likely due to a combination of the presence of hyperfine couplings on both radicals, relaxation, and exchange coupling.[91]

3.2.4 At high magnetic fields

Considering the high field limit, where $B_0 \gg a$, the spins are quantised along the field direction, and the $T_\pm$ states are energetically isolated from the S, T_0 states; interconversion between $T_\pm$ and the S, T_0 manifold cannot occur under this Hamiltonian.

The S and T_0 states, in the $\alpha\beta$ basis, are $\frac{1}{\sqrt{2}}(|\alpha\beta\rangle - |\beta\alpha\rangle)$ and $\frac{1}{\sqrt{2}}(|\alpha\beta\rangle + |\beta\alpha\rangle)$ respectively. Within the vector model of spin (Section 1.1.4), the two states differ simply with respect to the phase between the two vectors. Any process which leads to a difference in phase of the two vectors will contribute to mixing between the two states (Figure 3.1). Examining Equation 3.1, there are two contributions which will change the relative phase of the two spin vectors, the difference in g-factors of the two electrons, and the hyperfine coupling.

3.2.4.1 Δg mixing

The first two terms on the right-hand side of Equation 3.1 are the Zeeman interaction of each electron with the magnetic field. If the g-factors of the two electrons are identical then the contribution of the Zeeman effect to the Larmor frequency of each electron is identical, and the relative phase of the two spin vectors will not change due to the Zeeman terms.

If the two g-factors are different, then the rate of phase change, and therefore the rate of interconversion between the T_0 and S states, contributed by the Zeeman terms will be

given by

$$\Delta\omega = \frac{\Delta g \mu_B}{\hbar} B_0. \tag{3.5}$$

At the fields used in the experiments in this thesis, the difference in g-factors of the two (carbon centred) radicals is generally small, and the contribution of this mechanism to spin mixing is negligible[†].

3.2.4.2 Hyperfine mixing

The third term is Equation 3.1 is the hyperfine coupling of electron A with a spin-$\frac{1}{2}$ nucleus.

For an isotropic hyperfine coupling, a, the contribution of the coupling to the difference in Larmor frequencies is

$$|\Delta\omega| = \frac{a}{2} \tag{3.6}$$

with the hyperfine coupling therefore driving a change in phase between S and T_0. This contribution to the spin mixing is independent of B_0.

3.2.4.3 Relaxation

Interconversion between singlet and triplet states can also occur via relaxation. Spin-lattice (Section 2.3.3.1) and spin-spin (Section 2.3.3.2) relaxation serve to mix $T_{\pm}$–S and S–T_0 states respectively.

[†]An upper bound on Δg might be 5×10^{-4},[92] giving a interconversion frequency of 0.12 MHz at 18 mT, compared to the hyperfine couplings of Hβ1 and Hβ2 on $TrpH^{+\cdot}$ of 44.8 MHz. In any case, the radical pair lifetime would have to be very long, greater than 10 µs, for spin mixing at 0.12 MHz to have an effect on the populations.

3.2.4.4 Spin mixing in the context of the Hamiltonian

The spin mixing processes as described above can also be understood by examining the matrix elements of the spin Hamiltonian:[93]

$$
\begin{array}{c}
 \\
|\mathrm{S},\alpha\rangle \\
|\mathrm{S},\beta\rangle \\
|\mathrm{T}_0,\alpha\rangle \\
|\mathrm{T}_0,\beta\rangle \\
|\mathrm{T}_+,\alpha\rangle \\
|\mathrm{T}_+,\beta\rangle \\
|\mathrm{T}_-,\alpha\rangle \\
|\mathrm{T}_-,\beta\rangle
\end{array}
\begin{array}{c}
\begin{array}{cccccccc}
|\mathrm{S},\alpha\rangle & |\mathrm{S},\beta\rangle & |\mathrm{T}_0,\alpha\rangle & |\mathrm{T}_0,\beta\rangle & |\mathrm{T}_+,\alpha\rangle & |\mathrm{T}_+,\beta\rangle & |\mathrm{T}_-,\alpha\rangle & |\mathrm{T}_-,\beta\rangle
\end{array} \\
\begin{pmatrix}
0 & 0 & A_1+B_1 & 0 & 0 & -A_2 & 0 & 0 \\
0 & 0 & 0 & -A_1+B_1 & 0 & 0 & A_2 & 0 \\
A_1+B_1 & 0 & 0 & 0 & 0 & A_2 & 0 & 0 \\
0 & -A_1+B_1 & 0 & 0 & 0 & 0 & A_2 & 0 \\
0 & 0 & 0 & 0 & A_1+B_2 & 0 & 0 & 0 \\
-A_2 & 0 & A_2 & 0 & 0 & -A_1+B_2 & 0 & 0 \\
0 & A_2 & 0 & A_2 & 0 & 0 & -A_1-B_2 & 0 \\
0 & 0 & 0 & 0 & 0 & 0 & 0 & A_1-B_2
\end{pmatrix}
\end{array}
$$

$$
\begin{aligned}
A_1 &= \frac{a}{4} \\
A_2 &= \frac{a}{2\sqrt{2}} \\
B_1 &= \frac{g_1 - g_2}{2}\mu_B B \\
B_2 &= \frac{g_1 + g_2}{2}\mu_B B.
\end{aligned} \tag{3.7}
$$

The off diagonal elements in the top left quadrant consist of hyperfine and Δg terms that mix S and T_0 states. These correspond to the Δg and hyperfine mechanisms described above. The diagonal terms in the bottom right quadrant consist of Zeeman and hyperfine terms that energetically isolate the $T_\pm$ states. Finally, there are hyperfine mixing terms in the top right and bottom left quadrants which can mix $T_\pm$–S and $T_\pm$–T_0. The rate of mixing between these states is therefore governed by the relative size of the aforementioned Zeeman terms and the hyperfine coupling - at fields where the terms are comparable, mixing can occur. As B_0 increases, the Zeeman terms dominate, and the rate of mixing between $T_\pm$–S and $T_\pm$–T_0 decreases.

3.2.4.5 Anisotropic spin mixing

In the above discussion we have assumed an isotropic hyperfine coupling. However, as discussed in Section 1.1.7, if the molecules are not tumbling there will be an anisotropic

contribution to the coupling and we must use the full hyperfine tensor, **A**. In this case the one-nucleus spin Hamiltonian is

$$\hat{H} = g_A \mu_B B_0 \hat{S}_{Az} + g_B \mu_B B_0 \hat{S}_{Bz} + \hat{S}_A^{\intercal} \cdot \mathbf{A} \cdot \hat{I}.$$

Note that strictly the full g-tensors should also be considered, but at the fields herein the anisotropy of **g** is so small that it can be neglected. With this Hamiltonian, in the high field limit, the contribution of the hyperfine coupling to the Larmor frequency depends on the orientation of the molecular frame in the magnetic field. The hyperfine contribution to the rate of spin mixing is therefore orientation dependent.

3.2.5 Magnetic field effects

The spin mixing processes discussed in Section 3.2 serve to interconvert radical pairs between singlet and triplet. In order to see the effect of this on the transient population of the radical pair, consider a scheme such as that in Figure 3.2, where the radical pair can undergo back electron transfer from the singlet state only. If the radical pair is formed entirely in the triplet state, in the absence of electron-electron couplings, then at zero field all three triplet states are degenerate with the singlet, and are free to mix with it. The rate of spin mixing (from Equation 3.7) is

$$\text{Zero field:} \qquad k_{\text{S–T}} = 2A_1 + 4A_2 = a\left(\frac{1}{2} + \sqrt{2}\right) \tag{3.8}$$

At high field, the $T_{\pm}$ states are energetically isolated from the T_0, S states, and mixing can only occur between T_0 and S. The rate of spin mixing is then

$$\text{High field:} \qquad k_{\text{S–T}} = 2A_1 = a\left(\frac{1}{2}\right) \tag{3.9}$$

For a triplet born RP, more radical pairs will remain as triplets under a large magnetic field compared to the zero field case. The number of RPs undergoing the BET pathway is therefore reduced, and the application of a magnetic field leads to an increase in the number of radicals that remain in solution. This increase in the transient yield of radicals also has an effect on the ground state population - fewer RPs undergoing BET means a lower ground state population. This is a *magnetic field effect* on the population of the radical pair and of the ground state.

This can also be understood from the populations of the spin states. Consider the case

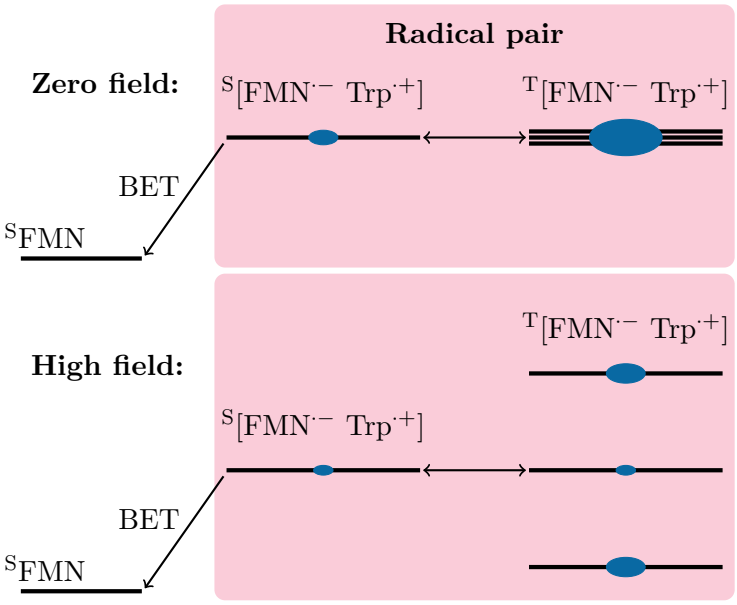

Figure 3.2: *Diagram showing a radical pair that can recombine from the singlet state only. At high field the $T_{\pm}$ states are energetically isolated from the S state, and therefore cannot mix with it. Energies not to scale.*

where the RP is being continuously formed with equal populations in each of the triplet sublevels, and the recombination is slow such that the populations of the RP sublevels are allowed to equilibrate according to transitions allowed by the Hamiltonian. At zero field, spin mixing can occur between all triplet and singlet states, and they are all degenerate, so the equilibrium fractional population in each state will be approximately 1/4. At high field, the $T_{\pm}$ states are energetically isolated. Only the T_0 state can mix with the singlet, so the equilibrium fraction population of the singlet will be close to 1/6. Now considering recombination from the singlet state, the rate of back electron transfer will change from $\sim k_{\mathrm{BET}}/4$ at zero field to $\sim k_{\mathrm{BET}}/6$ at high field, corresponding to a reduction in the ground state population under a magnetic field. This is shown schematically in Figure 3.2, and is summarised in Table 3.2.

Zero field		**High field**	
State	Population	State	Population
S	$\frac{1}{4}$	S	$\frac{1}{6}$
T_0	$\frac{1}{4}$	T_0	$\frac{1}{6}$
T_+	$\frac{1}{4}$	T_+	$\frac{1}{3}$
T_-	$\frac{1}{4}$	T_-	$\frac{1}{3}$

Table 3.2: *Summary of the approximate equilibrium populations of each radical pair state under zero and high magnetic fields.*

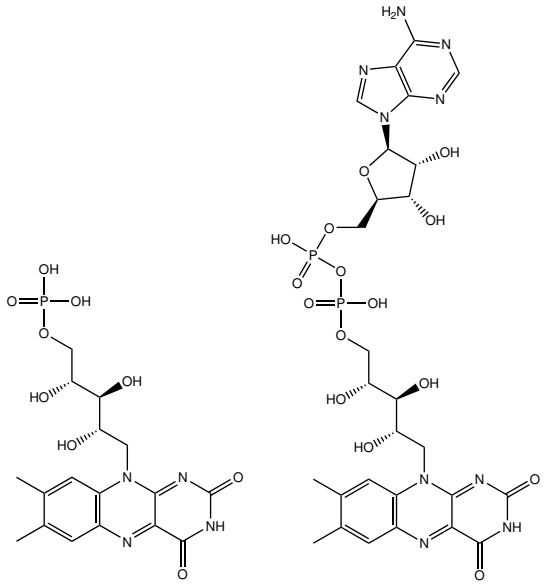

Figure 3.3: *Structures of flavin mononucleotide (FMN), as used in these experiments, and flavin adenine dinucleotide (FAD), as is found in cryptochromes. Both cofactors share the three-membered isoalloxazine ring and ribityl side chain.*

3.2.6 The FMN-HEWL system

Flavin mononucleotide and hen egg white lysozyme together is a system that, suitably photoilluminated, forms SCRPs.[87,94–96] These radical pairs may undergo magnetic field dependent spin mixing, with their singlet and triplet states experiencing different fates.

FMN is a biomolecule, consisting of a three-membered isoalloxazine ring and ribityl side chain, as shown in Figure 3.3. The isoalloxazine acts as the chromophore in the cofactors of a wide range of blue-light photoreceptors,[97] and can undergo electron transfer reactions to give semiquinone (one e^-) and fully reduced (two e^-) forms. A range of flavins are found in nature, including flavin adenine dinucleotide, the cofactor in photolyases and cryptochromes, also shown in Figure 3.3. The flavins all share the isoalloxazine moiety, but differ in the identity of the side chain. This structural similarity means that the flavins as a class share similar photochemical and redox properties.

Hen egg white lysozyme is an enzyme that catalyses hydrolysis of polysaccharides in bacterial cell walls. HEWL contains solvent exposed tryptophan residues which can undergo electron transfer to oxidising agents, such as FMN.[94]

The photocycle of the FMN-HEWL system is shown in Figure 3.4. Firstly, a photon of the appropriate wavelength excites the ground state of the chromophore, ^{S}FMN, to the singlet excited state, ^{S}FMN*. This state has a lifetime of 4.6 ns[98–100] either returning to

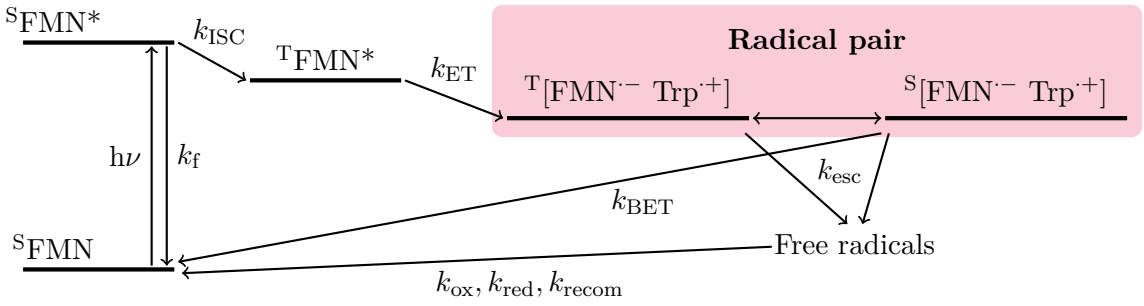

Figure 3.4: *FMN-HEWL photocycle, showing excitation (hν), fluorescence (k_f), intersystem crossing (k_{ISC}), electron transfer (k_{ET}), back electron transfer (k_{BET}), escape (k_{esc}), oxidation/reduction processes (k_{ox}, k_{red}), and free radical recombination (k_{recom}).*

the ground state via radiative or non-radiative processes, or moving to the ^{T}FMN* state by intersystem crossing within around 10 ns.[101] From the triplet excited state ($\tau = 0.5 - 2$ µs),[102] the flavin can undergo electron transfer from nearby reductants, giving a SCRP formed exclusively in the triplet state (by conservation of spin). For FMN reacting with HEWL, this electron transfer occurs primarily from tryptophan residues.[94]

The triplet radical pair can now proceed along one of two main pathways. Firstly, direct recombination of the triplet radical pair back to the ground state is a spin forbidden process, but escape of the radicals from the solvent cage ($\sim 10^3$ s^{-1}) and subsequent reduction/oxidation by redox agents or other free radicals in solution ($\sim 10^9 - 10^{10}$ M^{-1} s^{-1}) can return the radicals to the ground state.

The second pathway is via the singlet radical pair, from which geminate recombination is allowed ($\tau \approx 10$ ns).[96] The spin mixing processes which can interconvert triplet and singlet radical pairs are as described in Section 3.2.1.

Application of a magnetic field reduces the rate of spin mixing and traps some RPs in the $T_{\pm}$ states. The rate of back electron transfer is reduced since there are fewer singlet RPs to undergo that process, and more RPs will escape to form free radicals, increasing the transient yield of radicals. This also corresponds to a decrease in the ground state population, and hence a reduction in the fluorescence observed from ^{S}[FMN]*. The rate of spin mixing, and consequently the effect of the applied magnetic field, can therefore be monitored by observing the fluorescence intensity of FMN.[96]

The FMN-HEWL system is used as a model magnetoreceptor for a variety of reasons. Firstly, the components are readily available and are rather inexpensive compared to recombinant expression of cryptochrome. Secondly, the system is relatively robust against degradation by light and heat, at least compared to cryptochromes, and in any case can

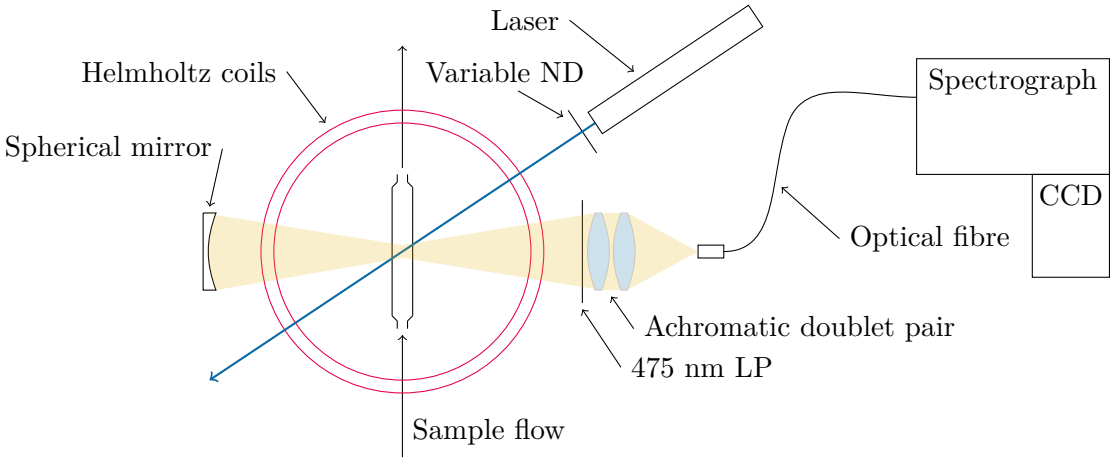

Figure 3.5: *'Bulk' fluorescence experiment setup as described in the text.*

simply be discarded and replaced if necessary. Thirdly, the radical pair (FMN and Trp) is similar to that in cryptochrome (FAD and Trp).

Of course, the radical pairs in cryptochrome and FMN-HEWL do differ, primarily in that cryptochrome forms an intramolecular radical pair,[86] while FMN-HEWL is an intermolecular system.[96] Both the electron transfer characteristics (cryptochrome forming a singlet born radical pair, FMN-HEWL being triplet born) and subsequent dynamics (diffusion, relaxation, etc) will differ between the two systems.[102] However, despite these differences, the use of FMN-HEWL as a model system both to investigate the magnetic field response in crystals and for methodology development is well justified.

3.3 Fluorescence detected MFEs

As stated in Section 3.2.6, application of a magnetic field can affect the ground state population, and hence the fluorescence intensity, of FMN. This fact can be used to monitor the magnetic field effect. The 'bulk' fluorescence experiment is shown in Figure 3.5. A diode laser (Power Technology, 405 nm, 350 mW) is used to excite FMN, causing both the formation of radical pairs as well as the FMN fluorescence. The beam is passed through an adjustable neutral density filter to control the intensity. The sample solution is contained within a flow-cell (Hellma, Quartz SUPRASIL, 130.427 QS), and is flowed using a micropump (Bartels, mp6-pp, $\sim 1\ \mathrm{mL\,min^{-1}}$) to replenish the probed area with fresh sample. Surrounding the sample cell is a pair of home-built Helmholtz coils, controlled by a computer. The coils provide a cw magnetic field at strengths of up to 16 mT.

The fluorescence is collected (with an exposure delay of 0.1 s after field switching) by

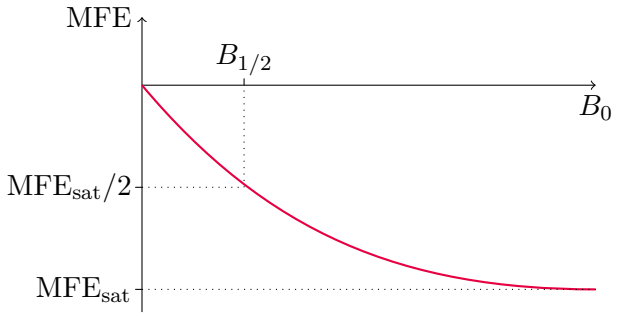

Figure 3.6: *Magnetically altered reaction yield (MARY) curve for a triplet born radical pair recombining from the singlet state only. The low field effect (Section 3.2.3) is neglected here. Highlighted is $B_{1/2}$, the field at which the MFE is half its saturation value.*

an achromatic doublet pair (including light reflected from behind the sample by a spherical mirror, to improve the collection efficiency) after passing through a 475 nm long pass filter to exclude scattered laser light. The collected fluorescence is then focussed onto the end of an optical fibre, which is in turn coupled via a ball lens into the slits of a spectograph (Andor Technology, Shamrock 303i). The spectograph disperses the light onto a CCD camera (Andor Technology, Newton 920) which is used to measure the intensity of the fluorescence at all visible wavelengths simultaneously. All experiments were carried out at room temperature.

A typical experiment consists of a series of measurements with and without the applied magnetic field. This series of 'on' (B_0) and 'off' ($B_0 = 0$) measurements can be done either at a fixed magnetic field, or varying the magnetic field. In either case, each 'on' measurement is compared to the interpolated value of the adjacent 'off' measurements, with the magnetic field effect being measured as

$$\begin{aligned} \Delta I_f(B_0) &= I_f(B_0) - I_f(B_0 = 0) \\ \mathrm{MFE}(B_0) &= \left(\frac{\Delta I_f}{I_f(B_0 = 0)} \right) \times 100 \end{aligned} \tag{3.10}$$

where ΔI_f is the 'subtraction' value, and the MFE is the percentage change in the fluorescence intensity on application of the magnetic field.

If the MFE is measured as a function of the applied magnetic field strength, then a curve such as the one in Figure 3.6 can be obtained. This is a 'magnetically altered reaction yield' or MARY curve. The magnitude of the MARY curve will increase with increasing B_0 as the $\mathrm{T}_\pm$ levels become increasingly energetically isolated, until they are completely separated and the MFE becomes saturated. The width of the MARY curve is

determined by the size of the hyperfine couplings and the relaxation of the radicals, and can be characterised by the $B_{1/2}$ value, the magnetic field at which the MFE is half of the saturation value. Weller *et al.* showed that the effective hyperfine field on an electron i is given by[103]

$$B_i = \left(\sum_k a_{ik}^2 I_k (I_k + 1) \right)^{1/2} \tag{3.11}$$

and that the $B_{1/2}$ can be related to the hyperfine field for the two electrons by

$$B_{1/2} = \frac{2(B_1^2 + B_2^2)}{B_1 + B_2}. \tag{3.12}$$

Weller and coworkers found this equation in good agreement for experiments on Pyrene/N,N-dimethylaniline. It is common, however, for exchange coupling and relaxation to broaden the MARY curve such that $B_{1/2}$ exceeds the value predicted by the Weller formula.

The fluorescence experiment has the advantage of higher sensitivity over more typical absorption techniques which monitor the radical concentration—magnetic field effects in the FMN-HEWL system have been observed down to nanomolar FMN concentrations using fluorescence.[96] This increased sensitivity is somewhat offset by the fact that under most conditions the radical population is rather small, so the ($\sim 10\%$) MFE on the radical population translates to a smaller MFE on the ground state population as measured by fluorescence ($\sim 10^{-1} - 10^{-4}\%$). The origin of this effect is discussed later in Section 3.7.1.

3.4 MFEs in protein crystals

In liquid samples, the isotropic orientation distribution and fast tumbling of both donor and acceptor means that any anisotropic interactions will be averaged, and no anisotropic MFE can be measured. In prior work, this problem has been solved using either polarised laser beams to selectively photoexcite the molecules in a frozen glass (photoselection), or using liquid crystals to force molecular alignment.[60] For photoselection, the chromophores are excited with a probability proportional to $\cos^2\theta$, where θ is the angle between the molecular transition dipole moment and the polarisation direction; a frozen solvent matrix holds the molecules so that their spin dynamics then occur with a fixed angle relative to the magnetic field. For the liquid crystal approach, the molecules are aligned within a liquid crystal matrix so that their orientation is fixed. In both cases, the anisotropy of the MFE can be monitored by changing the angle of the magnetic field relative to the

orientation axis.

For protein systems, another practical solution might be to use crystallisation as a method of aligning the molecules. This solution has the advantage of potentially providing a high degree of alignment, depending on the space group of the crystal. For instance, in P1, the only symmetry operations are translations, meaning that all molecules are aligned in a particular direction.

To investigate the practicality of using crystallisation as a method of alignment, and to investigate magnetic field effects within the crystal environment, HEWL crystals containing FMN were grown.

3.5 Protein crystallisation

Proteins can be crystallised, just as small molecules or ionic salts can. There are, however, several complications in macromolecular crystallisation that make the process different.

For all crystallisations the goal is to precipitate a crystalline form of the solid from solution (or, from a melt or the gas phase). For, say, sodium chloride, this can be accomplished by saturating a volume of water with the salt, followed by cooling or evaporation of the solvent in order to cause supersaturation and promote crystal growth. With salts, this process can be relatively straightforward. However, for proteins, many combinations of conditions will cause the protein to amorphously precipitate out of solution.

The crystallisation phase transition can be illustrated on a diagram such as that shown in Figure 3.7. In this diagram, the two axes are protein concentration and precipitant concentration. Other experimental parameters, such as pH, temperature, etc, could also be represented on the axes. In the undersaturation area, the protein is soluble and crystallisation will not occur. In the supersaturation area precipitation will occur, and the behaviour of the system can be further divided into three zones. Firstly, there is a precipitation zone, where the protein is very supersaturated, and it will amorphously precipitate out of solution. Secondly, there is a nucleation zone, at moderate supersaturation, where a small number of molecules will come together to form clusters. If the nucleus is too small, then it will simply redissolve, but under the correct conditions stable nuclei with the molecules arranged in an ordered structure will form. Finally, at low supersaturation there is a 'metastable zone', where crystal growth, but not nucleation, will occur.

Crystallisation occurs in two steps. The first is nucleation, when an ordered cluster of molecules forms. This defines the structure of the subsequent crystal. The second step

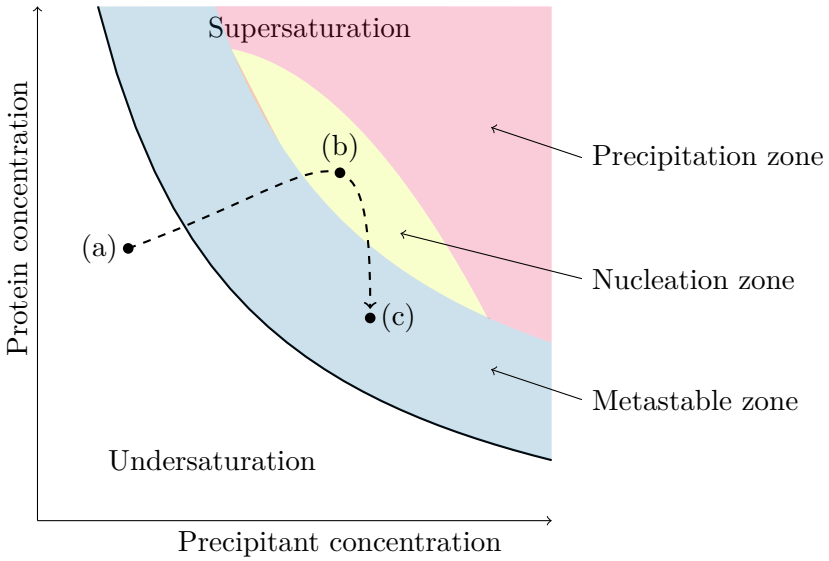

Figure 3.7: *Protein crystallisation phase diagram, showing points where the protein is soluble, (a), and where nucleation, (b), and crystal growth, (c), are occurring. The dotted line shows a path along which the system might move if the solvent is allowed to evaporate.*

is crystal growth; the nuclei grow in an ordered manner to form macroscopic crystals. In order for this to occur, the system must move across the phase diagram in a suitable path, as shown in Figure 3.7 for example.

The system can be moved along this path in a number of different ways, with perhaps the most common method being evaporation of the solvent. Along this path, the system starts in the undersaturation zone, at point (a). Here both the protein and precipitant concentrations are such that the protein is soluble. As the solvent evaporates, the protein and precipitant concentrations will both rise, moving the system through the metastable zone and into the nucleation zone. At point (b) nuclei will form, and growth follows. As the crystals grow, the protein concentration will drop, moving the system into the metastable zone towards point (c), where crystal growth will continue, but nucleation will cease.

If the path taken across the phase diagram moves through the precipitation zone, then the protein will amorphously precipitate instead of forming crystals. Additionally, if the system spends too long in the nucleation zone, then a large number of nuclei will be formed, and the experiment will not produce large, high quality crystals. Careful control of all experimental parameters is therefore crucial to obtain the best crystals (or, indeed, crystals at all).

3.5.1 Crystallisation methods

Crystallisation can be promoted in a number of ways. These include:[104]

Batch and microbatch In the batch method the sample is mixed with precipitant and other additives such that a supersaturated solution is created, and sealed in a small vial before being left to crystallise. The microbatch method uses a small droplet of the solution immersed in an inert oil drop, preventing evaporation. In both methods nucleation occurs when the protein and precipitant solutions are first mixed, with the final mixture being in the metastable zone, where crystal growth can occur. The only movement across the phase diagram is due to the reduction in protein concentration caused by crystal growth.

Dialysis The dialysis method uses diffusion of the precipitant molecule through a semi-permeable membrane to increase the precipitant concentration and move the system into the supersaturation zone. This can be carried out either using dialysis tubes, or using a 'Cambridge button', where a small (5–100 µL) drop is placed on top of the button, and covered with dialysis membrane; the button can then be placed into the precipitant solution.

Free interface diffusion This method involves layering precipitant solution on top of the protein solution in a narrow capillary, which is then sealed with wax. At the boundary between the solutions there is a region of high supersaturation where nucleation is promoted. The system moves into the metastable zone as the solutions mix. This method can also be carried out by connecting droplets of protein and precipitant solution using a needle to form a 'liquid bridge'.

Hanging drop vapour diffusion This method controls the protein and precipitant concentrations by allowing diffusion of the solvent out of a droplet. A 'well' is prepared containing precipitant solution. A droplet containing the protein and a lower concentration of precipitant (typically half that in the well) is placed on a siliconized glass cover slip that is then inverted and sealed over the well. Solvent molecules will then diffuse out of the droplet, into the well, in order to equalise the precipitant concentrations. The evaporation of solvent from the droplet raises the protein and precipitant concentrations, moving the system into the supersaturation zone and promoting crystallisation. Variants of this method include 'sitting drop', where the droplet is placed on a small bridge inside

the well, and 'sandwich drop', where the droplet is placed between two cover slips, one of which seals the well.

In the experiments in this thesis the hanging drop vapour diffusion method was chosen for a number of reasons. Firstly, the technique is relatively simple, and the conditions for crystallising HEWL by this method are well studied.[105] Secondly, the crystals are grown on a glass coverslip, which can be used directly in microscope experiments, instead of having to transfer the crystal onto a slide. This greatly simplifies the handling of the crystals.

3.5.2 Crystallisation protocol

The crystals used in this thesis were grown using the following protocol. Crystallisation was carried out using 24 well pregreased Linbro plates (Crystalgen Superclear) by the hanging drop method. Solutions were prepared to the following recipes.

Stock solutions of 2.5 M NaCl, 500 mM NaOAc buffer at pH 3.8 to 4.4, and 2.5, 5, and 7.5 mM FMN were prepared, filtered through 0.2 µm syringe filters, and stored at –20°C in sterile falcon tubes.

Well solutions consisting of 100 mM NaOAc buffer at pH 3.8 to 4.4 and 0.7 to 1.2 mM NaCl were made up in-situ in the wells using the stock solutions and deionised, sterile-filtered water. pH and [NaCl] gradients could be set up on the two axes of the plates to screen these conditions.

Droplet solutions of 100 mM NaOAc buffer at pH 3.8 to 4.4, 20 to 50 $\mathrm{mg\,mL^{-1}}$ HEWL, and 0.01 to 5 mM FMN were made up using the stock solutions and deionised, sterile-filtered water. [HEWL] and [FMN] gradients could be set up on the two axes of the plates to screen these conditions.

Droplets were pipetted out onto circular siliconised glass cover slips (Jena Bioscience GmbH), 1 µL of well solution mixed in situ with 1 µL of droplet solution. Typically three droplets were deposited per cover slip. The slips were inverted and sealed over the matching well, and the plates were placed in the dark at room temperature. Plates were checked periodically, and crystals were usually observed to grow to a few hundred microns across within a few days.

The crystals ranged from pale to strong yellow in colour, depending on the concentration of FMN in the droplet. Representative crystals both with and without FMN were measured by X-ray crystallography by Dr Steven Johnson. The crystals were in the space

group $P4_32_12$ with lattice parameters $a = b = 78.4$ Å, $c = 37.1$ Å. Checks for crystal pathologies showed no unusual statistics, ruling out twinning, anisotropy, data incompleteness or other pathologies. The resolution was between 1 and 1.5 Å. For the crystals containing FMN, there was no evidence of ordered FMN in the crystals from the X-ray data.[106]

3.6 Confocal microscopy

Typical protein crystals are a few hundred microns across, meaning that they can be difficult to handle. Furthermore, protein crystals are typically $\sim 40\%$ solvent,[107] and are extremely fragile. Crystal handling is greatly simplified if the crystals need not be removed from their mother liquor. This would, however, complicate a fluorescence experiment as described in Section 3.3, as the laser beam would excite fluorophore in the mother liquor, making the obtained data a convolution of fluorescence from both crystal and solution.

A better experiment is to exploit the spatial resolution of a confocal microscope in order to probe only a small volume of crystal. This ensures that the measurement is of the MFE inside the crystal, and not that of the surrounding solution.

Laser scanning confocal microscopy (LSCM) is a fluorescence microscopy technique characterised by the use of a pinhole placed in front of the detector, in the focal plane, in order to obtain good depth resolution and contrast.

The instrument works as shown in Figure 3.8. A laser beam is reflected from a dichromic mirror before passing through the objective. The light is focussed by the objective to a diffraction limited spot in the sample, typically 0.25 to 0.8 µm in diameter. This spot can be scanned across the focal plane in a raster pattern by adjusting mirrors within the microscope.

The light is absorbed by fluorophores in the sample, and re-emitted as fluorescence, which is collected by the objective. Although the laser has been focussed to a spot in the focal plane, fluorescence is also emitted by molecules above and below the focal plane. The fluorescence has a longer wavelength than the laser, so passes through the dichromic mirror, through a 475 nm long-pass filter (which removes scattered laser light), towards the detector, normally a photomultiplier tube.

In front of the detector is a pinhole. The pinhole is in the same focal plane as the focus of the objective, so fluorescence emitted from molecules in the focal plane passes through the pinhole. Light emitted from above and below the focal plane is not focussed to this

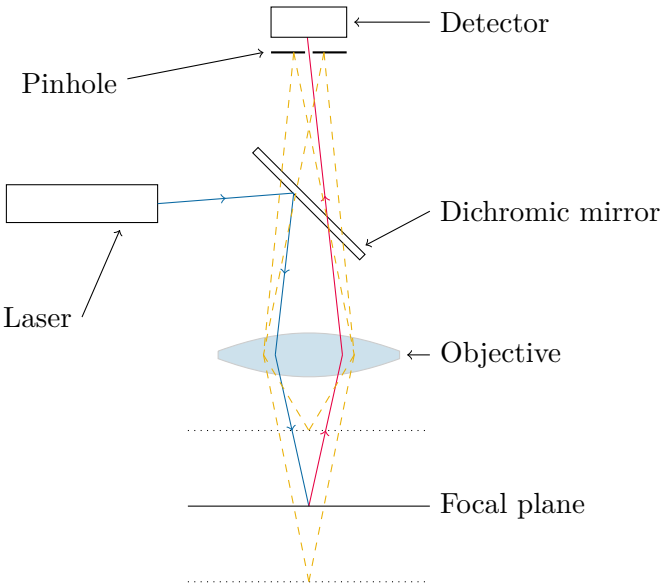

Figure 3.8: *Simplified scheme for a laser scanning confocal microscope. Beam paths of the laser (blue) and fluorescence (red) are only partially shown for clarity. Off focal-plane fluorescence (yellow) is mostly rejected by the pinhole.*

point, so is mostly excluded.

In this way a focal plane of very thin section (µm) can be chosen by moving the objective in the z-axis, and the image can be built by scanning the laser across the sample (in x and y). The resolution in the z-axis can be controlled with the size of the pinhole, a smaller pinhole being more selective as to the light it rejects, and therefore the z-axis resolution. 3D images can be built up by scanning a series of focal planes and assembling the resulting images.

The experiments presented here were performed using a Zeiss LSM5 laser scanning confocal microscope. The laser was a 25 mW Argon laser operating at 458 nm, which could be varied in power from 0.2 to 100% of the maximum power. All experiments were performed at room temperature.

3.6.1 MFE detection by confocal microscopy

Confocal microscopy can be used to detect magnetic field effects by monitoring the fluorescence intensity as a function of magnetic field, just as in the 'bulk' experiment described in Section 3.3.

For liquid samples, a flow cell can be used to ensure rapid replenishment of the sampled volume, minimising the effect of photobleaching. The MFE can be calculated by interpolating adjacent 'off' data points over each 'on' point, and calculating the MFE us-

ing Equation 3.10. This can be done using linear interpolation since the flowing sample ensures that that the photobleaching of the sample is minimised, with the bleached sample being replaced continually by flow.

However, for protein crystals the same section of sample must be probed repeatedly in order to compare the response with and without the magnetic field. The act of probing the sample causes the fluorescence intensity to change (via photobleaching), so it is not possible to simply compare $I_f(B_0 = 0)$ and $I_f(B_0)$. Instead the modulation of the fluorescence intensity by the magnetic field is superimposed on a decaying signal, and the two must be deconvoluted to find the pure magnetic field-response signal.

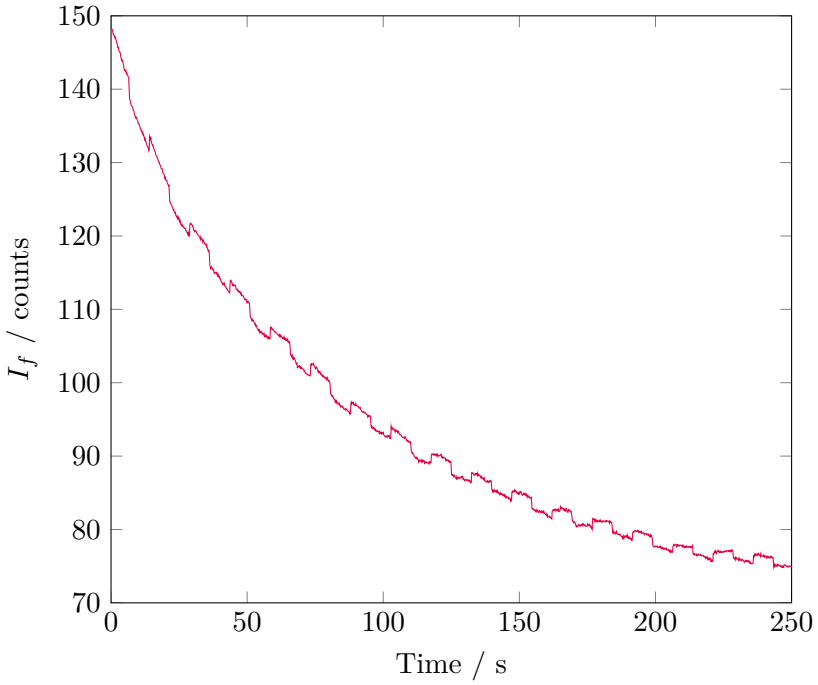

Figure 3.9: *Fluorescence intensity time trace collected by confocal microscopy. The steps in I_f are caused by changing magnetic field. Note that I_f falls by half during the experiment, making extraction of the MFE difficult.*

A typical confocal measurement of a HEWL crystal containing FMN is shown in Figure 3.9. The crystallisation conditions here were 2 mM HEWL, 1.6 mM FMN, 1 M NaCl, 0.1 M NaOAc buffer at pH 4.8. B_0 was 17 mT for the measurement. The mean fluorescence intensity value for the entire image is plotted against time, with the magnetic field being modulated 'on' and 'off' for 50 frames each (∼7 s). The whole trace is the convolution of the magnetic field step function with an unknown, non-exponential decay due to photobleaching, which makes any attempt to fit the decay and extract the MFE modulation difficult.

However, over two adjacent 'off' steps, $I_f(B_0 = 0)$ can be fitted to good residual using a double exponential function, as shown in Figure 3.10 (the 'off' steps, shown in red, are fitted to give the black line.) This function can then be interpolated to find the expected value of $I_f(B_0 = 0)$ at intervening times. The data from the 'on' step (shown in blue) can then be used to calculate the MFE, defined as

$$\mathrm{MFE}(B_0) = \left(\frac{I_f(B_0) - I_f(B_0 = 0, \mathrm{fit})}{I_f(B_0 = 0, \mathrm{fit})} \right) \times 100 \tag{3.13}$$

An example result is shown in Figure 3.11, with the $\sim -1.6\%$ field effect being clearly visible. This process can be repeated for each 'on' step, with the standard deviation or standard error of the MFE being calculable for each 'on' step.

Towards the end of the experiment, photobleaching has caused the mean fluorescence intensity to fall to less than half of the initial value. The decrease in the signal to noise ratio can interfere with the fitting process. In this case, the fitting procedure can be rejected as no longer suitable when the R^2 drops below a certain level, chosen here to be 0.95.

The experiments performed herein used a set of home-built Helmholtz coils that could provide magnetic fields up to 17 mT. The magnetic field strength was varied between 0 and 17 mT in a square wave function (period = 14.78 s, duty cycle = 50%) using a function generator (Rigol DG1022).

3.6.2 Fluorescence recovery after photobleaching

The spatial control of the confocal microscope can also be used to perform experiments to measure the diffusion taking place in the sample.

Fluorescence recovery after photobleaching (FRAP) uses a high power laser beam to photobleach an area of the sample, and the recovery of the fluorescence intensity is then monitored as non-photobleached molecules diffuse into the bleached area. This experiment can be performed in a number of different ways;[108] the approach taken here is as follows.[109]

Firstly, a square shaped area, smaller than the total view of the microscope, is bleached using the full power of the laser (25 mW nominal, 0.786 s per scan). This is done by repeatedly scanning (50 iterations) the same area until a large proportion of the molecules have been bleached. The laser is then drastically reduced in power (1 mW nominal, 0.8181 s per scan), and used to monitor the fluorescence intensity over the entire field of view. Over time, non-bleached molecules will diffuse into the bleached area and vice versa.

The image immediately after this bleaching process is as shown in Figure 3.12, left.

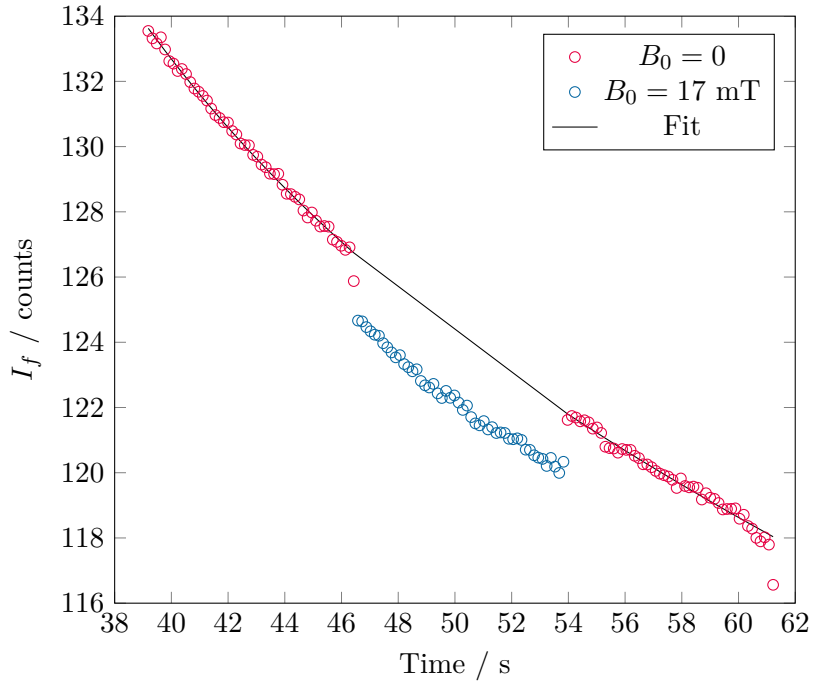

Figure 3.10: *The fluorescence intensity at zero field ($I_f(B_0 = 0)$) is fitted using a double exponential function. The expected value of $I_f(B_0 = 0)$ during the intervening field-on step can thus be interpolated, and MFE calculated.*

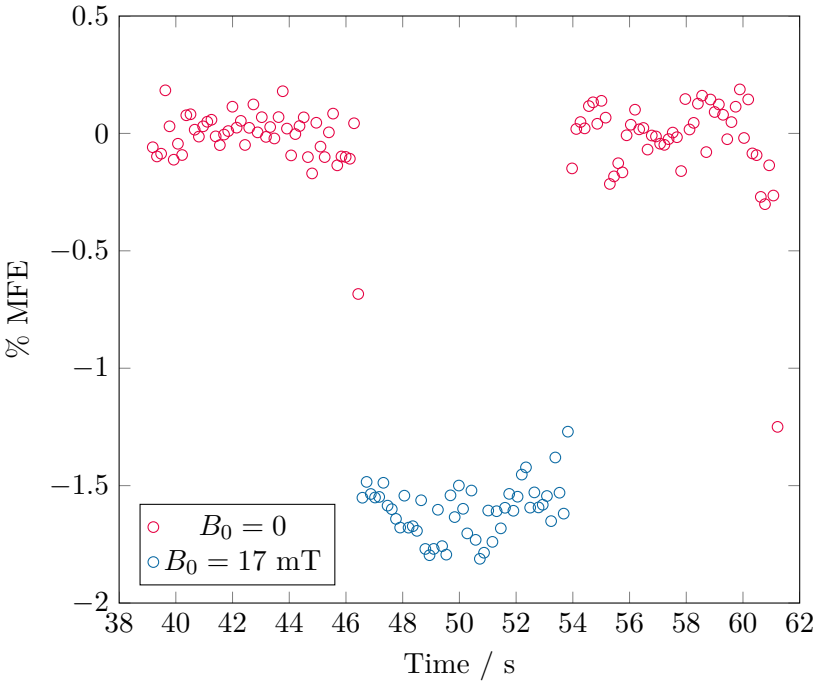

Figure 3.11: *%MFE as calculated using the fitting procedure above. The intermediate-valued points at ∼ 46 and 61* s *are due to the field switching during a frame. The field is not capable of being synchronised to the microscope, so some intermediate points are captured while the field is switching.*

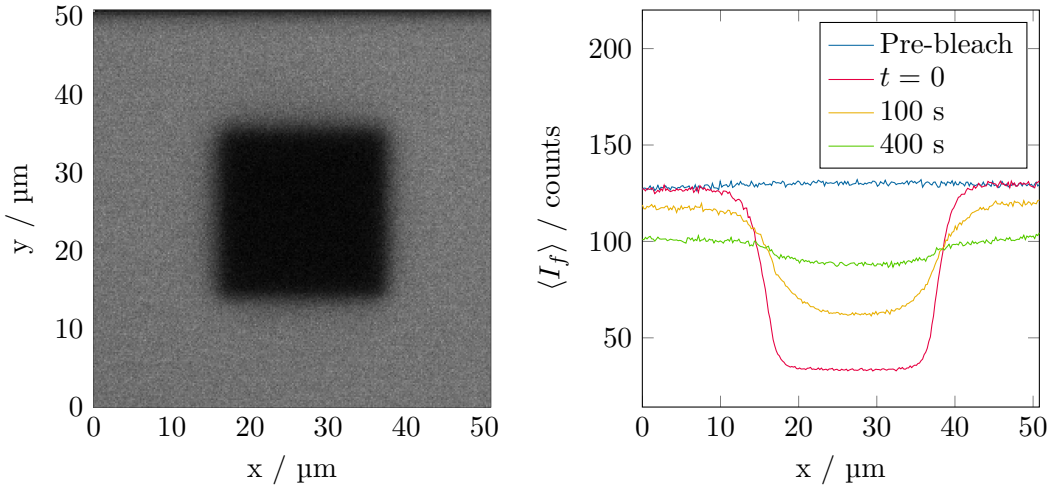

Figure 3.12: *FRAP experiment, showing bleached area, left, and* $\langle I_f \rangle$ *at various times after the bleach, right. The diffusion constant,* D*, can be extracted by fitting the shape of the bleached area. Note that, over time, the intensity of the non-bleached area is reduced due to photobleaching by the laser.*

The bleached area is clearly visible as the black square at centre. In order to analyse the diffusion, the mean intensity is taken for a section in the y direction, in this case from $y = 17$ to 37 µm, and plotted against x. This is shown in Figure 3.12, right, for various times after the bleach. Over time the fluorescence in the bleached area recovers towards that of the non-bleached area. The intensity profile around the edges of the bleached area can be described in the following way.

Firstly, the probability of finding a fluorescent particle at position x at time t, given an initial position x_0, is

$$p(x, x_0, t) = \sqrt{\frac{1}{4\pi Dt}} \exp\left(-\frac{(x - x_0)^2}{4Dt}\right) \tag{3.14}$$

where D is the diffusion coefficient. The position axis is then divided into two sections about the edge of the bleached region, one from $x = -\infty$ to 0, which contains the unbleached section, the other and from $x = 0$ to ∞ which contains the bleached section. The probability of finding a fluorescent particle at position x, independent of its starting position x_0, is

$$p(x, t) = \int_{-\infty}^{0} p(x, x_0, t) \mathrm{d}x_0 = \frac{1}{2}\left(1 - \mathrm{erf}\left[\frac{x}{2\sqrt{Dt}}\right]\right) \tag{3.15}$$

where $\mathrm{erf}(z)$ is the error function. This expression is simply equal to the normalised intensity profile around the edge of the bleached region. In practice, the finite width of the laser beam causes a deviation from the above formula, with the normalised intensity profile

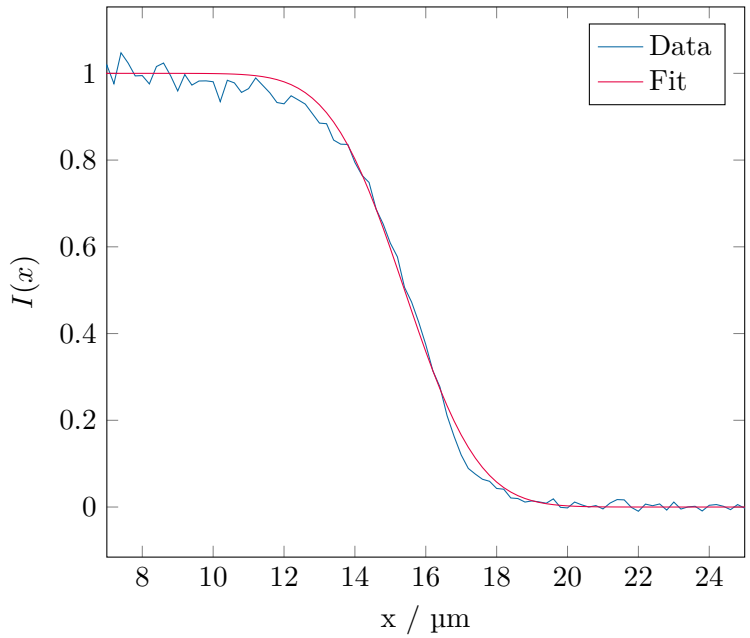

Figure 3.13: *Fitting of edge of the bleached region using Equation 3.16. Plotting the width parameter, C, against t allows extraction of the diffusion constant, D.*

instead being given by

$$I(x) = \frac{1}{2}\left(1 - \text{erf}\left[\frac{x}{2\sqrt{Ct}}\right]\right)$$
$$C = Dt + b \tag{3.16}$$

where b is a broadening parameter related to the half width of the laser beam. The parameter C can be found for each time t by taking the intensity profiles shown in Figure 3.12, normalising and fitting them around each edge using Equation 3.16 (an example fit is shown in Figure 3.13). Plotting C against t then allows a determination of the diffusion coefficient D.

3.7 Results

3.7.1 Laser power dependence for HEWL crystals

For cw illumination, the magnetic field effect is dependent on the power density of the excitation source. This is not due to a direct effect on the spin-mixing process, but can be understood by considering how the pumping rate affects the proportion of FMN in the radical state.

A higher power density leads to faster formation of ^{S}FMN*, with more RP subsequently

being formed:

$$^{\mathrm{S}}\mathrm{FMN} \xrightarrow{h\nu} {}^{\mathrm{S}}\mathrm{FMN}^{*} \xrightarrow{k_{\mathrm{ISC}}} {}^{\mathrm{T}}\mathrm{FMN}^{*} \xrightarrow[+\mathrm{HEWL}]{k_{\mathrm{ET}}} {}^{\mathrm{T}}[\mathrm{FMN}^{\cdot -}\ \mathrm{Trp}^{\cdot +}] \tag{3.17}$$

A larger proportion of FMN-HEWL therefore undergoes magnetic field-dependent spin mixing, and hence becomes trapped in the radical state. This leads to a smaller ground state population. Now, application of a magnetic field causes a fractional increase in the (larger) absolute radical population and corresponding (larger) absolute decrease in ground state population. The percentage decrease in the ground state population is therefore larger at higher pumping rates.

This effect is shown numerically in Table 3.3. For a total population of 100 FMN molecules, and a 5% change in radical population on application of a magnetic field (independent of pumping rate), the observed MFE on the ground state population increases from -1.25% to -3.33% when the radical population is doubled by, say, increasing the pumping rate.

Low pumping rate

	$B_0 = 0$	$B_0 \neq 0$
n_{rad}	20	21
n_{gs}	80	79

High pumping rate

	$B_0 = 0$	$B_0 \neq 0$
n_{rad}	40	42
n_{gs}	60	58

$$\mathrm{MFE} = \tfrac{(79-80)}{80} \times 100 = \mathbf{-1.25}\% \quad \mathrm{MFE} = \tfrac{(58-60)}{60} \times 100 = \mathbf{-3.33}\%$$

Table 3.3: *Calculation showing how a larger radical population, n_{rad}, caused by a higher pumping rate, can serve to increase the size of the observed magnetic field effect on the ground state population, n_{gs}, for a fixed percentage change on the radical population (5% here).*

The magnetic field effect for crystals grown with 1 mM FMN is shown in Figure 3.14. The magnitude of the MFE increases with increasing laser power as expected; higher laser power leads to a larger radical population, and hence a greater change in the ground state population on application of the magnetic field.

In Figure 3.14, it appears that the magnitude of the MFE will not continue to rise indefinitely, but will stabilise somewhere around -4%. This is most likely due to increasingly fast recombination of free radicals, the rate of which, in the limit of $k_{\mathrm{ox}} = k_{\mathrm{red}}$, goes with the free radical concentration squared (Equation 3.19). This causes increasingly fast repopulation of the ground state at higher laser powers, balancing the rising radical

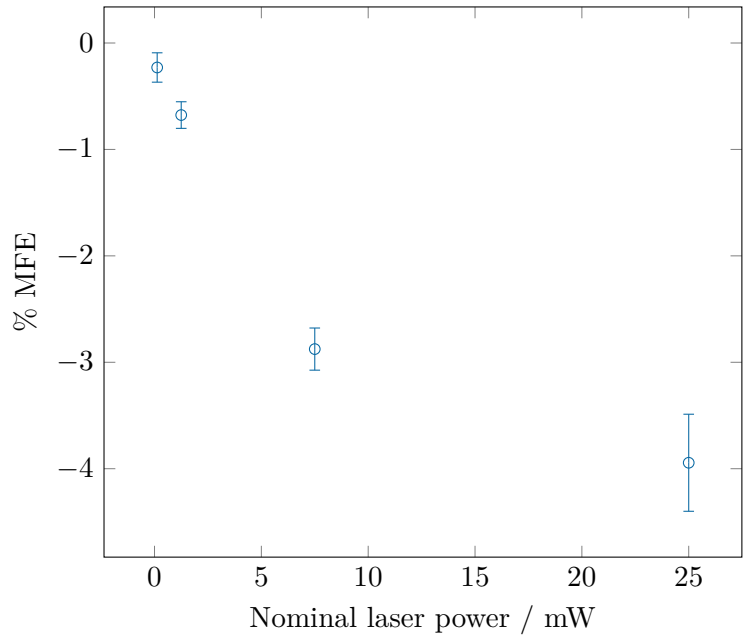

Figure 3.14: *Laser power dependence of the magnetic field effect for a HEWL crystal (3.5* mM *HEWL, 1* mM *FMN, 1* M *NaCl, 0.1* M *NaOAc buffer, pH 4.4). The laser power is plotted as direct output from the laser, before the objective; some loss of power will necessarily occur through the objective and other optics. The wavelength of the laser was 458* nm*, scan time 147.8* ms *per frame. Error bars show the standard deviation of the calculated MFE.*

population:

$$\mathrm{FMN}^{\cdot-}_{\mathrm{free}} + \mathrm{Trp}^{\cdot+}_{\mathrm{free}} \xrightarrow{k_{\mathrm{recom}}} \mathrm{FMN} + \mathrm{Trp} \tag{3.18}$$

$$\begin{aligned} \mathrm{Rate} &= k_{\mathrm{recom}}[\mathrm{FMN}^{\cdot-}_{\mathrm{free}}][\mathrm{Trp}^{\cdot+}_{\mathrm{free}}] \\ &\approx k_{\mathrm{recom}}[\mathrm{FMN}^{\cdot-}_{\mathrm{free}}]^2 \end{aligned} \tag{3.19}$$

As is often the case, there is the temptation here to work at the highest possible laser power, both to maximise the MFE and the fluorescence intensity. However, as can be seen from the figure, the signal to noise ratio actually becomes significantly worse at higher laser powers. This is due to the fact that photobleaching of the sample becomes increasingly strong at high laser powers, both reducing the measured fluorescence, and making fitting of the data more difficult. A balance must therefore be struck between the various factors.

The power density of the pump laser is perhaps the most crucial difference between the bulk and confocal experiments, when performed on identical solutions. Although both experiments use a nominally similar laser power (25 mW for confocal, 350 mW for bulk) the power density is vastly different due to the area over which the laser is focussed. For the

bulk experiment, the area is approximately 5 mm^2, giving a power density of 70 $mW\,mm^{-2}$. The confocal experiment focusses the beam to an area of a few square microns, with an estimated power density of 100 $kW\,mm^{-2}$, six orders of magnitude higher. There will hence most likely be a dramatic difference in the size fluorescence-detected field effects as discussed above.

3.7.2 Solution phase concentration dependence

A comparison of the results from the 'bulk' and confocal experiments using solution phase samples was carried out in order to ensure that behaviour observed for the crystals was due to the samples themselves, and not some quirk of the confocal experiment. To this end, presented here are comparisons of the MFE as measured by 'bulk' (Section 3.3) and confocal (Section 3.6.1) experiments, studying the effect of FMN and HEWL concentration.

The size of the magnetic field effect within a given experiment setup will depend on the concentrations of donor and acceptor. This effect acts partly through the rate of electron transfer, which will depend on the amount of HEWL in solution: a higher concentration of HEWL relative to FMN allows electron transfer to compete more effectively with pathways which return ^{T}FMN* to the ground state (quenching by oxygen, reverse ISC, or triplet-triplet annihilation, for instance[88]):

$$\mathrm{FMN} \xleftarrow{k_{\mathrm{Q}},\, k_{\mathrm{ISC'}},\, k_{\mathrm{TT}}} {}^{\mathrm{T}}\mathrm{FMN}^{*} \xrightarrow[+\mathrm{HEWL}]{k_{\mathrm{ET}}} {}^{\mathrm{T}}[\mathrm{FMN}^{\cdot -}\ \mathrm{Trp}^{\cdot +}] \tag{3.20}$$

More subtly, the MFE will also depend on the concentration of FMN since the rate of return to the ground state by pairs of FMN and HEWL free radicals (k_{recom}), in the limit of $k_{\mathrm{ox}} = k_{\mathrm{red}}$, depends on the free radical concentration squared (Equations 3.18 and 3.19). A high concentration of FMN therefore increases the rate of return to the ground state, and hence decreases the magnetic field effect on that state.

The dependence of the magnetic field effect on FMN concentration is shown in Figure 3.15 for both bulk and confocal experiments. All experiments were performed with 1.5 mM HEWL, with the trend clearly the same for both experiments; the magnetic field effect decreases with increasing FMN concentrations, as expected from the above discussion.

The magnetic field effect is approximately ten times higher for the confocal experiment compared to the bulk fluorescence. This is due to the higher power density of the confocal beam, as discussed in Section 3.7.1.

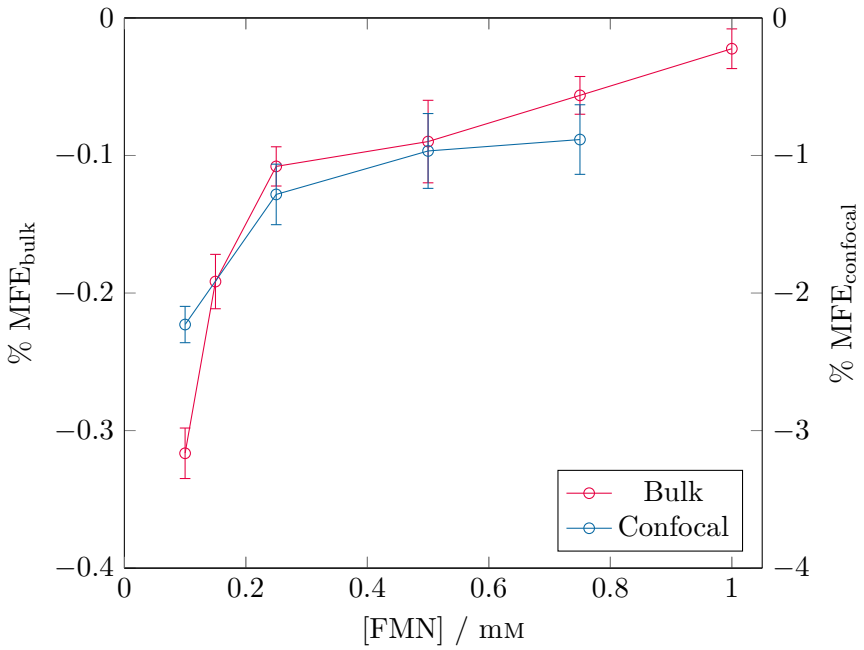

Figure 3.15: *Magnetic field effect plotted against [FMN] for both bulk fluorescence and confocal experiments. The magnitude of the MFE decreases with increasing [FMN] due to the increasingly fast recombination of free radicals. The solutions also contained 1.4* mM *HEWL, 0.1* M *NaOAc at pH 4.2, 50% v/v glycerol.*

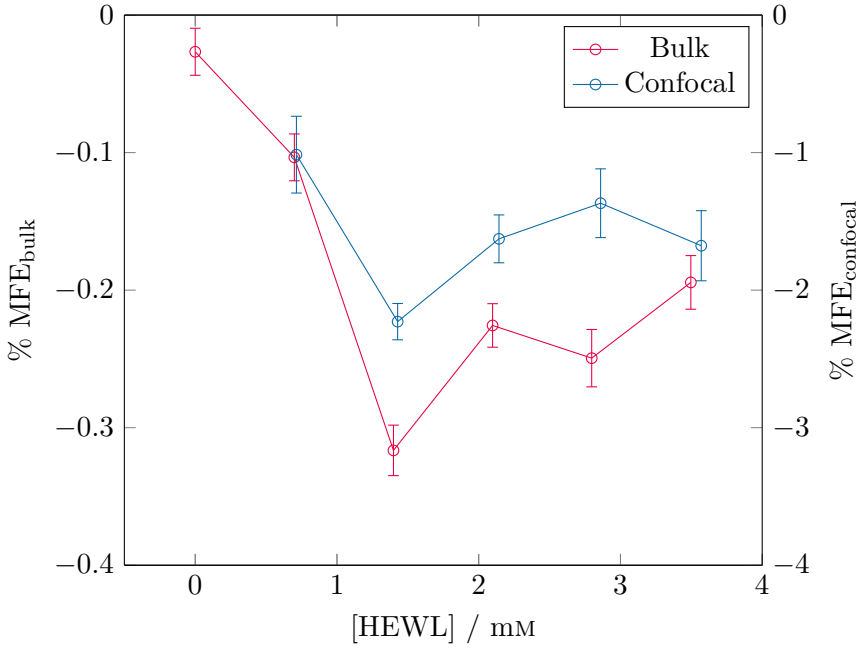

Figure 3.16: *Magnetic field effect plotted against [HEWL] for bulk fluorescence and confocal experiments. At low concentrations the MFE is limited by the availability of donor tryptophan residues. The solutions also contained 100* µM *FMN, 0.1* M *NaOAc at pH 4.2, 50% v/v glycerol.*

The dependence of MFE on HEWL concentration is also similar for both experiments (Figure 3.16). The magnitude of the MFE is also approximately ten times higher for the confocal experiment, and a similar trend is seen. Here the MFE reaches a peak at around 1.5 mM HEWL ([FMN] = 100 µM for all experiments). At low HEWL concentration, the rate of formation of radical pairs is limited by available donor tryptophans, reducing the MFE. Above 1.5 mM the MFE decreases slightly. One explanation for this trend is that the rate of formation of singlet radical pair from the singlet excited state ($k_{\mathrm{ET,S}}$) increases relative to intersystem crossing as the the donor concentration is increased:

$$^{\mathrm{S}}[\mathrm{FMN}^{\cdot-}\ \mathrm{Trp}^{\cdot+}] \xleftarrow[+\mathrm{HEWL}]{k_{\mathrm{ET,S}}} {}^{\mathrm{S}}\mathrm{FMN}^{*} \xrightarrow{k_{\mathrm{ISC}}} {}^{\mathrm{T}}\mathrm{FMN}^{*} \xrightarrow[+\mathrm{HEWL}]{k_{\mathrm{ET}}} {}^{\mathrm{T}}[\mathrm{FMN}^{\cdot-}\ \mathrm{Trp}^{\cdot+}] \tag{3.21}$$

$$\frac{\mathrm{d}[^{\mathrm{S}}\mathrm{FMN}^{*}]}{\mathrm{d}t} = -k_{\mathrm{ET,S}}[^{\mathrm{S}}\mathrm{FMN}^{*}][\mathrm{HEWL}] - k_{\mathrm{ISC}}[^{\mathrm{S}}\mathrm{FMN}^{*}] \tag{3.22}$$

These singlet radical pairs show the opposite sign MFE to triplet born ones, and hence decrease the apparent magnitude of the MFE. This effect has been observed with FMN in unpublished data by Evans, who could observe the sign of the MFE changing from negative (triplet born) to postive (singlet born) as the donor (ascorbic acid) concentration was increased.[110]

In this analysis, some of the more complex photochemistry, such as the production of lumichrome and disproportionation reaction has been neglected. In recently published work by Evans and coworkers, it was suggested that these effects can indeed be ignored if the sample is flowed.[96] Evans does, however, note that *'these processes are expected to impact the viability of the two-state model ... in determining flavin populations from MARY experiments obtained by prompt fluorescence'*.

3.7.3 MFEs in crystals

Hen egg white lysozyme crystals were produced using the protocol described in Section 3.5.2. The crystals varied in size, but were typically between 50 and a few hundred microns across. The crystals were observed to be more fluorescent than the surrounding solutions at all concentrations below 3.5 mM FMN (droplet concentration), above which the fluorescence intensity was comparable. This suggests that, given the quantum yield of fluorescence would be expected to decrease inside the crystal due to the higher concentration of available electron donors, FMN must be accumulating inside the crystals.

The concentration of FMN used in the droplet solutions for crystal growth was varied

between 0.01 and 5 mM. Over this range, the MFE varied between −1 and −3%, with no clear trend of the MFE on the concentration of FMN being discernible. The MFE also varied between −1 and −3% between different crystals grown under the same conditions, and between different points in each crystal when the position of the crystal or focal plane was moved.

For experiments where the crystal was not moved between measurements, the MFE was found to be consistent over the field of view. This would suggest that either a) the magnetic field effect depends strongly on structural effects not visible in this experiment (across distances greater than 50 µm), or b) other factors, such as the depth of the focal plane inside the crystal or the structure of the crystal lying between the objective and the focal plane, affect the size of the observed MFE. This variation of the MFE at different points in a crystal may be due to differences in the laser power reaching the focal plane. If the crystal is positioned such that the laser must pass through a large depth of crystal before reaching the focal plane, then scattering or absorption of the laser before it reaches the focal plane will cause a decrease in the effective laser power at the detected region, and hence a corresponding decrease in the MFE. This effect will vary depending on the specific orientation of the crystal and the chosen focal plane.

3.7.4 Spatially resolved MFEs

While the magnitude of the magnetic field effect varies between different crystals, making quantitative comparisons difficult, it is possible to compare the size of the MFE in different parts of the image, say between the crystal and the surrounding solution.

Figure 3.17 shows the intensity profile at the edge of the crystal at various times after the start of the experiment. The drastic photobleaching inside the crystal can be observed, with the fluorescence intensity within the crystal dropping to a third of the initial value after 15 seconds of illumination. Notable is the relatively small drop in fluorescence from the solution; the rapid diffusion of FMN means that the bleached fluorophores are exchanged with non-bleached molecules quickly. This was confirmed by FRAP experiments on FMN-HEWL solutions, where the bleached area was completely replenished before the first measurement frame could be scanned.

The higher fluorescence intensity at the crystal-solution interface, and at the left-hand edge of the frame can also be attributed to diffusion, the replenishment of bleached FMN in these areas being faster than in the centre of the observed region of the crystal. The

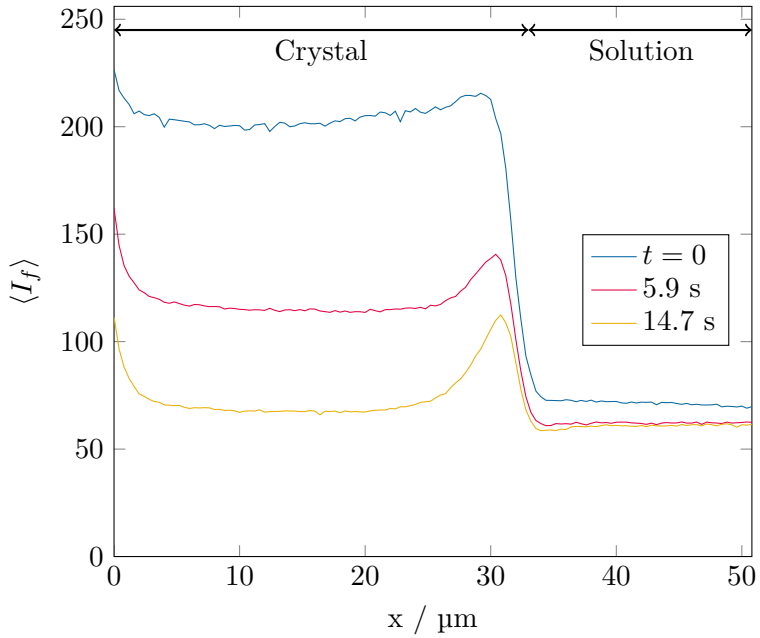

Figure 3.17: *$\langle I_f \rangle$ plotted against position across the frame for various times. The crystal extends from $x = 0$ to $\sim$ 33 µm, and the solution from $x =\sim$ 33 to 50 µm. Note the dramatic photobleaching of the crystal, and the higher fluorescence intensity at the crystal's edge ($\sim$ 33 µm) and frame edge (0 µm) relative to the centre of the crystal.*

exchange of bleached and unbleached FMN at the crystal-solution interface is faster than at the edge of the frame due to constant replenishment of the solution at the interface by fast diffusion. This can be seen in Figure 3.19, where an area of the crystal was bleached in order to observe the diffusion; recovery of the fluorescence is faster from the edges of the crystal than from the boundary between bleached and non-bleached areas inside the crystal.

The difference in brightness at the crystal-solution interface could also be attributed to a difference in the scattering of the laser in this region. If the crystal solution interface were sloped slightly, and not precisely parallel to the z-direction, then the laser power density could be slightly higher at the interface than in the bulk of the crystal. However, the fact that the photobleaching is *less* intense at the interface, and the fact that the fluorescence intensity is also higher at the left-hand edge of the frame (where there is unlikely to be some structural feature that produces this effect), suggests that this is not the case.

The MFE can be resolved spatially with respect to the position x, as shown in Figure 3.18. Firstly, the MFE is $-0.17 \pm 0.07\%$ in the solution. This is in line with the solution-phase data in Section 3.7.2 for an FMN concentration of 1 mM.

The MFE is approximately -3% in the crystal, much higher than the solution MFE,

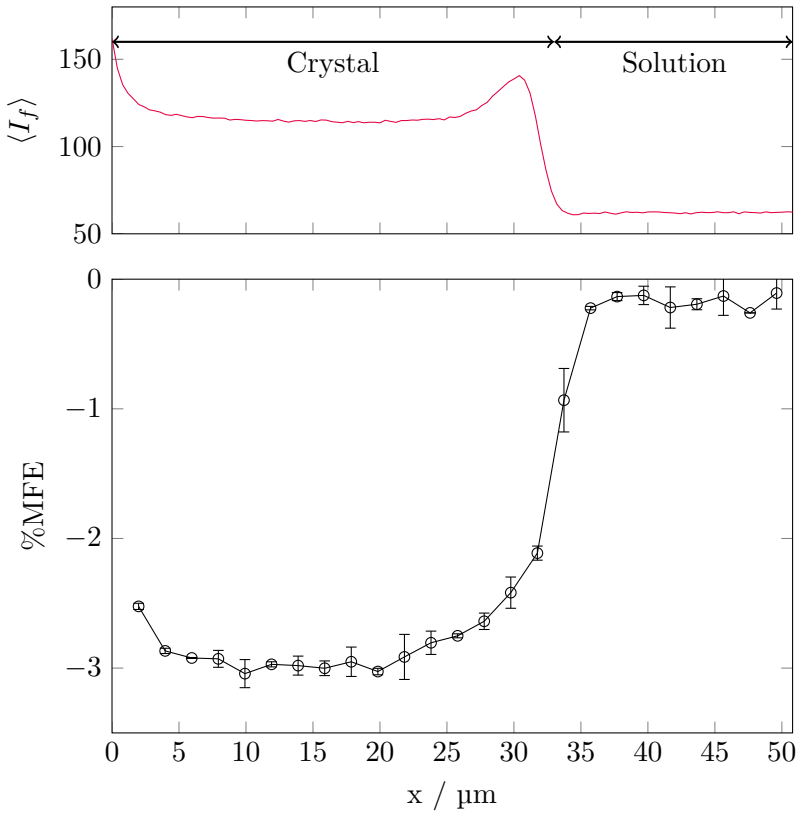

Figure 3.18: *Top: $\langle I_f \rangle$ at $t = 5.9$ s, as also shown in Figure 3.17. %MFE for the data in Figure 3.17, plotted with respect to position, x. The magnitude of the MFE is much lower in solution than in the crystal, and the MFE is also lower at the edge of the crystal and frame.*

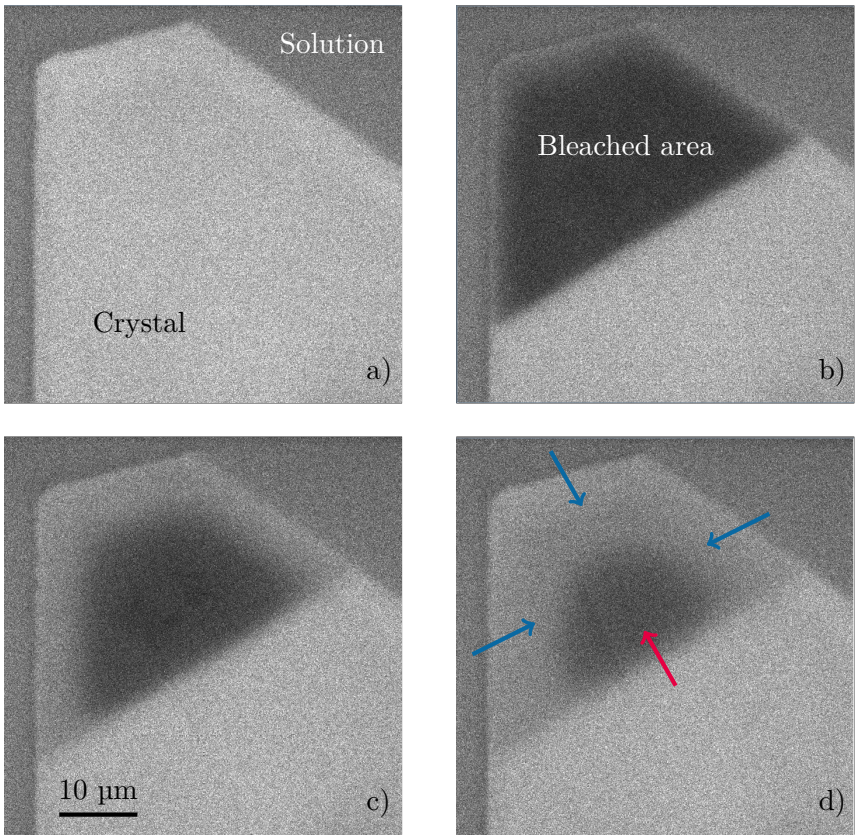

Figure 3.19: *Bleached area showing faster diffusion of FMN into the crystal from solution than from inside the crystal itself. a) Pre-bleach, b) $t = 0$ after bleach, c) $t = 90$ s, d) $t = 180$ s. The blue arrows in d) demonstrate the direction of diffusion from the surrounding solution, the red arrow from inside the crystal.*

despite the fact that the FMN concentration is higher in the crystal than in the solution, which would be expected to *decrease* the magnitude of the MFE. Also noticeable is the fact that, within the crystal, the MFE is lower at the crystal-solution interface and at the left-hand edge of the frame where the fluorescence intensity is higher.

This result can be explained by considering the diffusion of FMN through the crystal. Bleached FMN can be more rapidly replenished at the edge of the crystal and of the frame, making the fluorescence intensity higher here. At the same time, FMN radicals can also diffuse out of these regions relatively quickly, and are replaced by ground state FMN molecules, effectively adding an additional return pathway to the ground state and reducing the concentration of trapped radical, and hence the MFE.

At the centre of the crystal region probed, relatively slow diffusion of the FMN will mean that the population of trapped radicals remains higher than at the edges, and the population of fluorescent FMN is lower, raising the MFE. The slower replenishment of

bleached FMN in this region also means that the effective FMN concentration is lower, which would be expected to increase the size of the MFE (in line with what is observed in solution.)

Another possible explanation of the observed behaviour is that reoxidation of free FMN radicals by molecular oxygen is responsible for the observed effect: O_2 inside the crystal is consumed rapidly on illumination, and diffusion of O_2 from the crystal edges increases the rate of this return pathway to the ground state, and hence reduces the MFE. This is unlikely however; the diffusion constant for molecular oxygen in protein crystals is likely similar to other small molecules, such as water, which has been found to have a diffusion constant of around 10^{-10} $m^2\,s^{-1}$.[111] This value is similar to that for fluorescein in bulk water.[112,113] Given that the diffusion of FMN was too fast to be observed in the solutions measured here, the diffusion of molecular oxygen in the protein crystal is also likely too fast to explain the observed effect.

3.7.5 Diffusion in lysozyme crystals

As discussed in Sections 3.7.3 and 3.7.4, the diffusion of FMN through the protein matrix is important in determining the size of the magnetic field effect. Cvetkovic *et al.* have studied the diffusion of fluorescein in HEWL crystals, with effective diffusion coefficients of between 6 and 120×10^{-15} $m^2\,s^{-1}$ being observed depending on the crystal morphology.[114] This is three to five orders of magnitude slower than that reported for water molecules in tetragonal HEWL crystals,[111] and for fluorescein in water.[112,113] Interestingly, the diffusion is anisotropic (described by a tensor, rather than a scalar coefficient), since the pores in the crystal through which molecules can pass are anisotropic.

In order to gather further evidence about whether the differences between magnetic field effects measured in crystals and in solution can be ascribed to the diffusion characteristics of each system, the diffusion coefficient of FMN in tetragonal HEWL crystals using FRAP was measured.

A square was bleached in the crystal using 50 iterations at 35 mW nominal laser power. The fluorescence intensity was then monitored over 400 s using 1.4 mW laser power. This is shown in Figure 3.20, along with the mean intensity over $y = 17$ to 37 µm against x position for various times.

The intensity profiles were then processed according to the procedure outlined in Section 3.6.2. This was carried out for all four edges of the square. In principle, if the ori-

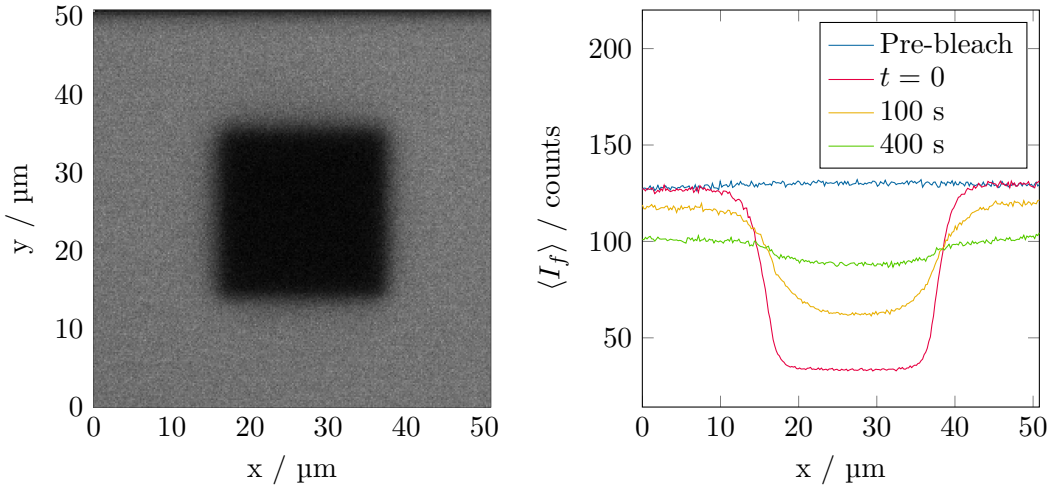

Figure 3.20: *Left: bleached area inside the protein crystal. Right:* $\langle I_f \rangle$ *plotted against position,* x*. The bleached area recovers over time to the average fluorescence. Note the minor amount of bleaching of the whole image over the experiment.*

entation of the crystal is known then the experiment could be arranged such that two of the components of the diffusion tensor could be measured using the adjacent sides of the square. However, lacking the ability to finely manipulate the position of the crystal within this experiment, this could not be achieved here, and the measured constants are effective coefficients for this particular orientation.

Figure 3.21 shows the plots of C against t (Equation 3.16). Fitting straight lines to the points allows extraction of D for the four edges. Note that the plots deviate from a straight line after approximately 200 s, and that the scatter of the points increases. In principle C should continue to increase without limit. However, photobleaching of the FMN continues even at the lower laser power. Furthermore, in this case the fluorescence of the bleached area does not recover to its pre-bleached value, even over the course of hours. The value of C does not therefore continue to increase linearly as expected. This fact indicates that either the crystal is somehow damaged by the laser, changing the properties and reducing the equilibrium concentration of FMN, or that some of the FMN is bound to the crystal and is not replaced by diffusion. The increased scatter in C after 200 s is due to the fact that the contrast between bleached and non-bleached area decreases with time as the fluorophore diffuses, reducing the accuracy of the fit.

The four measured values of D are listed in Table 3.4, with an average value of 25.4×10^{-15} $\mathrm{m^2\,s^{-1}}$, broadly in line with that reported for fluorescein. These data suggest that the diffusion of FMN can account for at least some of the increase in the magnitude of the MFE observed in FMN-doped lysozyme crystals, as well as the spatial variation of the

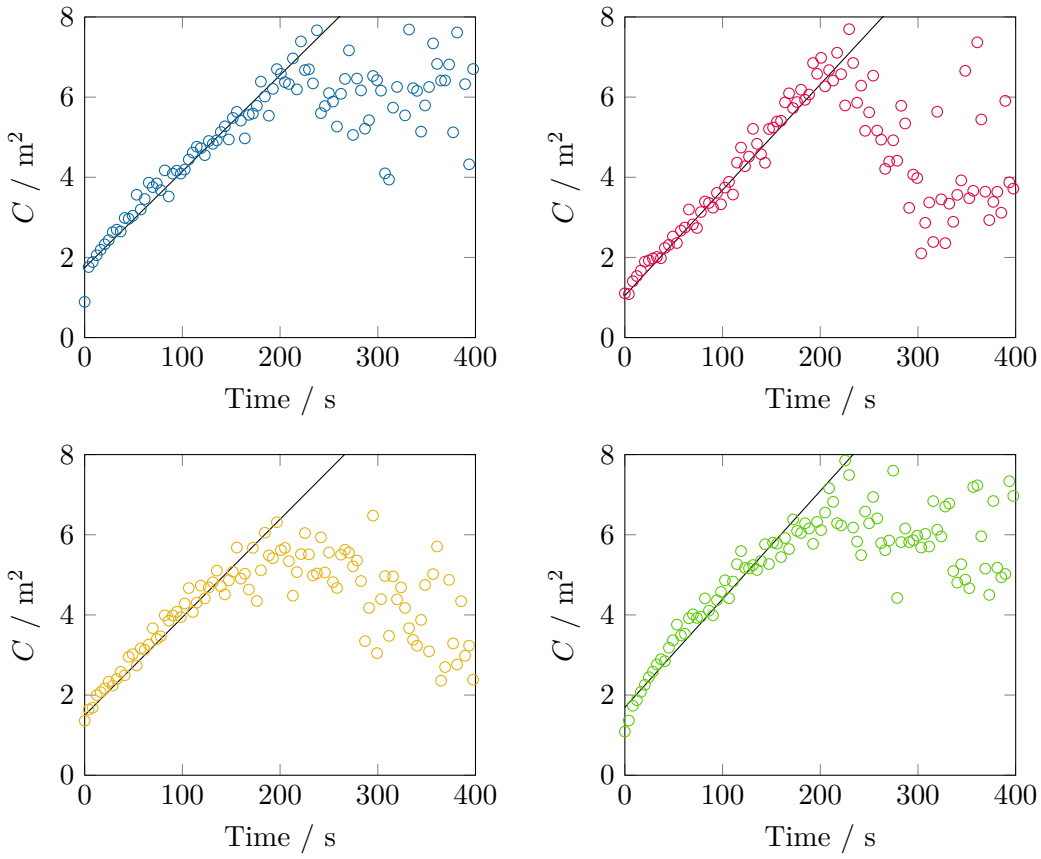

Figure 3.21: *Plots of C against t from fitting the four sides (clockwise from top left: left, right, bottom, and top) of the bleached area using Equation 3.16. The gradient of the fitted lines gives D, the diffusion coefficient.*

Edge	D / 10^{-15} m^2 s^{-1}
Left	24.0
Right	26.2
Top	24.5
Bottom	27.0

Table 3.4: *Diffusion constants measured from the four sides of the square bleached in Figure 3.20*

MFE observed at the crystal-solution interface.

3.8 Conclusions and future directions

The experiments presented here demonstrate that magnetic field effects in solution and in protein crystals can be studied using confocal microscopy. MFE experiments performed on identical solutions using confocal detection and conventional bulk-fluorescence show that, although the magnitude of the magnetic field effect was approximately ten times higher for confocal detection due to the higher power density of the microscope, similar trends with FMN and HEWL concentration occur in both experiments.

Hen egg white lysozyme was crystallised in the presence of FMN; the yellow colour and fluorescence of the crystals indicated that FMN was contained within, although no ordering of the FMN could be observed by X-ray crystallography. The crystals were found to be in the space group $P4_32_12$, with no crystal pathologies.

The high power density of the laser in the confocal microscope experiment resulted in significant photobleaching of FMN. This could be mitigated by flowing the solution phase sample, but was unavoidable for the crystals, the MFE experiment traces being a convolution of the MFE step function with a non-exponential decay. A fitting procedure was therefore devised in order to obtain reliable measurements of the MFE.

In the HEWL crystals containing FMN, the magnitude of the magnetic field effect was observed to increase with increasing laser power, attributed to the decreasing ground state population. This effect is counterbalanced at the highest laser powers by increased free radical recombination. The MFE was typically observed to be between -1 and -3% for crystals grown with 0.01 to 5 mM FMN. Although the MFE was consistent for a given crystal position, it was observed to vary for different crystals grown in the same droplet, or for different places in the same crystal. This discrepancy is most likely due to the variation of effective laser power density with focal plane due to scattering or absorption.

A magnetic field effect could be observed simultaneously in solution and in the crystal, and the MFE could be resolved with respect to position. It was found to be slightly lower at the edge of the crystal, and at the edge of the frame. This effect can be explained with reference to the diffusion of FMN through the crystal: faster replacement of bleached with non-bleached FMN at the edges contributes an additional return path to the ground state, which reduces the size of the MFE. The diffusion constant for FMN through HEWL crystals was measured by FRAP and found to be $\sim 25 \times 10^{-15}$ $\mathrm{m^2\,s^{-1}}$, three to five orders

of magnitude slower than in solution. The relatively slow replacement of bleached and free radical FMN by ground state FMN by diffusion likely accounts for at least some of the difference observed between the crystals and surrounding solutions.

Further work could extend this technique to a range of other systems, including crystals of other molecules of interest, such as riboflavin[115] or lumiflavin.[116]

In addition, the ability to monitor the diffusion of fluorophores by FRAP is a potentially powerful way to investigate the effect of diffusion on magnetically-sensitive systems.

Although no evidence of ordered FMN could be observed in HEWL crystals by X-ray crystallography, confocal microscopy is potentially a powerful way to measure anisotropic MFEs in protein systems. For cryptochromes, the fixed position of the FAD cofactor within the protein allows its orientation to be controlled by crystallisation of the protein; crystallisation may therefore allow measurement of anisotropic magnetic field effects in these systems, a tantalising possibility.

Chapter 4

Evanescent-wave broadband cavity enhanced absorption spectroscopy

4.1 Optical spectroscopy methods

Ultraviolet-visible absorption spectroscopy is one of the fundamental spectroscopic techniques. Probing electronic transitions, it is used for a variety of purposes ranging from simple quantitative determination[8] to monitoring ultrafast kinetics.[117]

The basic principle of direct absorption spectroscopy is that the sample of interest can be studied by monitoring a change in the absorption of light, either between the presence and absence of the sample, or by some change that occurs to the sample (chemical reaction, adsorption, photoexcitation, etc.) A huge variety of techniques has been developed around this principle; the ones most relevant to the work in this thesis are as follows.

4.1.1 UV/vis spectroscopy

The most basic of the techniques presented here, UV/vis spectroscopy at its most simple uses a broad-band light source, typically an arc lamp. Light is passed through the sample before being dispersed by a monochromator and measured by a detector, often a photomultiplier tube or photodiode. The ratio of the light intensity in the presence and absence of the sample at each wavelength gives the absorbance, and can, for instance, be used to calculate the concentration of the sample using the Beer-Lambert law (Equation 1.32). A more sophisticated experiment might monitor the change in absorbance with time, following the kinetics of a reaction in real time.

4.1.2 Multipass spectroscopy

For a sample with either a small extinction coefficient or low concentration, the absorbance may be very small; in this case, depending on the inherent noise of the instrument, the absorbance may fall below the limit of detection. A simple solution to this problem would be to increase the path length; this, however, requires a larger volume of sample. In cases where this would be difficult, expensive, or impossible to obtain, an alternative approach is required. One such approach is to increase the effective path length by passing the light through the sample multiple times, typically using reflective mirrors. For a number of passes, n, the Beer-Lambert law then becomes

$$I(\lambda) = I_0(\lambda)10^{-\epsilon(\lambda)cnl} \tag{4.1}$$

and, for a fixed minimum detectable change in I/I_0, the limit on measurable concentration is n times lower. Many different mirror geometries have been considered, the most common being as follows, and as shown in Figure 4.1.

Pfund cell A Pfund cell[118] uses two spherical mirrors, each with the same radius of curvature and a hole bored into the centre. The mirrors are placed a distance apart equal to half the radius of curvature, and the light is passed into the cell through the central hole in one of the mirrors. The beam is reflected twice before exciting through the hole in the other mirror, passing through the sample three times.

White cell A White cell[119] uses three spherical mirrors (one large and two small) with matching radii of curvature at a distance apart equal to the radius of curvature. The number of passes can be controlled by adjusting the rotation of one of the small mirrors, with over 100 passes being common.

Herriott cell A Herriott cell[120] has two spherical mirrors, one of which has a hole bored into the centre which serves as both an entrance and an exit for the light. The number of passes can be controlled by changing the separation of the two mirrors.

Limitations on the above geometries include the fact that the light passes through a range of different paths in the cell, limiting the extent to which the sample volume can be miniaturised.

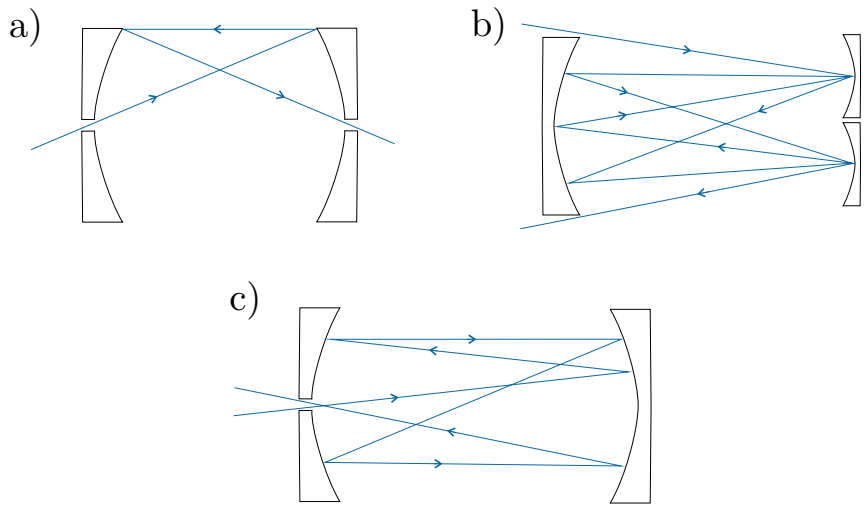

Figure 4.1: *Examples of multipass cell geometries which can be used to increase the number of passes a beam of light makes through a sample. (a) Pfund,*[118] *(b) White,*[119] *and (c) Herriott*[120] *multipass cells.*

4.2 Cavity methods

The multipass idea—reflecting the light multiple times through the sample—can be taken to its ultimate extreme using an optical cavity, or resonator, to increase the number of passes through a particular volume. An optical cavity consists of a set of mirrors that can support standing waves.

4.2.0.1 The étalon

One of the simplest types of optical cavity is an étalon, or Fabry-Pérot interferometer, which consists of a transparent plate with two reflecting surfaces or a pair of parallel mirrors. The transmittance of this device varies with wavelength due to interference between reflections. Consider a beam that enters the étalon and undergoes reflections as shown in Figure 4.2. The phase difference between each transmitted pair (T_1–T_2, etc) is[121]

$$\delta = \left(\frac{2\pi}{\lambda}\right) 2nl\cos\theta \tag{4.2}$$

where λ is the wavelength of the light, n is the refractive index of the material between the reflecting surfaces, l is the thickness, and θ is the angle at which the light enters the étalon.

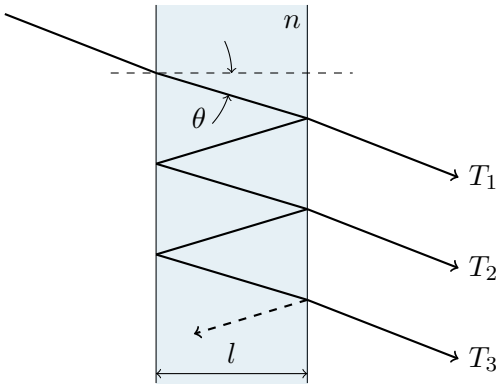

Figure 4.2: *An étalon, a simple optical resonator consisting of two parallel reflecting surfaces. The total transmittance is a function of the angle of the beam, θ, the refractive index of the material, n, the thickness of the étalon, l, and the reflectances of two surfaces.*

For a resonator with both surfaces having a reflectance R, the transmittance is

$$T = \frac{(1-R)^2}{1+R^2-2R\cos\delta}. \tag{4.3}$$

Maximum transmission through the étalon occurs when $2nl\cos\theta$ is equal to an integer number of wavelengths, corresponding to maximal constructive interference between waves. The separation of the maxima (or free spectral range), $\Delta\lambda$, is given by

$$\Delta\lambda = \frac{\lambda_0^2}{2n_g l\cos\theta + \lambda_0} \tag{4.4}$$

where λ_0 is the central wavelength of the nearest transmission peak, n_g is the group refractive index, and m is an integer.

The free spectral range is related to the FWHM of the transmission peaks, $\delta\lambda$, by the finesse, $\mathcal{F}$[122]

$$\mathcal{F} = \frac{\Delta\lambda}{\delta\lambda} \approx \frac{\pi\sqrt{R}}{1-R}. \tag{4.5}$$

Increasing reflectivity of the mirrors leads to a higher finesse, and a corresponding narrowing of the transmission maxima relative to the free spectral range. The cavity therefore becomes more selective to the wavelengths it transmits. Increasing the length of the cavity decreases the free spectral range, and increases the density of longitudinal modes that the cavity will support. For an air-filled, 10 cm long cavity, the free spectral range in the visible region is around a picometer, with the finesse being approximately 300 for $R = 0.99$.

4.2.0.2 Spherical mirror cavities

An optical cavity can also be set up using a pair of spherical mirrors. For a Gaussian beam, polarised in the x direction, entering a cavity with spherical mirrors, the lowest order intensity distribution in the plane orthogonal to the cavity axis (z) is[123]

$$I = I_0 \left(\frac{\omega_0}{\omega(z)}\right)^2 \exp\left[-\frac{2(x^2+y^2)}{\omega_0^2}\right] \tag{4.6}$$

with ω_0 being the minimum spot size (at the beam waist, $z = 0$) and the width, $\omega(z)$, being

$$\omega(z) = \omega_0 \left[1 + \left(\frac{z}{z_0}\right)^2\right]^{\frac{1}{2}} \tag{4.7}$$

$$z_0 = \frac{\pi\omega_0^2}{\lambda}. \tag{4.8}$$

This is the familiar Gaussian transverse mode. The radius of curvature of the wavefronts is

$$r(z) = z + \frac{z_0^2}{z} \tag{4.9}$$

ranging from ∞ at $z = 0$ to a minimum at z_0, and growing thereafter linearly with z for large z. By inserting mirrors with radii of curvature matching that of the wavefronts the beam will retrace itself and, if the round trip phase shift is a multiple of 2π, then the beam can exist self-consistently within the boundary conditions created by the mirrors.

The phase of a Gaussian beam is[123]

$$\varphi(\rho, z) = kz - \zeta(z) + \frac{k\rho^2}{2r(z)} \tag{4.10}$$

where $\zeta(z) = \tan^{-1}(z/z_0)$ and $\rho = x^2 + y^2$. On the cavity axis ($\rho = 0$), at the mirror positions z_1 and z_2 the phase is

$$\begin{aligned} \varphi(0, z_1) &= kz_1 - \zeta(z_1) \\ \varphi(0, z_2) &= kz_2 - \zeta(z_2) \end{aligned} \tag{4.11}$$

and the phase change between the two mirrors is

$$\Delta\varphi = kd - \Delta\zeta \tag{4.12}$$

where $d = z_2 - z_1$ and $\Delta\zeta = \zeta(z_2) - \zeta(z_1)$. Since the mirrors have been chosen such that their radii of curvature match the wavefronts, this is true at all points on the mirrors. The round-trip phase change is therefore $2kd - 2\Delta\zeta$, and the resonance condition is

$$2kd - 2\Delta\zeta = 2q\pi \quad q = 0, \pm 1, \pm 2, ... \tag{4.13}$$

Substituting $k = 2\pi\nu/c$ and $\nu_F = c/2d$, the longitudinal modes supported by the cavity are

$$\nu_q = q\nu_F + \frac{\Delta\zeta}{\pi}\nu_F. \tag{4.14}$$

The spacing between adjacent modes is $c/2d$, the same as for the étalon.

The spherical mirror cavity will also support higher order modes, corresponding to the Gauss-Hermite polynomials:[123]

$$I_{mn} = I_0 \left(\frac{\omega_0}{\omega(z)}\right)^2 H_m^2\left(\frac{x\sqrt{2}}{\omega(z)}\right) H_n^2\left(\frac{y\sqrt{2}}{\omega(z)}\right) \exp\left[-\frac{2(x^2+y^2)}{\omega_0^2}\right]. \tag{4.15}$$

The resonance frequencies are then given by

$$\nu_{mnq} = q\nu_F + (m+n+1)\frac{\Delta\zeta}{\pi}\nu_F. \tag{4.16}$$

The index q covers the longitudinal modes, and modes of different q but identical m and n have the same intensity distributions. m and n cover the transverse modes. Note that the resonance frequencies in Equation 4.16 depend only on the sum of m and n, not each index individually; modes of equal $m + n$ are degenerate.

In practice, with a cavity length on the order of centimeters and a broad-band light source, myriad cavity modes will be excited, and we need not worry about the particular mode structure.

4.2.0.3 Stability of the cavity

In building an optical cavity, variables such as the radii of curvature and spacing of the mirrors must be chosen. For some combinations, the size of a beam propagating through the system will grow without limit until it is greater than the size of the mirrors – light is then lost from the cavity. This type of cavity is *unstable*. A *stable* cavity is one where the beam is periodically refocussed such that it cannot escape from the cavity beyond the limit of the mirrors.

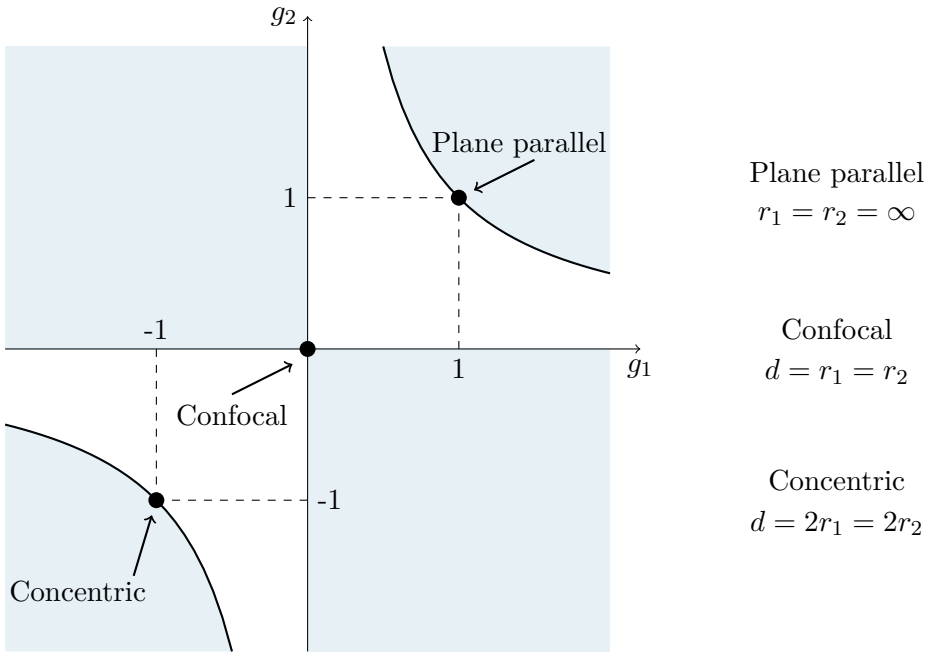

Figure 4.3: *Cavity stability diagram, showing unstable cavity arrangements (shaded regions). Highlighted are plane-parallel (étalon), confocal, and concentric configurations. Figure adapted from Lipson et al.*[125]

The stability condition is[124]

$$0 < \left(1 - \frac{d}{r_1}\right)\left(1 - \frac{d}{r_2}\right) < 1 \tag{4.17}$$

where d is the distance between the mirrors and r_1 and r_2 are the radii of curvature. This can be represented graphically, as in Figure 4.3, where

$$g_1 = \left(1 - \frac{d}{r_1}\right), \; g_2 = \left(1 - \frac{d}{r_2}\right). \tag{4.18}$$

The unstable regions, where light is not completely refocussed into the cavity, are shaded. The plane parallel (corresponding to the étalon discussed in Section 4.2.0.1), confocal, and concentric arrangements are highlighted. In each of these arrangements the cavity is conditionally stable, and highly sensitive to misalignment.

4.2.1 Cavity ring-down

An elegant extension of the multipass arrangement is cavity ring-down spectroscopy (CRDS). Developed as a method of measuring mirror reflectivity,[126,127] and first employed spectroscopically in gas-phase measurements,[128] CRDS measures the rate of decay of a light pulse trapped within a high finesse optical cavity. The rate of light loss from the cavity,

as monitored by the light transmitted through the exit mirror of the cavity, is typically a simple exponential with decay components corresponding to mirror loss, scatter, and absorption by the sample. This can be understood by considering the light intensity with respect to the number of round trips made through the cavity.

In CRDS the light pulse enters the cavity through the centre of the first mirror. During a round-trip period through an empty cavity, t_r, the intensity will fall due to the non-unity reflectance of the mirrors, as well as due to scattering, so the output intensity, $S(t)$, will drop in accordance with[129]

$$\begin{aligned} S(t + nt_r) &= R^{2n} S(t) \\ &= \exp[2n \ln(R)] S(t) \end{aligned} \tag{4.19}$$

where n is the number of round trip passes, and R is the effective mirror reflectivity, taking into account all intracavity losses not due to an absorber. For $R \sim 1$, $\ln(R) \sim -(1 - R)$, and defining the round trip losses for the empty cavity as $L_0 = 2(1 - R)$, the output intensity becomes

$$S(t + nt_r) = \exp(-nL_0) S(t). \tag{4.20}$$

Typically the detector is not fast enough to detect individual output pulses or the round-trip time is shorter than the pulse duration, so the parameter n can be replaced with the time such that $t = 2nt_r$, and

$$S(t) = \exp(-L_0 t) S(0). \tag{4.21}$$

The exponential decay of the output intensity can therefore be fitted to find the losses due to the mirrors.

Filling the intra-mirror volume with an absorber with absorption coefficient α, the round trip losses now include a term $2\alpha l$, where l is the length of the cavity. The loss coefficient is now

$$L = 2[(1 - R) + \alpha l] \tag{4.22}$$

and the absorbance is therefore given by

$$\alpha l = \frac{1}{2}(L - L_0). \tag{4.23}$$

By taking the ring-down times for the two situations, $\tau = t_r/L$ and $\tau_0 = t_r/L_0$, the

absorbance can be related to the measured ring-down times by

$$\alpha l = \frac{L_0}{2}\frac{\tau_0 - \tau}{\tau}$$

$$= (1 - R)\frac{\tau_0 - \tau}{\tau}. \tag{4.24}$$

The absorbance of a solution can therefore be measured using the ring-down times of the empty and filled cavity. No other calibration (for instance, measurement of a sample of known absorbance) is necessary, and the technique is insensitive to fluctuations in laser power, the time constant of the exponential decay being the important parameter. The laser wavelength can also be scanned in order to measure the absorption spectrum.

Several experimental requirements must be fulfilled to achieve optimum sensitivity and precision. Firstly, in conventional CRDS the linewidth of the laser is often larger than the free spectral range of the cavity, meaning that several longitudinal and transverse modes are excited simultaneously.[130,131] Beating of these modes introduces high frequency structure into the cavity decay that can complicate fitting. Secondly, if the laser linewidth is wider than the absorption feature, then the absorption coefficient $\alpha(\lambda)$ is not a constant, and the decay will be non-exponential,[129] further complicating fitting. Since linewidths in the gas phase are typically narrow, 0.1 cm^{-1} or less, very narrow-band lasers are necessary to obtain a single exponential decay.[131] This can be achieved using a narrow-band continuous-wave laser to 'charge up' the cavity before switching the laser off and observing the resulting decay. This approach entails experimental challenges of its own in frequency matching the laser and cavity.[122]

There is nothing that prevents the use of CRDS in condensed phase applications, beyond certain experimental difficulties, and this technique has been applied successfully to solutions.[132,133] In this case the cavity loss includes an additional term for the losses caused by introducing a cell into the cavity.

4.2.2 Cavity enhanced absorption spectroscopy

Complementary to CRDS is cavity enhanced absorption spectroscopy (CEAS), also known as integrated cavity output spectroscopy (ICOS). First implemented by O'Keefe,[134] CEAS uses a continuous-wave laser to pump the cavity, but monitors the integrated output from the cavity instead of the ring-down. In this case, the integrated output intensity of the cavity is given by taking the sum over all passes (Figure 4.4). For the first pass, the output

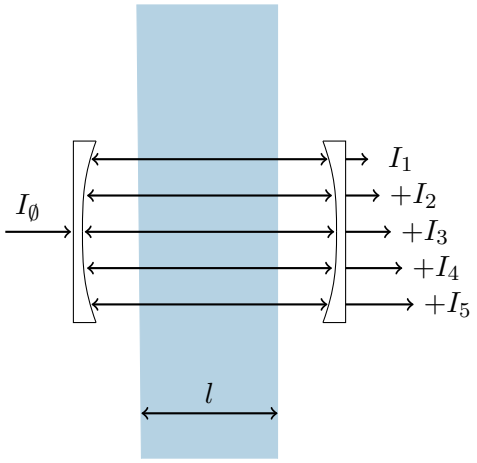

Figure 4.4: *Optical cavity containing an absorber of length l, continually pumped by an input intensity, $I_\emptyset$, showing the output of one of the mirrors after each pass. This figure shows curved mirrors; the theory is equally applicable to any stable resonator.*

intensity, I_1 is

$$I_1 = I_\emptyset(1-R)^2(1-A) \tag{4.25}$$

where $I_\emptyset$ is the input light intensity, R is the effective mirror reflectivity (taking into account all non-absorptive intracavity losses), and A is the sample absorbance. The output for the second pass is

$$I_2 = I_1(1-A)^2R^2 \tag{4.26}$$

$$= I_\emptyset(1-R)^2(1-A)^3R^2. \tag{4.27}$$

Taking the sum of the output intensities over an infinite number of passes, the total output intensity, I, is

$$I = I_\emptyset(1-R)^2(1-A)\sum_{n=0}^{\infty} R^{2n}(1-A)^{2n}. \tag{4.28}$$

This expression can be rewritten as the sum of a geometrical progression since $R < 1$ and $A < 1$,

$$I = I_\emptyset \frac{(1-R)^2(1-A)}{1-R^2(1-A)^2}. \tag{4.29}$$

Taking the ratio of intensities without (I_0) and with (I) the absorber, and substituting $(1-A) = \mathrm{e}^{-\alpha l}$ from the Beer-Lambert law,

$$\frac{I_0}{I} = \frac{1-(R\mathrm{e}^{-\alpha l})^2}{(1-R^2)\mathrm{e}^{-\alpha l}}. \tag{4.30}$$

In the limit $R \to 1$ and $\alpha \to 0$, this simplifies to give

$$\alpha = \frac{1-R}{l}\left(\frac{I_0}{I} - 1\right) \tag{4.31}$$

or alternatively, with the decadic extinction coefficient, and remembering that the above applies at all wavelengths,

$$\epsilon(\lambda)c = \frac{1-R(\lambda)}{\ln 10 \cdot l(\lambda)}\left(\frac{I_0(\lambda)}{I(\lambda)} - 1\right). \tag{4.32}$$

The per-pass absorbance of the sample can therefore be calculated by measuring the output intensities in the absence and presence of the sample, assuming that the effective reflectivity of the mirrors is known. Often the $1-R(\lambda)$ term in this expression is expressed in terms of the 'cavity enhancement factor', CEF(λ), a measure of the increased sensitivity due to the cavity, with $\mathrm{CEF}(\lambda) = (1-R(\lambda))^{-1}$.

The cavity enhancement factor is an experimental parameter that depends on the nominal reflectivity of the mirrors, the transmittance of any intra-cavity elements, as well as the alignment and contamination of all elements in the cavity. This is an unknown parameter for any particular setup, and must be calibrated in order to obtain quantitative measurements of ϵc. This calibration can be done using a dye of known absorbance (taken using a UV/vis spectrometer). Performing a measurement of the known absorber in the aligned cavity, the only unknown term in Equation 4.32 is then CEF(λ), which can be calculated. Samples of unknown absorbance can then be measured quantitatively using the calibration value for CEF(λ).

The error on the approximation made in deriving Equation 4.32 depends on R and I_0/I, and decreases with increasing R and decreasing I_0/I. Calculations comparing it to the exact result for a range of mirror reflectivities are shown in Figure 4.5. For $R = 0.999$, the error is less than 0.15% for $I_0/I < 100$, making this approximation acceptable for the experiments described herein.

4.2.3 Broad-band CEAS

In the original paper reporting CEAS,[134] O'Keefe employed a pulsed dye laser as a tunable light source to scan the wavelength axis between 688.5 and 690.5 nm. A similar experiment was reported almost simultanously by Engeln *et al.* using tunable diode lasers.[135] While wide enough to cover the measured oxygen $b^1\Sigma_g^+(\nu = 0)$–$X^3\Sigma_g^-(\nu = 0)$ band, the

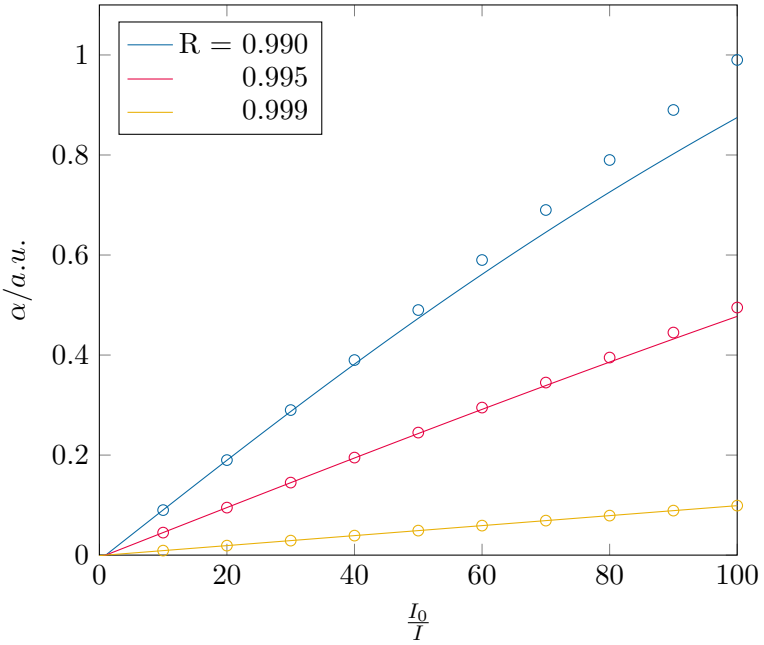

Figure 4.5: *Calculations comparing Equation 4.32 (∘) to the exact result (–) for a range of effective reflectivities, R. The error on the approximation decreases with increasing R and decreasing I_0/I. For $R = 0.999$ and $I_0/I < 100$ (well outside the typical range in these experiments) the error is less than 0.15%.*

small wavelength range of tunable dye or diode lasers is of limited use in monitoring multiple species or broad absorption bands. In the condensed phase in particular, bands are significantly wider, spanning potentially hundreds of nanometres.

Fiedler *et al.* reported incoherent broad-band CEAS (IBBCEAS), using a short-arc Xe-lamp as the light source, and monochromator and intensified photodiode array as the detector. The use of an arc lamp allows transitions over a 190 nm–10 µm wavelength range to be probed, including wavelength regions that are difficult to reach using diode lasers. Furthermore, this approach is relatively simple compared to CRDS or tunable-laser based CEAS. While the spectral resolution of this technique is limited by the detector (∼0.026nm vs ∼0.003nm for CRDS), in many cases extremely high wavelength resolution is not necessary (for example, if the spectra are inhomogeneously broadened) and higher resolution measurements are in principle possible at the expense of sensitivity using a longer monochromator.

Ball and coworkers developed a broad-band CEAS (BBCEAS) system using red and green light emitting diodes to achieve a bandwidth of 60 nm,[136] approaching the limits of the CRDS mirrors used. Ball was able to measure the spectra of NO_3, NO_2, and I_2, but was only able to quantify the absolute absorbances within an uncertainty of approximately 15%

due to systematic errors in measurement of the mirror reflectivities using water vapour bands and uncertainty in the absorption cross sections of the species themselves. Later work by the same workers used LEDs and a miniature bench-top spectrometer intended for *in situ* field measurements of atmospheric NO_2.[137]

The first application of broad-band CEAS to the condensed phase was by Fiedler *et al.* in 2005, who modified a commercial UV/vis spectrophotometer to accept cavity mirrors surrounding the cuvette.[138] They used $R \approx 0.99$, 415–640 nm mirrors to achieve a close to theoretical maximum improvement in the signal to noise ratio.* This use of a commercial spectrophotometer somewhat nullifies the advantage of the broad-band light source due to having to scan the monochromator to record the spectrum. However, the simplicity and low cost of this setup makes it an attractive approach. Fiedler also reported a home-built broad-band CEAS setup using a polychromator and CCD array in the same paper.

An interesting variant for condensed phase measurements was introduced by McGarvey and coworkers, who used a wet-mirror setup to measure Bacteriochlorophyll *a* in solution.[139] In their work a high finesse Fabry-Pérot resonator was filled with liquid sample, similar to an approach used in CRDS previously.[132,140] The elimination of the intra-cavity cell reduces the background cavity loss, improving sensitivity. Their experiments were not broad-band, but did achieve very high sensitivities (being able to measure Bacteriochlorophyll *a* concentrations down to ∼200 pM.)

Islam *et al.* used a 2 mm long cuvette, LEDs, and compact CCD spectrograph to study a number of analytes in solution. Cavity enhancement factors of ∼40 to 100 were achievable using this setup, and the entire spectrum could be measured at once. However, the divergent nature of the LEDs meant that much light was lost attempting to coupled light into the cavity, ultimately setting the limit of detection.

The advantage of using broad-band sources such as LEDs or arc lamps, including low cost and simplicity as well as the broad spectral range, is somewhat mitigated by the increased difficulty in coupling light into the cavity. Laser sources generally produce more collimated beams, and this fact was used by Johnston *et al.* in 2008, who used a supercontinuum laser source. In this work, broad-band light (500–1750 nm) was generated by pumping ∼ 20 m of highly nonlinear photonic crystal fibre using a 1064 nm, 10 ns pulsed laser running at 30 kHz. Interestingly, the cavity was formed using two Brewster's

*In fact, Fiedler reported an improvement of ∼10, larger than the theoretical maximum of 7, due to quantisation error in the adc of the single-pass experiment. Presumably the actual improvement in the signal to noise ratio was close to the theoretical maximum.

angle retroreflector prisms, instead of a pair of mirrors. A spectrograph and CCD detection allowed simultaneous detection of the entire broad-band spectrum.

Schnippering *et al.* also demonstrated the use of a supercontinuum source (SCS) to monitor the interfacial generation of Ir(IV).[141] This work was continued in 2010 by van der Sneppen and coworkers, comparing the supercontinuum source to a white LED source[142†]. They found that '*one of the major advantages of incorporating an SC light source within a BB-CEAS arrangement is that the enhanced spectral irradiance it provides over other light sources permits the rapid acquisition of spectra with a high signal to noise ratio*', and noted that the collimation of the SCS beam allowed a smaller sample volume to be probed compared to using an LED.

The use of supercontinuum radiation was continued by Kiwanuka *et al.* in 2010,[143] who used a fibre laser-pumped photonic crystal fibre to generate light with a bandwidth of 480 to 1800 nm. Using an intra-cavity cell, they were able to monitor the oscillating Belousov-Zhabotinsky reaction across almost the entire visible region. Similar experiments by Neil *et al.* used a commercial supercontinuum source to monitor microfluidic droplets[144] and magnetic field effects in cryptochrome proteins[145] across the visible region.

Ultimately BBCEAS, compared to CRDS, trades wavelength resolution, calibration-free absolute absorption measurements, and some sensitivity, for spectral bandwidth. This exchange may be useful in order to measure several gas-phase species simultaneously, or in the case of condensed phase measurement where spectral bands are typically broad.

4.2.4 Evanescent-wave CEAS

BBCEAS has been widely applied to low concentration samples in pursuit of increased sensitivity. Comparing the Beer-Lambert law (Equation 1.32) and the absorbance measured by CEAS (Equation 4.32), we can see that the CEF is a measure of the increased sensitivity of the CEAS experiment versus a single pass. In the limit of small ϵcl, when $\exp(-\epsilon cl) \approx 1 - \epsilon cl$

$$\text{Single pass:} \qquad \ln 10 \cdot \epsilon cl = \frac{I_0}{I} - 1 \tag{4.33}$$

$$\text{CEAS:} \qquad \text{CEF} \cdot \ln 10 \cdot \epsilon cl = \frac{I_0}{I} - 1 \tag{4.34}$$

[†]Both of these papers will be further discussed with regards to the interfacial nature of the measurements in Section 4.2.4.2

Typical CEF values for 99.98% reflective mirrors with a quartz sample cell or intra-cavity prism are in the range 300–600. In most application, this enhancement has been applied with the aim of reducing the lowest detectable concentration. However, it is equally applicable to situations where the path length is short due to miniaturisation of the sample cell, or due a desire to probe interfacial processes where the path length is intrinsically short. This second situation is the case in evanescent-wave CEAS (EW-CEAS).

4.2.4.1 The evanescent wave

Consider an electromagnetic wave directed at a transition between materials with refractive indices, n_1 and n_2 (for instance, the boundary between fused silica and water). For a beam coinciding with the boundary at an angle $\hat{\imath}$ to the surface normal (Figure 4.6), the reflection and transmission coefficients for polarisations parallel, $||$, and perpendicular, $\perp$, to the surface normal, are[125]

$$\mathcal{R}_{\perp} = \frac{\cos\hat{\imath} - n_r \cos\hat{r}}{\cos\hat{\imath} + n_r \cos\hat{r}} \tag{4.35}$$

$$\mathcal{T}_{\perp} = \frac{2\cos\hat{\imath}}{\cos\hat{\imath} + n_r \cos\hat{r}} \tag{4.36}$$

$$\mathcal{R}_{||} = \frac{\cos\hat{r} - n_r \cos\hat{\imath}}{\cos\hat{r} + n_r \cos\hat{\imath}} \tag{4.37}$$

$$\mathcal{T}_{||} = \frac{2\cos\hat{r}}{\cos\hat{r} + n_r \cos\hat{\imath}} \tag{4.38}$$

where $n_r = n_2/n_1$ and $\hat{r}$ is the angle between the surface normal and the angle of refraction. These concepts are familiar from Snell's law:

$$\sin\hat{\imath} = n_r \sin\hat{r}. \tag{4.39}$$

Taking Snell's law, if $n_r < 1$, then there is no real solution for $\hat{r}$ if $\hat{\imath} < \sin^{-1} n_r$. This is total internal reflection (TIR), where the incident angle $\hat{\imath}$ is greater than the critical angle. In this case, both $|\mathcal{R}_{\perp}|$ and $|\mathcal{R}_{||}|$ are unity. Neither transmission coefficient is zero, however. The space dependent parts of the transmitted waves are

$$\begin{aligned} E &= E_0 \exp[-\mathrm{i}(kz\cos\hat{r} + kx\sin\hat{r})] \\ &= E_0 \exp(-k\beta z)\exp[-\mathrm{i}kx(1+\beta^2)^{1/2}], \quad \cos\hat{r} = \pm\mathrm{i}\beta \end{aligned} \tag{4.40}$$

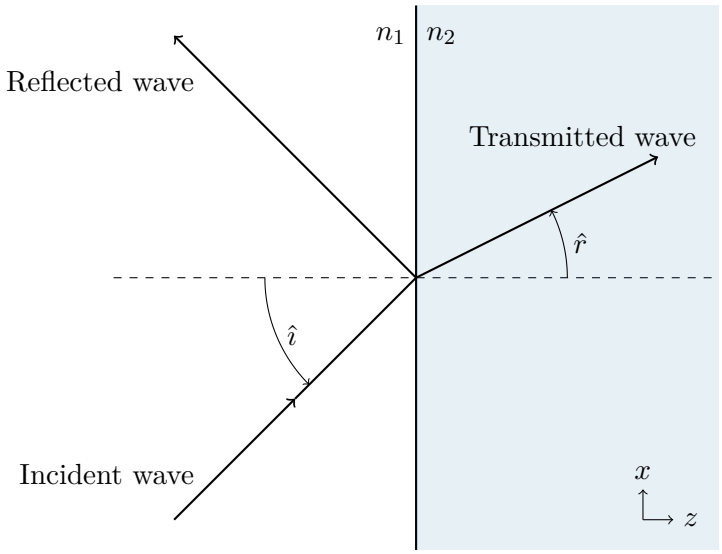

Figure 4.6: *Total internal reflection at the boundary between media of different refractive indices.*

where E is the electric field strength. A small amount of the wave is therefore transmitted beyond the boundary, forming an evanescent wave. Note that the transmitted part of the wave decays to zero as $z \to \infty$, with characteristic length $(k\beta)^{-1}$. We can define a penetration depth, d_p, which is the depth at which the magnitude of the electric field has decayed to 1/e as

$$d_\mathrm{p} = \frac{\lambda}{2\pi\sqrt{n_1^2 \sin^2 \hat{\imath} - n_2^2}}. \tag{4.41}$$

The penetration depth therefore depends on both the angle of incidence and wavelength, and the intensity of the evanescent wave decays exponentially. A more convenient measure of the amount of material probed is the 'effective thickness', d_e, the thickness of material required to give the same absorbance at normal incidence:

$$d_{\mathrm{e},||} = \frac{n_r \lambda_1 (2\sin^2 \hat{\imath} - n_r^2) \cos \hat{\imath}}{\pi(1 - n_r^2)[(1 + n_r^2)\sin^2 \hat{\imath} - n_r^2](\sin^2 \hat{\imath} - n_r^2)^{1/2}} \tag{4.42}$$

$$d_{\mathrm{e},\perp} = \frac{n_r \lambda_1 \cos \hat{\imath}}{\pi(1 - n_r^2)(\sin^2 \hat{\imath} - n_r^2)^{1/2}}. \tag{4.43}$$

The effective thickness is different for waves polarised parallel (||, or p-wave) and perpendicular ($\perp$, or s-wave) to the surface normal, the || case penetrating further. An example calculation is shown in Figure 4.7.

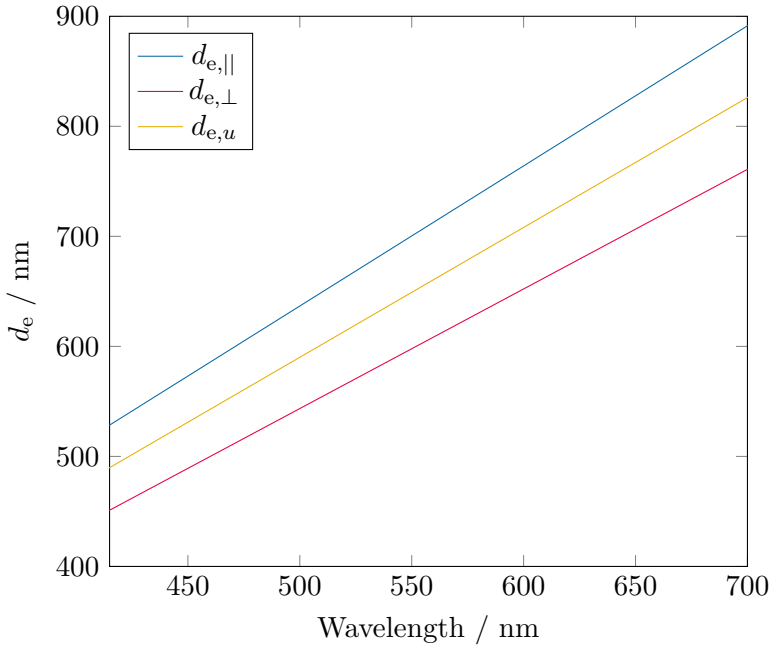

Figure 4.7: *Effective thickness of* $||$, $\perp$, *and unpolarised waves, calculated for* $\hat{\imath} = 72°$, $n_1 = 1.46965$, $n_2 = 1.35$. *The p-wave (electric field aligned parallel to the surface normal) penetrates further into the medium than the s-wave (electric field perpendicular to the surface normal).*

4.2.4.2 Evanescent wave spectroscopy

The short penetration depth of the evanescent wave can be used spectroscopically to probe only those species close to the boundary. An example of this is attenuated total reflection (ATR) spectroscopy. In this method the sample is placed atop a prism, with total internal reflection occurring at the boundary. The evanescent wave can then be used to measure the absorbance of the sample. Since the effective thickness of the absorber, and hence sensitivity of a single pass, is small, multiple total internal reflections can be used to boost the sensitivity of the technique. This can require prisms several centimeters long, and hence relatively large sample volumes. Another possibility is the use of an optical fibre which has been stripped of its cladding. TIR events along the stripped portion can then be used to probe the sample.

Applying the cavity approach to this problem, a prism can be contained within an optical cavity, the TIR being part of the beam path. The light will therefore undergo many TIRs, drastically increasing the sensitivity, and the probed volume can be miniaturised, in principle to microlitres or less.

Pipino *et al.* demonstrated in 1997 that an evanescent-wave CRDS experiment can be designed to probe molecules at surfaces.[146,147] They described both a monolithic ring

resonator, formed of a six-sided polygonal fused-silica cavity, and a Pellin-Broca prism encased in a conventional mirror-cavity used to probe I_2 at the silica surface. Pipino also reported using a four-sided monolithic minicavity to measure the orientation of I_2 at the surface by detecting the || and $\perp$ polarisations separately.[148]

Shaw and coworkers reported a similar experiment in 2003, using a Dove prism to investigate the interfacial absorbance of crystal violet as a function of bulk pH, monitoring at 640 nm.[149] This was extended further in 2005,[150] modelling asdorption isotherms after measuring the interfacial absorbance as a function of bulk concentration.

Li and Zare used polarised EW-CRDS in 2005 to study the orientation of methylene blue at the silica–air interface as a function of surface concentration.[151] They observed a decrease in the average orientation angle relative to the surface normal as the concentration increased, interpreted as the molecules moving from almost flat to the surface at low coverages to 'standing up' as more packed onto the surface. Li and Zare did speculate, however, that an appreciable amount of H-type dimer formed at the higher concentrations studied, and were unable to interpret their orientation-angle data taking the dimer into account.

Li, Zare, and coworkers also went on to study crystal violet at the silica-CH_3CN interface using EW-CRDS.[152] Here they were able to deduce the tilt angle of the molecules sitting on two different types of silanol groups at the interface: they found that the molecules were bound isotropically to the isolated, type I SiO^- sites, but had a distribution biased to adsorption flat to the surface at the vicinal, type II, sites in order to minimise intermolecular repulsion.

EW-CRDS has also been applied to such varied studies as polymer/solvent interaction,[153] ice monolayers,[154] electrochemical deposition[141,155] of $Fe(CN)_6^{3-}$ and $IrCl_6^{3-}$, and the adsorption of colloidal gold nanoparticles.[156]

In 2008 Schnippering and coworkers reported the development of EW-CEAS,[141] combining the broad-band nature of conventional solution phase CEAS with the surface specificity of the evanescent wave. They used this technique to monitor deposition of $IrCl_6^{2-}$ in this paper, and again in 2010.[142] A similar setup has also been reported by Ruth and Lynch, who used a short-arc Xe lamp as the light source to measure metallo-octaethyl porphyrins in acteone films and on fused silica.[157]

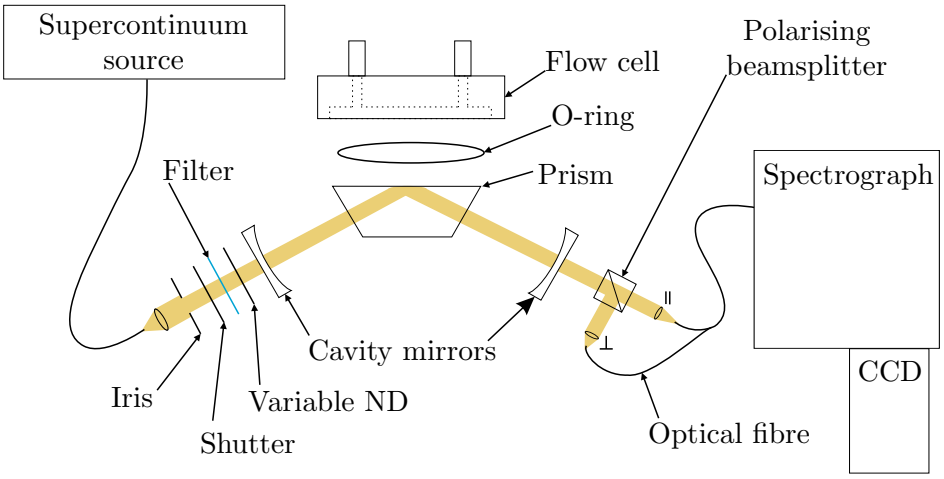

Figure 4.8: *Experimental apparatus for polarised evanescent-wave broad-band CEAS.*

4.2.5 Polarisation-sensitive evanescent-wave broad-band CEAS

One of the major strengths of the EW-CRDS experiments described above is the ability to measure || and ⊥ polarisations separately in order to determine the molecular orientation at the surface. Extending this approach to broad-band CEAS, we present here polarisation-sensitive evanescent-wave broad-band CEAS.

The experiment, as employed in these studies, is shown in Figure 4.8. A supercontinuum source provides pseudo-cw light across the entire visible region. A variable neutral density filter is used to attenuated the brightness of the SCS. Additionally, a blue-coloured filter is placed at the SCS output. The SCS is brighter at the red end of the spectrum, reducing the effective dynamic range of the CCD at the blue end; the blue filter reduces the brightness of the red light, 'balancing' the brightness across the visible region, increasing the usable dynamic range in the blue. The light from the SCS is coupled via an optical fibre into the cavity, formed of two broad-band, spherical mirrors. An intra-cavity fused silica prism folds the light path, total internal reflection occurring at the silica–solvent interface. Either an open sample cell or flow cell can be made atop the prism using an o-ring to seal a PTFE cell to the prism.

After the cavity output mirror, a polarising beamsplitter separates the || and ⊥ polarisations, with subsequent polarisers ensuring the purity of the polarisations. The two polarisations are focussed by achromatic doublet pairs onto two leads of a multichannel optical fibre, and are dispersed by a spectrograph onto separate vertical regions of the CCD detector.

The two polarisations, $||$ and $\perp$ can be monitored separately by binning the two vertical regions of the CCD independently. The observables for the experiment are therefore the intensities for the two polarisations, both in the presence ($I^{||}$ and $I^{\perp}$) and absence ($I_0^{||}$ and $I_0^{\perp}$) of the sample. The extinction for each polarisation is then simply

$$\epsilon c_{||} = \left(\frac{I_0^{||}}{I^{||}} - 1\right) \frac{1}{\ln 10 \cdot l^{||} \cdot \mathrm{CEF}^{||}} \tag{4.44}$$

$$\epsilon c_{\perp} = \left(\frac{I_0^{\perp}}{I^{\perp}} - 1\right) \frac{1}{\ln 10 \cdot l^{\perp} \cdot \mathrm{CEF}^{\perp}}. \tag{4.45}$$

Here both the effective thickness, l, and the cavity enhancement factor are specified individually for $||$ and $\perp$ polarisations. As described in Section 4.2.4.1, the effective thickness depends on the polarisation of the incoming beam. The effective reflectivities, and hence the cavity enhancement factor, will also depend on the incoming polarisation, to a greater or lesser extent depending on the alignment of the cavity. In either case, it is trivial to measure the CEF for each polarisation with a procedure effectively identical to that described in Section 4.2.2.

Using the extinctions for $||$ and $\perp$ polarisations, it is possible to define a molecular orientation parameter. Firstly, defining unit vectors for the two polarisation directions, $\mathbf{E}^{\perp}$ and $\mathbf{E}^{||}$, and for the transition dipole moment, $\boldsymbol{\mu}$,

$$\mathbf{E}^{\perp} = \begin{bmatrix} 1 \\ 0 \\ 0 \end{bmatrix} \qquad \mathbf{E}^{||} = \begin{bmatrix} 0 \\ 0 \\ 1 \end{bmatrix} \qquad \boldsymbol{\mu} = \begin{bmatrix} \sin\theta\cos\phi \\ \sin\theta\sin\phi \\ \cos\theta \end{bmatrix} \tag{4.46}$$

These vectors are shown in Figure 4.9. The extinction, ϵc, for each polarisation direction, assuming ϵ is independent of the orientation of the TDM, is then given by

$$\epsilon c_{\perp} \propto \int_0^{2\pi} \int_0^{\pi} |\mathbf{E}^{\perp} \cdot \boldsymbol{\mu}|^2 \mathrm{P}(\theta, \phi) \mathrm{d}\theta \mathrm{d}\phi \tag{4.47}$$

$$\epsilon c_{||} \propto \int_0^{2\pi} \int_0^{\pi} |\mathbf{E}^{||} \cdot \boldsymbol{\mu}|^2 \mathrm{P}(\theta, \phi) \mathrm{d}\theta \mathrm{d}\phi \tag{4.48}$$

where $P(\theta, \phi)$ is the orientational probability distribution of the molecules. Now, assuming

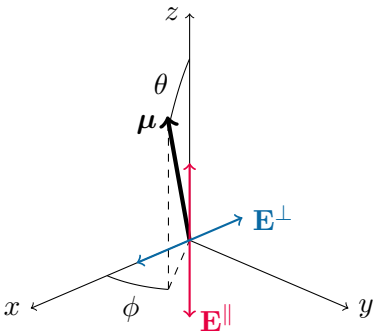

Figure 4.9: *The orthogonal polarisation directions of the evanescent wave,* $\mathbf{E}^{\perp}$ *and* $\mathbf{E}^{||}$*, and the angles* θ *and* ϕ *which parameterise the direction of the transition dipole moment,* $\boldsymbol{\mu}$*, are defined as shown here. The prism surface is in the* x*–*y *plane, and the propagation direction of the light is in the* y*–*z *plane.*

an isotropic distribution of the TDMs in ϕ (i.e. around the surface normal[‡]),

$$\epsilon c_{\perp} \propto \int_0^{2\pi}\int_0^{\pi} \sin^2\theta\cos^2\phi \mathrm{P}(\theta,\phi)\mathrm{d}\theta\mathrm{d}\phi \tag{4.49}$$

$$= \pi\int_0^{\pi} \sin^2\theta \mathrm{P}(\theta)\mathrm{d}\theta. \tag{4.50}$$

$$\epsilon c_{||} \propto \int_0^{2\pi}\int_0^{\pi} \cos^2\theta \mathrm{P}(\theta,\phi)\mathrm{d}\theta\mathrm{d}\phi \tag{4.51}$$

$$= 2\pi\int_0^{\pi} \cos^2\theta \mathrm{P}(\theta)\mathrm{d}\theta. \tag{4.52}$$

This expression cannot be used to extract information about the precise orientational probability distribution. However, using the property of a delta function that

$$\int_{\alpha-\epsilon}^{\alpha+\epsilon} f(x)\delta(x-\alpha)\mathrm{d}x = f(\alpha) \tag{4.53}$$

to evaluate the integral, the expectation value of the angle to the surface normal, $\langle\theta\rangle$, is related to $\epsilon c_{\perp}$ and $\epsilon c_{||}$ by

$$\frac{\epsilon c_{\perp}}{\epsilon c_{||}} = \frac{\tan^2\langle\theta\rangle}{2} \tag{4.54}$$

$$\langle\theta\rangle = \arctan\left(\sqrt{2\frac{\epsilon c_{\perp}}{\epsilon c_{||}}}\right). \tag{4.55}$$

Note that we cannot distinguish between the case where the TDMs all lie at a specific orientation (where $\langle\theta\rangle = \theta$) and a distribution of TDMs with that expectation value. For an isotropic distribution of TDMs, $\langle\theta\rangle = 54.7°$ (the magic angle), and $\epsilon c_{\perp} = \epsilon c_{||}$. In the

[‡]This assumption is justified on the basis that there is no inherent directionality in the plane of the fused silica prism surface to induce long range order within that plane.

case that the orientation of the TDM within the molecular framework is known, it is possible to specify the orientation of that molecular axis.

The advantage of the CEAS experiment over CRDS is the ability to monitor all visible wavelengths simultaneously. This approach means that it is possible to monitor multiple adsorbing species, the change in the shape of absorption bands over time, as well as the molecular orientation of each species, or any other spectral feature, in real time. This comes at the cost of time resolution (tens of ms vs µs for CRDS), as well as the necessity of calibration.

A note about ϵc Equations 4.44 and 4.45 above are both written in terms of ϵc, the 'attenuation coefficient'; they could, of course, be reformulated in terms of the more familiar A, the unitless 'absorbance'. However this has two drawbacks. Firstly, the effective thickness of the evanescent wave, l, depends on wavelength (Figure 4.7), distorting the shape of the absorption band. This may or may not be important depending on the application. Secondly, the effective thickness of the evanescent wave is $\sim 10^4$ times smaller than the path length typically used in a single-pass experiment. Handling the data in terms of ϵc normalises the data with respect to l, and allows direct quantitative comparison of EW-CEAS and data taken by conventional single-pass spectrometry (for instance, a doubling of ϵc in the evanescent wave compared to the bulk corresponds to a doubling of the effective concentration at the surface). It is therefore much more convenient to use ϵc as the measure in most cases where direct comparison is advantageous.

4.3 The silica-water interface

4.3.1 The silica surface

The broad-band nature and surface-sensitivity of EW-CEAS make it trivial to monitor differences in the absorption bands of molecules at the interface as compared to in bulk solution, as well as track real-time changes in the spectra. An understanding of the nature of the interface is therefore crucial in interpreting EW-CEAS data.

The surface of a piece of silica formed under normal conditions consists principally of siloxane linkages (Si–O–Si) and silanol groups (Si–OH). The silanols at the surface exist as both isolated and vicinal groups, with populations of 19 and 81% respectively.[158,159] Isolated silanols are $>$ 5.5 Å from each other. In contrast, the vicinal groups are close enough that they can form hydrogen bonds either directly with their neighbours ($<$ 3.3 Å,

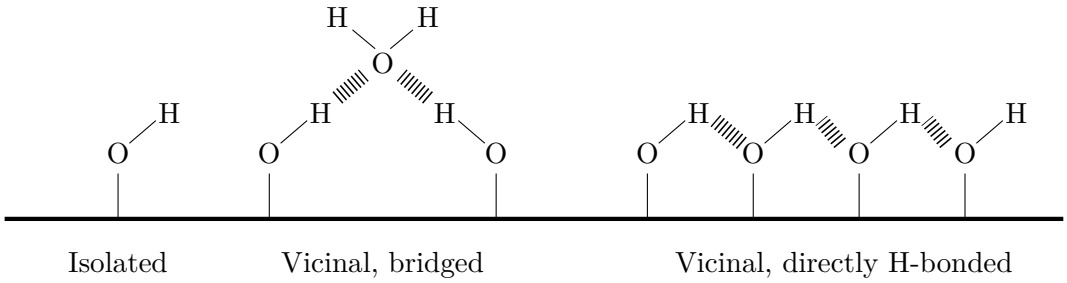

Figure 4.10: *Different types of silanol groups found at the silica surface in H_2O. The pK_a is 4.9 and 8.5 for isolated and vicinal sites, respectively.*

46%) or via a bridging water molecule (3.3–5.5 Å, 35%). These configurations are shown in Figure 4.10.

The isolated silanol sites have a pK_a of 4.9, and can be deprotonated at neutral pH, giving the surface a negative charge.[158] The pK_a of the vicinal groups is higher, at 8.5.

The isolated silanols were further categorised into two types by Dong *et al.*, who used crystal violet in acetonitrile as a probe in second harmonic generation studies.[160] They were able to discern two types of isolated silanol groups by modelling the adsorption isotherm of crystal violet onto the surface. Type-I groups are surrounded by a large empty area ($\geq$120 Å), and Dong proposed that crystal violet adsorbs flat on-top of this type of silanol. Type-II groups include the rest of the isolated silanols, with a tilted adsorption geometry for crystal violet due to repulsion from neighbouring silanol groups. Later work by Fan and coworkers showed, however, that at low concentrations in acetonitrile, crystal violet adsorbs isotropically to type-I sites, with the molecules aligning laterally at type-II sites as the concentration is increased.[152]

4.3.2 Aggregation at the surface

One process at the silica-solvent interface which might be monitored by EW-CEAS is aggregation.

Aggregation of dyes is common at the solid-liquid interface, modifying both the local concentration and spectral properties of the dye. Spectral shifts due to aggregation can be categorised into two types: H-type aggregation, which corresponds to a blue-shift in the absorption bands, is caused by face-to-face stacking; J-type aggregation, which corresponds to a red-shift in the absorption bands, is due to end-to-end stacking of the molecules.

The shifts can be understood within the context of molecular exciton theory.[161,162] Figure 4.11 is an energy level diagram for H- and J-type dimers as compared to the monomer.

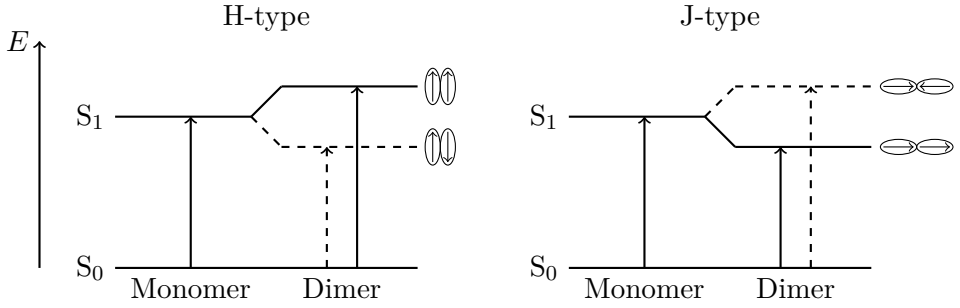

Figure 4.11: *Energy level diagram for H- and J-type aggregates. The S_1 level is split by the inter-molecular potential, with the transition-moment being almost zero for the antiparallel dipole case. Adapted from Kasha.*[161]

The intermolecular potential causes a splitting of the S_1 state: for H-type aggregates the parallel dipole exciton state is the higher energy one; for J-type aggregates, the parallel case is the lower energy level. The transition moment for the dimer is the vector sum of the individual transition dipole moments; since, in order for the transition to be allowed, the perturbation of each molecule should be in-phase, transition to the antiparallel state is forbidden, while transition to the parallel case is allowed. This, combined with the relative energies of the exciton states, corresponds to a blue-shifting of the absorption band for H-type aggregates, and a red-shift for J-type.

Figure 4.12 shows how the relative energy of the two levels varies with stacking angle, α. The absorption band is blue-shifted as the dimers move from the end-on-end configuration to face-to-face.[163]

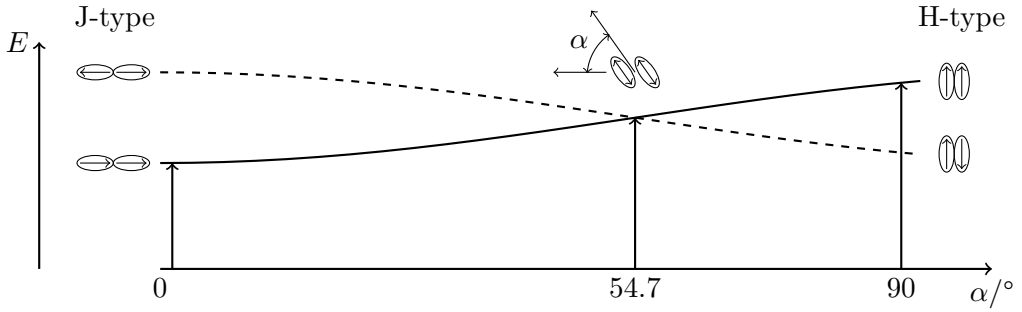

Figure 4.12: *The relative energies of parallel and antiparallel dipole configurations vary with stacking angle, α. Adapted from Severino.*[163]

Manufacturer	Layertec GmbH
Wavelength range	400–800 nm
Reflectivity	99.85–99.98
Radius of curvature	500 mm
Diameter	12.7 – 0.1 mm
Thickness	6.35 ± 0.1 mm
Wedge	<5 min
Front flatness	$\lambda/4$
Back flatness	$\lambda/10$
Back coating	AR < 1%
Order	A-30657/8
Batch	R0209025

Table 4.1: *Specifications of the cavity mirrors used in these experiments.*

4.4 Experimental considerations

4.4.1 Cavity mirrors

The cavity mirrors used here are broad-band dielectric mirrors, that provide a high degree of reflectivity over the entire visible region. These are made by depositing multiple layers of dielectric coatings onto a substrate, with interference between layers creating reflectivity at particular wavelengths. The mirrors are engineered such that the reflectivity is within a certain range over the specified wavelength region, and due to this, the reflectivity spectrum is not flat, but has a large amount of structure. This mirror structure is taken into account in the cavity enhancement factor. The specifications of the mirrors used in these experiments are shown in Table 4.1.

4.4.2 Prisms

The prisms used herein were 'dual-cut' from fused silica, with all four side faces cut at an angle to the top face. This design provides optical access on the non-cavity axis, which can be used to photoexcite the sample via an evanescent wave, hence minimising photodegradation of the sample. In these experiments, the long axis of the prism was designated the cavity axis; stringent tolerances were specified for these faces, such that their normals lie in the same plane. The dimensions of the prisms are given in Figure 4.13. The cleanliness of the prism is crucial to obtain the highest CEF, as well as for repeatability of adsorption to the surface. Three faces of the prism form part of the cavity, and any scattering from these surfaces will contribute to the cavity losses. Additionally, the top surface forms one half of the studied interface, and the condition of the surface

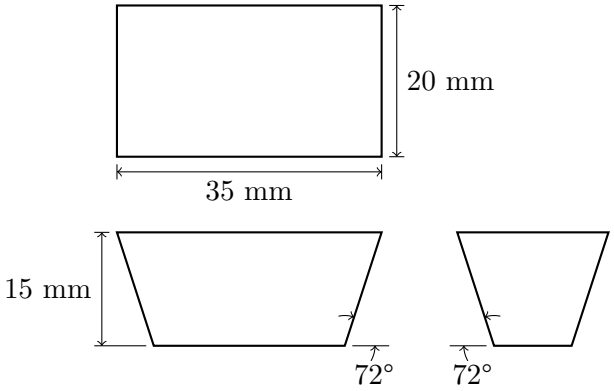

Figure 4.13: *Dual-cut prism as used in these experiments. Manufacturer: Tower Optical Corporation.*

(contamination, surface roughness, charge, etc) may have a large role in determining the adsorption properties.

This effect of the surface condition on measurements has been observed by Mazurenka *et al.*, who studied the deposition of citrate stabilised colloidal gold nanoparticles at the silica surface.[156] They did not observe interfacial adsorption of the nanoparticles onto new optical-quality prisms that had been cleaned using plasma ashing; they did however observe some adsorption onto prisms which were shown by subsequent AFM imaging to be significantly scratched or contaminated. They speculated that previously reported multilayer adsorption of citrate stabilised AuNPs onto silica[164] could be due to initial deposition into scratches, that acted as nucleation sites for further adsorption.

Before each set of measurements presented here the prism was cleaned by wiping with fresh optic cleaning tissues moistened with spectroscopic grade methanol, rinsed with Milli-Q grade water, and plasma ashed. Care was taken throughout the procedure not to handle the prism by the top or cavity axis faces to prevent contamination.

4.4.3 Supercontinuum source

The cavity light source used in this thesis is a Fianium SC400-4 supercontinuum source (SCS). This is a laser light source that produces broad-band light using non-linear optical processes in a laser-pumped photonic crystal fibre.

The Fianium SCS produces light between 400 and 2600 nm, with 4 W over the entire spectrum. In these experiments, the SCS was coupled via optical fibre to a 'splitter' (Fianium Splitter-950). This was used to select a portion of the output (400 to 950 nm), the rest being discarded. Over this region the power is >600 mW.

The SCS is a pseudo-cw source, operating at a pulse rate of 40 MHz, with a 6 ps fundamental pulse length. The shortest integration time of the CCD detector being 4 ms, this is treated as effectively cw.

An acousto-optical tunable filter (Fianium AOTF) was also used in conjunction with the SCS to give narrow band output which could be used to align the cavity. The experiment could then be switched over to the full visible output of the SCS while maintaining alignment by switching the optical fibres from the AOTF to the 'splitter'.

The SCS light was passed through a blue glass filter (Thorlabs FGS900S) before entering the cavity to reduce the brightness of the red end of the visible, as discussed in Section 4.2.5.

4.4.4 Spectrograph and CCD

After exciting the cavity, the light is split into $\parallel$ and $\perp$ polarisations by a polarising beamsplitter (Thorlabs CM1-PBS251), with the polarisation purity being ensured by two Glan-Taylor polarisers (Thorlabs GT10-A) placed at the beamsplitter outputs.

The beams are each focussed by an achromatic doublet pair onto the end of a two-way fibre bundle (Andor SR-OPT-8020). This fibre bundle has two 'legs' as inputs, with the cores of the legs being arranged into two collinear groups at the output. The output can then be positioned at the slits of a spectrograph such that the light from each leg is dispersed onto the CCD in the wavelength (horizontal) direction normally, but separated vertically. The binning of the CCD can be controlled such that the spectrum from each leg, therefore each polarisation, is recorded independently (in 'multi-track' mode).

The spectrograph was an Andor Shamrock 303i. This 303 mm spectrograph has a wavelength resolution of 0.1 nm, much higher than is necessary for these experiments.

An Andor Newton 902 CCD camera was the detector. The Newton camera is a full-frame CCD, meaning that the bins remain sensitive to light while being read out. A mechanical shutter was therefore placed before the cavity to block the SCS during read-out, and prevent the two polarisations 'mixing' together when using the multi-track binning mode.

The maximum cycle rate for the CCD is 250 Hz; in most experiments in this thesis any kinetics were much slower than this, and a longer integration time was used to improve the signal to noise ratio.

4.4.4.1 Optimum integration time

In optimising the signal to noise ratio of the experiment, it is necessary to consider the integration time of the acquisition. Consider an experiment where a total of N shots are acquired, and the number of shots to integrate over to give us the best signal to noise ratio is to be found. The standard deviation over all shots taken individually is σ

$$\sigma = \sqrt{\frac{1}{N}\sum_{i=1}^{N}[x_i - \mu]^2} \tag{4.56}$$

where μ is the mean. The standard deviation of the measurements can be reduced by integrating over groups containing a number of shots, y. In this case, the limit of detection is then given by the standard deviation over the integrated groups, σ_g,

$$\sigma_g = \sqrt{\frac{1}{M-1}\sum_{i=1}^{M}[x_i(y) - \mu]^2} \tag{4.57}$$

where $M = N/y$. When white noise dominates, the spread of the measurements decreases with $\sqrt{y}$ as expected. However, as the integration time is increased, long term drift in the measurement will serve to introduce additional errors. The optimum integration time for a particular experiment is a balance between the high-frequency noise and low frequency drift, and can be determined using the Allan variance, σ_A[165, 166]

$$\sigma_A = \sqrt{\frac{1}{2(M-1)}\sum_{i=1}^{M-1}[x_{i+1}(y) - x_i(y)]^2}. \tag{4.58}$$

The Allan variance is a measure of the difference between adjacent measurements, and as such captures long term drift. As the integration time is increased, the Allan variance will decrease as the high-frequency white noise is averaged. At some point, long term drift in the experiment will cause the difference between adjacent integration periods to increase, and the Allan variance will also increase, indicating that the long period drift is coming to dominate the noise. The standard deviation and Allan variance for the experiment in this thesis are shown in Figure 4.14.

The Allan deviation decreases with increasing integration time between 4×10^{-3} and 5×10^{-2} s (the plot is a straight line of gradient -0.5, indicating white-noise is dominating). However, although the standard deviation continues to decrease with increasing integration time, the Allan variance has a minimum at between 0.05 and 0.5 s, depending

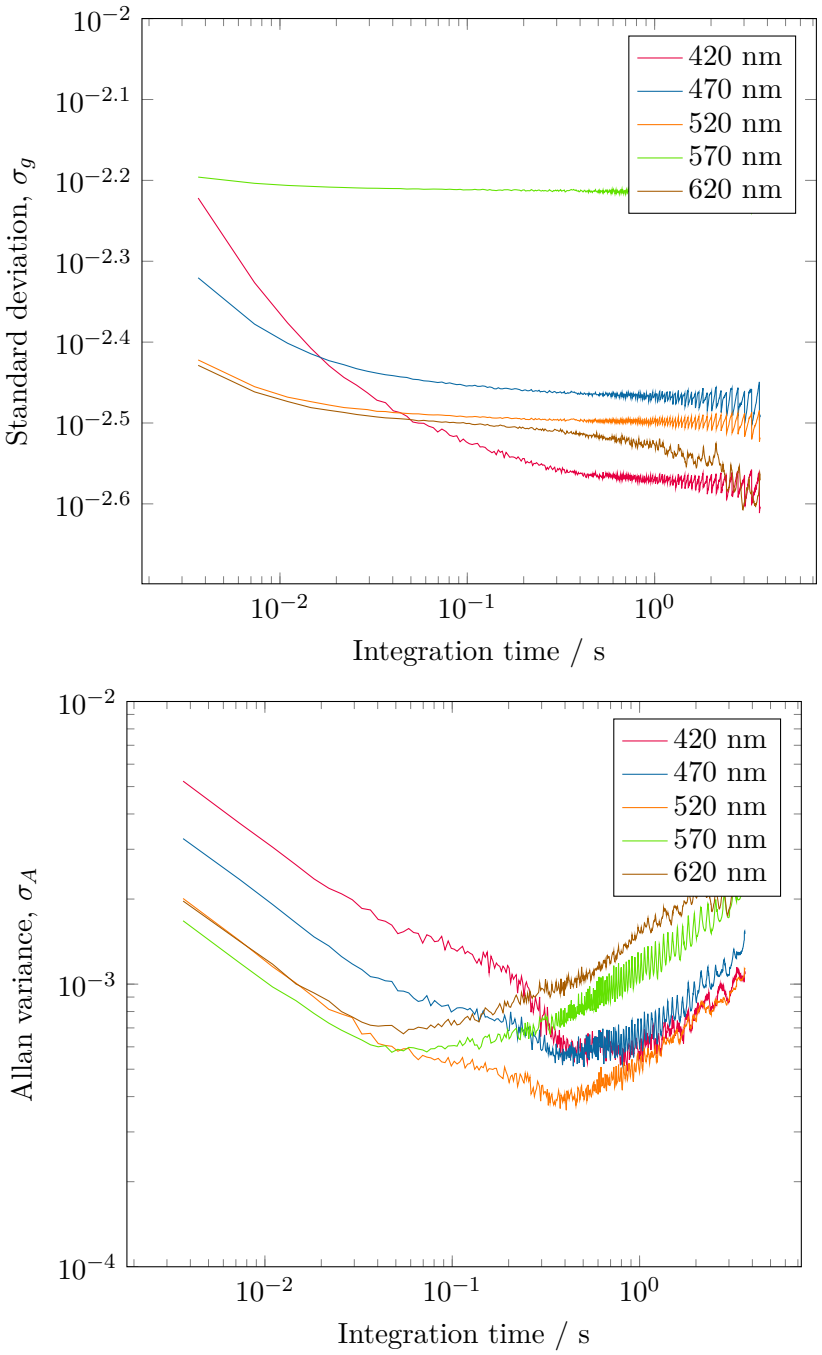

Figure 4.14: *Standard deviation and Allan variance for this instrument, plotted as a function of integration time. Based on these data, an integration time of between 0.1 and 1* s *was typically used.*

on wavelength. No additional improvement in the signal to noise ratio can therefore be gained by increasing the integration time above this, as long term drift of the experiment dominates the noise.

4.4.5 Cavity calibration

In order to measure ϵc quantitatively, the effective mirror reflectivities, which include the effect of intracavity losses, must be known. CEAS therefore requires calibration, normally using a sample of known absorbance, or by CRDS. The accuracy of this calibration is key to obtaining quantitative measurements from the technique.

In the experiments performed here, a mixture of dyes of known absorbance, 1 mM amaranth with 1 mM acid green 25, was used to calibrate the cavity. It was found that aggregates or other particulate matter in the solution interfered with the calibration measurement, so the dye mixture was filtered through a 0.2 µm syringe filter and stored in the dark. The spectrum ($\epsilon(\lambda)c$) of the filtered mixture was taken using a UV-vis spectrophotometer, and the CEF could therefore be found from the measured $I_0(\lambda)$ and $I(\lambda)$.

An example of several measurements of the cavity enhancement factor for the same cavity alignment is shown in Figure 4.15. Repeated measurement of the CEF shows a mean standard deviation of 1.4% across the visible region. This uncertainty will translate directly into the calculated ϵc.

The optimum integration time for the experiment, as discussed in Section 4.4.4.1, was found to be between 0.1 and 1 s depending on wavelength. The Allan variance captures the long term drift of the output intensity of the cavity between the sample-free, I_0, measurement, and the subsequent I measurements. However, there is also a contribution to the long term drift from the effective reflectivities of the mirrors. Any process which causes these to change (drift in the cavity alignment, dirt on any intracavity element, etc) will induce a drift in the CEF over time, reducing the accuracy of quantitative measurements. A new CEF calibration was therefore taken after each realignment of the cavity, typically taking place after cleaning of the prism.

4.4.6 Limit of detection

Following from Equation 4.32, the limit of detection of the CEAS experiment is[122]

$$\epsilon c_{\min} = \frac{1}{\ln 10 \cdot \mathrm{CEF} \cdot l} \left(\frac{\Delta I_{\min}}{I_0} \right) \tag{4.59}$$

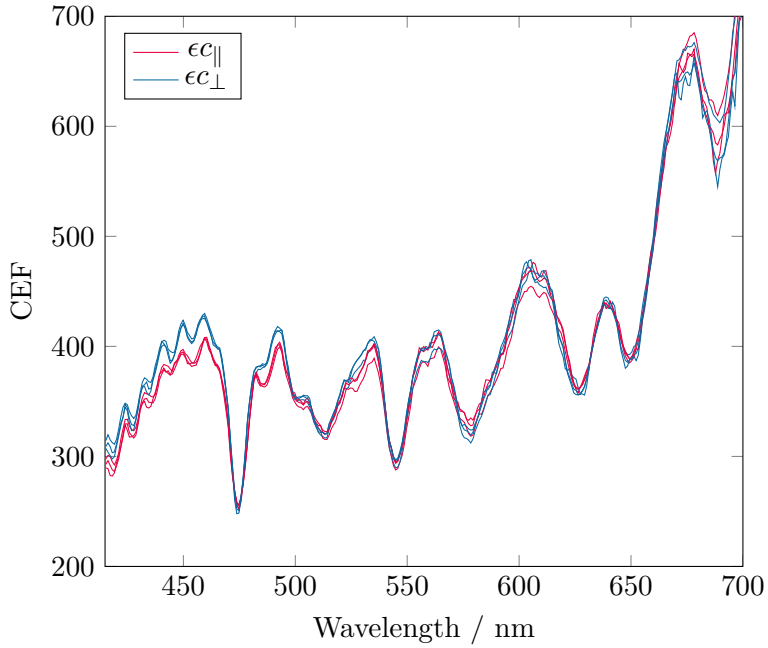

Figure 4.15: *Repeated measurements of the cavity enhancement factor using a non-adsorbing dye mixture of known absorbance (1* mM *amaranth and 1* mM *acid green 25). The CEF shows an average standard deviation of 1.4% across the visible region.*

where ΔI_{min} is the minimum detectable change in the output intensity. Comparing this to the equation for single-pass spectroscopy,

$$\epsilon c_{\text{min}} = \frac{1}{\ln 10 \cdot l} \left(\frac{\Delta I_{\text{min}}}{I_0} \right) \tag{4.60}$$

the cavity has reduced the limit of detection by a factor of CEF. In the cavity experiments presented here, noise on the output intensity dictates the minimum detectable change in output intensity. Defining this as three times the noise level, the minimum detectable change in ϵc for this experiment over the spectrum as a whole is around 0.05 cm^{-1}. This corresponds to a minimum detectable absorbance of around 3×10^{-6}, comparable to other CRDS and CEAS experiments.[167] An example of a spectrum with an attenuation coefficient of approximately 0.05 cm^{-1} is shown in Figure 4.16.

It should be noted that, in the condensed phase, the limit of detection will not continue to decrease linearly with increasing mirror reflectivity. Scattering losses due to the prism and solution are, per pass, effectively fixed. For increasingly weak absorbers, the intracavity losses will eventually be dominated by scattering, and no increase in signal-to-noise ratio will be gained by increasing the number of passes.

The maximum detectable ϵc is in practice limited by the approximation made in deriv-

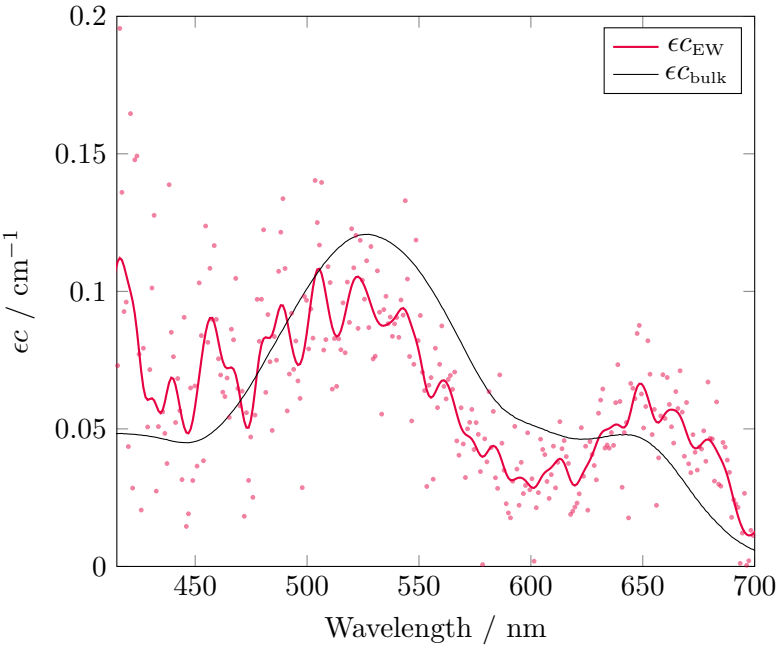

Figure 4.16: *Example of a sample (5* µM *amaranth and 5* µM *acid green 25) with small ϵc, demonstrating the limit of detection of the EW experiment. The data has been smoothed for clarity using a moving average filter (span =* 15 nm*).*

ing Equation 4.32 (that $R \approx 1$ and $\alpha \approx 0$). For mirrors with $R = 0.999$, this approximation holds within 0.15% for $I_0/I < 100$, which corresponds to an ϵc of around 10^5 for CEF = 600 to 200. This approximately 100 times larger than the highest value of ϵc measured in these experiments.

4.4.7 Angular resolution

By measuring the intensity of the cavity output polarised parallel and perpendicular to the surface normal it is possible to calculate an expectation value for the angle of the transition dipole moment relative to the surface, $\langle\theta\rangle$, using Equation 4.55. The angular resolution of this measurement is limited by the birefringence and optical activity of the cavity, which serve to cause rotation of the polarisation within the cavity.

Dielectric mirrors have an intrinsic birefringence caused by the mirror structure, ranging from 10^{-7} to 10^{-3} rad per reflection.[168] Additionally, mechanical and thermal stress can induce additional birefringence in the mirrors. Birefringence in fused silica prisms has also been observed by EW-CRDS; Li[169] observed an angular dependence of the ring-down time, but did not investigate the origin of this effect.

In addition to these effects, the cavity itself possesses optical activity. The phase shifts

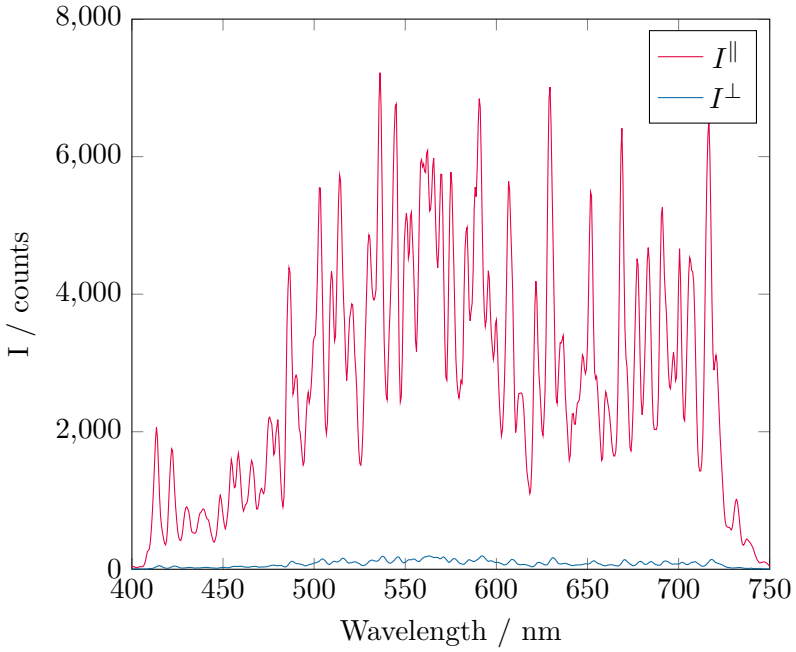

Figure 4.17: *$I^{||}$ and $I^{\perp}$ measured with the cavity input beam being plane-polarised parallel to the surface normal. A small amount of light is detected at the cavity output polarised perpendicular to the surface normal (3.25% over 400–750* nm*), indicating some optical activity in the cavity.*

upon total internal reflection, δ, for $||$ and $\perp$ polarisations are given by[170]

$$\tan\left(\frac{\delta^{||}}{2}\right) = \frac{n_r(n_r^2\sin^2(\hat{r}-\hat{r}_c)-1)^{1/2}}{\cos(\hat{r}-\hat{r}_c)} \tag{4.61}$$

$$\tan\left(\frac{\delta^{\perp}}{2}\right) = \frac{(n_r^2\sin^2(\hat{r}-\hat{r}_c)-1)^{1/2}}{n_r\cos(\hat{r}-\hat{r}_c)} \tag{4.62}$$

where $\hat{r}_c$ is the critical angle and the other symbols are as defined in Section 4.2.5. The multitude of optical paths through the cavity will therefore serve to each introduce their own phase shift, and if the beam is plane-polarised before entering the cavity, it will exhibit a range of polarisations at the cavity output depending on the balance of the above factors. This is shown in Figure 4.17, where the mean ratio $I^{\perp}/I^{||}$ is 0.0325 over the range 400 to 750 nm for an input plane polarisation parallel to the surface normal.

The uncertainty on $\langle\theta\rangle$ depends on the per pass absorbance and angular distribution of the transition dipole moments, and is therefore difficult to quantify in a general way. It can be said, however, that the difference between the measured expectation value for the angle of the transition dipole moment and the magic angle (*i.e.* $|\langle\theta\rangle - 54.7°|$) is a lower bound, since the effect of any optical activity in the cavity is to make this measure appear

more isotropic.

An estimate of the statistical uncertainty in the measurement can be obtained from repetition of any particular experiment. For the work presented here studying crystal violet at the bare silica interface (Section 4.8.3), the value of $\langle\theta\rangle$ was found to be repeatable to between 0.5 and 2°. The uncertainty that can be attributed to the instrument is difficult to estimate, however, without an independent measurement of $\langle\theta\rangle$.

4.5 Cresol red

Cresol Red (*o*-Cresolsulfonephthalein) is the triarylmethane dye shown in Figure 4.18. It is a pH indicator (pKa = 8.2), with a colour change from yellow to red at pH 7.2–8.8. A solution made up in milli-Q grade water was observed to be an orangey-red colour. Measuring a flowing (5 $\mathrm{mL\,min^{-1}}$) solution of cresol red by EW-CEAS, a sharp rise in ϵc was observed upon introducing the sample into the cell, with no further increase in ϵc being seen over time (Figure 4.19). The initial rise in ϵc (Figure 4.19, inset) occurs over the course of $\sim$ 0.7 s, and can be attributed to the time taken for the solution front to sweep across the probed region.

The spectrum of the dye is shown in Figure 4.20. $\epsilon c_{||}$ and $\epsilon c_{\perp}$ are equal, and very close to the bulk measurement taken by a single-pass UV/vis spectrophotometer. This indicates that the dye monomers are not adsorbing to the surface, and the EW-CEAS experiment is simply probing a thin, isotropic, layer of solution next to the interface.

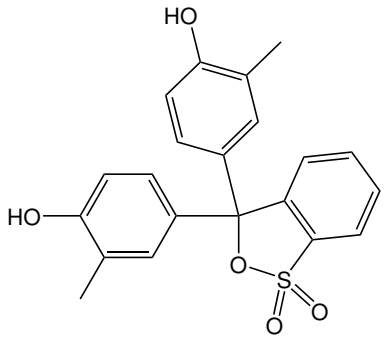

Figure 4.18: *Structure of Cresol Red.*

Of minor note in the spectrum are two small bands in addition to the one observed in the bulk spectrum. Firstly, there is a band between 500 and 600 nm, most likely due to the deprotonated form of the dye.[171] Secondly, the small band between 620 and 670 nm is a possible indication of J-type aggregation occurring at the surface. This band, however, is only a minor component of the total spectrum, and interpretation of its precise nature is therefore difficult.

The broad lack of adsorption behaviour for cresol red at the interface means that the EW-CEAS experiment is not necessarily any more useful than a 'bulk' single-pass experiment. The fact that the value of ϵc matches for bulk and EW experiments does, however, confirm that the experiment is capable of quantitative measurement.

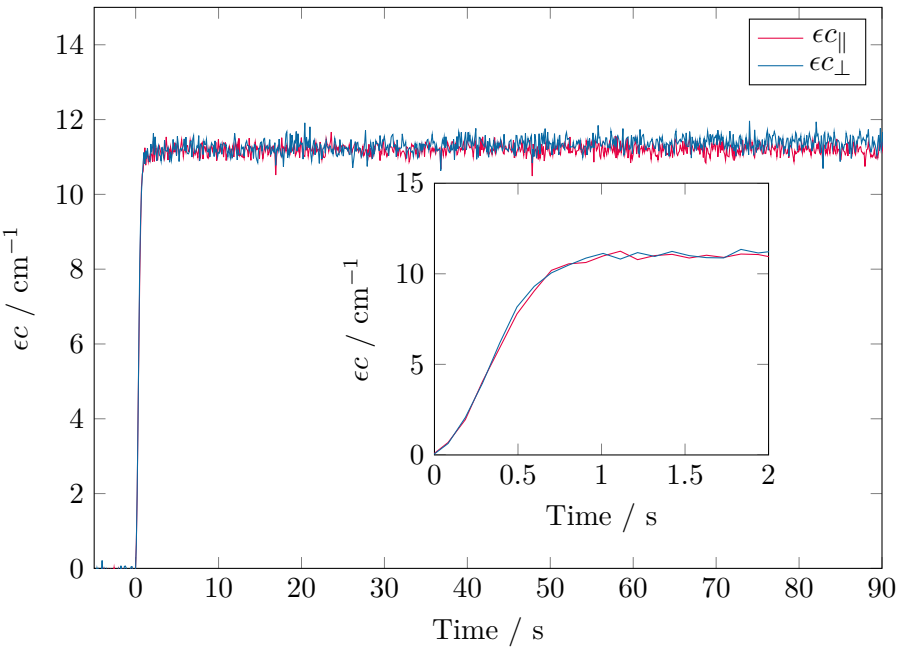

Figure 4.19: *Kinetic trace of cresol red (flow = 5* $\mathrm{mL\,min^{-1}}$*) measured by EW-CEAS, shown at 450* nm*. The inset shows the initial rise in ϵc, taking place over approximately 0.7* s*, commensurate with the estimated rise time for this flow rate. The sharp rise and subsequent unchanging, equal values of $\epsilon c_{\parallel}$ and $\epsilon c_{\perp}$ indicate that cresol red does not adsorb to the silica surface.*

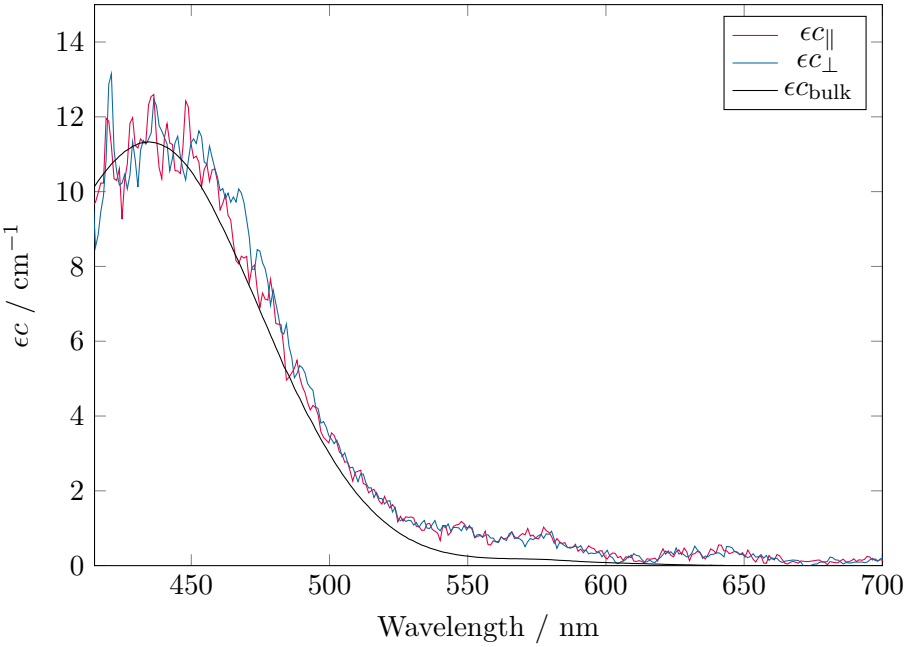

Figure 4.20: *Spectra of cresol red as measured by EW-CEAS and a conventional UV-vis spectrometer. The almost identical spectra add further evidence that cresol red is not adsorbed.*

4.6 Gold nanoparticles

Colloidal gold nanoparticles (AuNPs) are submicron sized particles of gold suspended in a solvent, commonly water. They can be produced by reduction of $HAuCl_4$ by citric acid, which is both the reducing agent and acts to charge stabilise the particles, with the size of the particles being controlled by the synthesis process. The colour of the resulting solution depends strongly on the size and aggregation of the particles, ranging from red to blue. The varying colour of the particles is due to two bands in the visible spectrum - the 5d–6sp cluster band of bulk gold, and the localized surface plasmon resonance (LSPR) centred around 525 nm.

The localized surface plasmon resonance is a coherent oscillation of electrons in the conduction band induced in nanoparticles smaller than the wavelength of the photon. For gold, this oscillation occurs in the visible region. The position of the LSPR peak, as well as the relative strength of the LSPR and cluster bands is determined by the size and shape of the particles, their aggregation state, and by environment of the particles, including the presence of ions and molecules.[172]

AuNPs have a large variety of uses as chemical and biological colorimetric sensors, ranging from metal ions and small molecules, to oligonucleotides and proteins.[173] A wide range of techniques such as FRET, electrochemical detection, quartz crystal microbalances, and SERS have been employed in similar sensors employing AuNPs.[174] In some cases, control over the structured deposition of nanoparticles is desired (for instance, into arrays).[175,176]

Mazurenka *et al.* studied solutions of 5 and 20 nm gold nanospheres depositing onto poly-L-lysine functionalized silica surfaces using EW-CRDS. They found that 5 nm particles readily and irreversibly adsorbed to the functionalized surface, forming a monodispersed submonolayer.[156]

The adsorption process can also be monitored by EW-CEAS, as is shown here. The silica surface of the prism was coated with poly-L-lysine by placing a solution of 1 mg mL^{-1} PLL in water onto the prism surface for 20 minutes prior to the experiment. The adsorption of AuNPs onto the PLL was then measured by removing the PLL solution with a pipette and replacing it with a solution of 5 nm citrate-stabilised gold nanoparticles ($\sim 5.5 \times 10^{12}$ particles mL^{-1}). This solution was left quiescent on the surface for the remainder of the experiment.

Figures 4.21 and 4.22 show the kinetic trace and spectrum of the gold nanospheres

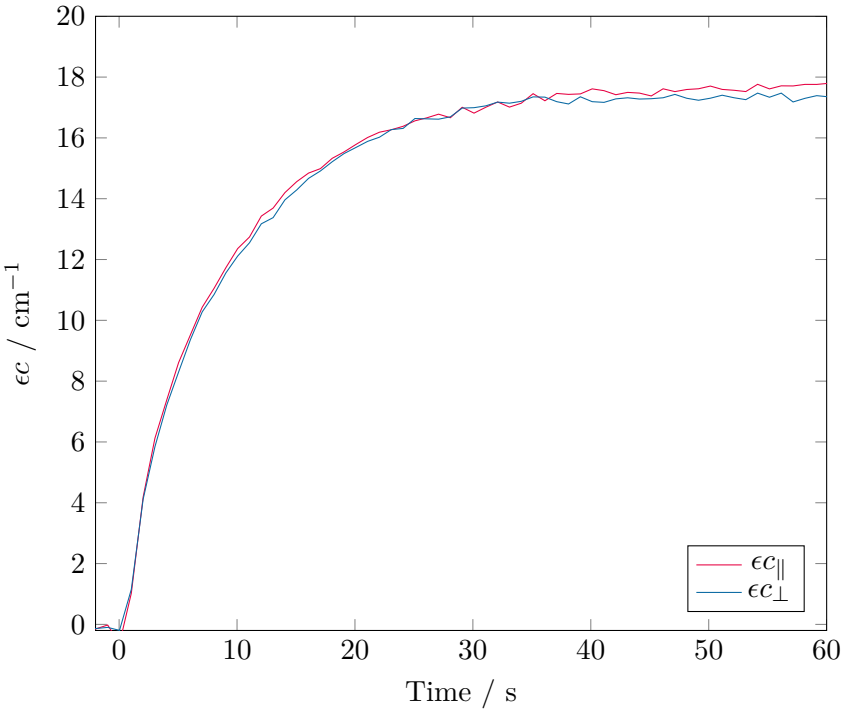

Figure 4.21: *Kinetic trace of 5* nm *gold nanspheres adosorbing onto a poly-L-lysine functionalized silica surface from quiescent solution, measured at 520* nm.

adsorbing onto the surface. The kinetic trace observed here is similar to that observed by Mazurenka, with the nanospheres adsorbing over the course of minutes until a maximum absorbance is reached. The kinetics as measured at 420 nm (bulk band) and 520 nm (LSPR band) are identical within the noise. In these experiments, the interfacial coverage corresponds to approximately 4×10^{-4} of a monolayer, around three times lower than observed by Mazurenka.[156]

Figure 4.22 shows a comparison of the evanescent-wave (left axis) and bulk (right axis) spectra. The magnitude of ϵc in the two cases is different, being larger in the EW case due to adsorption of the NPs onto the surface. The shape of the spectra match quite well, indicating that the particles are monodispersed; if aggregation were occurring, the LSPR peak would be expected to shift to longer wavelengths. For the EW spectra, ϵc for each polarisation is identical within the signal to noise.

The relatively slow adsorption of the AuNPs is well suited to monitoring by this technique, with the broad-band nature making it possible to study aggregation properties, or for colourimetric measurement of analytes at the silica surface. Furthermore, the ability to measure ϵc in an orientation sensitive manner could be applied to, for instance, gold nanorods, which show differences between longitudinal and transverse surface plasmon

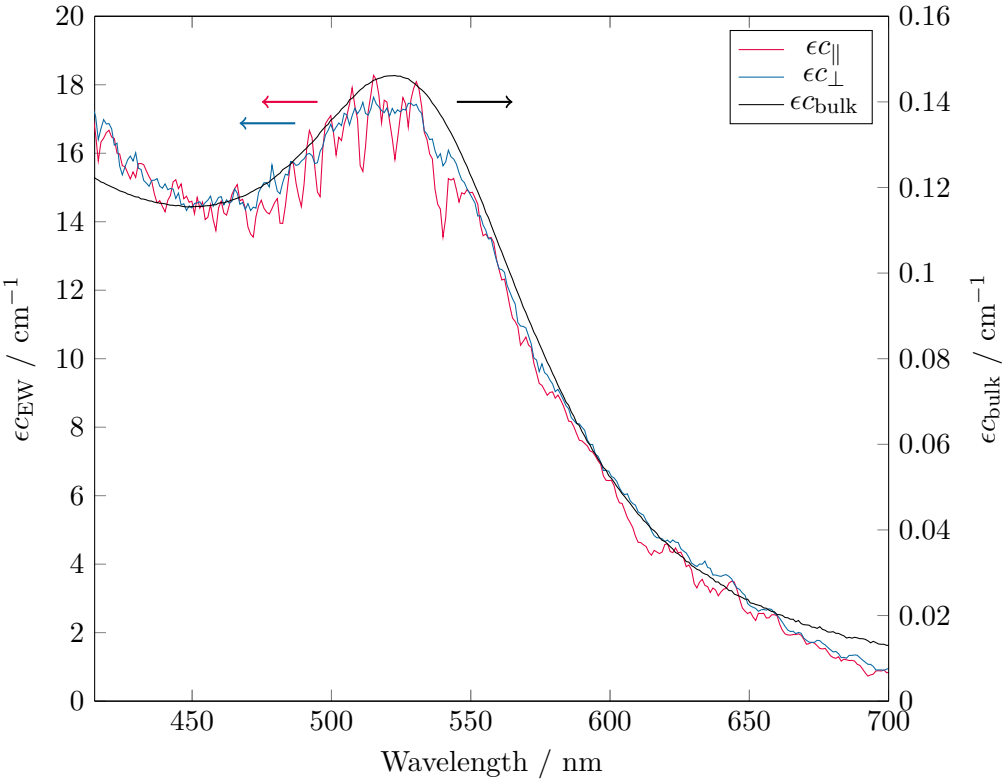

Figure 4.22: *Comparison of the spectra of 5* nm *gold nanospheres on a poly-L-lysine funcitionalized silica surface (left axis) and in the bulk (right axis). Note the almost identical values of* $\epsilon c_{||}$ *and* $\epsilon c_{\perp}$ *for the EW experiment.*

resonances.[177]

4.7 Methylene blue

Methylene blue (MB) is a tricyclic aromatic dye with the structure shown in Figure 4.23. MB has a wide variety of uses, including as a redox indicator and a biological stain. It is also commonly used in the textile industry;[178] much work has therefore been carried out studying the adsorption process, with regard to removal of MB from waste-water.[179–183]

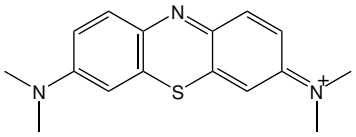

Figure 4.23: *Structure of methylene blue.*

4.7.1 Bulk absorption spectra

The bulk absorption spectra of methylene blue in ethanol and water are shown in Figures 4.24 to 4.27.

In ethanol, methylene blue exists as the monomer only. The shape of the bulk absorption spectrum (Figure 4.24) does not change with concentration, as can be seen clearly in the normalised spectra (Figure 4.25).

In water the spectrum can be described by a monomer-dimer equilibrium at concentrations below 1.25×10^{-4} M.[184] The monomer spectrum has a peak centred at 664 nm, with a shoulder at ~ 600 nm. The dimer spectrum has a major peak at 600 nm, with an additional minor peak at 696 nm. The shift from monomer to dimer as the concentration is increased can be seen in the normalised spectra (Figure 4.27) with the dimer peak growing in at 600 nm. Between 1 and 26 µM there is a minor increase in the amount of dimer present in the bulk solution; the monomer remains the dominant species, however.

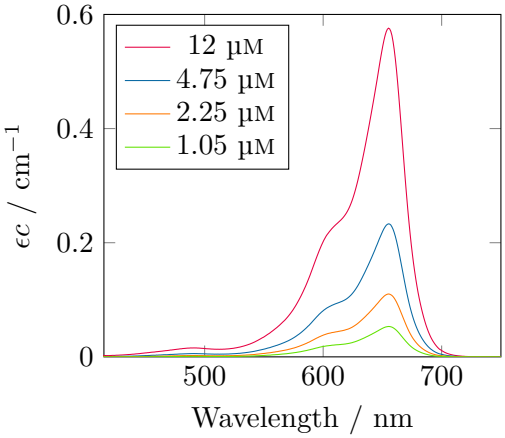

Figure 4.24: *Bulk absorption spectrum of MB in EtOH at various concentrations.*

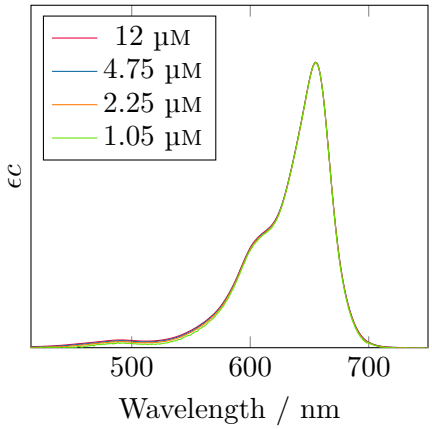

Figure 4.25: *Bulk absorption spectrum of MB in EtOH, normalised to the main peak.*

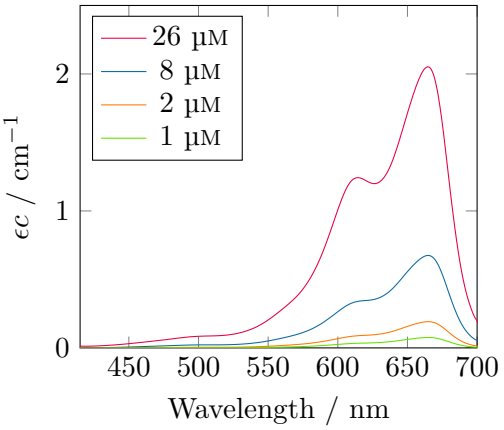

Figure 4.26: *Bulk absorption spectrum of MB in water at various concentrations.*

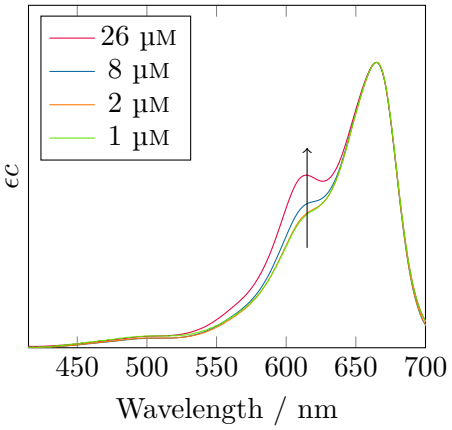

Figure 4.27: *Bulk absorption spectrum of MB in water, normalised to the main peak, with the growth of the dimer peak indicated by the arrow.*

4.7.2 Methylene blue at the silica/ethanol interface

Figure 4.28 shows EW-CEAS spectra of methylene blue in ethanol, at the same concentrations as in the bulk spectra in Section 4.7.1. The spectra for the 26 µM solutions are compared in Figure 4.30. The spectra of the dye at the interface are clearly different to that of the bulk, with the shoulder at 600 nm being more pronounced relative to the maximum at 656 nm. Additionally, ϵc for the evanescent wave is approximately 50 times that of the bulk measurement, indicating significant adsorption of the dye to the surface.

The increased intensity of the shoulder at the surface compared to the bulk, as well as the increased strength of the shoulder at higher concentrations (Figure 4.29) also suggests the formation of some H-type dimer at the surface. Ohline *et al.* have previously shown that methylene blue forms dimers on silica in dried films.[185] A similar effect has also been observed by Severino and coworkers in SDS micelles and AOT reverse micelles.[163]

Although there is a difference between the bulk and EW spectra, indicating the presence of dimers, the change is relatively minor, suggesting that the majority of the molecules at the surface are monomers.

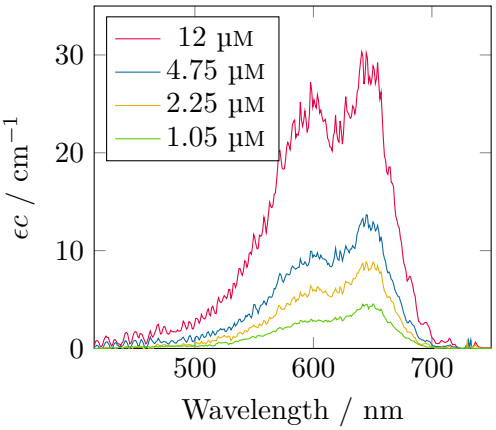

Figure 4.28: *EW spectrum of MB in EtOH at various concentrations.*

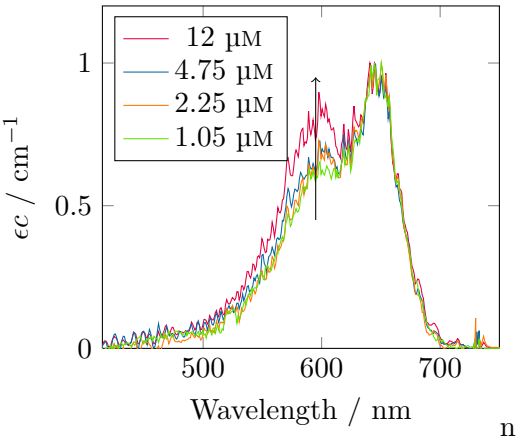

Figure 4.29: *EW spectrum of MB in EtOH, normalised to the main peak, with arrow indicating the growth of the shoulder.*

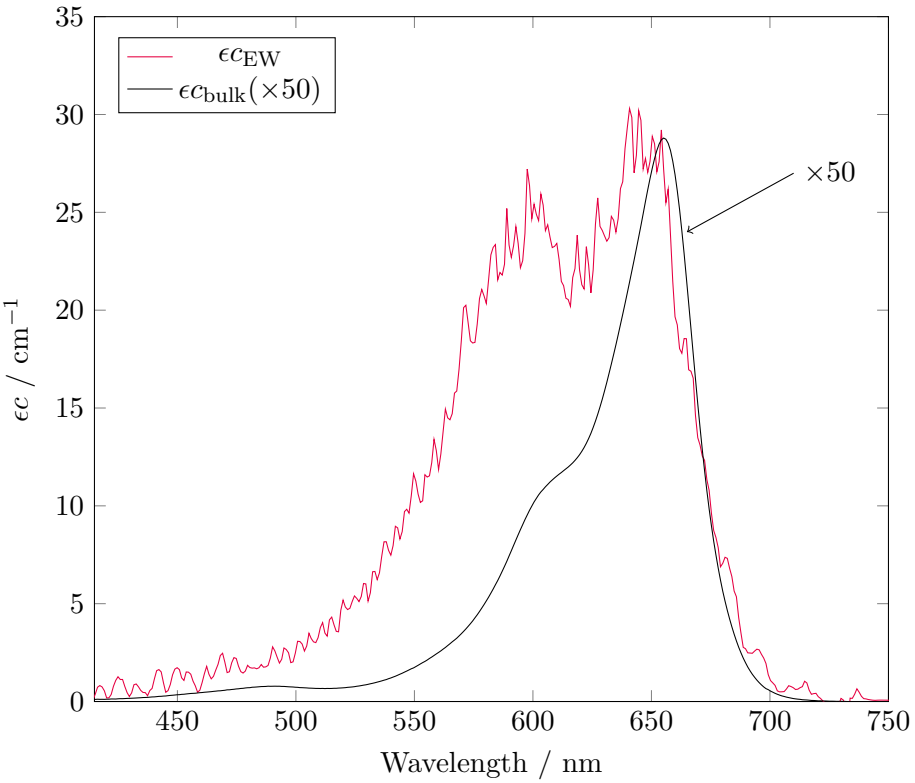

Figure 4.30: *Comparison of the spectra of 12* µM *methylene blue in EtOH as taken for the bulk using a commercial UV-vis spectrometer (using a 1* cm *cell) and using the EW-CEAS apparatus. The difference in spectral shape and in ϵc suggest adsorption of the MB to the silica surface.*

4.7.3 Methylene blue at the silica/water interface

In aqueous solution, methylene blue shows quite different adsorption behaviour than in ethanol. In Figures 4.31 to 4.34 the EW-CEAS spectra of four concentrations of methylene blue in water at various times after introduction to the surface can be seen.

Firstly, note that in all cases, ϵc increases steadily over the course of minutes, indicating relatively slow adsorption to the surface (as can be seen in the kinetic traces in Figure 4.35).

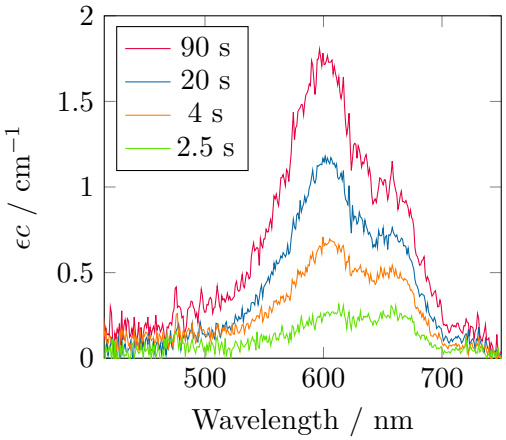

Figure 4.31: *EW spectrum of 156* nM *methylene blue.*

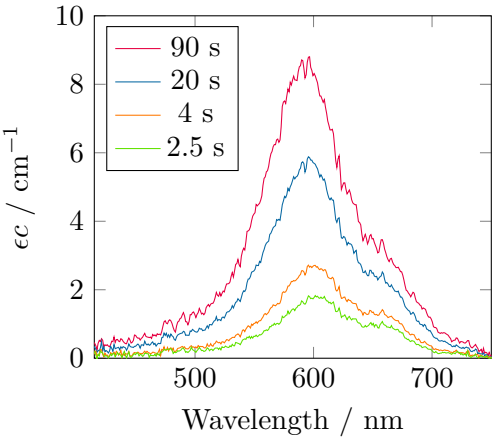

Figure 4.32: *EW spectrum of 312* nM *methylene blue.*

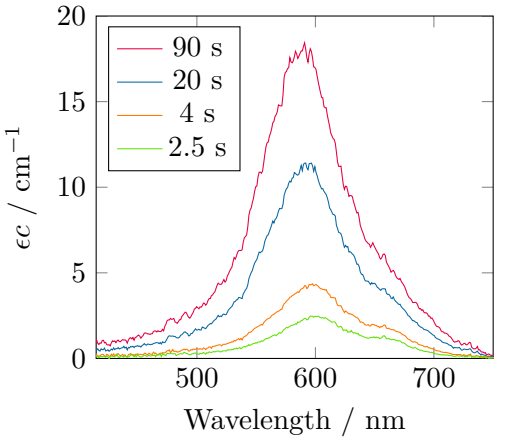

Figure 4.33: *EW spectrum of 625* nM *methylene blue.*

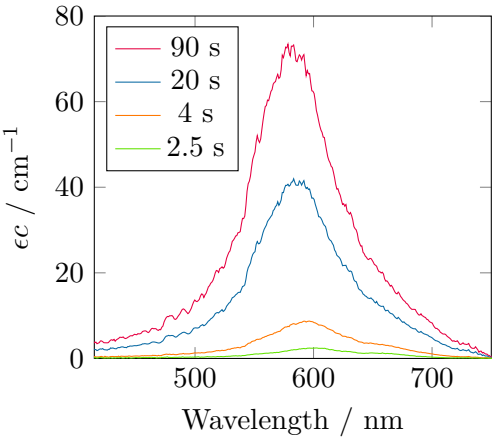

Figure 4.34: *EW spectrum of 1.25* µM *methylene blue.*

For the 156 nM spectrum, two peaks can clearly be observed, the monomer peak at approximately 660 nm, and the H-type dimer at 600 nm. Over time, the dimer peak increases in strength relative to the monomer, corresponding to an increase in the dimer population as more MB packs onto the surface. This can be seen in Figure 4.36, where

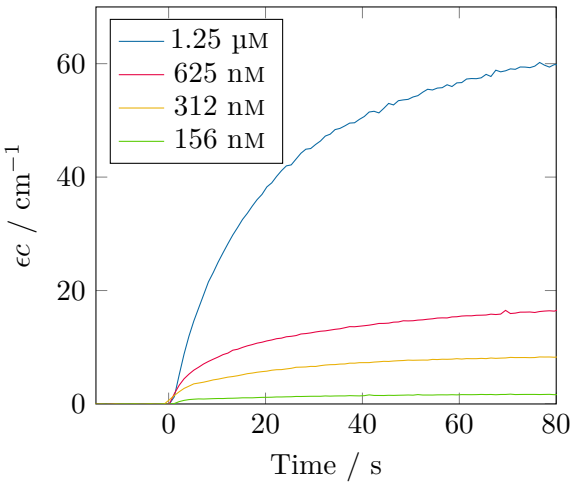

Figure 4.35: *Kinetic traces of the interfacial absorbance of 156 to 1250* nM *methylene blue, monitored at 600* nm*. Note the relatively slow adsorption, over the course of minutes, before a limiting value is reached.*

the spectrum has been normalised to 666 nm.

As the solution concentration is increased, the population of the H-type dimer increases relative to the monomer, with the dimer peak almost completely dominating at 1.25 µM. In addition, the peak blue-shifts at higher concentrations, suggesting either a change in the stacking angle of the dimer,[163] or the formation of higher order aggregates,[186] or both.

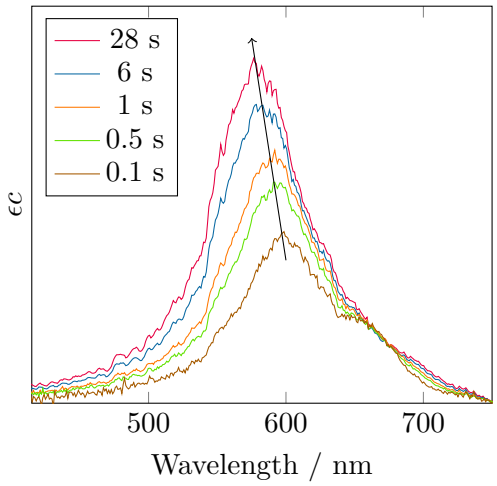

Figure 4.36: *Spectra of 1.25* µM *methylene blue measured by EW-CEAS. Note the increasing strength and blue-shift of the multimer peak (indicated by the arrow) as MB adsorbs to the surface.*

4.7.4 Fitting the methylene blue spectra

In order to further analyse the spectra, deconvolution into the constituent species (monomer, dimer, etc) can be carried out.

Ohline and coworkers have carried out similar work for methylene blue at the silica surface, employing singular value decomposition of the spectra.[185] This approach cannot be used in this case, however, as it relies upon elemental conservation, the fact that the total surface concentration is the weighted sum of each species; in the experiments performed here, the total surface concentration is unknown, and so the spectra cannot be decomposed into individual species in this way.

It is possible, however, to remove the contribution of the monomer from the spectra, assuming the spectral shape is the same in solution and at the surface. Taking the lowest concentration, 156 nM, Figure 4.31, the spectrum can be decomposed into two components, shown in Figure 4.41. The remaining EW spectra can then be fitted using these two components, using the relative amount of each species as the only parameters.

The fitted spectra for all four of the above concentrations are shown in Figures 4.37 to 4.40. At 156 nM the spectra are fitted quite well at all times up to 90 s, suggesting that the only species present are indeed monomers and dimers. As the concentration is increased, the spectra remain well-fitted at earlier times. The fit becomes less good over time, however, as the multimer peak blue-shifts.

Turning to the kinetics of dimer formation, the kinetic traces at 520 nm are shown in Figure 4.42. This wavelength corresponds to mostly dimer/multimer, with a minor contribution of the monomer. It can be easily seen that increasing concentration in solution leads to both an increased equilibrium concentration and a higher rate of formation of dimers at the surface. The very start of the adsorption is shown in Figure 4.43. The slopes of the traces are linear in this initial region, and correspond to the rate of formation of dimer.

The rate constant of formation of the dimer can be extracted from these data using the initial rates method. For a reaction

$$2\mathrm{A} \rightleftharpoons B \tag{4.63}$$

with rate equation

$$\frac{\mathrm{d[B]}}{\mathrm{d}t} = k[\mathrm{A}]^2 \tag{4.64}$$

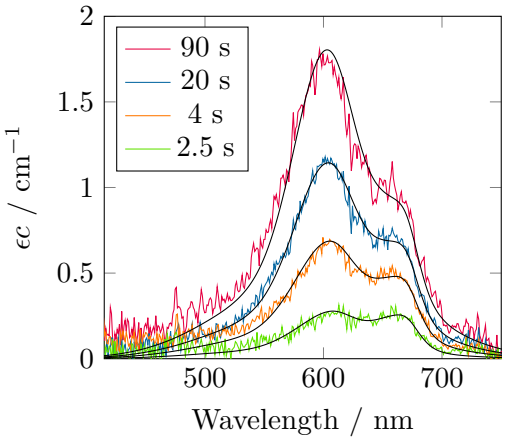

Figure 4.37: *Fitted spectra of 156* nM *MB.*

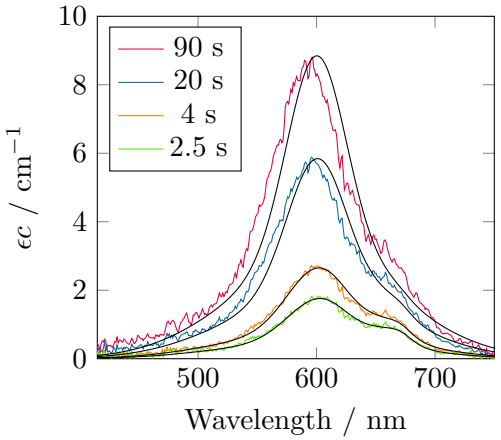

Figure 4.38: *Fitted spectra of 312* nM *MB.*

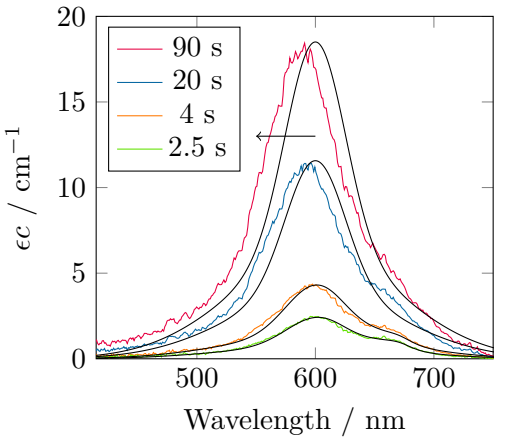

Figure 4.39: *Fitted spectra of 625* nM *MB. Arrow indicates shifting peak.*

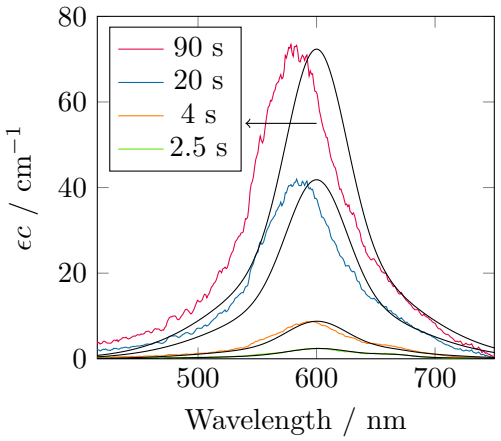

Figure 4.40: *Fitted spectra of 1.25* µM *MB. Arrow indicates shifting peak.*

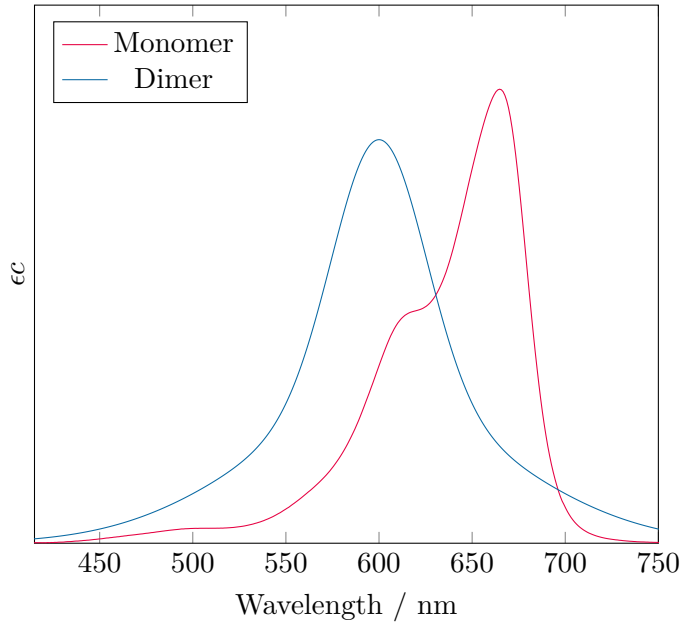

Figure 4.41: *Spectra of monomer and dimer of methylene blue, deconvoluted from the data in Figure 4.37*

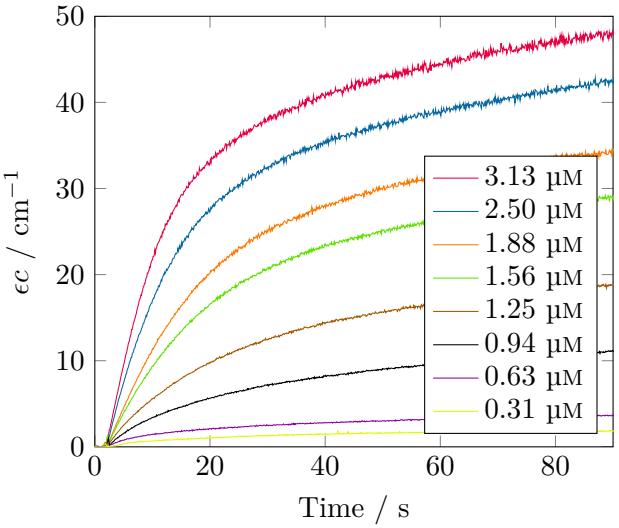

Figure 4.42: *Kinetic traces of methylene blue adsorption at 520* nm*, corresponding to multimer formation.*

a plot of the initial rate of formation of B against $[A]^2$ should give a straight line of slope k. For the data in Figure 4.43, the plot of the initial rate against $[MB]^2$ is shown in Figure 4.44. At low concentrations the plot is linear, indicating that the assumption that dimers are the dominant species is valid. At higher concentrations, the initial rate is not linear in $[MB]^2$, indicating the formation of higher order aggregates.

The effective rate constant extracted from Figure 4.44 is 0.53 $cm^{-1}\,\mu M^{-2}\,s^{-1}$. The extinction coefficient of the dimer at 520 nm is 3.3×10^{-2} $\mu M^{-1}\,cm^{-1}$,[185] giving a final rate constant of 16 $\mu M^{-1}\,s^{-1}$ for the formation of the dimer.

One point of note is that, over repeated experiments, while the amount of monomer at the surface reaches a repeatable value, the limiting amount of dimer varies between runs by as much as 50%, as seen in Figure 4.45. One interpretation of this is that that the condition of the surface is very important in determining the resulting build-up of MB.

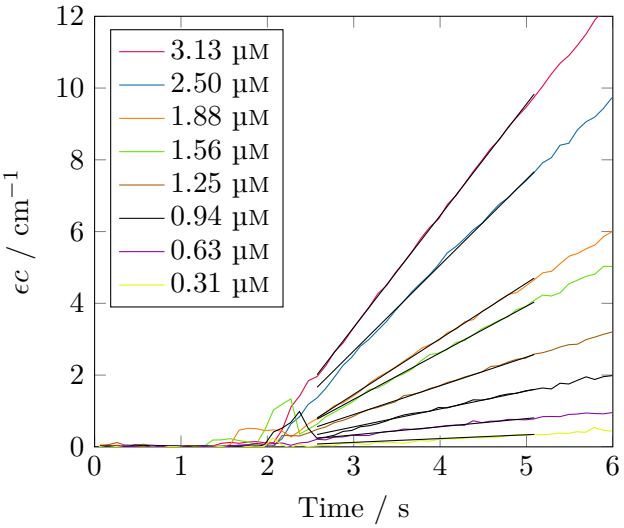

Figure 4.43: *The early portion of the traces in Figure 4.42, fitted to extract initial rates.*

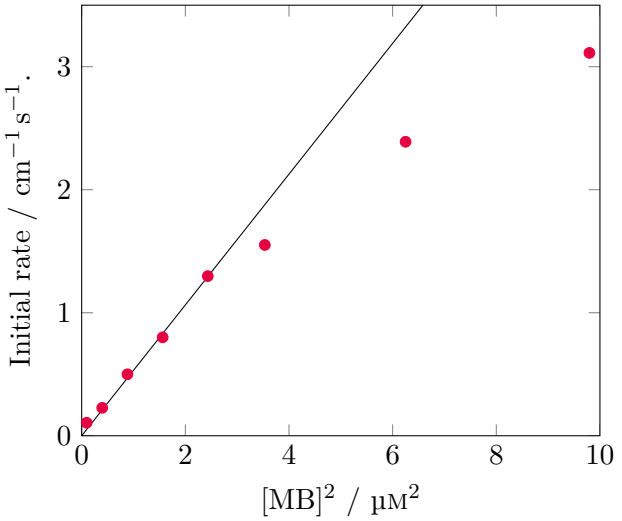

Figure 4.44: *The initial rates fitted in Figure 4.43 plotted against [MB]^2.*

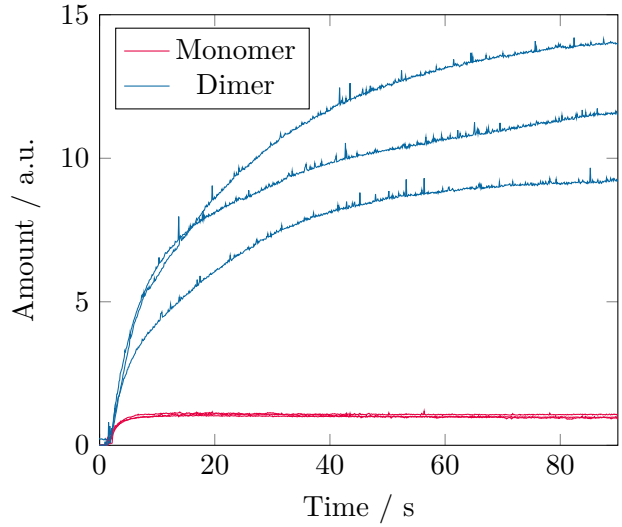

Figure 4.45: *Comparison of the fitted amounts of monomer and dimer for three experiments, all performed with 312* nM *methylene blue. Note that the three monomer traces lie almost on top of each other, but the dimer traces show almost 50% variability in the limiting value. One interpretation of this effect is that the limiting amount of dimer formed is heavily dependent on the surface condition.*

4.8 Crystal violet

Crystal violet (CV) is a triarylmethane dye used as a histological stain, the structure of which is shown in Figure 4.46

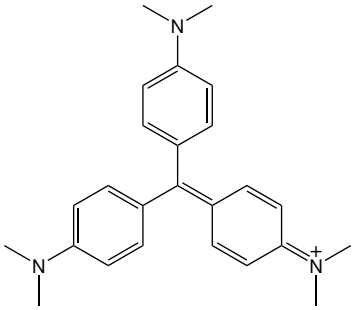

Figure 4.46: *Structure of crystal violet.*

The adsorption of crystal violet has been widely studied, both with regard to the use of low cost adsorbents as a method of removing it from solution,[180,187] and studying its adsorption behaviour onto silica[149,150,152,188,189] and mineral[190–193] surfaces.

The aqueous, bulk absorption spectrum of crystal violet is shown in Figure 4.47. There are two bands, the main peak at around 600 nm, with a shoulder near 550 nm. The origin of the shoulder has been a source of controversy for 75 years, starting with work by Lewis, Magel, and Lipkin, who found that the shoulder shrinks with decrease temperature.[194] They posited that the two bands were due to isomerisation of the molecule, with the main band being due to the symmetrical helical (or 'propeller') isomer, and the shoulder being due to a distorted helical structure.

This hypothesis can be rejected, however, based on calculations by Lueck *et al.* indicating that rotational isomerism could not explain the observed spectra, and by studies of CV in acetone and toluene, where the relative intensities were found to be independent of temperature.[195] Lueck instead argued that the shoulder is the result of splitting of the S_1 state due to the electronic interaction of the dimethylamino groups with dipoles or anions. The aggregation of crystal violet in solution was also studied by Lueck and coworkers, who were able to deconvolute the spectra of monomer, dimer, and trimer.[196]

Femtosecond pump-probe experiments by Maruyama *et al.*, however, suggest that CV has two ground states.[197] Maruyama found that the temporal rise of the shoulder depended on the excitation wavelength, and concluded that there are two ground state conformations, the 'propeller' D_3, and pyramidal C_3.

Photodissociation spectra recorded by Loison and coworkers of the unsolvated CV

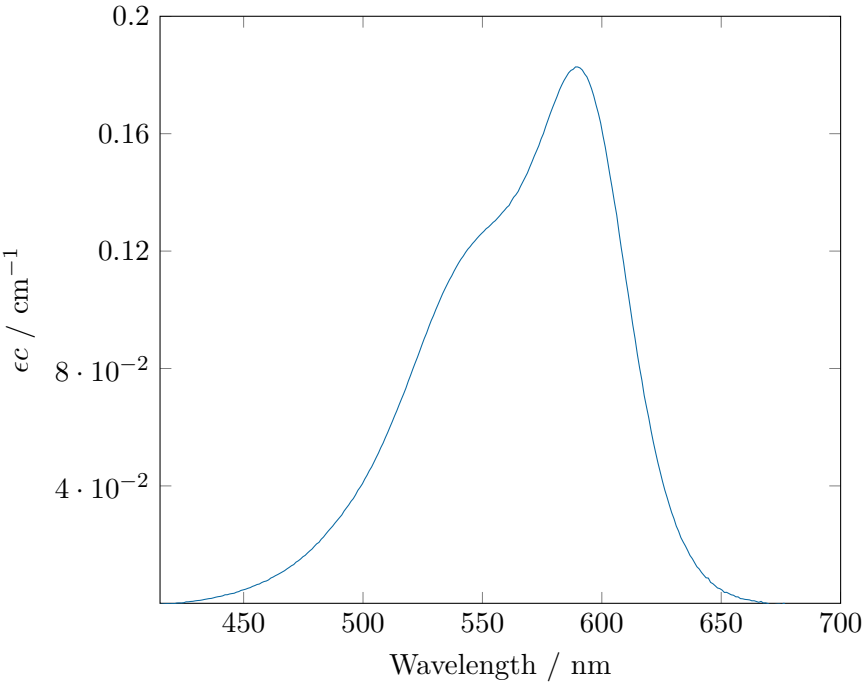

Figure 4.47: *Bulk absorption spectrum of 2* µM *crystal violet, measured using a commercial spectrometer and a 1* cm *cell.*

molecule show a single band, and calculations suggest that the main contribution to the shoulder in solution is the interaction of a solvent molecule at the central carbon.[198] Further computational studies by Macovez *et al.* add evidence that the pyramidal C_3 conformation is responsible for the shoulder.[199]

Much work has also been done studying the spectrum of crystal violet adsorbed to surfaces. Coon *et al.* found that a reversible transition between monomers and aggregate on the surface of titanium dioxide resulted in a spectral change, similar to that for aggregation in solution.[192] Yamaoka and Sasai studied the adsorption of CV on to montmorillonite clay, and were able to deduce the profile of eight sub-bands in the spectrum, and the angle of each relative to the surface.[191]

Fan *et al.* used EW-CRDS to characterise the adsorption of crystal violet to the silanol groups on fused silica surfaces.[152] They found that there were two types of bound CV molecules: at type I, isolated, silanol groups, the molecules are oriented randomly; at type II sites, where there are neighbouring silanols, the orientation of the molecules is restricted by repulsion from neighbouring groups and the tilt angle increases with concentration as more molecules adsorb. The interaction of crystal violet with anionic surfactants has also been used by Lin and coworkers in order to determine the critical hemimicelle concentration at the surface by EW-CRDS.[189]

Few of these experiments have been able to study both spectral and kinetic behaviour simultaneously. Making use of the broad-band range of EW-CEAS, presented here is a spectral and kinetic study of crystal violet adsorbing onto silica, and onto the highly charged surfaces of poly-L-lysine and poly-L-glutamic acid coated silica.

4.8.1 Crystal violet adsorption on the poly-L-lysine/water interface

Poly-L-lysine (PLL) is the polymer of L-lysine, the amino acid with the side chain $(CH_2)_4NH_2$. The conjugate acid of the side chain amine has a pKa of 10.54, making PLL positively charged at neutral pH. Application of a solution of poly-L-lysine to a bare silica surface results in a deposited layer on the surface, resulting in a positively charged surface. All PLL coated surfaces here were created by placing a 1 $\mathrm{mg\,mL^{-1}}$ solution of PLL onto the bare silica surface for 20 minutes.

Crystal violet, being positively charged in aqueous solution, would be expected not to bind to the PLL coated surface. Figure 4.48 shows the spectrum of 25 µM crystal violet in water (flow rate = 5 $\mathrm{mL\,min^{-1}}$) shortly after its introduction to the PLL-coated surface. The spectrum for both $||$ and $\perp$ polarisations matches the bulk spectrum, suggesting that there is little immediate adsorption to the surface.

There is a small discrepancy in the height of the shoulder relative to the mean peak as compared to the bulk solution spectrum. Two mechanisms could explain this change. Firstly, the interaction of CV with PLL coated surface could cause a change in population of the conformers present, changing the ratio of main peak to shoulder. This would be consistent with a change in the conformations present, towards either fully planar or with a reduction in the pyramidal angle of the D_3 conformer, or both. Alternatively, the presence of PLL could promote dimerisation, which would enhance the dimer band at 550 nm. In either case, the slight reduction in ϵc for the EW spectrum suggests that the local concentration at the surface is marginally lower than in the bulk, as might be expected due to the like charge on the surface and molecule. At this time the average orientation angle is $54.9 \pm 1.6°$ across the spectrum, the isotropic value of 54.7° being within the uncertainty, indicating there is negligible preferential orientation of CV at the interface (Figure 4.51).

Over the course of eight minutes the spectrum evolves to that shown in Figure 4.49, the kinetic trace being shown in Figure 4.50. There is an increase in both $\epsilon c_{||}$ and $\epsilon c_{\perp}$ over time, indicating some adsorption to the surface. Whether this involves displacement of PLL from the surface is unclear from this data. Note that after the initial rise, $\epsilon c_{\perp}$

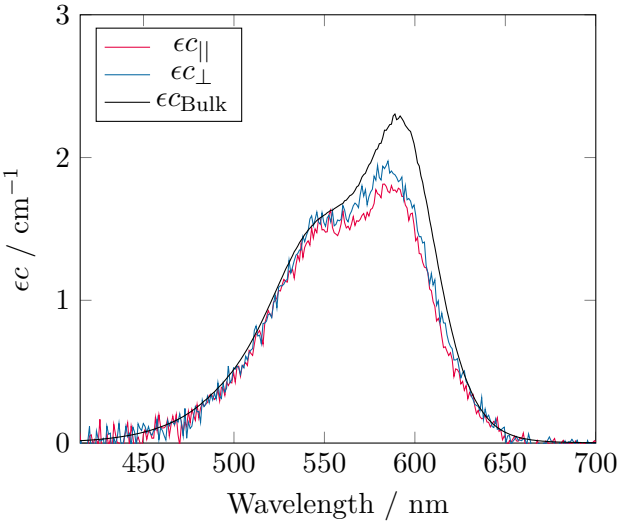

Figure 4.48: *The spectrum of 25* µM *crystal violet on a PLL coated prism* $t = 8$ s *after introduction of the dye solution to the surface.*

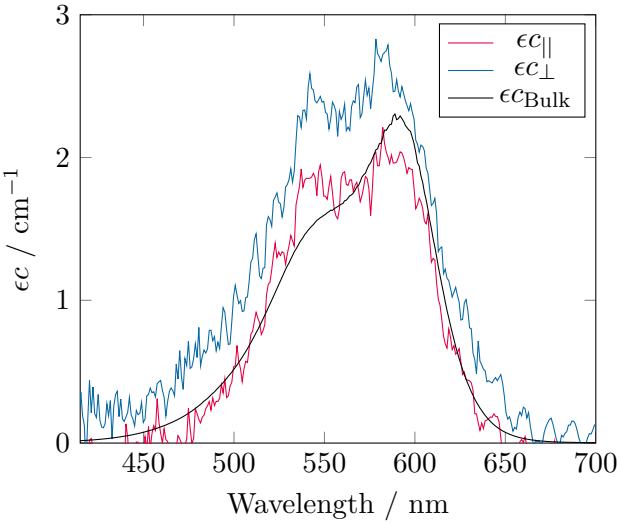

Figure 4.49: *The spectrum of 25* µM *crystal violet on a PLL coated prism* $t = 8$ min *after introduction of the dye solution to the surface.*

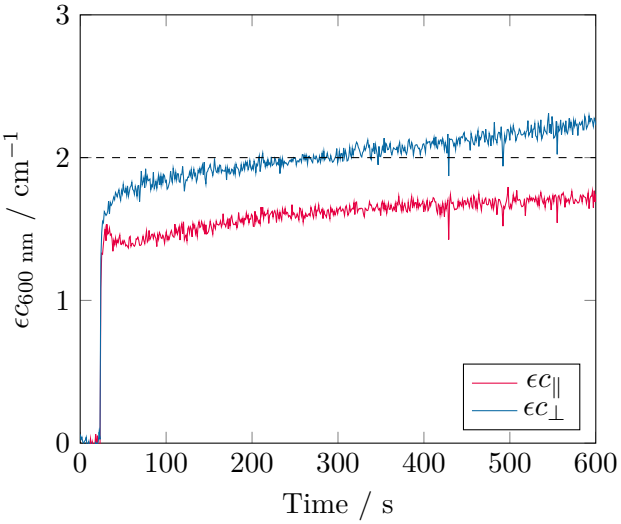

Figure 4.50: *Kinetic trace of 25* µM *crystal violet on a PLL coated prism at 600* nm*. The dashed line indicates* ϵc *for the bulk solution at the same wavelength.*

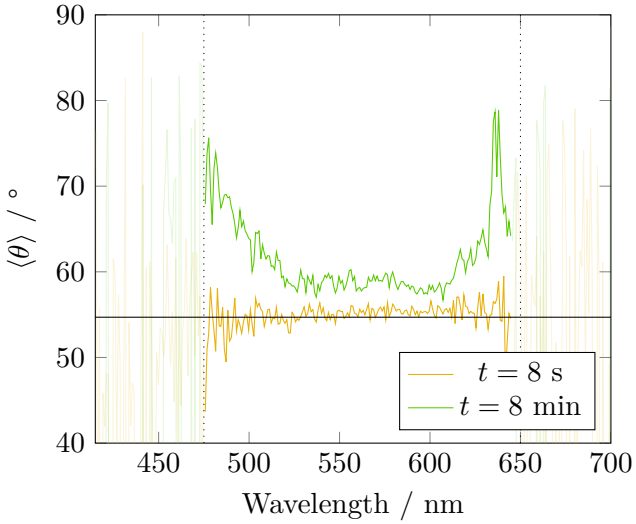

Figure 4.51: *The average orientation angle of CV on PLL at* $t = 8$ s *and* $t = 8$ min*. The black line indicates 54.7°, corresponding to an isotropic distribution.* $\langle\theta\rangle$ *outside the range 475 to 650* nm *is unreliable due to the small absorbance in these regions.*

is greater than $\epsilon c_{||}$, indicating that the molecules are partially aligned with TDMs tilted towards the surface. At this time the average orientation angle over the range 530–600 nm is $58.6 \pm 0.8°$ to the surface normal, the molecules being moderately tilted towards the surface. This can be seen in Figure 4.51.

In contrast, in Figure 4.49 there is clearly an additional contribution to $\epsilon c_{\perp}$ around 450–500 nm, and between 620 and 660 nm. This causes the average orientation angle in these regions to approach 70° (Figure 4.51). The appearance of these additional bands suggests the formation of both H- and J-type aggregates (as discussed in Section 4.3.2) with a strong preference for alignment with TDMs flat to the surface. However, the relatively small change in $\langle\theta\rangle$ suggests that the majority of molecules exist as monomers here.

4.8.2 Crystal violet adsorption on the bare silica/water interface

On the bare silica surface, the adsorption behaviour is more complex than on PLL, depending strongly on the concentration of the solution. Presented below are three concentrations, 250 nM, 1.25 µM, and 25 µM, which cover the range of behaviour exhibited.

4.8.2.1 At 250 nM

The EW-CEAS spectrum of a solution of 250 nM crystal violet in water being flowed (10 mL min^{-1}) over a bare silica prism is shown in Figure 4.52.

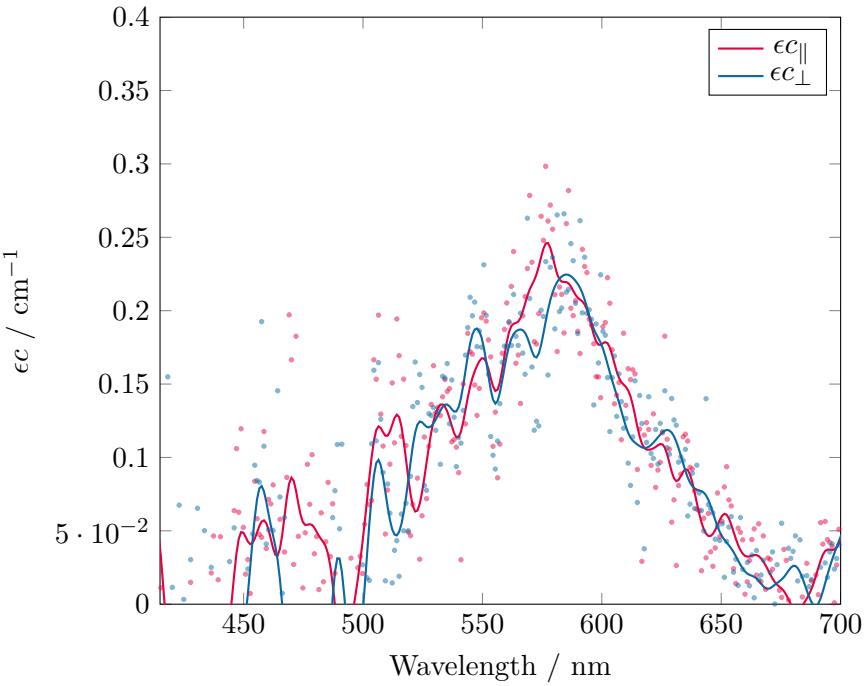

Figure 4.52: *Evanescent-wave spectrum of 250* nM *crystal violet, t = 60* s *after being introduced to a bare silica surface. Data has been smoothed using a running average (span = 15* nm*) for clarity.*

Here a step change in ϵc is observed as the dye solution is introduced to the surface (Figure 4.53). $\epsilon c_{\max}$ is approximately 12 times that of the bulk solution, indicating that the dye is adsorbed to the surface. Although the signal-to-noise ratio makes the shape of the spectrum quite difficult to observe, it is clearly similar to the monomer spectrum, suggesting that little aggregation is occurring, and that CV molecules sit individually on the surface.

$\epsilon c_{||}$ and $\epsilon c_{\perp}$ are identical within the noise, giving an average orientation angle of close to the magic angle. This is consistent with an isotropic distribution of molecular orientations, as found by Fan *et al.* for CV sitting at type I silanol sites.[152]

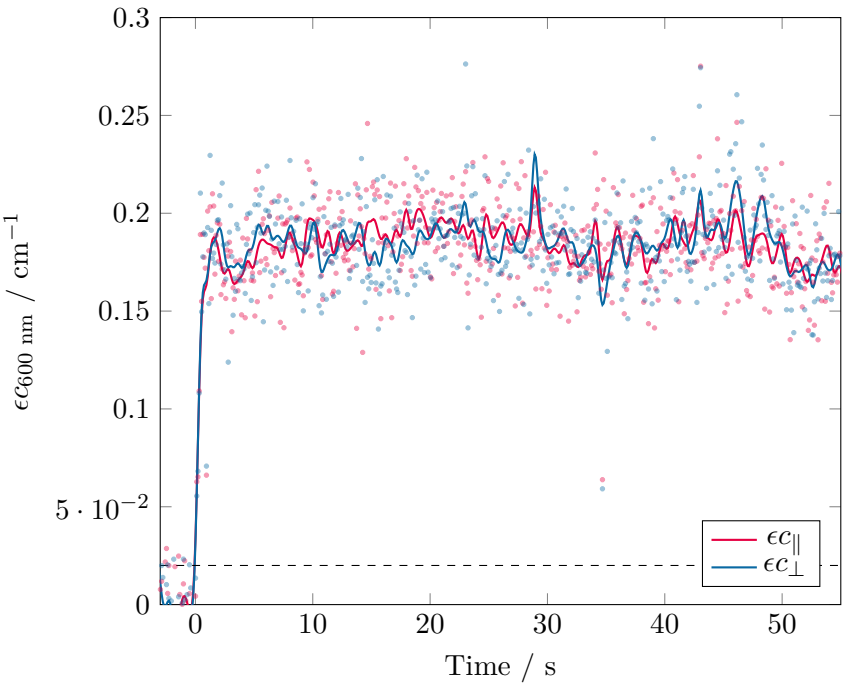

Figure 4.53: *Evanescent-wave kinetic trace of 250* nM *crystal violet at the bare silica/water interface, monitored at 600* nm *(flow rate =* 10 $\mathrm{mL\,min^{-1}}$*). The data have been smoothed using a moving average filter (span =* 1 s*) for clarity. The dashed line indicates ϵc for the bulk solution at the same wavelength.*

4.8.2.2 At 1.25 μM

At 1.25 µM the spectrum (Figure 4.54) is again similar to that at 250 nM. ϵc is around ten times higher than for the bulk solution (0.1 cm^{-1} at 600 nm), and $\epsilon c_{||}$ is almost identical to $\epsilon c_{\perp}$, implying an isotropic distribution of orientations indicating that at this concentration, the spectrum remains dominated by isolated monomers at the silica surface, isotropically oriented at type-I silanol sites.

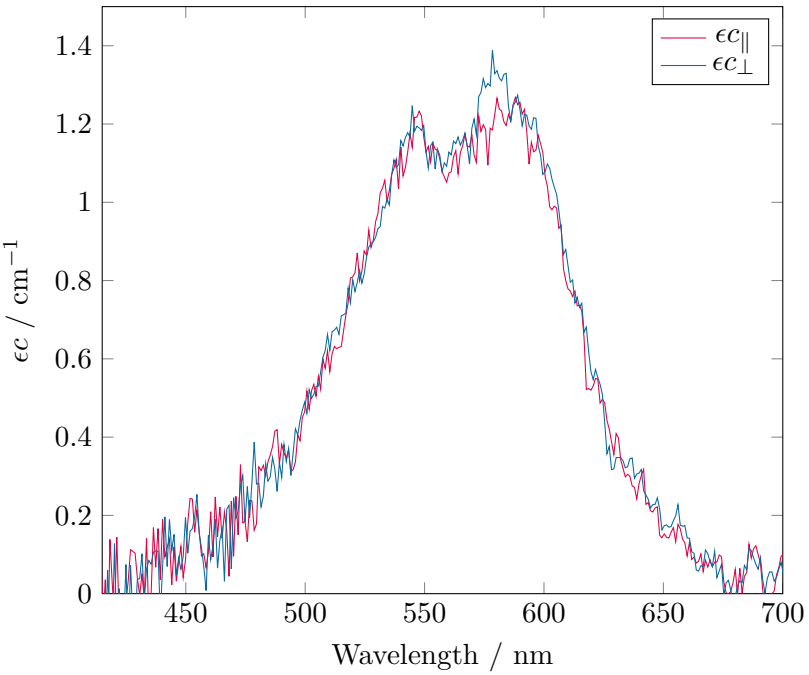

Figure 4.54: *Spectrum of 1.25* µM *crystal violet flowed (10* $mL\,min^{-1}$*) on a bare silica surface,* $t = 60$ s *after introduction to the surface. No change in the spectral shape is discernible over the course of the experiment.*

At 1.25 µM the spectral shape is clearer than at 250 nM. The shoulder is more intense relative to the main peak than in bulk solution, similar to the spectrum observed on the poly-L-lysine coated surface (Figure 4.48). The similar observation with both PLL and bare silica suggests that either dimerisation or direct contact with the silica is responsible for the change, and not interaction with PLL.

In the kinetic trace (Figure 4.55), there is a sharp rise in ϵc as the solution is introduced to the cell, followed by a small peak which falls to the equilibrium value within seconds. One possible supposition might be that small aggregates fall close to the surface, causing a minor increase in the local concentration, but are quickly disrupted by interaction with the surface to form adsorbed monomers; there is, however, no spectral evidence in favour of such a hypothesis. No changes in the spectral shape are discernible over the course of

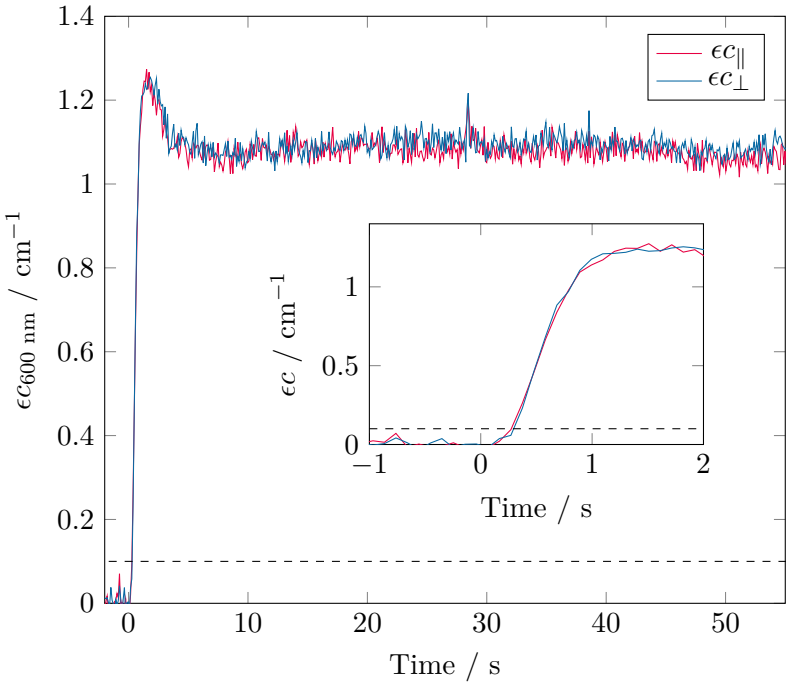

Figure 4.55: *Kinetic trace of 1.25* µM *crystal violet being flowed (10* mL min^{-1}*) on a bare silica surface, shown for 600* nm*. The inset shows the initial rise in ϵc, corresponding to the solution sweeping over the probed area (see text). The dashed lines indicate ϵc for the bulk solution at the same wavelength.*

the experiment.

The inset in the figure shows the initial rise as the sample is introduced to the cell. This occurs over less than 1 s, similar to the value for the non-adsorbed cresol red system, suggesting that the adsorption occurs faster than the flow of the solution across the probed area; as such the bulk cannot be readily distinguished from the interfacial adsorption.

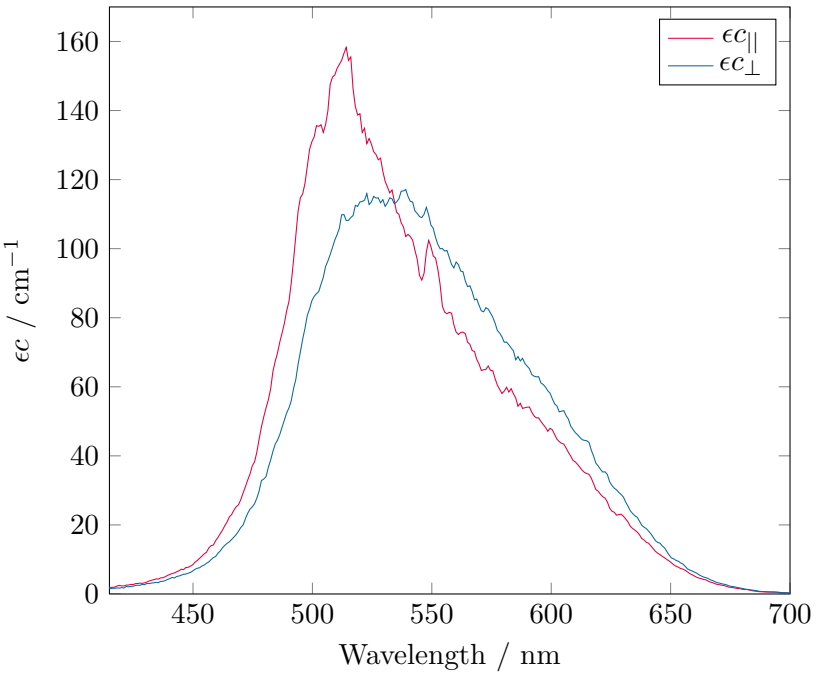

Figure 4.56: *EW spectrum of 25* µM *crystal violet with a bare silica prism, at* $t = 60$ s *after introduction of the solution to the surface. Note the difference between the two polarisations, indicating ordering of the CV molecules.*

4.8.2.3 At 25 μM

At higher bulk concentrations of crystal violet, the adsorption behaviour is more complex. The spectrum of 25 µM crystal violet adsorbed onto bare silica is shown in Figure 4.56. Here the spectrum is vastly different to that of the bulk solution, with the absorption maximum significantly blue-shifted.

The ratio of $\epsilon c_{||}/\epsilon c_{\perp}$ varies across the spectrum, with $\epsilon c_{||}$ being larger at the blue end, and $\epsilon c_{\perp}$ being larger in the red. This suggests that multiple species are present at the interface, each with a different, non-isotropic orientation. Qualitatively, there is a shoulder at around 600 nm, visible in both || and $\perp$ polarisations, suggesting that there is a contribution to the spectrum from the monomer. In addition to this, there are two other, clearly visible components to the spectrum: firstly, there is an intense band at around 505 nm, seen most strongly in the || spectrum; additionally, there must be at least an additional band at around 540 nm to account for the peak of the $\perp$ spectrum, and also for the remaining intensity of the || spectrum.

The kinetics at 600 nm are shown in Figure 4.57. Here there is a slow rise in ϵc over the course of a minute, in contrast to the situation at lower concentrations, where an equilibrium is reached within seconds. This rise was observed to continue over time,

reaching a steady interfacial absorbance within 10 min (Figure 4.57, inset).

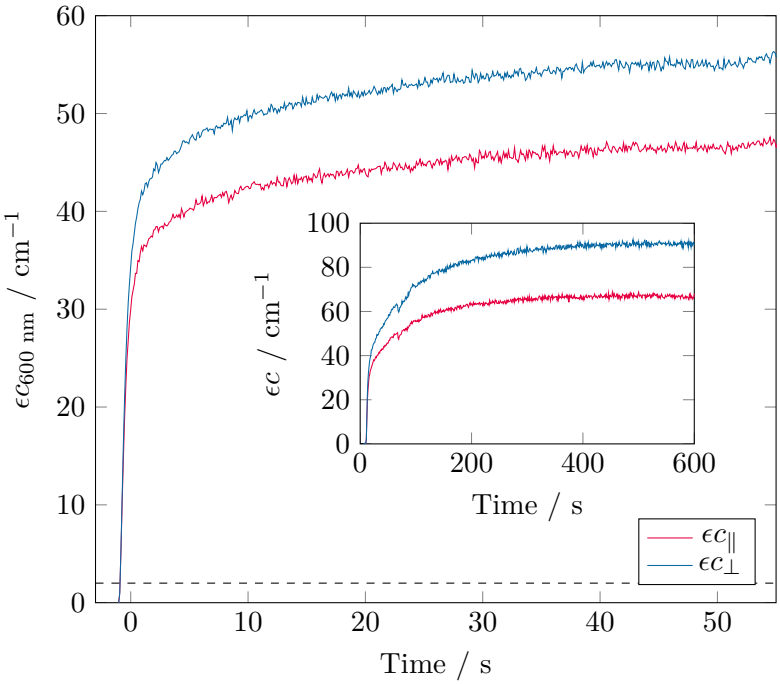

Figure 4.57: *Kinetic trace of 25* µM *crystal violet flowed (10* $\mathrm{mL\,min^{-1}}$*) on a bare silica surface at 600* nm*. The dashed line indicates ϵc for the bulk solution at the same wavelength. Inset: the rise in interfacial absorbance continues over the course of* $\sim$ 10 min *before reaching a steady value (data from second experiment).*

After the above experiment was completed, the solution flowing over the prism was changed to water (flow rate = 10 $\mathrm{mL\,min^{-1}}$), and the interfacial absorbance again recorded. The interfacial absorbance was observed to fall to almost zero within a few seconds of the commencement of water flow (Figure 4.58).

The spectra over the course of the water flow experiment are shown in Figure 4.59, normalised to the shoulder at 600 nm. From these spectra, it is easily seen that, although the interfacial absorbance decreases across the spectrum, the band at 505 nm falls more rapidly than the shoulder at 600 nm. This is further evidence of the presence of more than one species at the interface.

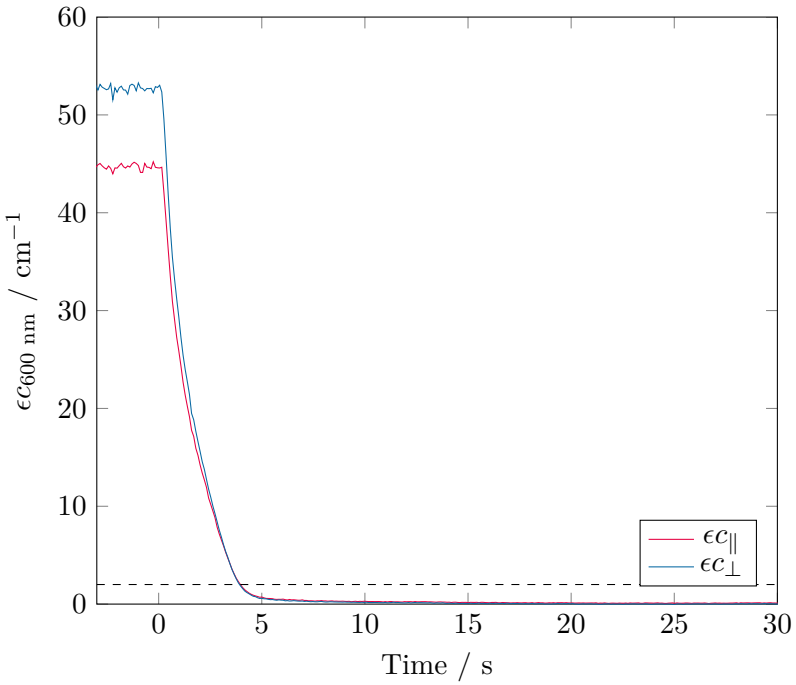

Figure 4.58: *Kinetic trace of crystal violet being washed from the prism surface by flowing water (10* mL min^{-1}*) after the experiment shown in Figures 4.56 and 4.57 (measured at 600* nm*). The interfacial absorbance falls to zero within seconds, indicating removal of the crystal violet to below levels detectable by this instrument. The dashed line indicates the bulk ϵc for the 25* µM *CV solution at the same wavelength.*

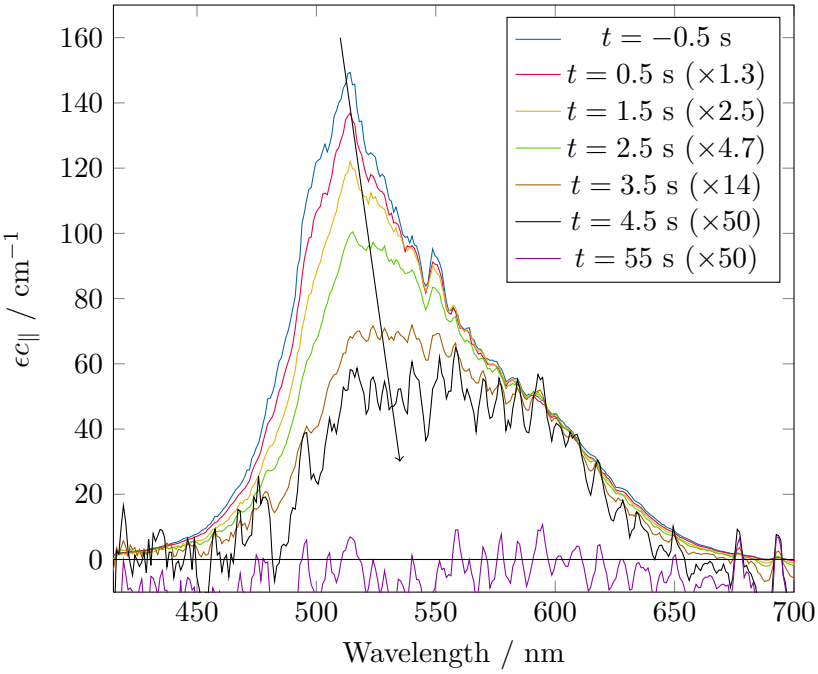

Figure 4.59: *EW spectra of 25* µM *crystal violet being washed from the bare silica/water interface by flowing water (10* mL min^{-1}*). Note that, although the interfacial absorbance decreases across the spectrum, the band at 505* nm *falls more rapidly than the shoulder at 600* nm*. No detectable interfacial absorbance remains after one minute.*

4.8.3 Fitting the crystal violet spectra

Moving beyond a purely qualitative description of the spectra can be accomplished in a number of ways. If the total surface concentration is known, in dried films for instance, spectra at a range of concentrations can be used to deconvolute spectra of the individual species using singular value decomposition, as described in Section 4.7.3. In the work presented here, however, the total surface concentration is not independently known so this approach cannot be used. Instead, using either a priori knowledge of the spectral features, or by performing a global fit to the spectra using sensibly shaped bands, the kinetics of individual components can be separated.

Prior work by Yamaoka *et al.* found that the spectrum of crystal violet in the presence of Montmorillonite K-10 clay could be decomposed into eight Gaussian sub-bands by analysing the reduced dichroism spectra.[191]

The spectra of 25 µM crystal violet adsorbing onto bare silica presented here (Figure 4.56) can be fitted well using three components, made up of six Gaussian sub-bands, as listed in Table 4.2. The main peaks occur at 505, 543 and 594 nm, consistent from the qualitative prediction from inspection of the spectrum.

Label	λ_{max} / nm	FWHM / nm	Relative intensity
505 nm	505	24	-
543 nm	485	35	1
	543	37	7.2
	618	15	1
594 nm	594	28	7.5
	640	30	1

Table 4.2: *List of partial absorption bands decuded from fitting the EW-CEAS spectra of 25* µM *CV adsorbing to a bare silica surface.*

Six Gaussian sub-bands were found to be the minimum number with which an acceptable fit was able to be achieved, and are broadly consistent with the peaks found by Yamaoka, although not a precise match for their measurements of either free CV or that bound to montmorillonite. This discrepancy can be attributed to the difference between the silica and clay surfaces.

The six Gaussian sub-bands found here could be grouped into three fitting components by their matching kinetics, relative intensities, and $\langle\theta\rangle$.

The fitted spectrum at 600 s can be seen in Figure 4.60, and contributions of the individual bands in Figure 4.62 and 4.64. As can be seen from the figure, the spectrum for both $\parallel$ and $\perp$ polarisations is fitted well by the three components listed in Table 4.2.

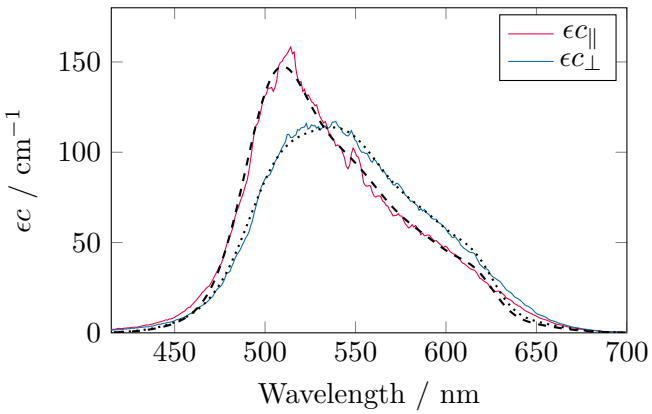

Figure 4.60: *Spectrum of 25* µM *crystal violet on a bare prism, 60 seconds after introduction to the surface. Fits are shown by the dotted and dashed lines.*

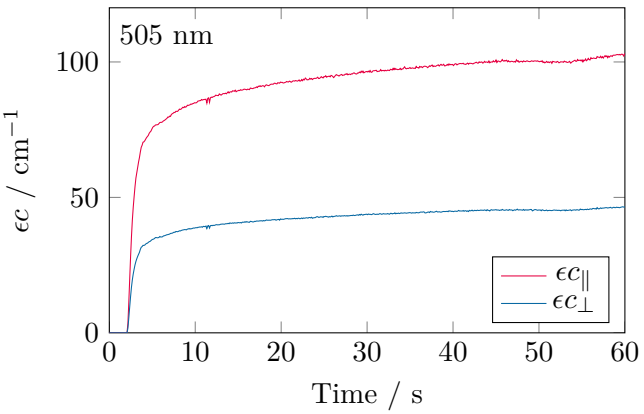

Figure 4.61: *Kinetic trace of the component at 505* nm.

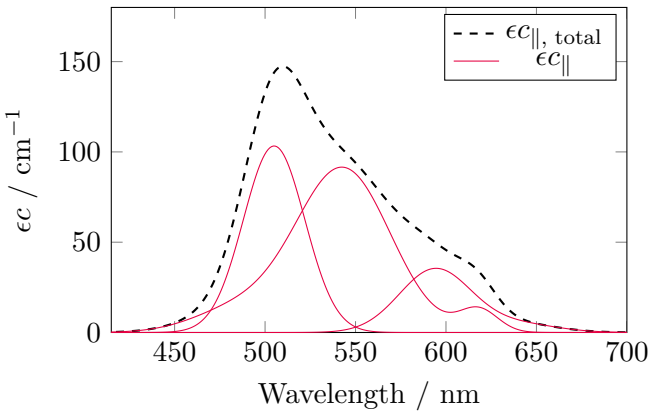

Figure 4.62: *Total fitted spectrum and three spectral components of* $\epsilon c_{\parallel}$ *from Figure 4.60.*

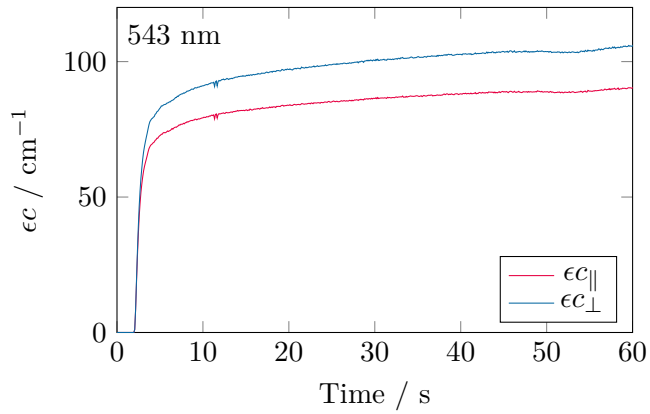

Figure 4.63: *Kinetic trace of the component at 543* nm.

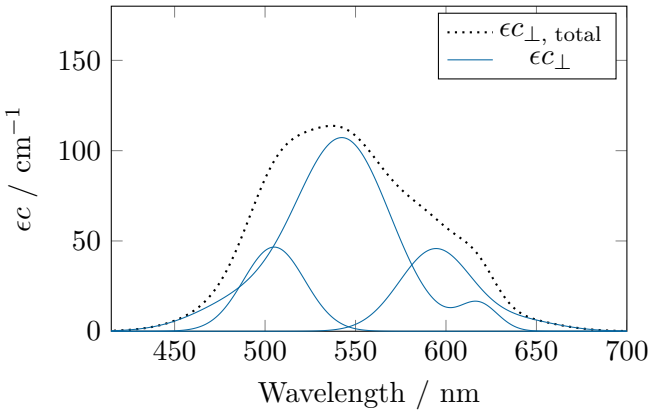

Figure 4.64: *Total fitted spectrum and three spectral components of* $\epsilon c_{\perp}$ *from Figure 4.60.*

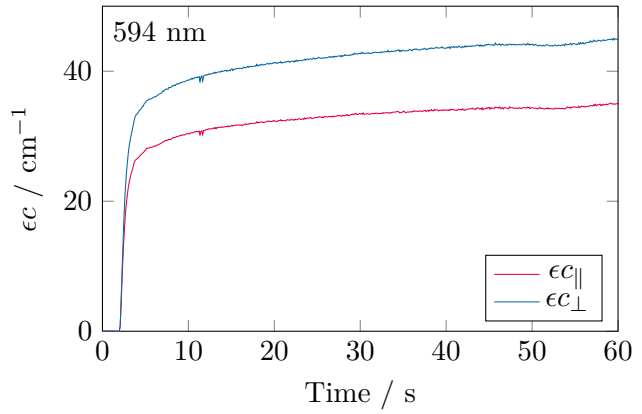

Figure 4.65: *Kinetic trace of the component at 594* nm.

Component	$\langle\theta\rangle$ / °
505 nm	43.6 ± 0.1 (± 0.25)
543 nm	56.7 ± 0.1 (± 1)
594 nm	58.0 ± 0.1 (± 0.5)

Table 4.3: *The expectation values for the angle of the TDM relative to the surface normal for the three components of the spectrum of 25* µM *crystal violet at the silica/water interface. The uncertainties are the variation of the calculated angle over the timescale of the experiment – this does not take into account the uncertainty in the measurement itself. Shown in brackets are estimates of the statistical uncertainty from repeated measurement.*

Fitting the intensity of each component at each time step, the kinetic behaviour of each component for both $\parallel$ and $\perp$ polarisations can be found, and are shown for this experiment in Figures 4.61, 4.63, and 4.65.

Note that we can assign sub-bands to the same species based on the fact that the kinetics of each are identical, and even more confidently if the average orientation angle is the same; it is unlikely that different species would have identical kinetic profiles and angular distributions. Here the three Gaussian sub-bands that make up the 543 nm band have identical kinetics and $\langle\theta\rangle$, as do the two Gaussian sub-bands of the component at 594 nm.

All three components show significant anisotropy, indicating ordered absorption for all three species. The average orientation angles for the three components are shown in Table 4.3.

Both the bands at 543 nm and 594 nm have orientation angle expectation values of 56.7° and 58.0° respectively, close to the magic angle, indicating a modest tilt of the TDM towards flat to the surface. The component at 505 nm, however, is more anisotropic, lying at 43.6° to the surface normal.

A possible assignment for the three components would be to monomer (594 nm), dimer (543 nm), and H-type aggregate (505 nm). This assignment would be consistent with Lueck *et al.*, who assigned the spectra of monomer, dimer, and trimer from solution data, with increasingly blue-shifted absorption maxima moving from monomer to dimer to trimer.[200]

The increased deposition of CV at 25 µM compared to 1.25 µM (and, indeed, qualitatively different behaviour) suggests some measure of cooperativity. At concentrations up to 1.25 µM, crystal violet adsorbs monomerically and isotropically, presumably at type-I silanol sites as found by Fan and coworkers.[152] The surface concentration is enhanced relative to the bulk, but is in proportion to the bulk concentration (increasing approximately

five times between 250 nM and 1.25 µM solution).

At 25 µM, however, the adsorption is markedly increased (ϵc being over ten times greater than the proportionate increase in concentration as compared to 1.25 µM). This, combined with the large blue-shift in the absorption maximum, is consistent with the formation of dimers and H-type higher aggregates; with increasingly concentrated solutions, a critical surface concentration is rapidly reached whereupon runaway aggregation occurs.

Even after deposition of crystal violet from 25 µM solution, the crystal violet can be completely removed from the surface within 60 s by flowing water across the prism.

One way to investigate the aggregation behaviour of crystal violet at the interface further would be to use poly-L-glutamic acid to increase the negative charge on the surface, and observe the effect on adsorption.

4.8.4 Crystal violet adsorption on the poly-L-glutamic acid/water interface

Poly-L-glutamic acid (PLGA) is a polymer made up of L-glutamic acid units, the carboxylic acid side chain of which has a pKa of 4.1, making it negatively charged at neutral pH. The deposition of a layer of PLGA therefore leaves a highly negatively charged surface in water.

Since the bare silica/water interface has a negative charge after plasma cleaning (due to the free silanol groups at the surface), it might be expected that crystal violet would adsorb in a similar way to PLGA as it does to a bare silica surface. The observed spectra do indeed show similarities. Experiments using 250 nM CV on PLGA show spectra similar to those seen at 25 µM on bare silica (the different concentrations being accounted for by the increased negative charge of PLGA). There are also key differences, however, with respect to the fate of the adsorbed molecules at long times.

In all experiments here, PLGA was deposited onto the silica surface by applying a solution of 1 mg mL^{-1} PLGA in water to the prism surface for 20 minutes.

4.8.4.1 At 250 nM

For a 250 nM solution of crystal violet in water, flowed at 5 mL min^{-1}, the EW-spectrum quickly gains the appearance as shown in Figure 4.66. Qualitatively similar to the spectrum of 25 µM CV on bare silica, the three components of the spectra are clearly visible, and can be fitted fairly well using the components listed in Table 4.2.

As in Section 4.8.2.3, the band at 505 nm has an average orientation angle of of 43.4° to the surface normal, while the components at 543 and 594 nm are oriented at 55.8° and 58.3° respectively. These values are similar to those calculated for the experiments at the bare silica interface, suggesting that similar aggregation processes are occurring on bare silica and PLGA, only at lower concentrations of CV on PLGA due to the increased surface charge.

The subsequent kinetic behaviour of the spectrum for PLGA (Figures 4.67 to 4.71), however, is drastically different to that observed for the bare silica case.

As can be seen in the kinetic traces of the components (Figures 4.67 to 4.71), approximately sixty seconds after the introduction of the solution to the cell there is a sudden and irreversible drop in ϵc for all three spectral components. The peak at 505 nm falls completely to zero, while the other two components fall to a lower, constant value. After

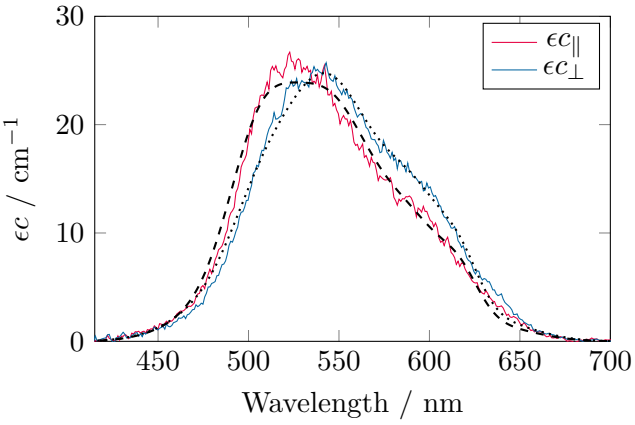

Figure 4.66: *Spectrum of 250* nM *crystal violet on a PLGA coated prism, 100 seconds after introduction to the surface. Fits are shown by the dotted and dashed lines.*

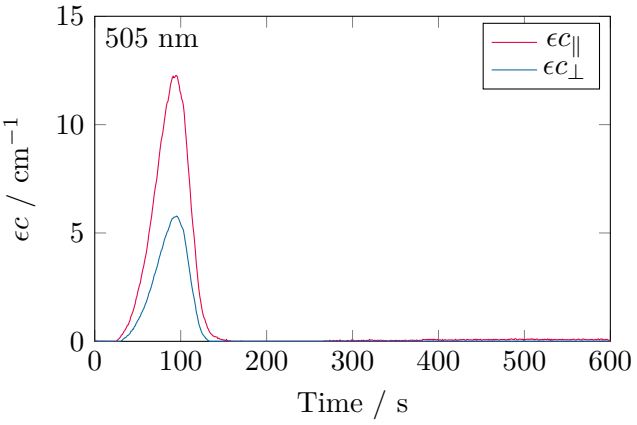

Figure 4.67: *Kinetic trace of the component at 505* nm*, showing adsorption, PLGA film rupture, and rapid loss of interfacial CV.*

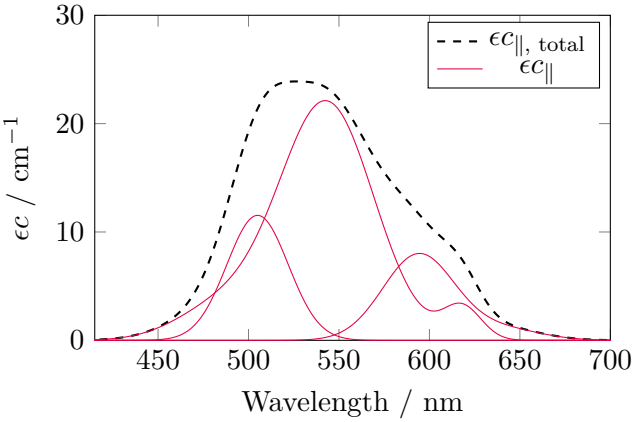

Figure 4.68: *Total fitted spectrum and three spectral components of $\epsilon c_{\parallel}$ from Figure 4.66.*

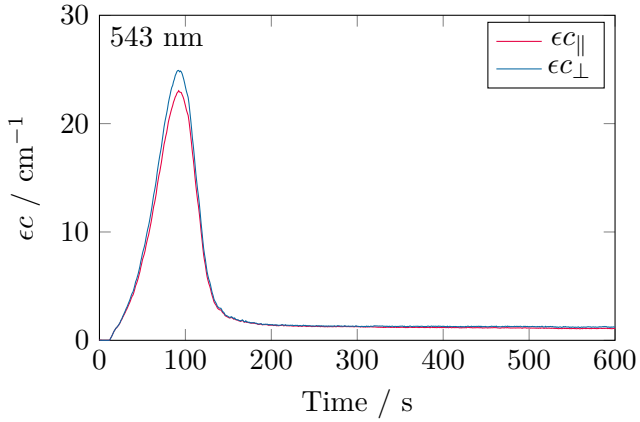

Figure 4.69: *Kinetic trace of the component at 543* nm*.*

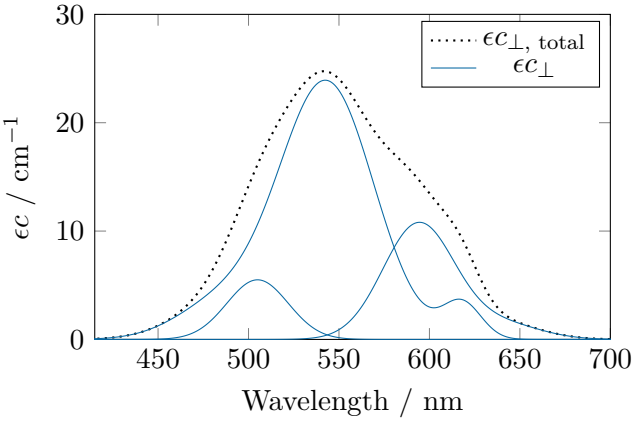

Figure 4.70: *Total fitted spectrum and three spectral components of $\epsilon c_{\perp}$ from Figure 4.66.*

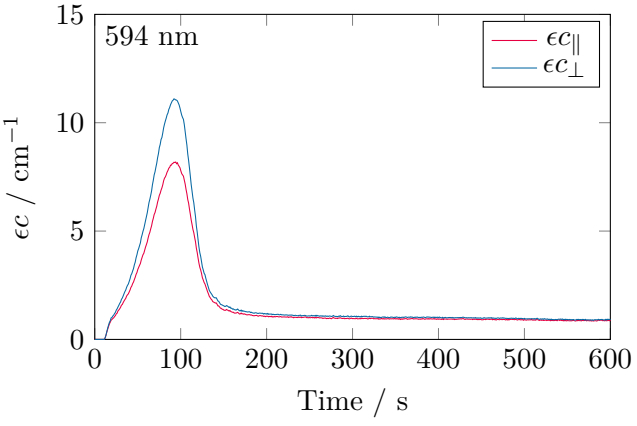

Figure 4.71: *Kinetic trace of the component at 594* nm*.*

Component	$\langle\theta\rangle$ / °
505 nm	43.4 ± 0.6
543 nm	55.8 ± 0.1
594 nm	58.3 ± 0.4

Table 4.4: *The expectation values for the angle of the TDM relative to the surface normal for the three components fitted for 250* nM *crystal violet at the PLGA/water interface. The uncertainties are the variation of the calculated angle over $t = 45$ to 100* s *– this does not take into account the uncertainty in the measurement itself.*

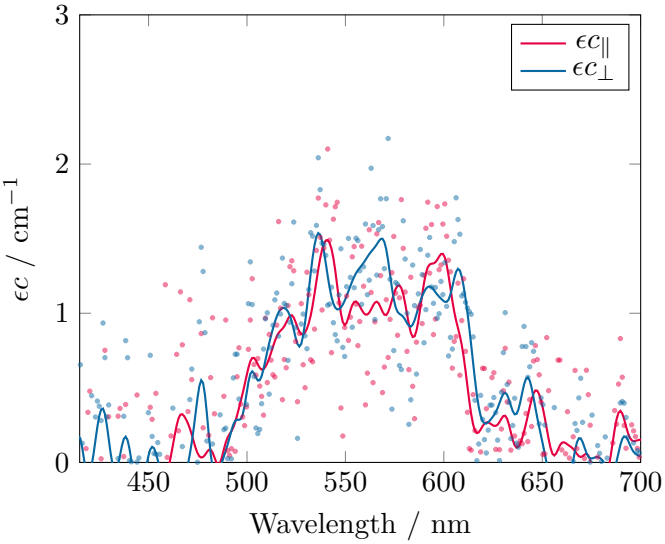

Figure 4.72: *EW-CEAS spectrum of a 250* nM *crystal violet solution adsorbed onto a PLGA coated prism, 600 seconds after introduction to the surface. Data has been smoothed using a running average filter (span = 15* nm*) for clarity.*

200 s, $\epsilon c_{||}$ and $\epsilon c_{\perp}$ for both remaining components become almost equal, indicating a close to isotropic distribution of molecules; $\langle\theta\rangle$ is $55.7 \pm 0.5°$ and $55.7 \pm 0.3°$ for the bands at 543 and 594 nm respectively. The spectrum at $t = 600$ s is shown in Figure 4.72. The lower signal to noise ratio here makes interpretation difficult, but the general shape appears similar to that for 250 nM CV on bare silica.

One potential explanation of this behaviour is that the initially negative surface of the PLGA film causes the positively charged CV molecules to adsorb more strongly than to the bare silica surface. After a short time, the increasingly neutral PLGA film can no longer remain attached to the surface, and 'peels off' the silica, taking most of the adsorbed crystal violet with it. All that then remains is a small amount of isotropically oriented monomer and dimer.

To test this hypothesis, experiments were performed at different flow rates, which correspond to different rates of adsorption. The effect of flow rate is shown in Figure 4.73.

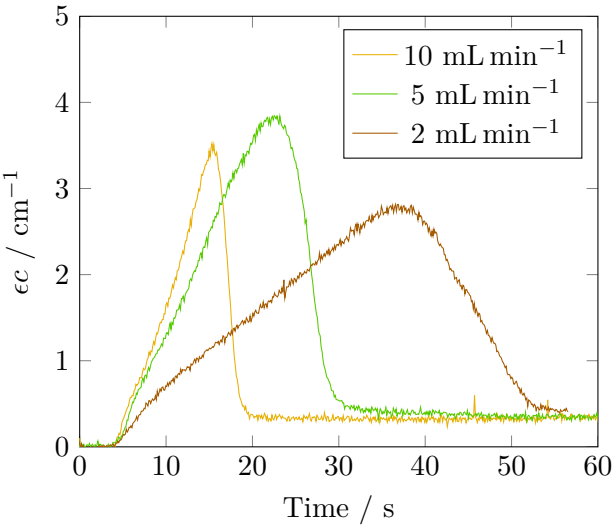

Figure 4.73: *ϵc at 600* nm *compared for various flow rates of 250* nM *CV on a PLGA coated surface. The rate of adsorption and subsequent loss of CV increases with increasing flow rate.*

An increased flow rate increases both the rate of build up of CV on the surface through increased mass transport, and the rate of subsequent loss. In each case, the rise in ϵc is approximately linear, and the maximum ϵc reached is similar, although not identical; ϵc after loss of the film is almost identical for each flow rate.

Firstly, this suggests that the loss process begins when a critical amount of CV is adsorbed. In each case, roughly the same value of ϵc is reached before it begins to fall.

Secondly, the fact that the rate of the fall in ϵc depends on flow rate suggests that the film is not lost suddenly once the critical concentration is reached, but piecemeal as the adhesion between the PLGA and the surface is reduced. This could either be due to more CV adsorbing, reducing adhesion between the film and the surface (which would happen faster at increased flow rates), or due to a higher shear force on the film (which would also be higher at increased flow rates).

Component	$\langle\theta\rangle$ / °
505 nm	36.8 ± 0.5
543 nm	63.8 ± 0.2
594 nm	65.3 ± 0.2

Table 4.5: *The expectation values for the angle of the TDM relative to the surface normal for the three components fitted for 25* µM *crystal violet at the PLGA/water interface. The uncertainties are the variation of the calculated angle over* $t = 45$ *to* 100 s – *this does not take into account the uncertainty in the measurement itself.*

4.8.4.2 At 25 μM

With 25 µM crystal violet in water flowed across a PLGA coated prism at 5 mL min^{-1}, the interfacial absorbance (Figure 4.74) is similar, but not identical, to that on bare silica. Firstly, the maximum value of ϵc reached is higher, over 800 cm^{-1}, compared to 160 cm^{-1}. This is due to the increased negative charge of PLGA compared to silica, driving interfacial adsorption. Secondly, the difference in || and $\perp$ polarisations is more pronounced, with $\epsilon c_{\perp}$ being much stronger at the red end of the spectrum; the orientational distribution of the different species has changed.

Fitting the spectra using the components from Table 4.2 is only partially successful. Firstly the position of the peak in ϵc is clearly blue-shifted compared the fitted component at 505 nm. This blue-shift indicates that stacking angle of the aggregate has moved further towards the face-to-face orientation, in accordance with Figure 4.12. Indeed, the average orientation angle for the fitted band is 36.8°, closer to the surface normal than for the results on bare silica (43.6°). Furthermore, the values of $\langle\theta\rangle$ for the components at 543 and 549 nm also change to be further from isotropic (63.8 and 65.3° compared to 56.7 and 58° on bare silica).

Secondly, the fit around 650 nm is poor, the fit under-representing the ϵc in this region. The increased absorbance here is likely due to the presence of J-aggregates, the absorption bands of which are red-shifted from the monomer.

The kinetic profile of each component is shown in Figures 4.75 to 4.79. Here, ϵc rapidly reaches a maximum before slowly falling over the course of minutes, unlike on bare silica where, at the same concentration, there is a continual rise over the course of minutes. The dramatic fall in ϵc observed with 250 nM CV on PLGA is not seen here, instead a more modest decrease occurs, and the component at 505 nm remains at long times.

The drop in ϵc can again be ascribed to the loss of the PLGA film, similar to the effect at lower concentration. This loss occurs more rapidly than at 250 nM (within 20 s vs. 60 s)

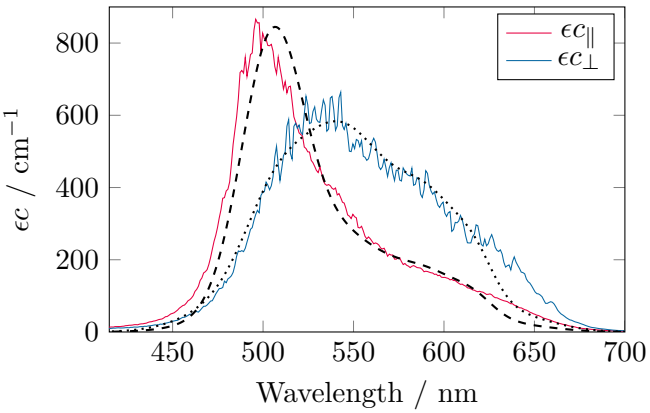

Figure 4.74: *Spectrum of 25* µM *crystal violet flowed (5* mL min^{-1}*) over a PLGA coated prism, 100 seconds after introduction to the surface. Fits are shown by the dotted and dashed lines.*

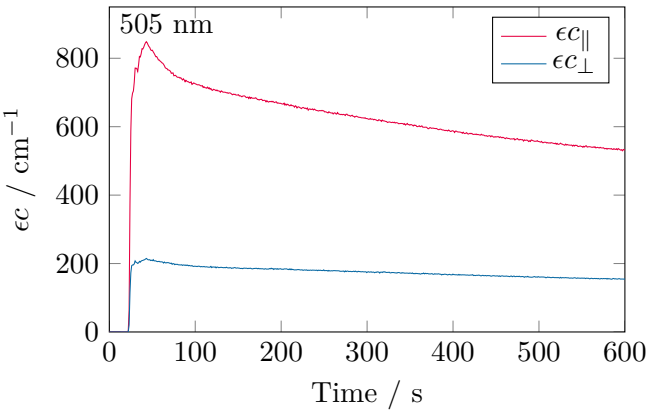

Figure 4.75: *Kinetic trace of the component at 505* nm*, showing rapid adsorption, PLGA film rupture, and slow loss of interfacial CV.*

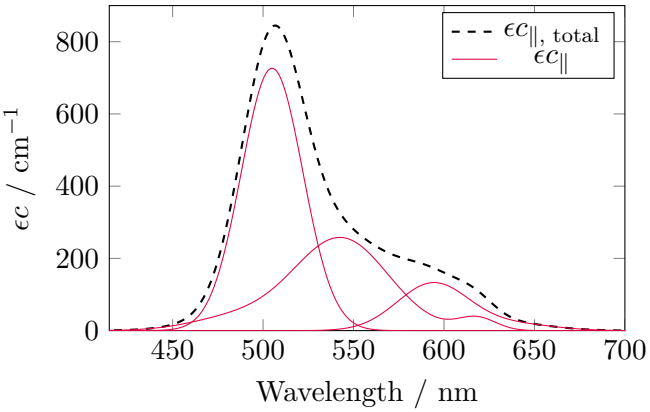

Figure 4.76: *Three fitted components of $\epsilon c_{\parallel}$ and $\epsilon c_{\perp}$ from Figure 4.74. The three components for each polarisation are summed to give the total fit.*

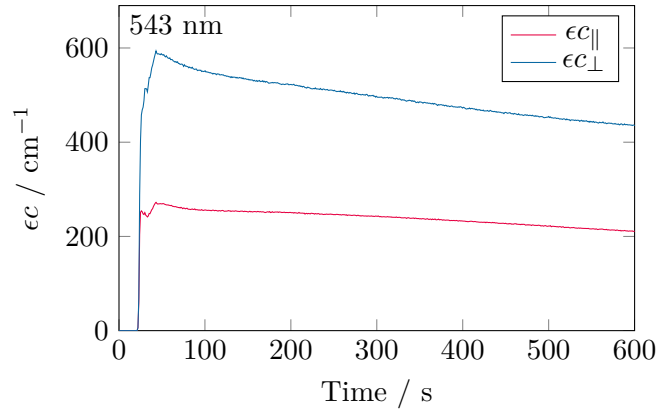

Figure 4.77: *Kinetic trace of the component at 543* nm.

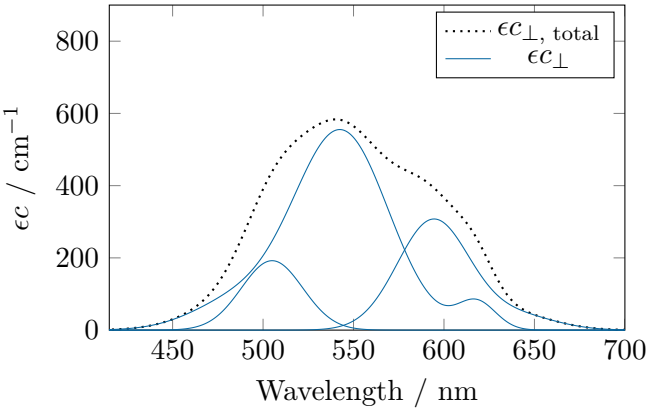

Figure 4.78: *Three fitted components of $\epsilon c_{\parallel}$ and $\epsilon c_{\perp}$ from Figure 4.74. The three components for each polarisation are summed to give the total fit.*

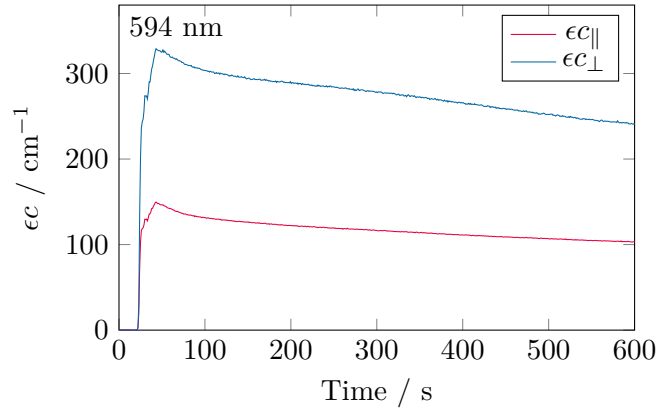

Figure 4.79: *Kinetic trace of the component at 594* nm.

as would be expected for a more highly concentrated solution.

The fact that the aggregate band remains even after the loss of the PLGA film is perhaps not surprising, given that the aggregate is seen even on bare silica at this concentration (Section 4.8.2.3). Once the bare silica surface has been exposed by the loss of the PLGA film, large aggregates are still able to be formed.

4.9 Radical pairs at the interface

In Chapter 3, the idea of using crystallisation to align a magnetoreceptor was introduced. That method had the benefit of a high degree of alignment; it is mainly applicable, however, to systems that are fluorescent, and to ones with a significant MFE on the fluorescent species. Additionally, the system must be one that crystallises readily, and where the MFE is not suppressed by crystallisation.

Another approach to measuring magnetic field effects in aligned systems is to use a surface as the source of alignment,[201] such as that provided by the silica-solvent interface in EW-CEAS. If the magnetoreceptor could be aligned at the interface, then the magnetic field effect on the radical absorption with respect to the field direction could be measured, potentially probing any MFE anisotropy. In addition to this, the small penetration depth of the evanescent field in EW-CEAS could allow miniaturisation of the sample volume to around a microlitre; previously precious samples could then be treated as effectively disposable. Furthermore, by using the dual-cut prism, the probed sample region can be laser-excited using the evanescent wave, closely matching the sample volume exposed to probe and pump beams. Light-induced degradation of the sample can therefore be minimised.

Presented here is a proof of principle for magnetic field effect measurement using EW-CEAS, using the FMN-HEWL model system.

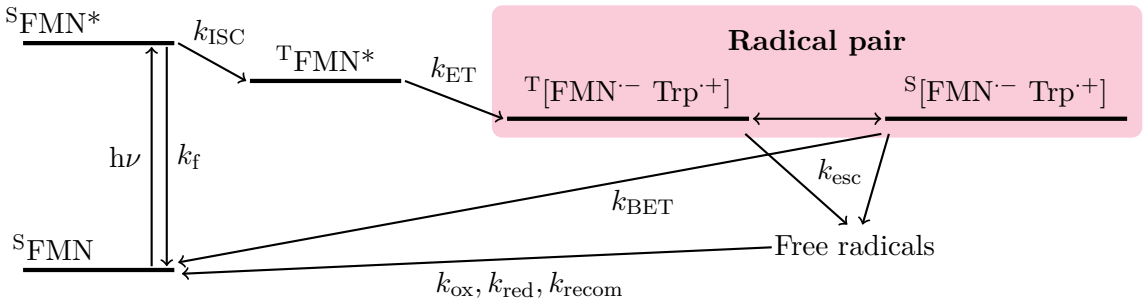

Figure 4.80: *FMN-HEWL photocycle, showing excitation (hν), fluorescence (k_f), intersystem crossing (k_{ISC}), electron transfer (k_{ET}), back electron transfer (k_{BET}), escape (k_{esc}), oxidation/reduction processes (k_{ox}, k_{red}), and free radical recombination (k_{recom}).*

4.9.1 Experimental considerations

The magnetic field effect experiments presented here were performed using the polarisation sensitive EW-CEAS instrument as described in Sections 4.2.5 and 4.4, with the addition

of a set of home-built Helmholtz coils and a 450 nm, 50 mW diode laser.

The diode laser was used to photoexcite the sample. The beam path was arranged such that it entered the prism along the non-cavity (short) axis, being totally internally reflected at the top surface, photoexciting the sample via the evanescent wave. This arrangement minimises photodegradation of the sample.

The magnetic field coils were placed surrounding the prism, centred around the probed region, with the direction of the magnetic field parallel to the prism surface normal. The coils could produce a magnetic field strength of up to 16 mT using a home built power supply.

The magnetic field effect experiments presented here were performed using a function generator (Rigol DG1022) to vary the magnetic field between 0 and 16 mT in a square wave function (period = 2 s, duty cycle = 50%). The exposure time of the CCD was set to be 0.5 s, with a cycle rate of 1 Hz. The square wave of the magnetic field was then synchronised manually to the CCD, ensuring that the switching of the field occurred when the CCD was not acquiring. The MFE could then be calculated as discussed in Section 3.3.

4.9.2 FMN

The spectrum of 1 mM FMN collected by EW-CEAS is displayed in Figure 4.81. FMN does not noticeably adsorb to the silica surface, as evidenced by the fact that ϵc for both polarisations are slightly less than the bulk value (indicating a non-enhanced local concentration and isotropic orientational distribution), and that the kinetic trace shows a step change in ϵc on introduction of the solution to the cell (Figure 4.82).

Photoillumination of FMN using 450 nm laser light causes excitation of FMN to the S_1 state. With FMN alone, the two return pathways to the ground state are by fluorescence from S_1, and via T_1. No radical pair is formed, and there is expected to be no magnetic field effect.

The MFE on application of a 16 mT field is shown in Figure 4.83; it is zero over the ground state region of FMN, as expected.

4.9.3 FMN-HEWL

Photoexcitation of FMN in the prescence of HEWL results in the formation of radical pairs between FMN and tryptophan residues on the surface of lysozyme;[87,94] the system

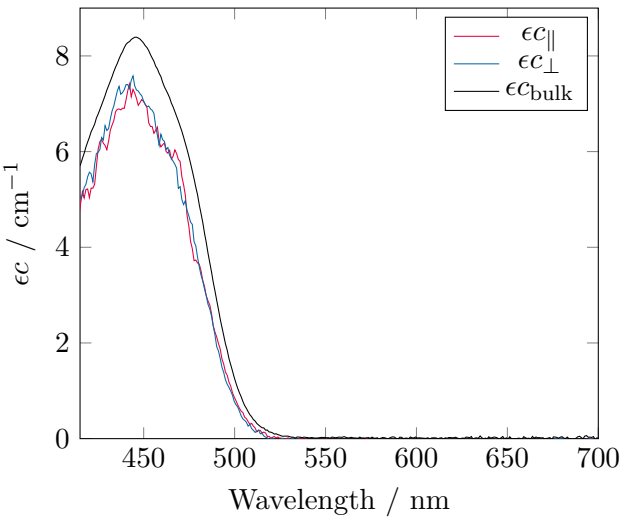

Figure 4.81: *EW-CEAS spectrum of 1* mM *FMN.* $\epsilon c_{\parallel}$ *and* $\epsilon c_{\perp}$ *are very similar across the entire spectrum, and are only slightly less than* ϵc_{bulk}*, suggesting little to no interfacial adsorption.*

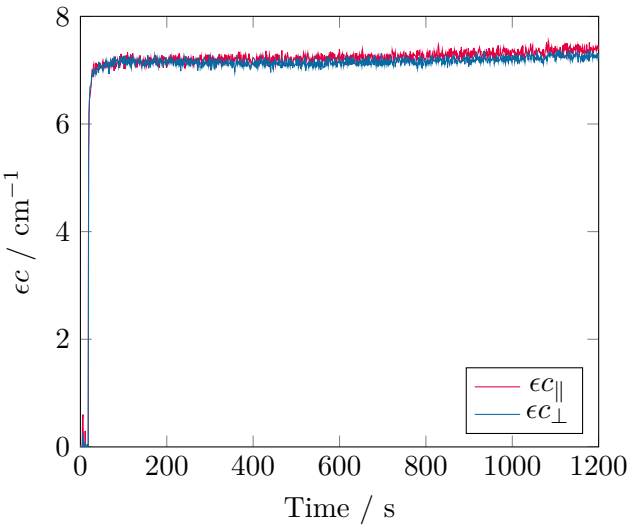

Figure 4.82: *Kinetic trace of 1* mM *FMN as it is introduced to the prism surface, measured at 450* nm*. The lack of any discernible growth in* ϵc *over this timescale suggests little to no interfacial adsorption.*

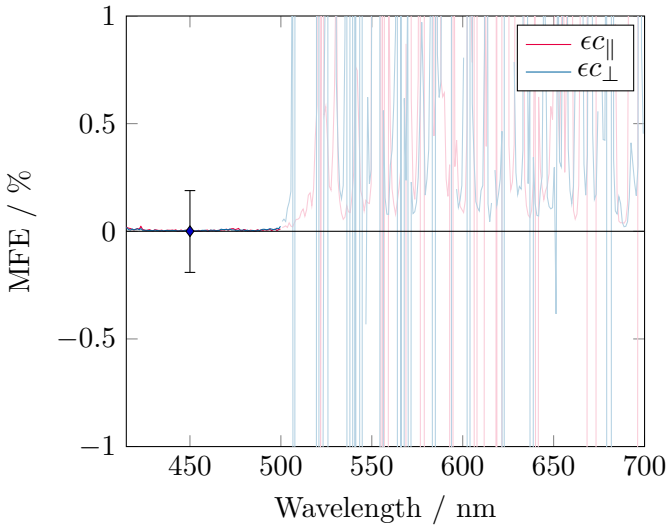

Figure 4.83: *MFE spectrum of 1* mM *FMN, as measured by EW-CEAS. There is no perceptible MFE across the FMN band (415–500* nm*). Note that the MFE measurement is unreliable above 500* nm*, since the absorbance of FMN is negligible in this region.*

can then cycle around the photoscheme shown in Figure 4.80.

The spectrum of a solution of 1 mM FMN, 1 mM HEWL is shown in Figure 4.84. There is a weak effect on the effective surface concentration of FMN caused by the addition of HEWL; there is a modest increase in ϵc (3×) compared to FMN alone, with a slight enhancement in $\epsilon c_{\perp}$ as compared to $\epsilon c_{||}$. Lysozyme is known to adsorb to silica,[202–204] with the change in surface charge likely being responsible for the enhancement of FMN concentration.

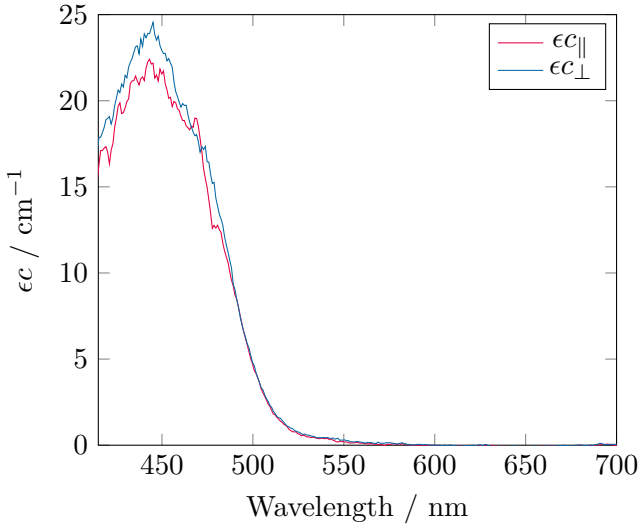

Figure 4.84: *EW spectrum of a 1* mM *FMN, 1* mM *HEWL solution. The slightly higher ϵc than for* mM *FMN alone suggests a small amount of co-adsorption of FMN and HEWL to the surface.*

Photoexcitation of the sample using a 450 nm laser results in the spectrum in Figure 4.85. There are two main features in this spectrum. Firstly, ground state bleaching can be seen between 400 and 500 nm. The change in ϵc is approximately 0.2 cm^{-1}; around 1% of the FMN has been pumped out of the ground state at any one time. Note also the scattered laser light at 450 nm.

The other band, between 500 and 700 nm, is the $FMNH^{\cdot}$ radical,[205] one half of the radical pair. The RP state is relatively long lived, tens of microseconds,[87] compared to the nanosecond lifetimes of S_1 and T_1. Consequently, only the ground and radical states are significantly populated, and the $FMNH^{\cdot}$ band appears approximately stoichiometrically with the bleached ground state[§]

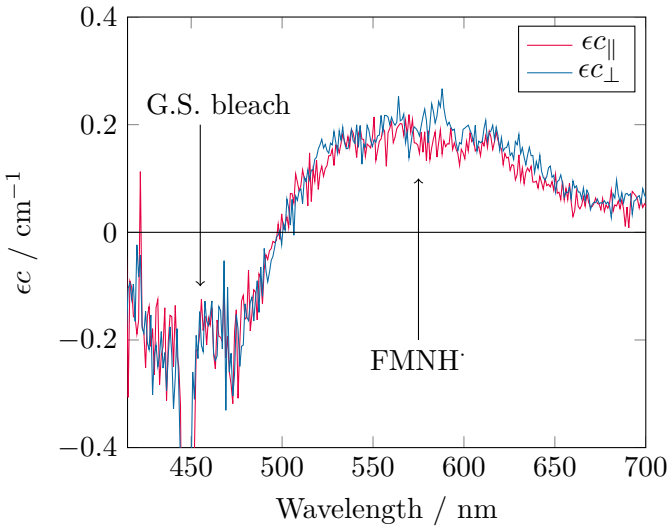

Figure 4.85: *Spectrum of photoexcited FMN-HEWL. The ground-state bleaching of FMN can be observed between 400 and 500* nm*; the* $FMNH^{\cdot}$ *radical band is observed between 500 and 700* nm.

Application of a magnetic field changes the rate of mixing between singlet and triplet radical pair states, as discussed in Section 3.2.6, and thence modifies both the radical and ground state populations via the radical pair mechanism. The percentage MFE in the radical region on application of a 16 mT magnetic field is shown in Figure 4.86. The MFE in the radical region between 525 and 600 nm is $0.42 \pm 0.19\%$; a similarly sized effect for that observed in the experiments on Chapter 3. A magnetic field effect on the ground state region is also expected here, but is obscured by noise. This is most likely due to the lower brightness of the SCS in the blue region, with the consequently lower signal-to-noise ratio obscuring the MFE in this region.

[§]This can be inferred from Liu *et al.*,[206] which gives the extinction coefficients of the FAD states; it

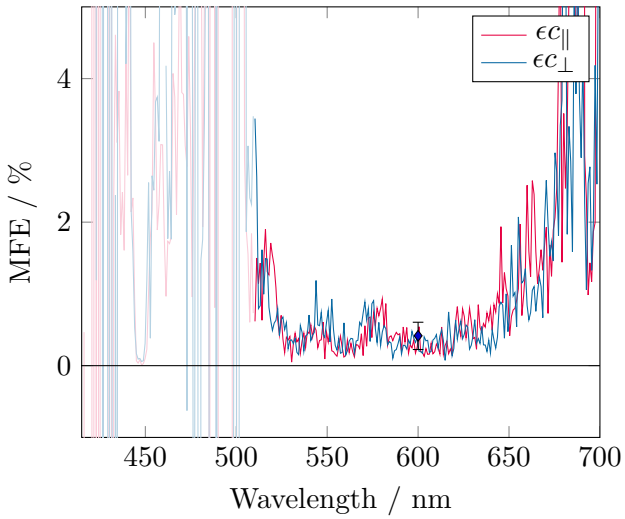

Figure 4.86: *%MFE spectrum of 1* mM *FMN with 1* mM *HEWL for an applied magnetic field strength of 16* mT*. The mean MFE across the radical region is* $0.42 \pm 0.19\%$*.*

is a reasonable assumption that FMN is similar.

4.10 Conclusions and future directions

Presented here are results from a variety of systems, showing the breadth of possibilities for EW-CEAS as a surface-sensitive optical spectroscopy method.

The use of an optical cavity to enhance the sensitivity of absorption measurements is now well established, covering a range of approaches from CRDS to broad-band CEAS. Each approach has benefits and drawbacks, and may be more of less suited to a particular problem. Previous work using the evanescent wave as a probe of the thin layer at an interface has focussed on EW-CRDS, which has the benefit of high time and spectral resolution and calibration-free absorbance measurements.

The EW-CEAS experiment presented here extends upon this work, using the intra-cavity prism design of EW-CRDS combined with the broad-band laser light source and CCD detection of BBCEAS. This change trades time resolution for the ability to record the entire visible region at once, with the minor additional cost of the CEF calibration.

Sections 4.5 to 4.9 show a variety of systems with different absorption behaviour measured by EW-CEAS. Cresol red does not adsorb to the silica surface, a fact easily discernible from the spectrum, which is quantitatively identical to that in the bulk, and the flat kinetic profile. Gold nanoparticles adsorb onto the PLL-coated surface over the course of minutes; the fact that they are monomerically dispersed can be inferred from the position of the LSPR peak, which does not shift on adsorption.

A taste of the real power of EW-CEAS as a probe of interfacial processes is shown in Section 4.7, which showing results of methylene blue adsorbing onto the surface. The spectrum shows a large shift in the absorption maximum compared to the bulk solution, which can be explained as dimerisation occurring at the surface. The spectrum of the dimer can be extracted, and the rate constant for dimer formation determined from the kinetic profiles.

The complex adsorption behaviour of crystal violet on silica and polyelectrolyte surfaces can be studied using polarisation sensitive EW-CEAS. Multimer formation occurs at the surface here, and the ability to capture the entire visible spectrum means that the kinetic behaviour of individual spectral components can be extracted and examined. Furthermore, polarisation-sensitive detection allows information about the orientation of each species relative to the surface to be determined.

The magnetic field effect experiments in Section 4.9 clearly establish the use of this technique in the study of MFEs. Here a relatively small MFE of 0.4% was easily measurable

for species with only a modestly increased surface concentration; a system which is strongly adsorbed or tethered to the surface could in principle be measured to even higher precision.

Bibliography

[1] Walther Gerlach and Otto Stern. Der experimentelle nachweis der richtungsquantelung im magnetfeld. *Zeitschrift für Physik*, 9(1):349–352, 1922.

[2] W. Pauli. Über den zusammenhang des abschlusses der elektronengruppen im atom mit der komplexstruktur der spektren. *Zeitschrift für Physik*, 31(1):765–783, 1925.

[3] G. E. Uhlenbeck and S. Goudsmit. Ersetzung der hypothese vom unmechanischen zwang durch eine forderung bezüglich des inneren verhaltens jedes einzelnen elektrons. *Die Naturwissenschaften*, 13(47):953–954, 1925.

[4] P. A. M. Dirac. On the theory of quantum mechanics. *Proceedings of the Royal Society of London A: Mathematical, Physical and Engineering Sciences*, 112(762):661–677, 1926.

[5] Christoph Riplinger, Joseph P. Y. Kao, Gerald M. Rosen, Velavan Kathirvelu, Gareth R. Eaton, Sandra S. Eaton, Andrei Kutateladze, and Frank Neese. Interaction of radical pairs through-bond and through-space: Scope and limitations of the point-dipole approximation in electron paramagnetic resonance spectroscopy. *Journal of the American Chemical Society*, 131(29):10092–10106, 2009.

[6] A. Abragam and M. H. L. Pryce. Theory of the nuclear hyperfine structure of paramagnetic resonance spectra in crystals. *Proceedings of the Royal Society of London A: Mathematical, Physical and Engineering Sciences*, 205(1080):135–153, 1951.

[7] Pierre Bouguer. Essai d'optique sur la gradation de la lumiere. pages 16–22, 1729.

[8] Beer. Bestimmung der absorption des rothen lichts in farbigen flüssigkeiten. *Annalen der Physik*, 162(5):78–88, 1852.

[9] Cyrus Levinthal. How to fold graciously. In *Mossbauer Spectroscopy in Biological Systems: Proceedings of a meeting held at Allerton House, Monticello, Illinois*, pages 22–24. University of Illinois Press, 1969.

[10] Cyrus Levinthal. Are there pathways for protein folding? *Journal de Chimie Physique*, 65(1):44–45, 1968.

[11] José Nelson Onuchic and Peter G Wolynes. Theory of protein folding. *Current Opinion in Structural Biology*, 14(1):70 – 75, 2004.

[12] Christian P. Schultz. Illuminating folding intermediates. *Nature Structural & Molecular Biology*, 7(1):7–10, 2000.

[13] Ken A. Dill and Justin L. MacCallum. The protein-folding problem, 50 years on. *Science*, 338(6110):1042–1046, 2012.

[14] G.N. Ramachandran, C. Ramakrishnan, and V. Sasisekharan. Stereochemistry of polypeptide chain configurations. *Journal of Molecular Biology*, 7(1):95–99, 1963.

[15] O B Ptitsyn. Stadiinyi mekhanizm samoorganizatsii belkovykh molekul (Stages in the mechanism of self-organization of protein molecules). *Dokl Akad Nauk SSSR*, 210(5):1213–1215, 1973.

[16] Kunihiro Kuwajima, Katsutoshi Nitta, Michio Yoneyama, and Shintaro Sugai. Three-state denaturation of α-lactalbumin by guanidine hydrochloride. *Journal of Molecular Biology*, 106(2):359–373, 1976.

[17] Kunihiro Kuwajima, Katsutoshi Nitta, and Shintaro Sugai. Electrophoretic investigations of the acid conformational change of α-lactalbumin. *Journal of Biochemistry*, 78(1):205–211, 1975.

[18] Katsutoshi Nitta and Shintaro Sugai. The evolution of lysozyme and α-lactalbumin. *European Journal of Biochemistry*, 182(1):111–118, 1989.

[19] H A McKenzie and F H White, Jr. Studies on a trace cell lytic activity associated with alpha-lactalbumin. *International Journal of Biochemistry*, 14(2):347–356, 1987.

[20] Naveen Chandra, Keith Brew, and K Ravi Acharya. Structural evidence for the presence of a secondary calcium binding site in human alpha-lactalbumin. *Biochemistry*, 37(14):4767–4772, 1998.

[21] Eric F Pettersen, Thomas D Goddard, Conrad C Huang, Gregory S Couch, Daniel M Greenblatt, Elaine C Meng, and Thomas E Ferrin. UCSF Chimera – a visualization system for exploratory research and analysis. *Journal of computational chemistry*, 25(13):1605–1612, 2004.

[22] Mikio Kataoka, Fumio Tokunaga, Kunihiro Kuwajima, and Yuji Goto. Structural characterization of the molten globule of α-lactalbumin by solution x-ray scattering. *Protein Science*, 6(2):422–430, 1997.

[23] Lawren C. Wu, Brenda A. Schulman, Zheng-yu Peng, and Peter S. Kim. Disulfide determinants of calcium-induced packing in α-lactalbumin. *Biochemistry*, 35(3):859–863, 1996.

[24] Brenda A. Schulman and Peter S. Kim. Proline scanning mutagenesis of a molten globule reveals non-cooperative formation of a protein's overall topology. *Nature Structural Biology*, 3(8):682–687, 1996.

[25] Brenda A. Schulman, Peter S. Kim, Christopher M. Dobson, and Christina Redfield. A residue-specific NMR view of the non-cooperative unfolding of a molten globule. *Nature Structural Biology*, 4(8):630–634, 1997.

[26] David Eliezer and Peter E. Wright. Is apomyoglobin a molten globule? structural characterization by NMR. *Journal of Molecular Biology*, 263(4):531–538, 1996.

[27] Christina Redfield, Brenda A. Schulman, Michael A. Milhollen, Peter S. Kim, and Christopher M. Dobson. α-lactalbumin forms a compact molten globule in the absence of disulfide bonds. *Nature Structural Biology*, 6(10):948–952, 1999.

[28] Stéphanie Ramboarina and Christina Redfield. Probing the effect of temperature on the backbone dynamics of the human α-lactalbumin molten globule. *Journal of the American Chemical Society*, 130(46):15318–15326, 2008.

[29] Stephan Schwarzinger, Gerard J. A. Kroon, Ted R. Foss, John Chung, Peter E. Wright, and H. Jane Dyson. Sequence-dependent correction of random coil NMR chemical shifts. *Journal of the American Chemical Society*, 123(13):2970–2978, 2001.

[30] F. Bloch. Nuclear induction. *Physical Review*, 70:460–474, 1946.

[31] A. D. Milov, K. M. Salikhov, and M. D. Shchirov. Use of the double resonance in electron spin echo method for the study of paramagnetic center spatial distribution in solids. *Fizika Tverdogo Tela*, 23(4):975–982, 1981.

[32] A.D. Milov, A.B. Ponomarev, and Yu.D. Tsvetkov. Electron-electron double resonance in electron spin echo: Model biradical systems and the sensitized photolysis of decalin. *Chemical Physics Letters*, 110(1):67 – 72, 1984.

[33] Irene M. C. van Amsterdam, Marcellus Ubbink, Gerard W. Canters, and Martina Huber. Measurement of a Cu–Cu distance of 26 Å by a pulsed EPR method. *Angewandte Chemie International Edition*, 42(1):62–64, 2003.

[34] M Pannier, S Veit, A Godt, G Jeschke, and H.W Spiess. Dead-time free measurement of dipole-dipole interactions between electron spins. *Journal of Magnetic Resonance*, 142(2):331–340, 2000.

[35] Gunnar Jeschke. DEER distance measurements on proteins. *Annual Review of Physical Chemistry*, 63(1):419–446, 2012.

[36] V. Pfannebecker, H. Klos, M. Hubrich, T. Volkmer, A. Heuer, U. Wiesner, and H. W. Spiess. Determination of end-to-end distances in oligomers by pulsed EPR. *The Journal of Physical Chemistry*, 100(32):13428–13432, 1996.

[37] Andrey Nikolayevich Tikhonov. ĐđĐś ÑČÑĄÑĆĐ"ĐźÑĞĐÿĐšĐ"ÑĄÑĆĐÿ Đ"ĐśÑĂĐřÑĆĐ · ÑŃÑĚ ĐůĐřĐţĐřÑĞ [on the stability of inverse problems]. *Doklady Akademii Nauk SSSR*, 39((5)):195–198, 1943.

[38] Yun-Wei Chiang, Peter P. Borbat, and Jack H. Freed. The determination of pair distance distributions by pulsed ESR using tikhonov regularization. *Journal of Magnetic Resonance*, 172(2):279–295, 2005.

[39] G. Jeschke, V Chechik, P. Ionita, A. Godt, H. Zimmermann, J. Banham, C.R. Timmel, D. Hilger, and H. Jung. DeerAnalysis2006–a comprehensive software package for analyzing pulsed eldor data. *Applied Magnetic Resonance*, 30(3-4):473–498, 2006.

[40] *MATLAB and Statistics Toolbox Release 2013b*. The MathWorks, Inc., Natick, Massachusetts, United States, 2013.

[41] Gunnar Jeschke. *Interpretation of Dipolar EPR Data in Terms of Protein Structure*, volume 152 of *Structure and Bonding*. Springer Berlin Heidelberg, 2013.

[42] G Jeschke. *DeerAnalysis2013 Manual*.

[43] Gunnar Jeschke and Yevhen Polyhach. Distance measurements on spin-labelled biomacromolecules by pulsed electron paramagnetic resonance. *Physical Chemistry Chemical Physics*, 9:1895–1910, 2007.

[44] Richard Ward, Andrew Bowman, Erman Sozudogru, Hassane El-Mkami, Tom Owen-Hughes, and David G. Norman. EPR distance measurements in deuterated proteins. *Journal of Magnetic Resonance*, 207(1):164–167, 2010.

[45] Sergey Milikisyants, Edgar J.J. Groenen, and Martina Huber. Observer-selective double electron–electron-spin resonance, a pulse sequence to improve orientation selection. *Journal of Magnetic Resonance*, 192(2):275–279, 2008.

[46] J.E. Banham, C.M. Baker, S. Ceola, I.J. Day, G.H. Grant, E.J.J. Groenen, C.T. Rodgers, G. Jeschke, and C.R. Timmel. Distance measurements in the borderline region of applicability of CW EPR and DEER: A model study on a homologous series of spin-labelled peptides. *Journal of Magnetic Resonance*, 191(2):202–218, 2008.

[47] Stefan Stoll and Arthur Schweiger. EasySpin, a comprehensive software package for spectral simulation and analysis in EPR. *Journal of Magnetic Resonance*, 178(1):42–55, 2006.

[48] Mark R. Fleissner, Eric M. Brustad, Tamás Kálai, Christian Altenbach, Duilio Cascio, Francis B. Peters, Kálmán Hideg, Sebastian Peuker, Peter G. Schultz, and Wayne L. Hubbell. Site-directed spin labeling of a genetically encoded unnatural amino acid. *Proceedings of the National Academy of Sciences*, 106(51):21637–21642, 2009.

[49] Christian Beier and Heinz-Jurgen Steinhoff. A structure-based simulation approach for electron paramagnetic resonance spectra using molecular and stochastic dynamics simulations. *Biophysical Journal*, 91(7):2647–2664, 2006.

[50] Fangyu Ding, Melinda Layten, and Carlos Simmerling. Solution structure of HIV-1 protease flaps probed by comparison of molecular dynamics simulation ensembles and EPR experiments. *Journal of the American Chemical Society*, 130(23):7184–7185, 2008.

[51] Deniz Sezer, Jack H. Freed, and Benoît Roux. Multifrequency electron spin resonance spectra of a spin-labeled protein calculated from molecular dynamics simulations. *Journal of the American Chemical Society*, 131(7):2597–2605, 2009.

[52] Yevhen Polyhach and Gunnar Jeschke. Prediction of favourable sites for spin labelling of proteins. *Spectroscopy*, 24(6):651–659, 2010.

[53] Yevhen Polyhach, Enrica Bordignon, and Gunnar Jeschke. Rotamer libraries of spin labelled cysteines for protein studies. *Physical Chemistry Chemical Physics*, 13:2356–2366, 2011.

[54] H. J. Steinhoff, O Dombrowsky, C Karin, and C Schneiderhahn. Two dimensional diffusion of small molecules on protein surfaces: an epr study of the restricted translational diffusion of protein-bound spin labels. *European Biophysics Journal*, 20(5):293–303, 1991.

[55] H. J. Steinhoff, N. Radzwill, W. Thevis, V. Lenz, D. Brandenburg, A. Antson, G. Dodson, and A. Wollmer. Determination of interspin distances between spin labels attached to insulin: comparison of electron paramagnetic resonance data with the x-ray structure. *Biophysical Journal*, 73(6):3287–3298, 1997.

[56] Janet Banham. *Exploring long range structure in chemical and biological systems using electron paramagnetic resonance.* PhD thesis, University of Oxford, 2006.

[57] Heike I. Rösner and Christina Redfield. The human α-lactalbumin molten globule: Comparison of structural preferences at pH 2 and pH 7. *Journal of Molecular Biology*, 394(2):351–362, 2009.

[58] Charles Tanford, Kazuo Kawahara, and Savo Lapanje. Proteins in 6 M guanidine hydrochloride : Demonstration of random coil behaviour. *Journal of Biological Chemistry*, 241(8):1921–1923, 1966.

[59] Christopher T. Rodgers and P. J. Hore. Chemical magnetoreception in birds: The radical pair mechanism. *Proceedings of the National Academy of Sciences of the United States of America*, 106(2):353–360, 2009.

[60] Kiminori Maeda, Kevin B. Henbest, Filippo Cintolesi, Ilya Kuprov, Christopher T. Rodgers, Paul A. Liddell, Devens Gust, Christiane R. Timmel, and P.J. Hore. Chemical compass model of avian magnetoreception. *Nature*, 453:387–390, 2008.

[61] P A Valberg, R Kavet, and C N Rafferty. Can low-level 50/60 Hz electric and magnetic fields cause biological effects? *Radiation Research*, 148(1):2–21, 1997.

[62] Richard G Stevens, Scott Davis, David B Thomas, Larry E Anderson, and Bary W Wilson. Electric power, pineal function, and the risk of breast cancer. *The FASEB Journal*, 6(3):853–60, 1992.

[63] Lee S Caplan, Elinor R Schoenfeld, Erin S O'Leary, and M.Cristina Leske. Breast cancer and electromagnetic fields—a review. *Annals of Epidemiology*, 10(1):31–44, 2000.

[64] Daniel Wartenberg. Residential magnetic fields and childhood leukemia: a meta-analysis. *American Journal of Public Health*, 88(12):1787–1794, 1998.

[65] N Day. Exposure to power-frequency magnetic fields and the risk of childhood cancer. *The Lancet*, 354(9194):1925–1931, 1999.

[66] Thorsten Ritz, Salih Adem, and Klaus Schulten. A model for photoreceptor-based magnetoreception in birds. *Biophysical Journal*, 78(2):707–718, 2000.

[67] Hannah Hogben. *Coherent spin dynamics of radical pairs in weak magnetic fields*. PhD thesis, University of Oxford, 2011.

[68] Margaret Ahmad, Paul Galland, Thorsten Ritz, Roswitha Wiltschko, and Wolfgang Wiltschko. Magnetic intensity affects cryptochrome-dependent responses in *Arabidopsis thaliana*. *Planta*, 225:615–624, 2007.

[69] Sue-Re Harris, Kevin B. Henbest, Kiminori Maeda, John R. Pannell, Christiane R. Timmel, P.J. Hore, and Haruko Okamoto. Effect of magnetic fields on cryptochrome-dependent responses in Arabidopsis thaliana. *Journal of The Royal Society Interface*, 6(41):1193–1205, 2009.

[70] Wolfgang Wiltschko and Roswitha Wiltschko. Magnetic compass of european robins. *Science*, 176(4030):62–64, 1972.

[71] JB Phillips. Two magnetoreception pathways in a migratory salamander. *Science*, 233(4765):765–767, 1986.

[72] S. Marhold, W. Wiltschko, and H. Burda. A magnetic polarity compass for direction finding in a subterranean mammal. *Naturwissenschaften*, 84(9):421–423, 1997.

[73] Joseph L. Kirschvink and James L. Gould. Biogenic magnetite as a basis for magnetic field detection in animals. *Biosystems*, 13(3):181–201, 1981.

[74] Robert C. Beason, Natalie Dussourd, and Mark E. Deutschlander. Behavioural evidence for the use of magnetic material in magnetoreception by a migratory bird. *The Journal of Experimental Biology*, 198(1):141–146, 1995.

[75] Carol E. Diebel, Roger Proksch, Colin R. Green, Peter Neilson, and Michael M. Walker. Magnetite defines a vertebrate magnetoreceptor. *Nature*, 406(6793):299–302, 2000.

[76] Wolfgang Wiltschko and Roswitha Wiltschko. Light-dependent magnetoreception in birds: the behaviour of european robins, *Erithacus rubecula*, under monochromatic light of various wavelengths and intensities. *Journal of Experimental Biology*, 204(19):3295–3302, 2001.

[77] Rachel Muheim, Johan Bäckman, and Susanne Åkesson. Magnetic compass orientation in european robins is dependent on both wavelength and intensity of light. *Journal of Experimental Biology*, 205(24):3845–3856, 2002.

[78] Christine Nießner, Susanne Denzau, Katrin Stapput, Margaret Ahmad, Leo Peichl, Wolfgang Wiltschko, and Roswitha Wiltschko. Magnetoreception: activated cryptochrome 1a concurs with magnetic orientation in birds. *Journal of The Royal Society Interface*, 10(88), 2013.

[79] Peter Thalau, Thorsten Ritz, Katrin Stapput, Roswitha Wiltschko, and Wolfgang Wiltschko. Magnetic compass orientation of migratory birds in the presence of a 1.315 MHz oscillating field. *Naturwissenschaften*, 92(2):86–90, 2005.

[80] Svenja Engels, Nils-Lasse Schneider, Nele Lefeldt, Christine Maira Hein, Manuela Zapka, Andreas Michalik, Dana Elbers, Achim Kittel, P. J. Hore, and Henrik Mouritsen. Anthropogenic electromagnetic noise disrupts magnetic compass orientation in a migratory bird. *Nature*, 509(7500):353–356, 05 2014.

[81] Klaus Schulten, Charles E. Swenberg, and Albert Weller. A biomagnetic sensory mechanism based on magnetic field modulated coherent electron spin motion. *Zeitschrift für Physikalische Chemie*, 111:1–5, 1978.

[82] Andrea Möller, Sven Sagasser, Wolfgang Wiltschko, and Bernd Schierwater. Retinal cryptochrome in a migratory passerine bird: a possible transducer for the avian magnetic compass. *Naturwissenschaften*, 91(12):585–588, 2004.

[83] Anthony R. Cashmore, Jose A. Jarillo, Ying-Jie Wu, and Dongmei Liu. Cryptochromes: Blue light receptors for plants and animals. *Science*, 284(5415):760–765, 1999.

[84] Corinne Aubert, Marten H. Vos, Paul Mathis, Andre P. M. Eker, and Klaus Brettel. Intraprotein radical transfer during photoactivation of dna photolyase. *Nature*, 405(6786):586–590, 06 2000.

[85] Sang-Tae Kim, Paul F. Heelis, and Aziz Sancar. Role of tryptophans in substrate binding and catalysis by DNA photolyase. In *Redox-active amino acids in biology*, volume 258 of *Methods in Enzymology*, pages 319–343. Academic Press, 1995.

[86] Baldissera Giovani, Martin Byrdin, Margaret Ahmad, and Klaus Brettel. Light-induced electron transfer in a cryptochrome blue-light photoreceptor. *Nature Structural & Molecular Biology*, 10(6):489–490, 06 2003.

[87] Tomoaki Miura, Kiminori Maeda Maeda, and Tatsuo Arai. Effect of coulomb interaction on the dynamics of the radical pair in the system of flavin mononucleotide and hen egg-white lysozyme (HEWL) studied by a magnetic field effect. *Journal Of Chemical Physics B*, 107(26):6474–6478, 2003.

[88] Kiminori Maeda, Simon R. T. Neil, Kevin Barry Henbest, Stefan Weber, Erik Schleicher, Peter John Hore, Stuart R. Mackenzie, and Christiane R. Timmel. Following radical pair reactions in solution: A step change in sensitivity using cavity ring-down detection. *Journal of the American Chemical Society*, 133(44):17807–17815, 2011.

[89] Yasuhiro Kobori and James R. Norris. 1D radical motion in protein pocket: Proton-coupled electron transfer in human serum albumin. *Journal of the American Chemical Society*, 128(1):4–5, 2006.

[90] Yasuhiro Kobori and Masaaki Fuki. Protein–ligand structure and electronic coupling of photoinduced charge-separated state: 9,10-anthraquinone-1-sulfonate bound to human serum albumin. *Journal of the American Chemical Society*, 133(42):16770–16773, 2011.

[91] Christiane R. Timmel. *Magnetic field effects on radical pair reactions.* PhD thesis, University of Oxford, 1998.

[92] Bernice G. Segal, Michael Kaplan, and George K. Fraenkel. Measurement of g values in the electron spin resonance spectra of free radicals. *The Journal of Chemical Physics*, 43(12):4191–4200, 1965.

[93] Jonathan Storey. *Magnetic field effects on electron-hole recombination reactions - theoretical and experimental developments.* PhD thesis, University of Oxford, 2014.

[94] Alice Bowen. *Photo-Chemically Induced Dynamic Nuclear Polarisation (photo-CIDNP) of ^{13}C and ^{1}H in Proteins.* D. Phil. Transfer Thesis, 2009.

[95] Jing Li. Fluorescence study for magnetosensitive measurements in FMN/HEWL and FAD solution. Personal Communication, 05 2012.

[96] Emrys W. Evans, Jing Li, Jonathan G. Storey, Kiminori Maeda, Kevin B. Henbest, Charlotte A. Dodson, P. J. Hore, Stuart R. Mackenzie, and Christiane R. Timmel. Sensitive fluorescence-based detection of magnetic field effects in photoreactions of flavins. *Physical Chemistry Chemical Physics*, 17:18456–18463, 2015.

[97] Eduardo Silva and Ana M Edwards. *Flavins: Photochemistry and Photobiology.* Royal Society of Chemistry, 2006.

[98] Antonie J.W.G. Visser and Franz Müller. Time-resolved fluorescence on flavins and flavoproteins. In Lemuel D. Wright Donald B. McCormick, editor, *Vitamins and Coenzymes Part E*, volume 66 of *Methods in Enzymology*, pages 373 – 385. Academic Press, 1980.

[99] Ph. Wahl, J.C. Auchet, A.J.W.G. Visser, and F. Müller. Time resolved fluorescence of flavin adenine dinucleotide. *FEBS Letters*, 44(1):67–70, 1974.

[100] W. Holzer, A. Penzkofer, M. Fuhrmann, and P. Hegemann. Spectroscopic characterization of flavin mononucleotide bound to the LOV1 domain of Phot1 from *Chlamydomonas reinhardtii*. *Photochemistry and Photobiology*, 75(5):479–487, 2002.

[101] Aba Losi, Eugenia Polverini, Benjamin Quest, and Wolfgang Gärtner. First evidence for phototropin-related blue-light receptors in prokaryotes. *Biophysical Journal*, 82(5):2627–2634, 2002.

[102] Emrys Evans. A study of magnetic field effects on chemical compass model systems using optical spectroscopy methods. Master's thesis, University of Oxford, 2012.

[103] A. Weller, F. Nolting, and H. Staerk. A quantitative interpretation of the magnetic field effect on hyperfine-coupling-induced triplet fromation from radical ion pairs. *Chemical Physics Letters*, 96(1):24–27, 1983.

[104] Irene Russo Krauss, Antonello Merlino, Alessandro Vergara, and Filomena Sica. An overview of biological macromolecule crystallization. *International Journal of Molecular Sciences*, 14(6):11643, 2013.

[105] K Samaya Mohan, Soma Das, C Chockalingam, V Shanthi, and K Sekar. Lysdb - lysozyme structural database. *Acta Crystallographica Section D*, 60(3):597–600, 2004.

[106] Steven Johnson. Personal communication.

[107] B.W. Matthews. Solvent content of protein crystals. *Journal of Molecular Biology*, 33(2):491–497, 1968.

[108] Tom K.L. Meyvis, Stefaan C. De Smedt, Patrick Van Oostveldt, and Joseph Demeester. Fluorescence recovery after photobleaching: A versatile tool for mobility and interaction measurements in pharmaceutical research. *Pharmaceutical Research*, 16(8):1153–1162, 1999.

[109] D G A L Aarts and H N W Lekkerkerker. Confocal scanning laser microscopy on fluid–fluid demixing colloid–polymer mixtures. *Journal of Physics: Condensed Matter*, 16(38):S4231, 2004.

[110] Emrys Evans. Personal Communication.

[111] V.N. Morozov, G.S. Kachalova, V.U. Evtodienko, N.F. Lanina, and T.Ya. Morozova. Permeability of lysozyme tetragonal crystals to water. *European Biophysics Journal*, 24(2):93–98, 1995.

[112] S.A. Rani, B. Pitts, and P.S. Stewart. Rapid diffusion of fluorescent tracers into staphylococcus epidermidis biofilms visualized by time lapse microscopy. antimicrob. *Agents Chemother*, 49(2):728–732, 2005.

[113] P. Galambos and F.K. Forster. *Micro Total Analysis Systems.*, chapter Micro-Fluidic Diffusion Coefficient Measurement. 1998.

[114] A. Cvetkovic, A. J. J. Straathof, D. N. Hanlon, S. van der Zwaag, R. Krishna, and L. A. M. van der Wielen. Quantifying anisotropic solute transport in protein crystals using 3-d laser scanning confocal microscopy visualization. *Biotechnology and Bioengineering*, 86(4):389–398, 2004.

[115] Donald Voet and Alexander Rich. The crystal and molecular structure of an intermolecular complex between riboflavin and an adenosine derivative. *Proceedings of the National Academy of Sciences of the United States of America*, 68(6):1151–1156, 06 1971.

[116] FE Scarbrough, H Shieh, and D Voet. Crystal structure of a complex between lumiflavin and 2,6-diamino-9-ethylpurine: a flavin adenine dinucleotide model exhibiting charge-transfer interactions. *Proceedings of the National Academy of Sciences of the United States of America*, 73(11):3807—3811, November 1976.

[117] Rudi Berera. Ultrafast transient absorption spectroscopy: principles and application to photosynthetic systems. *Photosynthesis Research*, 101(2-3):105–18, 2009.

[118] A. H. Pfund. Atmospheric contamination. *Science*, 90(2336):326–327, 1939.

[119] John U. White. Long optical paths of large aperture. *Journal of the Optical Society of America*, 32(5):285–285, 1942.

[120] D. Herriott, H. Kogelnik, and R. Kompfner. Off-axis paths in spherical mirror interferometers. *Applied Optics*, 3(4):523–526, 1964.

[121] G. Hernandez. *Fabry-Pérot Interferometers*. Cambridge University Press, 1986.

[122] Mikhail Mazurenka, Andrew J. Orr-Ewing, Robert Peverall, and Grant A. D. Ritchie. Cavity ring-down and cavity enhanced spectroscopy using diode lasers. *Annual Reports on the Progress of Chemistry, Section C: Physical Chemistry*, 101:100–142, 2005.

[123] Orazio Svelto. *Principles of Lasers*. Springer, 2010.

[124] H. Kogelnik and T. Li. Laser beams and resonators. *Applied Optics*, 5(10):1550–1567, 1966.

[125] Ariel Lipson, Stephen G. Lipson, and Henry Lipson. *Optical Physics*. Cambridge University Press, 4th edition, 2010.

[126] J. M. Herbelin, J. A. McKay, M. A. Kwok, R. H. Ueunten, D. S. Urevig, D. J. Spencer, and D. J. Benard. Sensitive measurement of photon lifetime and true reflectances in an optical cavity by a phase-shift method. *Applied Optics*, 19(1):144–147, 1980.

[127] Dana Z. Anderson, Josef C. Frisch, and Carl S. Masser. Mirror reflectometer based on optical cavity decay time. *Applied Optics*, 23(8):1238–1245, 1984.

[128] Anthony O'Keefe and David A. G. Deacon. Cavity ring-down optical spectrometer for absorption measurements using pulsed laser sources. *Review of Scientific Instruments*, 59(12):2544–2551, 1988.

[129] Piotr Zalicki and Richard N. Zare. Cavity ring-down spectroscopy for quantitative absorption measurements. *The Journal of Chemical Physics*, 102(7):2708–2717, 1995.

[130] Joseph T. Hodges, J. Patrick Looney, and Roger D van Zee. Response of a ring-down cavity to an arbitrary excitation. *The Journal of Chemical Physics*, 105(23):10278–10288, 1996.

[131] Roger D. van Zee, Joseph T. Hodges, and J. Patrick Looney. Pulsed, single-mode cavity ringdown spectroscopy. *Applied Optics*, 38(18):3951–3960, 1999.

[132] Alexander J. Hallock, Elena S. F. Berman, and Richard N. Zare. Direct monitoring of absorption in solution by cavity ring-down spectroscopy. *Analytical Chemistry*, 74(7):1741–1743, 2002.

[133] Kate L. Snyder and Richard N. Zare. Cavity ring-down spectroscopy as a detector for liquid chromatography. *Analytical Chemistry*, 75(13):3086–3091, 2003.

[134] Anthony O'Keefe. Integrated cavity output analysis of ultra-weak absorption. *Chemical Physics Letters*, 293(5–6):331–336, 1998.

[135] Richard Engeln, Giel Berden, Rudy Peeters, and Gerard Meijer. Cavity enhanced absorption and cavity enhanced magnetic rotation spectroscopy. *Review of Scientific Instruments*, 69(11):3763–3769, 1998.

[136] Stephen M. Ball, Justin M. Langridge, and Roderic L. Jones. Broadband cavity enhanced absorption spectroscopy using light emitting diodes. *Chemical Physics Letters*, 398(1,3):68–74, 2004.

[137] Justin M. Langridge, Stephen M. Ball, and Roderic L. Jones. A compact broadband cavity enhanced absorption spectrometer for detection of atmospheric NO_2 using light emitting diodes. *Analyst*, 131:916–922, 2006.

[138] Sven E. Fiedler, Achim Hese, and Albert A. Ruth. Incoherent broad-band cavity-enhanced absorption spectroscopy of liquids. *Review of Scientific Instruments*, 76(2):023107, 2005.

[139] Timothy McGarvey, André Conjusteau, and Hideo Mabuchi. Finesse and sensitivity gain in cavity-enhanced absorption spectroscopy of biomolecules in solution. *Optics Express*, 14(22):10441–10451, 2006.

[140] L. van der Sneppen, A. Wiskerke, F. Ariese, C. Gooijer, and W. Ubachs. Improving the sensitivity of HPLC absorption detection by cavity ring-down spectroscopy in a liquid-only cavity. *Analytica Chimica Acta*, 558(1–2):2–6, 2006.

[141] Mathias Schnippering, Patrick R. Unwin, Johan Hult, Toni Laurila, Clemens F. Kaminski, Justin M. Langridge, Roderic L. Jones, Mikhail Mazurenka, and Stuart R. Mackenzie. Evanescent wave broadband cavity enhanced absorption spectroscopy using supercontinuum radiation: A new probe of electrochemical processes. *Electrochemistry Communications*, 10(12):1827–1830, 2008.

[142] Lineke van der Sneppen, Gus Hancock, Clemens Kaminski, Toni Laurila, Stuart R. Mackenzie, Simon R. T. Neil, Robert Peverall, Grant A. D. Ritchie, Mathias Schnippering, and Patrick R. Unwin. Following interfacial kinetics in real time using broadband evanescent wave cavity-enhanced absorption spectroscopy: a comparison of light-emitting diodes and supercontinuum sources. *Analyst*, 135:133–139, 2010.

[143] Ssegawa-Ssekintu Kiwanuka, Toni Laurila, and Clemens F. Kaminski. Sensitive method for the kinetic measurement of trace species in liquids using cavity enhanced absorption spectroscopy with broad bandwidth supercontinuum radiation. *Analytical Chemistry*, 82(17):7498–7501, 2010.

[144] Simon R. T. Neil, Cathy M. Rushworth, Claire Vallance, and Stuart R. Mackenzie. Broadband cavity-enhanced absorption spectroscopy for real time, in situ spectral analysis of microfluidic droplets. *Lab on a Chip*, 11:3953–3955, 2011.

[145] Simon R. T. Neil, Jing Li, Dean M. W. Sheppard, Jonathan Storey, Kiminori Maeda, Kevin B. Henbest, P. J. Hore, Christiane R. Timmel, and Stuart R. Mackenzie. Broadband cavity-enhanced detection of magnetic field effects in chemical models of a cryptochrome magnetoreceptor. *The Journal of Physical Chemistry B*, 118(15):4177–4184, 2014.

[146] Andrew C. R. Pipino, Jeffrey W. Hudgens, and Robert E Huie. Evanescent wave cavity ring-down spectroscopy with a total-internal-reflection minicavity. *Review of Scientific Instruments*, 68(8):2978–2989, 1997.

[147] Andrew C.R Pipino, Jeffrey W Hudgens, and Robert E Huie. Evanescent wave cavity ring-down spectroscopy for probing surface processes. *Chemical Physics Letters*, 280(1–2):104–112, 1997.

[148] Andrew C. R. Pipino. Ultrasensitive surface spectroscopy with a miniature optical resonator. *Physical Review Letters*, 83:3093–3096, 1999.

[149] Andrew M. Shaw, Theresa E. Hannon, Fuping Li, and Richard N. Zare. Adsorption of crystal violet to the silica-water interface monitored by evanescent wave cavity ring-down spectroscopy. *The Journal of Physical Chemistry B*, 107(29):7070–7075, 2003.

[150] Jonathan D. Fisk, Robin Batten, Glenn Jones, Josephine P. O'Reill, and Andrew M. Shaw. pH dependence of the crystal violet adsorption isotherm at the silica-water interface. *The Journal of Physical Chemistry B*, 109(30):14475–14480, 2005.

[151] Fuping Li and Richard N. Zare. Molecular orientation study of methylene blue at an air/fused-silica interface using evanescent-wave cavity ring-down spectroscopy. *The Journal of Physical Chemistry B*, 109(8):3330–3333, 2005.

[152] Hsiu-Fang Fan, Fuping Li, Richard N. Zare, and King-Chuen Lin. Characterization of two types of silanol groups on fused-silica surfaces using evanescent-wave cavity ring-down spectroscopy. *Analytical Chemistry*, 79(10):3654–3661, 2007.

[153] Theresa E. Hannon, Soonwoo Chah, and Richard N. Zare. Evanescent-wave cavity ring-down investigation of polymer/solvent interactions. *The Journal of Physical Chemistry B*, 109(15):7435–7442, 2005.

[154] I. M. P. Aarts, A. C. R. Pipino, J. P. M. Hoefnagels, W. M. M. Kessels, and M. C. M. van de Sanden. Quasi-ice monolayer on atomically smooth amorphous SiO_2 at room temperature observed with a high-finesse optical resonator. *Physical Review Letters*, 95:166104, 2005.

[155] Mikhail Mazurenka, Lucas Wilkins, Julie V. Macpherson, Patrick R. Unwin, and Stuart R. Mackenzie. Evanescent wave cavity ring-down spectroscopy in a thin-layer electrochemical cell. *Analytical Chemistry*, 78(19):6833–6839, 2006.

[156] Mikhail Mazurenka, Suzanne M. Hamilton, Patrick R. Unwin, and Stuart R. Mackenzie. In-situ measurement of colloidal gold adsorption on functionalized silica surfaces. *The Journal of Physical Chemistry C*, 112(16):6462–6468, 2008.

[157] Albert A. Ruth and Kieran T. Lynch. Incoherent broadband cavity-enhanced total internal reflection spectroscopy of surface-adsorbed metallo-porphyrins. *Physical Chemistry Chemical Physics*, 10:7098–7108, 2008.

[158] Shaowei Ong, Xiaolin Zhao, and Kenneth B. Eisenthal. Polarization of water molecules at a charged interface: second harmonic studies of the silica/water interface. *Chemical Physics Letters*, 191(3):327 – 335, 1992.

[159] C. E. Maceil. *The Encyclopedia of Nuclear Magnetic Resonance*. Wiley, 1996.

[160] Ying Dong, Sastry V. Pappu, and Zhi Xu. Detection of local density distribution of isolated silanol groups on planar silica surfaces using nonlinear optical molecular probes. *Analytical Chemistry*, 70(22):4730–4735, 1998.

[161] Michael Kasha. Energy transfer mechanisms and the molecular exciton model for molecular aggregates. *Radiation Research*, 20(1):55–70, 1963.

[162] M. Kasha, H. R. Rawls, and M. Ashraf El-Bayoumi. The exciton model in molecular spectroscopy. *Pure and Applied Chemistry*, 11(3-4):371, 1965.

[163] Divinomar Severino, Helena C. Junqueira, Marcos Gugliotti, Dino S. Gabrielli, and Mauricio S. Baptista. Influence of negatively charged interfaces on the ground and excited state properties of methylene blue. *Photochemistry and Photobiology*, 77(5):459–468, 2003.

[164] Jonathan D. Fisk, Maxim Rooth, and Andrew M. Shaw. Gold nanoparticle adsorption and aggregation kinetics at the silica-water interface. *The Journal of Physical Chemistry C*, 111(6):2588–2594, 2007.

[165] David W. Allan. Statistics of atomic frequency standards. *Proceedings of the IEEE*, 54(2):221–230, 1966.

[166] Justin M. Langridge, Stephen M. Ball, Alexander J. L. Shillings, and Roderic L. Jones. A broadband absorption spectrometer using light emitting diodes for ultrasensitive, in situ trace gas detection. *Review of Scientific Instruments*, 79(12):123110, 2008.

[167] Simon R. T. Neil. *Condensed-Phase Applications of Cavity-Based Spectroscopic Techniques*. PhD thesis, University of Oxford, 2012.

[168] F. Bielsa, A. Dupays, M. Fouché, R. Battesti, C. Robilliard, and C. Rizzo. Birefringence of interferential mirrors at normal incidence. *Applied Physics B*, 97(2):457–463, 2009.

[169] Jing Li. *Applications of Optical Cavity-Based Spectroscopic Techniques in the Condensed Phase*. PhD thesis, University of Oxford, 2013.

[170] R. M. A. Azzam. Phase shifts that accompany total internal reflection at a dielectric–dielectric interface. *Journal of the Optical Society of America*, 21(8):1559–1563, 2004.

[171] Liam Byrne, King Tong Lau, and Dermot Diamond. Monitoring of headspace total volatile basic nitrogen from selected fish species using reflectance spectroscopic measurements of ph sensitive films. *Analyst*, 127:1338–1341, 2002.

[172] Eleonora Petryayeva and Ulrich J. Krull. Localized surface plasmon resonance: Nanostructures, bioassays and biosensing—a review. *Analytica Chimica Acta*, 706(1):8–24, 2011.

[173] Krishnendu Saha, Sarit S. Agasti, Chaekyu Kim, Xiaoning Li, and Vincent M. Rotello. Gold nanoparticles in chemical and biological sensing. *Chemical Reviews*, 112(5):2739–2779, 2012.

[174] Kathryn M. Mayer and Jason H. Hafner. Localized surface plasmon resonance sensors. *Chemical Reviews*, 111(6):3828–3857, 2011.

[175] Wyatt P. McConnell, James P. Novak, Louis C. Brousseau, Ryan R. Fuierer, Robert C. Tenent, and Daniel L. Feldheim. Electronic and optical properties of chemically modified metal nanoparticles and molecularly bridged nanoparticle arrays. *The Journal of Physical Chemistry B*, 104(38):8925–8930, 2000.

[176] Louis C. Brousseau III, James P. Novak, Stella M. Marinakos, and Daniel L. Feldheim. Assembly of phenylacetylene-bridged gold nanocluster dimers and trimers. *Advanced Materials*, 11(6):447–449, 1999.

[177] S. Link, M. B. Mohamed, and M. A. El-Sayed. Simulation of the optical absorption spectra of gold nanorods as a function of their aspect ratio and the effect of the medium dielectric constant. *The Journal of Physical Chemistry B*, 103(16):3073–3077, 1999.

[178] Yuh-Shan Ho, R Malarvizhi, and N Sulochana. Equilibrium isotherm studies of methylene blue adsorption onto activated carbon prepared from delonix regia pods. *Journal of environmental protection science*, 3:111–116, 2009.

[179] R Malarvizhi and N Sulochana. Sorption isotherm and kinetic studies of methylene blue uptake onto activated carbon prepared from wood apple shell. *Journal of Environmental Protection Science*, 2:40–46, 2008.

[180] C. Mahamadi and E. Mawere. Kinetic modeling of methylene blue and crystal violet dyes adsorption on alginate-fixed water hyacinth in single and binary systems. *American Journal of Analytical Chemistry*, 4(10):17–24, 2013.

[181] Li Wang, Junping Zhang, and Aiqin Wang. Fast removal of methylene blue from aqueous solution by adsorption onto chitosan-g-poly (acrylic acid)/attapulgite composite. *Desalination*, 266(1–3):33–39, 2011.

[182] Jianhui Shi, Xiaozhen Ren, Lizhu Tong, Xiaodong Chen, Xuwei Yang, and Hua Yang. In situ assembly of monodisperse, multifunctional silica microspheres embedded with magnetic and fluorescent nanoparticles and their application in adsorption of methylene blue. *Physical Chemistry Chemical Physics*, 15:18642–18648, 2013.

[183] Zohre Shahryari, Ataallah Soltani Goharrizi, and Mehdi Azadi. Experimental study of methylene blue adsorption from aqueous solutions onto carbon nano tubes. *International Journal of Water Resources and Environmental Engineering*, 2:16–28, Mar 2010.

[184] K. Bergmann and C. T. O'Konski. A spectroscopic study of methylene blue monomer, dimer, and complexes with montmorillonite. *The Journal of Physical Chemistry*, 67(10):2169–2177, 1963.

[185] Shane M. Ohline, Sunyoung Lee, Stacie Williams, and Connie Chang. Quantification of methylene blue aggregation on a fused silica surface and resolution of individual absorbance spectra. *Chemical Physics Letters*, 346(1–2):9–15, 2001.

[186] Emory Braswell. Evidence for trimerization in aqueous solutions of methylene blue. *The Journal of Physical Chemistry*, 72(7):2477–2483, 1968.

[187] Yonghui Lin, Xingbing He, Guomin Han, Qijian Tian, and Wenyong Hu. Removal of crystal violet from aqueous solution using powdered mycelial biomass of ceriporia lacerata P2. *Journal of Environmental Sciences*, 23(12):2055–2062, 2011.

[188] L. van der Sneppen, J. B. Buijs, C. Gooijer, W. Ubachs, and F. Ariese. Evanescent-wave cavity ring-down spectroscopy for enhanced detection of surface binding under flow injection analysis conditions. *Applied Spectroscopy*, 62(6):649–654, 2008.

[189] Meng-Chen Lin and King-Chuen Lin. Interaction between crystal violet and anionic surfactants at silica/water interface using evanescent wave-cavity ring-down absorption spectroscopy. *Journal of Colloid and Interface Science*, 379(1):41–47, 2012.

[190] Z. Chernia, D. Gill, and S. Yariv. Electric dichroism. the effect of dialysis on the color of crystal violet adsorbed to montmorillonite. *Langmuir*, 10(11):3988–3993, 1994.

[191] Kiwamu Yamaoka and Ryo Sasai. Pulsed electric linear dichroism of triphenylmethane dyes adsorbed on montmorillonite K10 in aqueous media. *Journal of Colloid and Interface Science*, 225(1):82–93, 2000.

[192] S. R. Coon, T. Y. Zakharian, N. L. Littlefield, S. P. Loheide, E. J. Puchkova, R. M. Freeney, and V. N. Pak. Reversible metachromasy of crystal violet on titanium dioxide: A new surface photophysical phenomenon. *Langmuir*, 16(25):9690–9693, 2000.

[193] Jianxi Zhu, Jingming Wei, Runliang Zhu, Yanhong Qing, Fei Ge, Peng Yuan, and Hongping He. Simultaneous and sequential adsorption of crystal violet and 2-naphthol onto montmorillonite: a microstructural and thermodynamic study. *Water Science & Technology*, 62(8):1767, 2010.

[194] Gilbert N. Lewis, Theodore T. Magel, and David Lipkin. Isomers of crystal violet ion. their absorption and re-emission of light. *Journal of the American Chemical Society*, 64(8):1774–1782, 1942.

[195] J. Korppi-Tommola and R. W. Yip. Solvent effects on the visible absorption spectrum of crystal violet. *Canadian Journal of Chemistry*, 59(2):191–194, 1981.

[196] Horst B. Lueck, Bobbie L. Rice, and Jeanne L. McHale. Aggregation of triphenylmethane dyes in aqueous solution: Dimerization and trimerization of crystal violet and ethyl violet. *Spectrochimica Acta Part A: Molecular Spectroscopy*, 48(6):819–828, 1992.

[197] Yoshihiro Maruyama, Mitsuru Ishikawa, and Hiroshi Satozono. Femtosecond isomerization of crystal violet in alcohols. *Journal of the American Chemical Society*, 118(26):6257–6263, 1996.

[198] Claire Loison, Rodolphe Antoine, Michel Broyer, Philippe Dugourd, Julien Guthmuller, and Daniel Simon. Microsolvation effects on the optical properties of crystal violet. *Chemistry – A European Journal*, 14(24):7351–7357, 2008.

[199] Roberto Macovez, Nuria Lopez, Marina Mariano, Marc Maymò, and Jordi Martorell. Molecular conformation in organic films from quantum chemistry *ab initio* calculations and second harmonic spectroscopy. *The Journal of Physical Chemistry C*, 116(51):26784–26790, 2012.

[200] Horst B. Lueck, Jeanne L. McHale, and W. D. Edwards. Symmetry-breaking solvent effects on the electronic structure and spectra of a series of triphenylmethane dyes. *Journal of the American Chemical Society*, 114(7):2342–2348, 1992.

[201] Kazuhiro Nakanishi, Takaharu Sakiyama, and Koreyoshi Imamura. On the adsorption of proteins on solid surfaces, a common but very complicated phenomenon. *Journal of Bioscience and Bioengineering*, 91(3):233–244, 2001.

[202] Jocelyne Ethève and Philippe Déjardin. Adsorption kinetics of lysozyme on silica at pH 7: Correlation between streaming potential and adsorbed amount. *Langmuir*, 18(5):1777–1785, 2002.

[203] G. Jackler, R. Steitz, and C. Czeslik. Effect of temperature on the adsorption of lysozyme at the silica/water interface studied by optical and neutron reflectometry. *Langmuir*, 18(17):6565–6570, 2002.

[204] Jian R Lu, Marcus J Swann, Louise L Peel, and Neville J Freeman. Lysozyme adsorption studies at the silica/water interface using dual polarization interferometry. *Langmuir*, 20(5):1827–1832, 2004.

[205] Andrew Osborne, Roger N. F. Thorneley, Chris Abell, and Stephen Bornemann. Studies with substrate and cofactor analogues provide evidence for a radical mechanism in the chorismate synthase reaction. *Journal of Biological Chemistry*, 275(46):35825–35830, 2000.

[206] Bin Liu, Hongtao Liu, Dongping Zhong, and Chentao Lin. Searching for a photocycle of the cryptochrome photoreceptors. *Current Opinion in Plant Biology*, 13(5):578–586, 2010.